

ABSTRACT

CATENACCI, JARED WILLIAM. Quantifying Degradation in Ceramic Matrix Composites Through Electromagnetic Interrogation and the Related Estimation Techniques. (Under the direction of Dr. Harvey Banks.)

Reflectance spectroscopy obtained from thermally treated silicon nitride carbon based ceramic matrix composites is used to quantify the oxidation products SiO_2 and SiN . The data collection is described in detail in order to point out the potential biasing present in the data processing. A probability distribution is imposed on selected dielectric model parameters, and then non-parametrically estimated. A non-parametric estimation is chosen since the exact composition of the material is unknown due to the inherent heterogeneity of ceramic composites. The probability distribution is estimated using the Prohorov metric framework (PMF) in which the infinite dimensional optimization is reduced to a finite dimensional optimization using an approximating space composed of linear splines. A weighted least squares estimation is carried out, and uncertainty quantification is performed on the model parameters. Our estimation results indicate a distinguishable increase in the SiO_2 present in the samples which were heat treated for 100 hours compared to those treated for 10 hours.

To establish probability measure estimation in a nonparametric model using the Prohorov Metric Framework, we first summarize the computational methods and related convergence results that were recently developed by our group. Results are presented on the bias and the variance due to the approximation and the pointwise asymptotic normality of the approximated probability measure estimator is established. We propose use of a model selection criterion to balance the bias and the variance, and compare the pointwise confidence bands constructed using the asymptotic normality results with that obtained by Monte Carlo simulations. Additionally, we propose a method in which the information provided by difference based approximations of the measurement errors is used as a way of determining the presence of statistical model discrepancy. A number of numerical examples are given to illustrate the effectiveness of these proposed methods.

Additionally, we investigate the feasibility of quantifying properties of a composite dielectric material through the reflectance in which we estimate an unknown probability measure by means of the PMF. We point out the limitation of the existing computational algorithms for this particular application. We then improve the algorithms, and demonstrate the feasibility of our proposed methods by numerical results obtained for both simulated data and experimental data for inorganic glass. We compare this with a second, more classical approach, where it is assumed that the permittivity is composed of a number of oscillators, and then a convolution is taken with a normal distribution. Each of these methods are able to fit the data well, yet

the ease in interpreting the estimation results in using the PMF approach, as well as the tight mathematical results guaranteeing convergence under the Prohorov metric, lead us to favor this approach.

Quantifying Degradation in Ceramic Matrix Composites Through
Electromagnetic Interrogation and the Related Estimation Techniques

by
Jared William Catenacci

A dissertation submitted to the Graduate Faculty of
North Carolina State University
in partial fulfillment of the
requirements for the Degree of
Doctor of Philosophy

Applied Mathematics

Raleigh, North Carolina

2016

APPROVED BY:

Dr. Amanda Criner
Technical Consultant

Dr. Kevin Flores

Dr. Shuhua Hu

Dr. Gerald LeBlanc

Dr. Ralph Smith

Dr. Harvey Banks
Chair of Advisory Committee

DEDICATION

To my parents, family, and close friends for their continued support.

BIOGRAPHY

Jared Catenacci was born in Ocala FL, at the age of 10 he landed in Appleton WI, in where he now considers to be his home town. He received his B.S. in Mathematics from the University of Wisconsin–Milwaukee in 2012. In August of that year, Jared began his graduate studies at North Carolina State Univeristy in Applied Mathematics with his Ph.D. advisor Dr. H.T. Banks.

ACKNOWLEDGEMENTS

I would like to thank my advisor and friend H.T. Banks for his continual encouragement and support. A very special thanks to Shuhua Hu, who patiently provided careful guidance and through her example set a standard to aspire toward in my own career. Thanks also to the many people who early in my academic career guided and inspired me as a student and young researcher, in particular, Gabriella Pinter, Istvan Lauko, and Sarah Patch.

This research was supported in part by Grant Number NIAID R01AI071915-10 from the National Institute of Allergy and Infectious Diseases, in part by the Air Force Office of Scientific Research under grant numbers AFOSR FA9550-12-1-0188, AFOSR FA9550-15-1-0298 and AFOSR-UDRI Contract RSCI5002, in part by the National Science Foundation under Research Training Grant (RTG) DMS-0636590, in part by the Army Research Office under contract number W911NF-13-P-0017, in part by the US Department of Education Graduate Assistance in Areas of National Need (GAANN) under grant number P200A120047.

TABLE OF CONTENTS

LIST OF TABLES	viii
LIST OF FIGURES	x
Chapter 1 Introduction	1
1.1 Motivation	1
1.2 Problem Description	3
1.2.1 Reflection Coefficient: Perpendicular Polarization	4
1.2.2 Reflection Coefficient: Parallel Polarization	6
1.2.3 Reflection Coefficient Between Free Space and a Lossy Material	7
1.2.4 Complex Permittivity	8
Chapter 2 The Prohorov Metric	9
2.1 Introduction	9
2.2 Theoretical and Computational Framework for Probability Measure Estimation	11
2.2.1 Consistency of the Probability Measure Estimator	13
2.2.2 Approximation Schemes for Probability Measure Estimation	14
2.2.3 Bias and Variance in Probability Measure Estimation	16
2.2.4 Pointwise Asymptotic Normality of the Approximate Probability Measure Estimator	18
2.3 Numerical Results	20
2.3.1 Optimal Value of M	21
2.3.2 Pointwise Confidence Band	22
2.4 Concluding Remarks and Future Research Questions	26
Chapter 3 Use of Difference-Based Methods to Explore Statistical and Mathematical Model Discrepancy in Inverse Problems	27
3.1 Introduction	27
3.2 Difference-Based Methods	33
3.3 Application on Determining an Appropriate Statistical Model	35
3.3.1 Numerical Results for Simulated Data Sets	35
3.3.2 Numerical Results for Experimental Data Sets	47
3.4 Application on Detecting Mathematical Model Misspecification and Bootstrapping	49
3.5 Concluding Remarks and Future Research Questions	55
Chapter 4 Estimation of Distributed Parameters in Permittivity Models of Composite Dielectric Materials Using Reflectance	56
4.1 Introduction	56
4.2 The Model for the Complex Dielectric Constant and the Reflection Coefficient	56
4.3 Computational Framework	58
4.3.1 Statistical Model	58
4.3.2 Inverse Problem	59
4.4 Numerical Results	60

4.4.1	Results Obtained Using Simulated Data When Estimating a Probability Measure on the Resonance Wavenumber	61
4.4.2	Results Obtained Using Inorganic Glass Data When Estimating a Probability Measure on the Resonance Wavenumber	65
4.4.3	Results Obtained Using Simulated Data When Estimating a Probability Measure on the Relaxation Time	70
4.5	Concluding Remarks and Future Research Efforts	75
Chapter 5 Method Comparison For Estimation Of Distributed Parameters In Permittivity Models Using Reflectance		77
5.1	Introduction	77
5.2	The Model for the Complex Permittivity and the Reflection Coefficient	78
5.2.1	Efimov model for permittivity	78
5.2.2	Prohorov Metric Framework Model for Permittivity	78
5.2.3	Reflection Coefficient	79
5.2.4	Statistical Model	80
5.2.5	Inverse Problem	80
5.3	Results	82
5.3.1	Simulated Data	82
5.3.2	Inorganic Glass Data	87
5.4	Concluding Remarks and Future Work	94
Chapter 6 Quantifying the Degradation in Thermally Treated Ceramic Matrix Composites		96
6.1	Introduction	96
6.2	The Model for the Complex Permittivity and the Reflectance	97
6.3	Interferogram to Spectrum	98
6.3.1	Measurement Errors	99
6.4	Inverse Problem	100
6.4.1	Statistical Model	100
6.4.2	Weighted Least Squares	104
6.4.3	Uncertainty Quantification	105
6.5	Results	107
6.5.1	Consistency as M Increases	107
6.5.2	Optimal Value of M	109
6.5.3	Comparison of Heat Treated Samples	111
6.5.4	Pointwise Confidence Bands	114
6.5.5	Comparison to Bootstrapping and Bayesian Estimation	120
6.6	Concluding Remarks	125
Chapter 7 Aggregate Data and the Prohorov Metric Framework: Efficient Gradient Computation		128
7.1	Introduction	128
7.2	Problem framework	129
7.2.1	Individual models	131

7.2.2	Aggregate models	133
7.3	Example: Sinko-Streifer Model	133
7.4	Example: Reflectance Spectroscopy Model	135
7.5	Conclusions	137
Chapter 8 Concluding Remarks		139
References		141

LIST OF TABLES

Table 2.1	The confidence intervals (CI) computed using the pointwise asymptotic normality (AN) results and the ones obtained using the Monte Carlo (MC) simulations.	25
Table 3.1	Results for the logistic example in the case where $\gamma = 0$: the true value of σ_0 as well as its estimates obtained using the three mentioned methods ($\hat{\sigma}_0^{1st}$ is obtained using the first-order differencing method, $\hat{\sigma}_0^{2nd}$ is obtained using the second-order differencing method, and $\hat{\sigma}_0^{1st-3}$ is obtained by the third-order differencing method).	36
Table 3.2	Results for the SIR example in the case where $\gamma_i = 0$, $i = 1, 2, 3$: the value of $\sigma_{0,i}$ as well as its estimates obtained using the three methods introduced in Section 3.2.	40
Table 3.3	The mean and standard error of the bootstrapping estimator for the logistic example of this section obtained using Algorithm 3.4.1 and Modified algorithm 3.4.2.	55
Table 4.1	Estimations obtained using the simulated data for various numbers of Dirac measures.	64
Table 4.2	Estimations obtained using the reflectance data for Vitreous Germania using various numbers of Dirac measures.	69
Table 4.3	Parameter estimates obtained using the reflectance data for Vitreous Silica employing various numbers of Dirac measures compared to experimental values (abbreviated as Expt. in the table) taken from [65].	74
Table 5.1	The estimated parameters using the Dirac and spline approximation methods for the discrete distribution.	84
Table 5.2	The estimated values of the intensities S_j , the relaxation times τ_j , the resonance wavenumbers $k_{0,j}$ and the standard deviations σ_j for each oscillator using the modified Efimov approach, using the simulated data with a discrete distribution.	84
Table 5.3	The estimated parameters using the Dirac and spline approximation methods for the simulated data with a continuous distribution.	85
Table 5.4	The estimated values of the intensities S_j , the relaxation times τ_j , the resonance wavenumbers $k_{0,j}$ and the standard deviations σ_j for each oscillator using the modified Efimov approach using the simulated data with a continuous distribution.	87
Table 5.5	The estimated parameter values using the Dirac and spline approximation methods to fit the Vitreous Silica data. The “true” parameter values θ_0 are the experimental values taken from [65].	89
Table 5.6	The estimated values of the intensities S_j , the relaxation times τ_j , the resonance wavenumbers $k_{0,j}$ and the standard deviations σ_j for each oscillator using the modified Efimov approach on the Vitreous Silica data.	89
Table 5.7	The estimated parameter values using the Dirac and spline approximation methods to fit the Vitreous Germania data.	91

Table 5.8	The estimated values of the intensities S_j , the relaxation times τ_j , the resonance wavenumbers k_{0_j} and the standard deviations σ_j for each oscillator using the modified Efimov approach on the data obtain from Vitreous Germania. . . .	91
Table 5.9	The estimated parameter values using the Dirac and spline approximation methods as compared to the Efimov method to fit the Sodium Silicate Silica data.	93
Table 5.10	The estimated values of the intensities S_j , the relaxation times τ_j , the resonance wavenumbers k_{0_j} and the standard deviations σ_j for each oscillator using the modified Efimov approach on the Sodium Silicate data.	93
Table 6.1	The estimated parameters using a data set from the 10 hour heat treated sample 32 for $M = 74$ and 75	108
Table 6.2	The estimated parameters using a data set from the 100 hour heat treated sample 13 for $M = 72$ and 74	109
Table 6.3	The estimated parameters using a data set from the 10 hour heat treated sample 4 for $M = 70, 71$ and 80	109
Table 6.4	Estimated parameters using the first 3 locations from each sample.	115
Table 6.5	The 95% confidence intervals for the estimated model parameters from a representative data set from the 10 and 100 hour heat treated samples. . . .	116
Table 6.6	The 95% confidence intervals (credible intervals for the Bayesian estimation) for the estimated model parameters from a representative data set from the 10 hour heat treated sample 32 using asymptotic theory (WLS), bootstrapping, and Bayesian estimation.	122
Table 6.7	The 95% confidence intervals (credible intervals for the Bayesian estimation) for the estimated model parameters from a representative data set from the 100 hour heat treated sample 1 using asymptotic theory (WLS), bootstrapping, and Bayesian estimation.	122

LIST OF FIGURES

Figure 1.1	A monochromatic uniform wave is incident at an angle ϕ on a plane interface between a free space and a nonmagnetic dielectric medium, where ω denotes the frequency of the wave.	3
Figure 2.1	Illustration of the bias and the variance in the probability measure approximation.	18
Figure 2.2	Illustration of the trade-off between the bias and the variance.	18
Figure 2.3	The AIC_c values for model (2.2.11) with $M = 5, 10, 15, 20, 25$ and 30	23
Figure 2.4	The pointwise confidence bands for the cumulative distribution function obtained using the pointwise asymptotic normality results (left) and the ones obtained using the Monte Carlo simulations (right).	25
Figure 3.1	Comparison of the plot of $\hat{\varepsilon}_j^{1st}$ (denoted as “estimates” in the legend) versus t_j and the plot of ε_j (denoted as “true value”) versus t_j : (left panel) results obtained for $\gamma = 0$; (right panel) results obtained for $\gamma = 1$, where $\hat{\varepsilon}_j^{1st}$ ’s are obtained by the first-order differencing method.	37
Figure 3.2	Comparison of the plot of the $\hat{\varepsilon}_j^{2nd}$ (denoted as “estimates” in the legend) versus t_j and the plot of ε_j (denoted as “true value”) versus t_j for the case $\gamma = 0$ (left panel) and the case $\gamma = 1$ (right panel), where the $\hat{\varepsilon}_j^{2nd}$ are obtained using the second-order differencing method.	37
Figure 3.3	Comparison of the plot of the $\hat{\varepsilon}_j^{1st-3}$ (denoted as “estimates” in the legend) versus t_j and the plot of ε_j (denoted as “true value”) versus t_j for the case $\gamma = 0$ (left panel) and the case $\gamma = 1$ (right panel), where the $\hat{\varepsilon}_j^{1st-3}$ are obtained by applying the first-order differencing operator for 3 times.	38
Figure 3.4	Plot of $\eta_j^{\tilde{\gamma}} = \hat{\varepsilon}_j^{1st-3}/ y_j - \hat{\varepsilon}_j^{1st-3} ^{\tilde{\gamma}}$ versus t_j for the case where the simulated data were generated with $\gamma = 1$: (left panel) $\tilde{\gamma} = 2$; (right panel) $\tilde{\gamma} = 1$	39
Figure 3.5	Plot of $\eta_j^{\tilde{\gamma}} = \hat{\varepsilon}_j^{2nd}/ y_j - \hat{\varepsilon}_j^{2nd} ^{\tilde{\gamma}}$ versus t_j for the case where the simulated data were generated with $\gamma = 1$: (left panel) $\tilde{\gamma} = 2$; (right panel) $\tilde{\gamma} = 1$	39
Figure 3.6	Comparison of the plot of $\hat{\varepsilon}_{ij}^{1st}$ (denoted as “estimates” in the legend) versus t_j and the plot of ε_{ij} (denoted as “true value”) versus t_j for the case $\gamma_1 = \gamma_2 = \gamma_3 = 0$ (left column) and the case $\gamma_1 = \gamma_2 = \gamma_3 = 1$ (right column). . . .	41
Figure 3.7	Comparison of the plot of $\hat{\varepsilon}_{ij}^{2nd}$ (denoted as “estimates” in the legend) versus t_j and the plot of ε_{ij} (denoted as “true value”) versus t_j for the case $\gamma_1 = \gamma_2 = \gamma_3 = 0$ (left column) and the case $\gamma_1 = \gamma_2 = \gamma_3 = 1$ (right column). . . .	42
Figure 3.8	Comparison of the plot of $\hat{\varepsilon}_{ij}^{1st-3}$ (denoted as “estimates” in the legend) versus t_j and the plot of ε_{ij} (denoted as “true value”) versus t_j for the case $\gamma_1 = \gamma_2 = \gamma_3 = 0$ (left column) and the case $\gamma_1 = \gamma_2 = \gamma_3 = 1$ (right column). . . .	43
Figure 3.9	Plot of $\eta_{ij}^{\tilde{\gamma}_i} = \hat{\varepsilon}_{ij}^{1st-3}/ y_{ij} - \hat{\varepsilon}_{ij}^{1st-3} ^{\tilde{\gamma}_i}$ versus t_j for the case where the simulated data were generated with $\gamma_1 = \gamma_2 = \gamma_3 = 1$: (left panel) $\tilde{\gamma}_1 = \tilde{\gamma}_2 = \tilde{\gamma}_3 = 2$; (right panel) $\tilde{\gamma}_1 = \tilde{\gamma}_2 = \tilde{\gamma}_3 = 1$	45

Figure 3.10	Plot of $\eta_{ij}^{\tilde{\gamma}} = \hat{\varepsilon}_{ij}^{2\text{nd}}/ y_{ij} - \hat{\varepsilon}_{ij}^{2\text{nd}} ^{\tilde{\gamma}}$ versus t_j for the case where the simulated data were generated with $\gamma_1 = \gamma_2 = \gamma_3 = 1$: (left panel) $\tilde{\gamma}_1 = \tilde{\gamma}_2 = \tilde{\gamma}_3 = 2$; (right panel) $\tilde{\gamma}_1 = \tilde{\gamma}_2 = \tilde{\gamma}_3 = 1$	46
Figure 3.11	Time plots for pseudo measurement errors obtained for the Daphnia data set presented in [1]: (left panel) using the second-order differencing method; (right panel) using the method for applying the first-order differencing operator for three times (right).	47
Figure 3.12	Plots for pseudo measurement errors obtained for the CFSE data set presented in [33, Section 3.5.3] by using the second-order differencing method: (left panel) plot of $\hat{\varepsilon}_j$ versus j ; (right panel) plot of $\eta_j^{\tilde{\gamma}} = \hat{\varepsilon}_j^{2\text{nd}}/ y_j - \hat{\varepsilon}_j^{2\text{nd}} ^{\tilde{\gamma}}$ versus j with $\tilde{\gamma} = 0.5$. The vertical lines delineate the pseudo measurement errors obtained in time intervals $[s_k, s_{k+1})$, $k = 1, 2, \dots, 7$	48
Figure 3.13	Plots for pseudo measurement errors obtained for the CFSE data set presented in [33, Section 3.5.3] by applying the first-order differencing operators for three times: (left panel) plot of $\hat{\varepsilon}_j$ versus j ; (right panel) plot of $\eta_j^{\tilde{\gamma}} = \hat{\varepsilon}_j^{1\text{st-3}}/ y_j - \hat{\varepsilon}_j^{1\text{st-3}} ^{\tilde{\gamma}}$ versus j with $\tilde{\gamma} = 0.5$. The vertical lines delineate the pseudo measurement errors obtained in time intervals $[s_k, s_{k+1})$, $k = 1, 2, \dots, 7$	50
Figure 3.14	Results for fitting exponential growth model (3.4.1) to the simulated data generated by the logistic growth model (3.3.1).	51
Figure 3.15	(left panel): plot of pseudo measurement errors $\hat{\varepsilon}_j^{2\text{nd}}$ versus t_j , where $\hat{\varepsilon}_j^{2\text{nd}}$'s are obtained by applying the second-order differencing method to the simulated data generated by the logistic growth model (3.3.1); (right panel): residual plot (i.e., a plot of r_j versus t_j) obtained by fitting exponential growth model (3.4.1) to the simulated data generated by logistic growth model (3.3.1).	52
Figure 4.1	The model fit to the simulated data (left) and the estimated distribution of wavenumbers (right), where the nodes are evenly placed over $[405, 1080]$ with $M = 25$	62
Figure 4.2	The model fit to the simulated data (left) and the estimated distribution of wavenumbers (right), where the nodes are evenly placed over $[405, 1100]$ with $M = 25$	62
Figure 4.3	Model fit (left) and estimated distribution (right) where the parameters $\varepsilon_s, \varepsilon_\infty$ and τ are fixed and the weights and node locations were optimized with $M = 25$	63
Figure 4.4	Model fit (left) and the estimated distribution (right) from the full inverse problem (4.4.3) where $M = 5$	64
Figure 4.5	Model fit (left) and the estimated distribution (right) from the full inverse problem (4.4.3) where $M = 10$	65
Figure 4.6	Model fit (left) and the estimated distribution (right) from the full inverse problem (4.4.3) where $M = 15$	65
Figure 4.7	Model fit (left) and the estimated distribution (right) from the full inverse problem (4.4.3) where $M = 20$	66
Figure 4.8	Model fit (left) and the estimated distribution (right) from the full inverse problem (4.4.3) where $M = 25$	66

Figure 4.9	Model fit (left) and the estimated distribution (right) from the full inverse problem (4.4.3) where $M = 30$	67
Figure 4.10	Model fit (left) and the estimated distribution (right) from the full inverse problem (4.4.3) where $M = 5$ for Vitreous Germania.	67
Figure 4.11	Model fit (left) and the estimated distribution (right) from the full inverse problem (4.4.3) where $M = 10$ for Vitreous Germania.	68
Figure 4.12	Model fit (left) and the estimated distribution (right) from the full inverse problem (4.4.3) where $M = 15$ for Vitreous Germania.	68
Figure 4.13	Model fit (left) and the estimated distribution (right) from the full inverse problem (4.4.3) where $M = 20$ for Vitreous Germania.	69
Figure 4.14	Model fit (left) and the estimated distribution (right) from the full inverse problem (4.4.3) where $M = 25$ for Vitreous Germania.	69
Figure 4.15	The estimated distributions for all values of M considered from the Vitreous Germania data.	70
Figure 4.16	Model fit (left) and the estimated distribution (right) from the full inverse problem (4.4.3) where $M = 5$ for Vitreous Silica.	71
Figure 4.17	Model fit (left) and the estimated distribution (right) from the full inverse problem (4.4.3) where $M = 10$ for Vitreous Silica.	71
Figure 4.18	Model fit (left) and the estimated distribution (right) from the full inverse problem (4.4.3) where $M = 15$ for Vitreous Silica.	72
Figure 4.19	Model fit (left) and the estimated distribution (right) from the full inverse problem (4.4.3) where $M = 20$ for Vitreous Silica.	72
Figure 4.20	Model fit (left) and the estimated distribution (right) from the full inverse problem (4.4.3) where $M = 25$ for Vitreous Silica.	73
Figure 4.21	The estimated distributions for all values of M considered from the Vitreous Silica data.	73
Figure 4.22	Model fit (left), and the estimated distribution (right) with $M = 15$ fixed nodes.	74
Figure 4.23	Model fit (left) and the estimated distribution (right) where both $M = 15$ node weights and locations were optimized.	74
Figure 4.24	Model fit (left), the derivative of reflectance fit (right), and the estimated distribution (bottom) where both $M = 15$ node weights and locations were optimized.	75
Figure 5.1	The model fits to the simulated data generated with a discrete distribution. The model fit using the Dirac approximation scheme is labeled as D45 and the spline approximation schemes as S45, where 45 is the number of nodes M , and the model fit using the modified Efimov method is labeled as E6 where $J = 6$ oscillators were used.	83
Figure 5.2	The estimated distributions to the simulated data using a discrete distribution using the Dirac approximation method with $M = 15, 25, 35$ and 45 nodes (left) and using the spline approximation method with $M = 25, 35, 45$ and 55 nodes (right).	83

Figure 5.3	The model fits to the simulated data generated with a continuous distribution. For the Dirac and spline approximation schemes the number of nodes was taken as $M = 25$ (labeled as D25 and S25 respectively) and for the Efimov approach we have $J = 2$ (labeled as E2).	86
Figure 5.4	The estimated distributions to the simulated data using a continuous distribution using the Dirac approximation method (left) and using the spline approximation method (right). For both methods we chose the number of nodes to be $M = 10, 15, 20$ and 25 .	86
Figure 5.5	The model fits to the Vitreous Silica data.. For the Dirac and spline approximation schemes the number of nodes was taken as $M = 50$ (labeled as D50 and S50 respectively) and for the Efimov approach we have $J = 8$ (labeled as E8).	88
Figure 5.6	The estimated distributions to the Vitreous Silica data using the Dirac approximation method (left) and using the spline approximation method (right). For both methods we chose the number of nodes to be $M = 30, 50$ and 80 .	88
Figure 5.7	The model fits to the Vitreous Germania data. For the Dirac and spline approximation schemes the number of nodes was taken as $M = 50$ (labeled as D50 and S50 respectively) and for the Efimov approach we have $J = 8$ (labeled as E8).	90
Figure 5.8	The estimated distributions to the Vitreous Germania data using the Dirac approximation method (left) and using the spline approximation method (right). For both methods we chose the number of nodes to be $M = 30, 50$ and 80 .	90
Figure 5.9	The model fits to the Sodium Silicate data. For the Dirac and spline approximation schemes the number of nodes was taken as $M = 25$ (labeled as D25 and S25 respectively) and for the Efimov approach we have $J = 9$ (labeled as E9).	92
Figure 5.10	The estimated distributions to the Sodium Silicate data using the Dirac approximation method (left) and using the spline approximation method (right). For both methods we chose the number of nodes to be $M = 25$ and 30 .	93
Figure 6.1	Example reflectance data sets from sample 4 which was heat treated for 10 hours (the black dots) and from sample 1 which was heat treated for 100 hours (the blue circles).	97
Figure 6.2	Double sided, bi-directional interferogram.	99
Figure 6.3	Estimated measurement error, in percent reflectance, obtained when using a zerofilling factor of 8 and averaging the spectrum from first and second ZPD.	101
Figure 6.4	Estimated measurement error obtained, in percent reflectance, when using a zerofilling factor of 8 and using only the spectrum from first ZPD.	101
Figure 6.5	Estimated measurement error obtained, in percent reflectance, when using no zero padding and using only the spectrum from first ZPD.	102
Figure 6.6	Estimated measurement error from a data set from Sample 1 obtained when using no zero padding and using only the spectrum from first ZPD.	102

Figure 6.7	Plot of the weights w_j (left) and $\hat{\eta}_j = w_j^{-1}\hat{\nu}_j$ (right) for the 100 hour heat treated sample 1.	103
Figure 6.8	Using a data set from the 10 hour heat treated sample 32, the model fit to the data (left) and the estimated density (right) using $M = 74$ and 75 nodes.	108
Figure 6.9	Using a data set from the 100 hour heat treated sample 13, the model fit to the data (left) and the estimated density (right) using $M = 72$ and 74 nodes.	108
Figure 6.10	Using a data set from the 10 hour heat treated sample 4, the model fit to the data (left) and the estimated density (right) using $M = 70, 71$ and 80 nodes.	109
Figure 6.11	A snapshot of the AIC_c values using a data set obtained from the 10 hour heat treated sample 4 with $M = 70, 71, \dots, 90$	112
Figure 6.12	The model fits (left) and estimated densities (right) using the first three locations of the data obtained from the 10 hour heat treated sample 4.	112
Figure 6.13	The model fits (left) and estimated densities (right) using the first three locations of the data obtained from the 10 hour heat treated sample 16.	113
Figure 6.14	The model fits (left) and estimated densities (right) using the first three locations of the data obtained from the 10 hour heat treated sample 32.	113
Figure 6.15	The model fits (left) and estimated densities (right) using the first three locations of the data obtained from the 100 hour heat treated sample 1.	114
Figure 6.16	The model fits (left) and estimated densities (right) using the first three locations of the data obtained from the 100 hour heat treated sample 13.	114
Figure 6.17	The estimated densities for each location from the 10 hour heat treated data obtained from sample 4 (top left), sample 16 (top right), and sample 32 (bottom center).	116
Figure 6.18	The estimated densities for each location from the 100 hour heat treated data obtained from sample 1 (left) and sample 13 (right).	117
Figure 6.19	The mean density for each sample.	117
Figure 6.20	The modified residuals versus wavenumber k (left) and versus the model solution (right) for the 10 hour heat treated sample 32.	118
Figure 6.21	The modified residuals versus wavenumber k (left) and versus the model solution (right) for the 100 hour heat treated sample 1.	118
Figure 6.22	The estimated density and the corresponding pointwise confidence band for a data set obtained from the 10 hour heat treated sample 32.	119
Figure 6.23	The estimated density and the corresponding pointwise confidence band for a data set obtained from the 100 hour heat treated sample 1.	119
Figure 6.24	Comparison of the estimated density using weighted least squares (WLS), bootstrapping, and Bayesian estimation for a 10 hour heat treated data set from sample 1.	123
Figure 6.25	Comparison of the 95% confidence/credible intervals (CI) for the estimated weights using asymptotic theory (WLS), bootstrapping, and Bayesian estimation for a 10 hour heat treated data set from sample 1.	123
Figure 6.26	Comparison of the estimated density using weighted least squares (WLS), bootstrapping, and Bayesian estimation for a 100 hour heat treated data set from sample 1.	124

Figure 6.27	Comparison of the 95% confidence/credible intervals (CI) for the estimated weights using asymptotic theory (WLS), bootstrapping, and Bayesian estimation for a 100 hour heat treated data set from sample 1.	124
Figure 7.1	The average cpu time (for 100 independent data sets) required to complete the optimization as M increases using both methods.	135
Figure 7.2	The average cpu time (for 100 independent data sets) required to compute the first 10 iterations of the optimization problems as M increases using both methods.	137

1.1 Motivation

There is a current interest in the incorporation of ceramic matrix composites (CMCs) for both static and rotating components in high temperature turbine engines, specifically in high-performance aircraft engines and other gas turbine engines [4, 74]. Over the course of a CMCs lifetime, oxidation occurs which can compromise the integrity of the desired material properties. Furthermore, collaborators at Wright-Patterson Air Force Base have hypothesized that as the CMC under study (a ceramic matrix with a silicon carbide fiber) is exposed to high temperatures, components of the material will transition from an amorphous to a crystalline state. In a crystalline state the material becomes more brittle. Together, these factors eventually lead to catastrophic failure. If these materials are going to be effectively integrated into modern turbine construction, then noninvasive techniques with the capability to detect the early stages of degradation must also be developed. Fourier Transform Infrared (FTIR) spectroscopy is a nondestructive electromagnetic interrogating method, which has been investigated as one possible non-destructive evaluation tool with the potential to quantify the oxidation behavior [50, 78, 80, 81]. Additionally, reflectance spectroscopy has previously been shown to have sensitivity to heat-treated ceramic thermal barrier coatings, which are being investigated for their use in turbine engines [63, 64]. Due to the fact that CMCs are optically dense, we will consider reflectance (rather than transmission or absorption) spectroscopy.

Our goal is to develop a technique for modeling the reflectance, obtained using an FTIR spectrometer, which can be used to quantify the levels of degradation. The development of a

reliable mathematical model and the accurate quantification of the model parameters may prove to be a useful tool in the development of systems designed to monitor material damage and/or degradation. Furthermore, due to the ease of data acquisition, it is plausible that the experiment may be amenable for adaptation to field use, giving near-real time results. With this in mind, we desire to develop a mathematical model and accompanying estimation procedure which is computationally efficient. These goals will guide our choices throughout this work as it pertains to the model development and estimation techniques employed.

The decomposition of a material’s electromagnetic response into the elementary component mechanisms responsible for observed phenomena is a fundamental problem of spectroscopy. In the setting of nonmagnetic materials, this involves determining the components of the permittivity using the measured spectral responses. Typically one would assume a particular combination of polarization models (Debye, Lorentz, Gaussian, etc.) with a predetermined number of dielectric parameters [10, 11, 15, 30]. However, in practice, the type of polarization model and the number of constituent dielectric mechanisms are usually unknown, particularly for complex, highly heterogeneous materials. In addition, the resulting decomposition may be non-unique or even nonphysical by using the reflectance (the readily observable in the primary experiment) alone. In a case where the material under study is inorganic glass, to alleviate this difficulty, a convolution of the Lorentz and Gaussian functions (a linear combination of normal distributions is imposed on the resonance frequency in the Lorentz model) was proposed by Efimov, et al., as early as in 1985 (e.g., see [59, 60]).

Our approach in the current effort is to impose an unknown probability distribution on the dielectric parameters, specifically, either the resonance frequencies or the relaxation times. Our goal is to place the weakest possible assumptions on the form of the underlying probability measure. For these reasons we are interested in non-parametrically estimating the probability measures. To carryout the estimation, we will make use of the Prohorov Metric Framework (PMF), which provides a solid theoretical foundation as well as a computational method for the non-parametric estimation of a probability distribution [5, 9, 30, 33, 79]. We will show that this framework has the potential to provide a sufficient description of the complex nature of the materials without the need for the development of a more detailed model which takes into account the microscopic structure.

In this work we will establish the appropriate mathematical techniques in which to apply the PMF to the electromagnetic interrogation of a complex heterogeneous material such as a ceramic matrix composite. The thesis is laid out as follows. In the remainder of this chapter we begin by introducing the necessary background information from electromagnetic theory which apply to our situation of interest. In Chapter 2 we formally introduce the PMF, as well as supply the required theoretical and computational framework. Chapter 3 introduces difference-based methods as a means to guide the statistical model and gives several practical applications. Later,

these methods will be applied to experimental reflectance spectroscopy data sets. Chapters 4–5 extensively investigate the feasibility of incorporating the PMF as a method to estimate an unknown distribution in spectroscopy data sets. The methods developed in the previous chapters are applied to a number of rich reflectance data sets provided by Wright-Patterson Air Force Base in Chapter 6. Finally, in Chapter 7 we conclude by providing computationally efficient methods in which to compute the gradients in PMF estimation problems.

1.2 Problem Description

For simplicity, we assume that a monochromatic uniform wave of frequency ω is incident at an angle ϕ on a plane interface between free space and a nonmagnetic dielectric medium as depicted schematically in Figure 1.1. This medium is assumed to be linear, homogeneous and isotropic. We first describe the reflection coefficient for the case where the wave is incident on a plane interface between two lossy media, where the permittivity, permeability and conductivity of medium ℓ are denoted by $\hat{\varepsilon}_\ell$, $\hat{\mu}_\ell$, and $\hat{\sigma}_\ell$, respectively. Once we have derived the formulas for the reflection coefficient in this case, we will simplify to the particular situation of interest here. We remark that the following arguments used in deriving the reflection coefficient are similar to those in [66, Section 9.3] and [3, Chapter 5]. Hence, we only sketch the ideas.

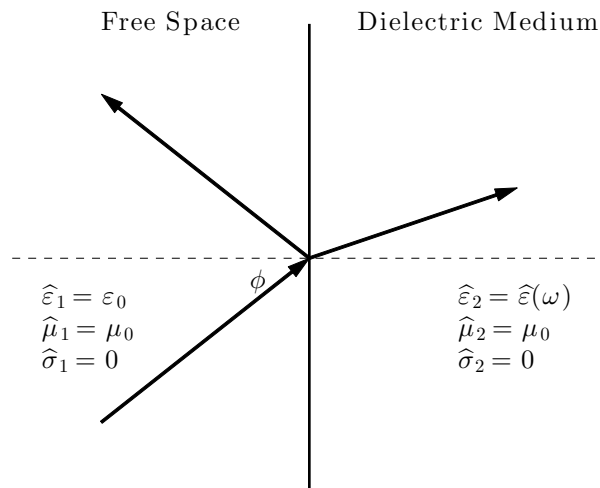


Figure 1.1: A monochromatic uniform wave is incident at an angle ϕ on a plane interface between a free space and a nonmagnetic dielectric medium, where ω denotes the frequency of the wave.

1.2.1 Reflection Coefficient: Perpendicular Polarization

To analyze the reflections and transmissions at an oblique angle of incidence for a general wave polarization, it is convenient to decompose the electric field into its perpendicular and parallel components, relative to the plane of incidence. Then the total reflected and transmitted fields will be the sum from each of the two polarizations.

We first assume that the electric field is polarized perpendicular to the plane of incidence (TE polarization). Let $\mathbf{d}^i = (\sin \phi_i, 0, \cos \phi_i)^T$ denote the unit vector for the direction of the incident wave. Then the incident electric field and incident magnetic fields can be written as

$$\begin{aligned}\mathbf{E}_\perp^i &= \hat{y}E_\perp^i e^{-i\gamma_1 \mathbf{d}^i \cdot \mathbf{r}} = \hat{y}E_0 e^{-i\gamma_1 (x \sin \phi_i + z \cos \phi_i)} \\ \mathbf{H}_\perp^i &= (-\hat{x} \cos \phi_i + \hat{z} \sin \phi_i) H_\perp^i e^{-i\gamma_1 \mathbf{d}^i \cdot \mathbf{r}} \\ &= (-\hat{x} \cos \phi_i + \hat{z} \sin \phi_i) \frac{E_0}{\eta_1} e^{-i\gamma_1 (x \cos \phi_i + z \sin \phi_i)},\end{aligned}$$

where

$$E_\perp^i = E_0, \quad H_\perp^i = \frac{E_\perp^i}{\eta_1} = \frac{E_0}{\eta_1}.$$

In the above equation, $\mathbf{r} = (x, y, z)^T$, and \hat{x}, \hat{y} and \hat{z} denote the unit vector in the x, y and z directions, respectively. In addition, γ_ℓ represents the propagation constant in medium ℓ , and η_ℓ denotes the complex intrinsic impedance in medium ℓ . They are, respectively, given by

$$\gamma_\ell = i\omega \sqrt{\hat{\varepsilon}_\ell^c(\omega) \hat{\mu}_\ell(\omega)}, \quad \eta_\ell = \sqrt{\frac{\hat{\mu}_\ell(\omega)}{\hat{\varepsilon}_\ell^c(\omega)}}, \quad \ell = 1, 2,$$

where i denotes the imaginary unit, and $\hat{\varepsilon}_\ell^c$ represents the complex permittivity of medium ℓ ,

$$\hat{\varepsilon}_\ell^c(\omega) = \hat{\varepsilon}_\ell(\omega) - i \frac{\hat{\sigma}_\ell(\omega)}{\omega}. \quad (1.2.1)$$

Similarly, using the reflection coefficient Γ_\perp the reflected fields can be expressed as

$$\begin{aligned}\mathbf{E}_\perp^r &= \hat{y}E_\perp^r e^{-i\gamma_1 \mathbf{d}^r \cdot \mathbf{r}} = \hat{y}\Gamma_\perp E_0 e^{-i\gamma_1 (x \sin \phi_r + z \cos \phi_r)} \\ \mathbf{H}_\perp^r &= (-\hat{x} \cos \phi_r + \hat{z} \sin \phi_r) H_\perp^r e^{-i\gamma_1 \mathbf{d}^r \cdot \mathbf{r}} \\ &= (-\hat{x} \cos \phi_r + \hat{z} \sin \phi_r) \frac{\Gamma_\perp E_0}{\eta_1} e^{-i\gamma_1 (x \cos \phi_r + z \sin \phi_r)},\end{aligned}$$

where

$$E_\perp^r = \Gamma_\perp E_\perp^i = \Gamma_\perp E_0, \quad H_\perp^r = \frac{E_\perp^r}{\eta_1} = \frac{\Gamma_\perp E_0}{\eta_1}.$$

In addition, with the transmission coefficient T_\perp , the transmitted fields can be written as

$$\begin{aligned}\mathbf{E}_\perp^t &= \hat{y}E_\perp^t e^{-i\gamma_1 \mathbf{d}^t \cdot \mathbf{r}} = \hat{y}T_\perp E_0 e^{-i\gamma_2(x \sin \phi_t + z \cos \phi_t)} \\ \mathbf{H}_\perp^t &= (-\hat{x} \cos \phi_t + \hat{z} \sin \phi_t) H_\perp^t e^{-i\gamma_2 \mathbf{d}^t \cdot \mathbf{r}} \\ &= (-\hat{x} \cos \phi_t + \hat{z} \sin \phi_t) \frac{T_\perp E_0}{\eta_2} e^{-i\gamma_2(x \cos \phi_t + z \sin \phi_t)},\end{aligned}$$

where

$$E_\perp^t = T_\perp E_\perp^i = T_\perp E_0, \quad H_\perp^t = \frac{E_\perp^t}{\eta_2} = \frac{T_\perp E_0}{\eta_2}.$$

By enforcing the boundary condition, namely that the tangential components of both the electric field and the magnetic field are continuous on the interface, we can obtain a relationship between the reflection and transmission coefficients and the incident ϕ_i , reflected ϕ_r , and transmitted (refracted) ϕ_t angles. That is,

$$\begin{aligned}\left(E_\perp^i + E_\perp^r\right)\Big|_{tan, z=0} &= \left(E_\perp^t\right)\Big|_{tan, z=0} \\ \left(H_\perp^i + H_\perp^r\right)\Big|_{tan, z=0} &= \left(H_\perp^t\right)\Big|_{tan, z=0},\end{aligned}$$

which leads to

$$e^{i\gamma_1 x \sin \phi_i} + \Gamma_\perp e^{-i\gamma_1 x \sin \phi_r} = T_\perp e^{-i\gamma_2 x \sin \phi_t} \quad (1.2.2)$$

$$\frac{1}{\eta_1} \left(-\cos \phi_i e^{-i\gamma_1 x \cos \phi_i} + \Gamma_\perp \cos \phi_r e^{-i\gamma_1 x \sin \phi_r} \right) = \frac{T_\perp}{\eta_2} e^{-i\gamma_2 x \sin \phi_t}. \quad (1.2.3)$$

Equations (1.2.2) and (1.2.3) are two complex equations with four unknowns ($\Gamma_\perp, T_\perp, \phi_r, \phi_t$), and solving these yields the relationships

$$\phi_r = \phi_i \quad (\text{Snell's law of reflection}) \quad (1.2.4)$$

$$\gamma_1 \sin \phi_i = \gamma_2 \sin \phi_t \quad (\text{Snell's law of refraction}). \quad (1.2.5)$$

Using Snell's law of reflection and refraction, we can manipulate equations (1.2.2) and (1.2.3) to arrive at

$$\begin{aligned}1 + \Gamma_\perp &= T_\perp \\ \frac{\cos \phi_i}{\eta_1} (-1 + \Gamma_\perp) &= -\frac{\cos \phi_t}{\eta_2} T_\perp.\end{aligned} \quad (1.2.6)$$

Finally, we can solve the above equations for the reflection coefficient

$$\Gamma_{\perp} = \frac{E_{\perp}^r}{E_{\perp}^i} = \frac{\eta_2 \cos \phi_i - \eta_1 \cos \phi_t}{\eta_2 \cos \phi_i + \eta_1 \cos \phi_t} = \frac{\sqrt{\hat{\mu}_2/\hat{\varepsilon}_2^c} \cos \phi_i - \sqrt{\hat{\mu}_1/\hat{\varepsilon}_1^c} \cos \phi_t}{\sqrt{\hat{\mu}_2/\hat{\varepsilon}_2^c} \cos \phi_i + \sqrt{\hat{\mu}_1/\hat{\varepsilon}_1^c} \cos \phi_t}. \quad (1.2.7)$$

Equation (1.2.7) is often referred to as the plane wave Fresnel reflection coefficient for perpendicular polarization.

1.2.2 Reflection Coefficient: Parallel Polarization

Now we assume that the electric field is polarized parallel to the plane of incidence. In this case we have that the incident electric and magnetic fields can be written as

$$\begin{aligned} \mathbf{E}_{\parallel}^i &= (\hat{x} \cos \phi_i - \hat{z} \sin \phi_i) E_0 e^{-i\gamma_1 \mathbf{d}^i \cdot \mathbf{r}} \\ &= (\hat{x} \cos \phi_i - \hat{z} \sin \phi_i) E_0 e^{-i\gamma_1 (x \sin \phi_i + z \cos \phi_i)} \\ \mathbf{H}_{\parallel}^i &= \hat{y} H_{\parallel}^i e^{-i\gamma_1 \mathbf{d}^i \cdot \mathbf{r}} = \hat{y} \frac{E_0}{\eta_1} e^{-i\gamma_1 (x \sin \phi_i + z \cos \phi_i)}, \end{aligned}$$

where

$$E_{\parallel}^r = \Gamma_{\parallel} E^i = \Gamma_{\parallel} E_0, \quad H_{\parallel}^r = \frac{E_{\parallel}^r}{\eta_1} = \frac{\Gamma_{\parallel} E_0}{\eta_1}.$$

The reflected fields are given by

$$\begin{aligned} \mathbf{E}_{\parallel}^r &= (\hat{x} \cos \phi_r - \hat{z} \sin \phi_r) E^r e^{-i\gamma_1 \mathbf{d}^r \cdot \mathbf{r}} \\ &= (\hat{x} \cos \phi_r - \hat{z} \sin \phi_r) \Gamma_{\parallel} E_0 e^{-i\gamma_1 (x \sin \phi_r - z \cos \phi_r)} \\ \mathbf{H}_{\parallel}^r &= -\hat{y} H_{\parallel}^r e^{-i\gamma_1 \mathbf{d}^r \cdot \mathbf{r}} = -\hat{y} \frac{\Gamma_{\parallel} E_0}{\eta_1} e^{-i\gamma_1 (x \sin \phi_r - z \cos \phi_r)}, \end{aligned}$$

where

$$E_{\parallel}^i = E_0, \quad H_{\parallel}^i = \frac{E_{\parallel}^i}{\eta_1} = \frac{E_0}{\eta_1}.$$

Finally, we express the transmitted fields as

$$\begin{aligned} \mathbf{E}_{\parallel}^t &= (\hat{x} \cos \phi_t - \hat{z} \sin \phi_t) E^t e^{-i\gamma_2 \mathbf{d}^t \cdot \mathbf{r}} \\ &= (\hat{x} \cos \phi_t - \hat{z} \sin \phi_t) T_{\parallel} E_0 e^{-i\gamma_2 (x \sin \phi_t + z \cos \phi_t)} \\ \mathbf{H}_{\parallel}^t &= \hat{y} H_{\parallel}^t e^{-i\gamma_2 \mathbf{d}^t \cdot \mathbf{r}} = \hat{y} \frac{T_{\parallel} E_0}{\eta_2} e^{-i\gamma_2 (x \sin \phi_t + z \cos \phi_t)}, \end{aligned}$$

where

$$E_{\parallel}^t = T_{\parallel} E^i = T_{\parallel} E_0, \quad H_{\parallel}^t = \frac{E_{\parallel}^t}{\eta_2} = \frac{T_{\parallel} E_0}{\eta_2}.$$

As before, by applying the appropriate continuity boundary conditions at the interface, we obtain

$$\cos \phi_i e^{-i\gamma_1 x \sin \phi_i} + \Gamma_{\parallel} \cos \phi_r e^{-i\gamma_1 x \sin \phi_r} = T_{\parallel} \cos \phi_t e^{-i\gamma_2 x \sin \phi_t} \quad (1.2.8)$$

$$\frac{1}{\eta_1} \left(e^{-i\gamma_1 x \sin \phi_i} - \Gamma_{\parallel} e^{-i\gamma_1 x \sin \phi_r} \right) = \frac{1}{\eta_2} T_{\parallel} e^{-i\gamma_2 x \sin \phi_t}. \quad (1.2.9)$$

These equations can also be reduced to Snell's law of reflection and refraction. Thus, obtaining the equation for the reflection coefficient due to parallel polarization

$$\Gamma_{\parallel} = \frac{-\eta_1 \cos \phi_i + \eta_2 \cos \phi_t}{\eta_1 \cos \phi_i + \eta_2 \cos \phi_t} = \frac{-\sqrt{\hat{\mu}_1/\hat{\varepsilon}_1^c} \cos \phi_i + \sqrt{\hat{\mu}_2/\hat{\varepsilon}_2^c} \cos \phi_t}{\sqrt{\hat{\mu}_1/\hat{\varepsilon}_1^c} \cos \phi_i + \sqrt{\hat{\mu}_2/\hat{\varepsilon}_2^c} \cos \phi_t}. \quad (1.2.10)$$

Next we turn our attention to simplifying the expression for the reflection coefficient due to perpendicular and parallel polarizations to match the formulation of the problem of interest.

1.2.3 Reflection Coefficient Between Free Space and a Lossy Material

In free space, $\hat{\mu}_1 \equiv \mu_0$ and $\hat{\varepsilon}_1^c \equiv \varepsilon_0$, where ε_0 , μ_0 are, respectively, the permittivity and permeability in free space. Also, since our material is nonmagnetic, we have that $\hat{\mu}_2 \equiv \mu_0$. The conductivity in a dielectric material is very small, and so we assume that it is negligible, that is, $\hat{\sigma} \equiv 0$. Thus, by (1.2.1) we have $\hat{\varepsilon}_2^c(\omega) = \hat{\varepsilon}_2(\omega)$.

Once we make the requisite substitutions in (1.2.7) and (1.2.10) we obtain

$$r_{\perp}(\omega) = \frac{\sqrt{\mu_0/\hat{\varepsilon}_2} \cos \phi_i - \sqrt{\mu_0/\varepsilon_0} \cos \phi_t}{\sqrt{\mu_0/\hat{\varepsilon}_2} \cos \phi_i + \sqrt{\mu_0/\varepsilon_0} \cos \phi_t}$$

$$r_{\parallel}(\omega) = \frac{-\sqrt{\mu_0/\varepsilon_0} \cos \phi_i + \sqrt{\mu_0/\hat{\varepsilon}_2} \cos \phi_t}{\sqrt{\mu_0/\varepsilon_0} \cos \phi_i + \sqrt{\mu_0/\hat{\varepsilon}_2} \cos \phi_t},$$

where r_{\perp} and r_{\parallel} denote the reflection coefficients for our problem of interest. Utilizing Snell's law of refraction to eliminate ϕ_t , we arrive at

$$r_{\perp}(\omega) = \frac{\cos \phi_i - \sqrt{\hat{\varepsilon}_r(\omega) - \sin^2 \phi_i}}{\cos \phi_i + \sqrt{\hat{\varepsilon}_r(\omega) - \sin^2 \phi_i}} \quad (1.2.11)$$

$$r_{\parallel}(\omega) = \frac{\sqrt{1 - \sin^2 \phi_i / \hat{\varepsilon}_r(\omega)} - \sqrt{\hat{\varepsilon}_r(\omega)} \cos \phi_i}{\sqrt{1 - \sin^2 \phi_i / \hat{\varepsilon}_r(\omega)} + \sqrt{\hat{\varepsilon}_r(\omega)} \cos \phi_i}, \quad (1.2.12)$$

where $\hat{\varepsilon}_r(\omega) = \hat{\varepsilon}_2(\omega)/\varepsilon_0$.

1.2.4 Complex Permittivity

The Lorentz oscillator model is derived by considering the polarization which results from the displacement of electrons from equilibrium under the effect of an applied electromagnetic field. It is assumed that an electron bound to the nucleus of an atom obeys Hooke's law, where the displacement of the electrons from equilibrium is a result of the applied electromagnetic field. Combining the Lorentz oscillator model with the Lorentz model for electronic polarization results in the Lorentz model for the complex permittivity with a single resonance given by

$$\hat{\varepsilon}_r(\omega) = \varepsilon_\infty - \frac{\omega_p^2}{\omega^2 - i\omega/\tau_f - \omega_0^2}. \quad (1.2.13)$$

In the above equation, ε_∞ denotes the relative permittivity of the medium at infinite frequency, τ_f is the relaxation time, $i = \sqrt{-1}$ is the imaginary unit, and $\omega_p = \omega_0\sqrt{\varepsilon_s - \varepsilon_\infty}$ is called the plasma frequency of the medium, where ω_0 is the resonance frequency, and ε_s is the relative permittivity of the medium at zero frequency, also known as the “static” dielectric constant.

In practice it is typical for the data to be collected as a function of k , the wavenumber, rather than frequency. Using the relationship that $k = \omega/(2\pi c)$, where c is the speed of light in cm/s, we obtain the relative permittivity as a function of wavenumber

$$\hat{\varepsilon}_r(k) = \varepsilon_\infty - \frac{k_p^2}{k^2 - ik/\tau_k - k_0^2}. \quad (1.2.14)$$

In the above equation $k_p = k_0\sqrt{\varepsilon_s - \varepsilon_\infty}$, $k_0 = \omega_0/(2\pi c)$, and $\tau_k = 2\pi c\tau_f$. We will refer to k_0 as the resonance wavenumber and we will omit the subscript on the relaxation time τ_k when it is clear that we are referring to the relaxation time for the permittivity in terms of wavenumber.

According to quantum mechanical dispersion theory, and allowing for a material to contain multiple oscillators, a more general model for the permittivity can be given by

$$\hat{\varepsilon}_r(k) = \varepsilon_\infty - \sum_{j=1}^J \frac{S_j}{k^2 - ik/\tau_j - k_{0j}^2}, \quad (1.2.15)$$

where S_j is understood to be the intensity of the j th oscillator. The intensities S_j are sometimes replaced by the contributions of the oscillators, $\Delta\varepsilon_{0j}k_{0j}^2 = S_j$, where

$$\sum_{j=1}^J \Delta\varepsilon_{0j} = \varepsilon_s - \varepsilon_\infty.$$

In the remaining chapters we will investigate imposing a distribution on either the resonance wavenumber or the relaxation time in equation (1.2.14), and the subsequent estimation problem.

CHAPTER 2

The Prohorov Metric

In this chapter we lay the theoretical and computational groundwork for nonparametric probability estimation through the Prohorov Metric Framework. The work in this chapter is based on the publication [19]:

H.T. Banks, J. Catenacci, and S. Hu. Asymptotic properties of probability measure estimators in a nonparametric model. *SIAM/ASA Journal on Uncertainty Quantification*, 3: 417–433, 2015.

2.1 Introduction

We begin by considering the general nonparametric estimation of an unknown probability measure in the case where the regression function is dependent on this measure. More precisely, the statistical model, the model describing the observation process, is described by

$$Y_j = f(t_j; G_0) + \mathcal{E}_j, \quad j = 1, 2, 3, \dots, N. \quad (2.1.1)$$

In the above equation, $f(t_j; G_0)$ denotes the observed part of the solution of a mathematical model with the true probability measure G_0 (unknown) at the measurement point t_j , \mathcal{E}_j is the measurement error at t_j , and N is the total number of observations, where $t_j \in [t_s, t_f]$, $j = 1, 2, 3, \dots, N$, with t_s and t_f being some real numbers (in the example below these numbers $t_j = k_j$ are actually wave numbers obtained in taking frequency sweeps). Following popular conventions we will not always distinguish between probability measures and their associated cumulative distribution functions in the discussions below.

Equation (2.1.1) is often referred to as a nonparametric model (a model with all the unknown

parameters being in an infinite-dimensional parameter space) in the statistics literature. Such models are motivated by a number of applications arising in biology and physics, for example, in modeling mosquitofish populations [28] and shrimp populations [24], in wave propagation in biotissue [39], in modeling of complex nonmagnetic dielectric materials [22, 30], and in HIV cellular models [12]. Here we only elaborate one of the motivating examples, which is the primary application of interest in this work. In this project, the goal is to develop a noninvasive technique to characterize the degradation of a complex nonmagnetic dielectric material by assessing the small physical and chemical changes in the material using reflectance spectroscopy. This involves determining the components of the permittivity of the dielectric medium using the measured spectral responses. Recall that the relative permittivity of the dielectric medium is described by

$$\widehat{\varepsilon}_r(k; G_0) = \varepsilon_\infty - \int_{\Omega_\theta} \frac{k_p^2}{k^2 - ik/\tau - k_0^2} dG_0(\theta). \quad (2.1.2)$$

For our discussions in this chapter, we assume that $\theta = k_0 \in \Omega_\theta \subset \mathbb{R}$. If we assume that a monochromatic uniform wave is incident at an angle zero on a plane interface between free space and a nonmagnetic dielectric medium with the electric field polarized perpendicular to the plane of incidence, then the reflection coefficient given by (1.2.11) is simplified to

$$r(k; G_0) = \frac{1 - \sqrt{\widehat{\varepsilon}_r(k; G_0)}}{1 + \sqrt{\widehat{\varepsilon}_r(k; G_0)}}, \quad (2.1.3)$$

where $\widehat{\varepsilon}_r$ is defined by (2.1.2). The observations f_j are the reflectance (the square of the magnitude of the reflection coefficient) at different wave numbers k_j ; that is, $f_j = |r(k_j; G_0)|^2$. The goal is then to use these observations to estimate the unknown probability measure G_0 .

We note here that the problem we outlined above is different from those, for example, in pharmacokinetics studies and HIV studies, where one desires to estimate both individual-specific parameters θ (such as clearance rate of the virus and infection rate in HIV studies) and their associated probability distribution function P_0 from blood samples taken serially in time from *individuals* in the population (e.g., see [31, 53]). This is because in these cases the data f_j is dependent on θ instead of P_0 ; that is, one has *individual* longitudinal data instead of *aggregate* longitudinal data (i.e., data collected by sampling from the population at large). Hence, the methods used to solve these two types of problems are *fundamentally different*. We refer the interested reader to [33, 37] for more details on this topic.

Traditional parametric methods, which assume the sought-after probability measure P_0 has a particular distributional form, are not preferred as they are overly restrictive and will produce inaccurate results if the parametric form is misspecified. Here we propose to use a least-squares approach for nonparametric estimation of probability measures. Least-squares methods

and their generalizations, as well as maximum likelihood estimation (MLE) methods, are two widely used frequentist-based approaches for parameter estimation. It is well-known that in the case that the parameter space is finite-dimensional both least-squares methods and maximum likelihood estimation methods have nice limiting properties for the parameter estimator, i.e., asymptotic normality and consistency (e.g., see [84]). However, MLE methods require knowledge of the probability density function of observations in order to define the likelihood function. Unfortunately, this knowledge is often not available in practice. In contrast, for least-squares methods, one only needs to assume the first two moments, i.e., the mean and variance or covariance matrix, of the measurement errors in order to define the cost function. To this point, we have not discussed the Bayesian approach, which is another widely used methodology for parameter estimation. The difficulties for a Bayesian analysis in a nonparametric model setting (the involved approach is often referred to as Bayesian nonparametric estimation) include prior (a stochastic process in this case) construction, algorithmic development (as it depends on the prior and the problem itself, and the common MCMC techniques cannot be directly applied to the aggregate data and infinite-dimensional parameter space setting) and posterior asymptotics. Thus, compared to frequentist approaches, the Bayesian nonparametric approach is more difficult to implement and hence we do not consider this approach in this presentation. We refer the interested reader to [49] for a review of recent developments on this topic.

The remainder of this chapter is organized as follows. In Section 2.2, we first give an overview of the computational methods developed by our group in the past two decades (see [5]) for probability measure estimation, and provide a consistency result for the probability measure estimator. Then we discuss the bias and the variance due to the approximation and present the asymptotic normality of the approximated probability measure estimator. In Section 2.3, we give some numerical results to illustrate the efficacy of our approach. Finally, in Section 2.4 we conclude the paper with some summary remarks and future research questions.

2.2 Theoretical and Computational Framework for Probability Measure Estimation

For notational convenience, we assume that observations Y_j in (2.1.1) are scalar (the multi-dimensional case can be treated similarly). We also assume throughout the remainder of this discussion that measurement errors \mathcal{E}_j , $j = 1, 2, 3, \dots, N$, are independent and identically distributed (i.i.d.) with zero mean and constant variance σ_0^2 . We note that the existence of a true probability measure, a standard assumption in statistical formulations, along with the assumption that the measurement errors have zero mean implies that $f(t; G_0)$ correctly describes the observed part of the dynamical system (that is, the underlying mathematical model is

correct).

With the i.i.d. assumption on the measurement errors, the estimator of G_0 can be obtained using the ordinary least-squares method as defined by

$$G^N = \operatorname{argmin}_{G \in \mathcal{P}(\Omega_\theta)} \sum_{j=1}^N (Y_j - f(t_j; G))^2, \quad (2.2.1)$$

where $\mathcal{P}(\Omega_\theta)$ denotes the set of probability measures on the space $\Omega_\theta \subset \mathbb{R}^{\kappa_\theta}$ with κ_θ being a positive integer. We remark that G^N itself is random in that it is a function of random variables Y_j (and hence \mathcal{E}_j) on a probability space $(\Omega, \mathcal{F}, \text{Prob})$. The corresponding realization \hat{G}^N of G^N can be calculated through

$$\hat{G}^N = \operatorname{argmin}_{G \in \mathcal{P}(\Omega_\theta)} \sum_{j=1}^N (y_j - f(t_j; G))^2, \quad (2.2.2)$$

where y_j is a realization of Y_j , $j = 1, 2, 3, \dots, N$. Thus, we can view G^N as a stochastic process (i.e., $G^N(\boldsymbol{\theta}; \cdot)$ as a one parameter ($\boldsymbol{\theta} \in \Omega_\theta$) family of random variables on the probability space $(\Omega, \mathcal{F}, \text{Prob})$) since each of its realizations yields a probability measure $\hat{G}^N \in \mathcal{P}(\Omega_\theta)$.

The existence of a minimizer to the least-squares optimization problem (2.2.1) or (2.2.2) can be established under the Prohorov metric framework. The Prohorov metric was introduced by the Russian probabilist Y.V. Prohorov [79] and is defined as follows (e.g., see [41, pp. 237–238]).

Definition 2.2.1. Let $\mathbb{F} \subset \Omega_\theta$ be any closed set and define \mathbb{F}^ϵ as follows:

$$\mathbb{F}^\epsilon = \left\{ \boldsymbol{\theta} \in \Omega_\theta : \inf_{\tilde{\boldsymbol{\theta}} \in \mathbb{F}} d(\boldsymbol{\theta}, \tilde{\boldsymbol{\theta}}) < \epsilon \right\},$$

where d denotes the metric on Ω_θ . For $P, G \in \mathcal{P}(\Omega_\theta)$, the *Prohorov metric* is given by

$$\begin{aligned} \rho(P, G) \\ = \inf \{ \epsilon > 0 \mid G(\mathbb{F}) \leq P(\mathbb{F}^\epsilon) + \epsilon \text{ and } P(\mathbb{F}) \leq G(\mathbb{F}^\epsilon) + \epsilon, \text{ for all } \mathbb{F} \text{ closed in } \Omega_\theta \}. \end{aligned}$$

It is clear from the definition above that the meaning of Prohorov metric is far from intuitive. Yet one can provide several useful characterizations. For example, convergence in the Prohorov metric is equivalent to the weak* convergence if we view $\mathcal{P}(\Omega_\theta) \subset C_B^*(\Omega_\theta)$, where $C_B^*(\Omega_\theta)$ denotes the topological dual of the space $C_B(\Omega_\theta)$ of bounded and continuous functions on Ω_θ . In other words, the statement $\rho(G_j, G) \rightarrow 0$ is equivalent to the statement

$$\int_{\Omega_\theta} h(\boldsymbol{\theta}) dG_j(\boldsymbol{\theta}) \rightarrow \int_{\Omega_\theta} h(\boldsymbol{\theta}) dG(\boldsymbol{\theta}) \text{ for any } h \in C_B(\Omega_\theta).$$

The Prohorov metric also possesses many useful and important properties. For example, if we assume that Ω_θ is compact, then $\mathcal{P}(\Omega_\theta)$ is a compact metric space when taken with the Prohorov metric ρ . We refer interested readers to [5, 33, 41, 57, 95] for more information on the Prohorov metric and its properties. Based on these discussions, we see that if Ω_θ is compact and f is continuous with respect to G , then there exists a solution to (2.2.1) or (2.2.2).

2.2.1 Consistency of the Probability Measure Estimator

The ideas for establishing the consistency of probability measure estimators follow closely to those given in [26] and [33]. Here we only present the necessary assumptions as well as the result, and refer the interested reader to [33, Section 5.5] for details. For a given *sampling set* $\{t_j\}_{j=1}^N$ in the interval $[t_s, t_f]$, one can define the empirical distribution function

$$\mu_N(t) = \frac{1}{N} \sum_{j=1}^N \Delta_{t_j}(t), \quad (2.2.3)$$

where Δ_{t_j} is the Dirac measure with atom at t_j ; that is,

$$\Delta_{t_j}(t) = \begin{cases} 0, & t < t_j \\ 1, & \text{otherwise.} \end{cases}$$

Clearly, $\mu_N \in \mathcal{P}([t_s, t_f])$, the space of probability measures (or, equivalently the cumulative distribution functions) on $[t_s, t_f]$. We assume

(A1) For each fixed N , \mathcal{E}_j , $j = 1, 2, \dots, N$, are independent and identically distributed with zero mean and constant variance σ_0^2 , and they are defined on some probability space $(\Omega, \mathcal{F}, \text{Prob})$.

(A2) There exists a measure μ on $[t_s, t_f]$ such that

$$\frac{1}{N} \sum_{j=1}^N h(t_j) = \int_{t_s}^{t_f} h(t) d\mu_N(t) \rightarrow \int_{t_s}^{t_f} h(t) d\mu(t)$$

for all $h \in C([t_s, t_f])$.

(A3) The space $\Omega_\theta \subset \mathbb{R}^{\kappa_\theta}$ is compact; the space $\mathcal{P}(\Omega_\theta)$ is taken with the Prohorov metric ρ .

(A4) The function f satisfies $f \in C([t_s, t_f], C(\mathcal{P}(\Omega_\theta)))$.

(A5) The functional J^0 defined by

$$J^0(G) = \sigma^2 + \int_{t_s}^{t_f} (f(t; G_0) - f(t; G))^2 d\mu(t)$$

is uniquely minimized at $G_0 \in \mathcal{P}(\Omega_\theta)$.

Theorem 2.2.2. *Under assumptions (A1)–(A5), $\rho(G^N, G_0) \xrightarrow{a.s.} 0$ as $N \rightarrow \infty$, where $\xrightarrow{a.s.}$ denotes convergence almost surely in $(\Omega, \mathcal{F}, \text{Prob})$. That is,*

$$\text{Prob} \left\{ \omega \in \Omega \mid \lim_{N \rightarrow \infty} \rho(G^N(\omega), G_0) = 0 \right\} = 1.$$

2.2.2 Approximation Schemes for Probability Measure Estimation

We note that (2.2.2) is an infinite-dimensional optimization problem. Hence, the infinite-dimensional space $\mathcal{P}(\Omega_\theta)$ must be approximated by some finite dimensional space $\mathcal{P}^M(\Omega_\theta)$ so that one has a computationally tractable finite-dimensional optimization problem given by

$$\hat{G}_M^N = \underset{G \in \mathcal{P}^M(\Omega_\theta)}{\text{argmin}} \sum_{j=1}^N (y_j - f(t_j; G))^2. \quad (2.2.4)$$

However, one needs to choose $\mathcal{P}^M(\Omega_\theta)$ in a meaningful way so that \hat{G}_M^N approaches the solution to (2.2.2) as $M \rightarrow \infty$.

One such approximation method involves using Dirac measures to approximate the probability measures. The following theorem is useful in establishing the convergence results as well as in constructing approximation schemes. We refer the interested reader to [9] for a proof of this result.

Theorem 2.2.3. *Assume $\Omega_\theta \subset \mathbb{R}^{\kappa_\theta}$ is compact. Let $\Omega_{\theta D} = \{\theta_j\}_{j=1}^\infty$ be an enumeration of a countable dense subset of Ω_θ . Define*

$$\begin{aligned} & \tilde{\mathcal{P}}_D(\Omega_\theta) \\ &= \left\{ G \in \mathcal{P}(\Omega_\theta) \mid G = \sum_{j=1}^M \alpha_j \Delta_{\theta_j}, \theta_j \in \Omega_{\theta D}, \alpha_j \in [0, 1] \cap \mathbb{Q}, \sum_{j=1}^M \alpha_j = 1, M \in \mathbb{N} \right\}, \end{aligned}$$

where Δ_{θ_j} is the Dirac measure with atom at θ_j , and $\mathbb{Q} \subset \mathbb{R}$ denotes the set of all rational numbers. (That is, $\tilde{\mathcal{P}}_D(\Omega_\theta)$ is the collection of all convex combinations of Dirac measures on Ω_θ with atoms $\theta_j \in \Omega_{\theta D}$ and rational weights.) Then $\tilde{\mathcal{P}}_D(\Omega_\theta)$ is dense in $(\mathcal{P}(\Omega_\theta), \rho)$, and thus $\mathcal{P}(\Omega_\theta)$ is separable.

Under this Dirac measure approximation framework, we define $\mathcal{P}^M(\Omega_\theta)$ to be the set of all atomic probability measures with nodes placed at the first M elements in the enumeration of the countable dense subset of Ω_θ ; that is,

$$\mathcal{P}^M(\Omega_\theta) = \left\{ G \in \mathcal{P}(\Omega_\theta) \mid G = \sum_{j=1}^M \alpha_j \Delta_{\theta_j}, \text{ where } \alpha_j \geq 0 \text{ and } \sum_{j=1}^M \alpha_j = 1 \right\}. \quad (2.2.5)$$

By Theorem 2.2.3 we know that we can approximate any element $G \in \mathcal{P}(\Omega_\theta)$ by a sequence $\{G_{M_j}\}$, $G_{M_j} \in \mathcal{P}^{M_j}(\Omega_\theta)$, such that $\rho(G_{M_j}, G) \rightarrow 0$ as $M_j \rightarrow \infty$. We also see that this Dirac measure approximation method can be used regardless of the smoothness of probability measures. This is especially useful in the situations where one has no knowledge of the sought-after probability measures.

Another family of approximation methods is based on linear spline approximations, which are designed for the case where the sought after probability measures are absolutely continuous so that their corresponding probability density functions exist. The following theorem is useful in establishing the convergence results as well as in constructing approximation schemes. We refer the interested reader to [39] for a proof of this result.

Theorem 2.2.4. *Assume $\Omega_\theta \subset \mathbb{R}^{\kappa_\theta}$ is compact. Define*

$$\begin{aligned} & \tilde{\mathcal{P}}_S(\Omega_\theta) \\ &= \left\{ G \in \mathcal{P}(\Omega_\theta) \mid G'(\boldsymbol{\theta}) = \sum_{j=1}^M \alpha_j l_j^M(\boldsymbol{\theta}), \alpha_j \in [0, \infty) \cap \mathbb{Q}, \sum_{j=1}^M \alpha_j \int_{\Omega_\theta} l_j^M(\boldsymbol{\xi}) d\boldsymbol{\xi} = 1, M \in \mathbb{N} \right\}, \end{aligned}$$

where G' denotes the derivative of G with respect to $\boldsymbol{\theta}$, the $\{l_j^M\}$ denote the usual piecewise linear splines, and $\mathbb{Q} \subset \mathbb{R}$ denotes the set of all rational numbers. Then $\tilde{\mathcal{P}}_S(\Omega_\theta)$ is dense in $\mathcal{P}(\Omega_\theta)$.

Under this linear spline approximation framework, we define $\mathcal{P}^M(\Omega_\theta)$ to be

$$\mathcal{P}^M(\Omega_\theta) = \left\{ G \in \mathcal{P}(\Omega_\theta) \mid G'(\boldsymbol{\theta}) = \sum_{j=1}^M \alpha_j l_j^M(\boldsymbol{\theta}), \text{ where } \alpha_j \geq 0 \text{ and } \sum_{j=1}^M \alpha_j \int_{\Omega_\theta} l_j^M(\boldsymbol{\xi}) d\boldsymbol{\xi} = 1 \right\}. \quad (2.2.6)$$

By Theorem 2.2.4 we know that we can approximate any element $G \in \mathcal{P}(\Omega_\theta)$ by a sequence $\{G_{M_j}\}$, $G_{M_j} \in \mathcal{P}^{M_j}(\Omega_\theta)$, such that $\rho(G_{M_j}, G) \rightarrow 0$ as $M_j \rightarrow \infty$.

The following theorem (which we state without proof for sake of brevity) provides a desired convergence result for the infinite dimensional theory given here. The general finite dimensional parameter space approximation theory developed in [38] can be used in the context of the infinite dimensional PMF along with the Theorems 2.2.3 and 2.2.4 given above to provide an

infinite dimensional asymptotic theory for the estimators of interest here. This guarantees a convergence theory in the context of the Prohorov metric.

Theorem 2.2.5. *Assume Ω_θ is compact and $\mathcal{P}(\Omega_\theta)$ is taken with the Prohorov metric ρ . If f is continuous with respect to G , then there exists a minimizer \hat{G}_M^N to (2.2.4) for each M and N , where $\mathcal{P}^M(\Omega_\theta)$ is chosen as either (2.2.5) or (2.2.6). Moreover, the sequence $\{\hat{G}_M^N\}_{M=1}^\infty$ has at least one convergent (as $M_k \rightarrow \infty$) subsequence $\{\hat{G}_{M_k}^N\}$ and the ρ -limit $\hat{G}^{N*} = \rho\text{-}\lim_{M_k \rightarrow \infty} \hat{G}_{M_k}^N$ of such a subsequence is a minimizer to the least-squares problem (2.2.2).*

Remark 2.2.6. Both the Dirac measure approximation methods and the spline-based approximation methods have been successfully used to estimate probability measures in a number of applications (e.g., see [22, 27, 28, 30, 39]). However, it was demonstrated in [23] that if the sought-after probability measure is absolutely continuous, then the spline-based approximation methods converge much faster than do the Dirac measure approximation methods (in terms of the value of M). In addition, it was observed in [23] that the spline-based approximation methods also provide convergence for the associated probability density functions while the Dirac measure approximation methods do not do this. This is not surprising since in the spline-based approximation methods one directly approximates the associated probability density functions instead of the cumulative distribution functions.

2.2.3 Bias and Variance in Probability Measure Estimation

As we discussed in the above section, what one actually does in practice is to minimize the cost functional in a finite-dimensional space; that is, one solves the optimization problem

$$G_M^N = \underset{G \in \mathcal{P}^M(\Omega_\theta)}{\operatorname{argmin}} \sum_{j=1}^N (Y_j - f(t_j; G))^2. \quad (2.2.7)$$

For example, if one uses the Dirac measure approximation methods, then $G_M^N = \Delta^T \mathbf{A}_M^N$, where $\Delta = \Delta(\theta) = (\Delta_{\theta_1}, \Delta_{\theta_2}, \dots, \Delta_{\theta_M})^T$, and

$$\mathbf{A}_M^N = \underset{\mathbf{a}_M^N \in \tilde{\mathbb{R}}^M}{\operatorname{argmin}} \sum_{j=1}^N \left[Y_j - f(t_j; \sum_{l=1}^M \alpha_{M,l}^N \Delta_{\theta_l}) \right]^2. \quad (2.2.8)$$

Here $\tilde{\mathbb{R}}^M = \left\{ \mathbf{a}^M = (\alpha_1^M, \alpha_2^M, \dots, \alpha_M^M)^T \mid \alpha_j^M \geq 0, j = 1, 2, \dots, M, \sum_{j=1}^M \alpha_j^M = 1 \right\}$. The corresponding realization of (2.2.7) is given by

$$\hat{G}_M^N = \underset{G \in \mathcal{P}^M(\Omega_\theta)}{\operatorname{argmin}} \sum_{j=1}^N (y_j - f(t_j; G))^2; \quad (2.2.9)$$

that is, $\widehat{G}_M^N = \mathbf{\Delta}^T \widehat{\mathbf{a}}_M^N$, where $\mathbf{\Delta} = (\Delta_{\boldsymbol{\theta}_1}, \Delta_{\boldsymbol{\theta}_2}, \dots, \Delta_{\boldsymbol{\theta}_M})^T$, and

$$\widehat{\mathbf{a}}_M^N = \operatorname{argmin}_{\mathbf{a}_M^N \in \widetilde{\mathbb{R}}^M} \sum_{j=1}^N \left[y_j - f(t_j; \sum_{l=1}^M \alpha_{M,l}^N \Delta_{\boldsymbol{\theta}_l}) \right]^2. \quad (2.2.10)$$

In essence, one presumes that the data was generated using the following statistical model

$$Y_j = \tilde{f}(t_j; \mathbf{a}_{0,M}) + \mathcal{E}_j, \quad j = 1, 2, 3, \dots, N. \quad (2.2.11)$$

In the above equation, $\tilde{f}(t_j; \mathbf{a}_{0,M}) = f(t_j; G_{0,M})$, where $G_{0,M} = \mathbf{\Delta}^T \mathbf{a}_{0,M} \in \mathcal{P}^M(\Omega_\theta)$, and $\mathbf{a}_{0,M} \in \widetilde{\mathbb{R}}^M$ is the one that minimizes

$$\tilde{J}^0(\mathbf{a}_M) = \sigma_0^2 + \int_{t_s}^{t_f} (f(t; G_0) - \tilde{f}(t; \mathbf{a}_M))^2 d\mu(t) \quad (2.2.12)$$

over $\widetilde{\mathbb{R}}^M$. In other words, the functional J^0 defined by

$$J^0(P) = \sigma_0^2 + \int_{t_s}^{t_f} (f(t; G_0) - f(t; G))^2 d\mu(t) \quad (2.2.13)$$

has a minimizer $G_{0,M}$ in $\mathcal{P}^M(\Omega_\theta)$ for each fixed M .

Thus, we have a model “misspecification”, which is due to the approximation of the infinite-dimensional space $\mathcal{P}(\Omega_\theta)$ by the finite-dimensional space $\mathcal{P}^M(\Omega_\theta)$. Under this framework, the total error between the true model (2.1.1) and the approximating model (2.2.11) can be characterized by (illustrated in Figure 2.1)

$$\rho(G_0, G_{0,M}) + \rho(G_{0,M}, \widehat{G}_M^N),$$

where the first term $\rho(G_0, G_{0,M})$ is a measure of the accuracy of the approximating model and is often called *bias* in the statistics literature, and the second term $\rho(G_{0,M}, \widehat{G}_M^N)$ is a measure of estimation accuracy and is often called *variance*. Using properties of the Prohorov metric and assumptions (A3)–(A5) as well as Theorems 2.2.3 and 2.2.4, we readily see that the bias $\rho(G_0, G_{0,M})$ approaches zero as $M \rightarrow \infty$. However, for fixed N the variance in general increases as the value of M increases (e.g., see [46]); that is, we have less confidence in the parameter estimates as the number of approximating parameters increases. Hence, there is a trade-off between the bias and the variance (illustrated in Figure 2.2). Model selection criteria such as the Akaike Information Criterion and the Bayesian Information Criterion have been widely used in the literature to select a best approximating model from a prior set of candidate models, and they all are based to some extent on the *principle of parsimony* (again see [33, 46]). The

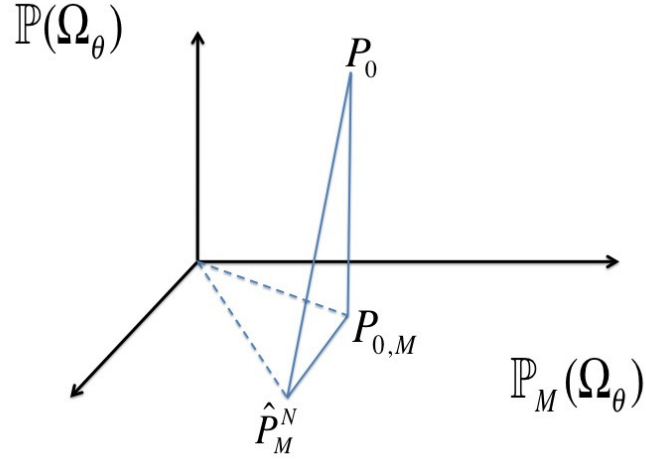


Figure 2.1: Illustration of the bias and the variance in the probability measure approximation.

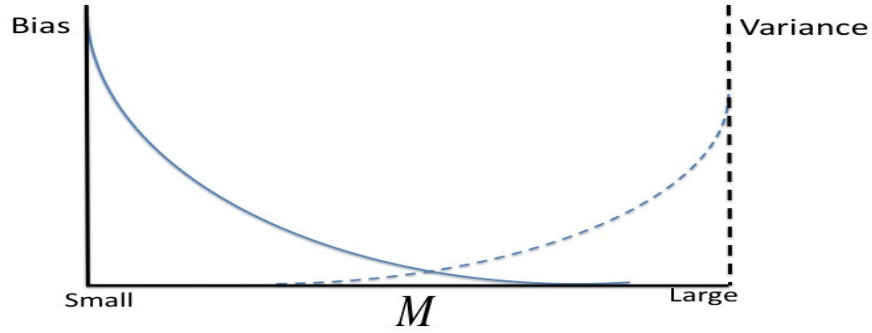


Figure 2.2: Illustration of the trade-off between the bias and the variance.

goal in model selection is to simultaneously minimize both bias (modeling error) and variance (estimation error). Thus one can use a model selection criterion to select a best M value (i.e., a best approximating model).

2.2.4 Pointwise Asymptotic Normality of the Approximated Probability Measure Estimator

In this section, we consider the pointwise asymptotic normality of the least-squares estimator G_M^N . Since for any given θ , $G_M^N(\theta)$ is linearly dependent on \mathbf{A}_M^N (for example, in the case

where the Dirac measure approximation is used, $G_M^N(\boldsymbol{\theta}) = (\boldsymbol{\Delta}(\boldsymbol{\theta}))^T \mathbf{A}_M^N$, we first consider the asymptotic normality of \mathbf{A}_M^N . As discussed in the above section, (2.2.11) is misspecified. Hence, the asymptotic normality results established in [94] for the parameter estimator in a misspecified nonlinear regression can be applied to our case. To ensure the results in [94] hold, we make the following additional assumptions.

(A6) For each fixed M , \tilde{J}^0 has a unique minimizer $\mathbf{a}_{0,M}$ in $\tilde{\mathbb{R}}^M$ (that is, J^0 has a unique minimizer $G_{0,M}$ in $\mathcal{P}^M(\Omega_\theta)$), and the minimizer $\mathbf{a}_{0,M}$ is interior to $\tilde{\mathbb{R}}^M$.

(A7) For each fixed M , \tilde{f} is twice continuously differentiable with respect to \mathbf{a}_M , and the matrices $\mathcal{H}(\mathbf{a}_{0,M})$ and $\mathcal{F}(\mathbf{a}_{0,M})$ defined by

$$\begin{aligned} \mathcal{H}(\mathbf{a}_M) &= \frac{\partial^2 \tilde{J}^0(\mathbf{a}_M)}{\partial \mathbf{a}_M^2} \\ &= 2 \int_{t_s}^{t_f} \left[\frac{\partial \tilde{f}(t; \mathbf{a}_M)}{\partial \mathbf{a}_M} \left(\frac{\partial \tilde{f}(t; \mathbf{a}_M)}{\partial \mathbf{a}_M} \right)^T - (f(t; G_0) - \tilde{f}(t; \mathbf{a}_M)) \frac{\partial^2 \tilde{f}(t; \mathbf{a}_M)}{\partial \mathbf{a}_M^2} \right] d\mu(t) \end{aligned} \quad (2.2.14)$$

and

$$\mathcal{F}(\mathbf{a}_M) = 4 \int_{t_s}^{t_f} \left[\sigma_0^2 + (f(t; G_0) - \tilde{f}(t; \mathbf{a}_M))^2 \right] \frac{\partial \tilde{f}(t; \mathbf{a}_M)}{\partial \mathbf{a}_M} \left(\frac{\partial \tilde{f}(t; \mathbf{a}_M)}{\partial \mathbf{a}_M} \right)^T d\mu(t) \quad (2.2.15)$$

are nonsingular.

Theorem 2.2.7. *Under assumptions (A1)–(A7), for each fixed M we have*

$$\sqrt{N} (\mathbf{A}_M^N - \mathbf{a}_{0,M}) \xrightarrow{d} \mathbf{Z} \sim \mathcal{N}(0, \Sigma_{0,M}), \text{ as } N \rightarrow \infty, \quad (2.2.16)$$

where \xrightarrow{d} denotes convergence in distribution, $\Sigma_{0,M} = (\mathcal{H}(\mathbf{a}_{0,M}))^{-1} \mathcal{F}(\mathbf{a}_{0,M}) (\mathcal{H}(\mathbf{a}_{0,M}))^{-1}$, and $\mathcal{N}(0, \Sigma_{0,M})$ represents a multivariate normal distribution with zero mean and covariance matrix $\Sigma_{0,M}$. A strongly consistent estimator of $\mathbf{a}_{0,M}$ is \mathbf{A}_M^N , and a strongly consistent estimator of $\Sigma_{0,M}$ is given by

$$\Sigma_M^N = (H^N(\mathbf{A}_M^N))^{-1} F^N(\mathbf{A}_M^N) (H^N(\mathbf{A}_M^N))^{-1}, \quad (2.2.17)$$

where “strongly consistent” means convergence almost surely, and

$$H^N(\mathbf{a}_M) = \frac{2}{N} \sum_{j=1}^N \left[\frac{\partial \tilde{f}(t_j; \mathbf{a}_M)}{\partial \mathbf{a}_M} \left(\frac{\partial \tilde{f}(t_j; \mathbf{a}_M)}{\partial \mathbf{a}_M} \right)^T - (Y_j - \tilde{f}(t_j; \mathbf{a}_M)) \frac{\partial^2 \tilde{f}(t_j; \mathbf{a}_M)}{\partial \mathbf{a}_M^2} \right], \quad (2.2.18)$$

and

$$F^N(\mathbf{a}_M) = \frac{4}{N} \sum_{j=1}^N \left[(Y_j - \tilde{f}(t_j; \mathbf{a}_M))^2 \left(\frac{\partial \tilde{f}(t_j; \mathbf{a}_M)}{\partial \mathbf{a}_M} \right) \left(\frac{\partial \tilde{f}(t_j; \mathbf{a}_M)}{\partial \mathbf{a}_M} \right)^T \right]. \quad (2.2.19)$$

Theorem 2.2.7 implies that for any sufficiently large N , we have

$$\mathbf{A}_M^N \sim \mathcal{N}(\hat{\mathbf{a}}_M^N, \frac{1}{N} \hat{\Sigma}_M^N). \quad (2.2.20)$$

Here $\hat{\Sigma}_M^N$ is given by

$$\hat{\Sigma}_M^N = (\hat{H}^N(\hat{\mathbf{a}}_M^N))^{-1} \hat{F}^N(\hat{\mathbf{a}}_M^N) (\hat{H}^N(\hat{\mathbf{a}}_M^N))^{-1}, \quad (2.2.21)$$

with

$$\hat{H}^N(\mathbf{a}_M) = \frac{2}{N} \sum_{j=1}^N \left[\frac{\partial \tilde{f}(t_j; \mathbf{a}_M)}{\partial \mathbf{a}_M} \left(\frac{\partial \tilde{f}(t_j; \mathbf{a}_M)}{\partial \mathbf{a}_M} \right)^T - (y_j - \tilde{f}(t_j; \mathbf{a}_M)) \frac{\partial^2 \tilde{f}(t_j; \mathbf{a}_M)}{\partial \mathbf{a}_M^2} \right], \quad (2.2.22)$$

and

$$\hat{F}^N(\mathbf{a}_M) = \frac{4}{N} \sum_{j=1}^N \left[(y_j - \tilde{f}(t_j; \mathbf{a}_M))^2 \left(\frac{\partial \tilde{f}(t_j; \mathbf{a}_M)}{\partial \mathbf{a}_M} \right) \left(\frac{\partial \tilde{f}(t_j; \mathbf{a}_M)}{\partial \mathbf{a}_M} \right)^T \right]. \quad (2.2.23)$$

If one uses the Dirac measure approximation method, then by (2.2.20) we know that for any sufficiently large N

$$G_M^N(\boldsymbol{\theta}) \sim \mathcal{N}((\boldsymbol{\Delta}(\boldsymbol{\theta}))^T \hat{\mathbf{a}}_M^N, \frac{1}{N} (\boldsymbol{\Delta}(\boldsymbol{\theta}))^T \hat{\Sigma}_M^N \boldsymbol{\Delta}(\boldsymbol{\theta})) \quad (2.2.24)$$

holds for any fixed $\boldsymbol{\theta} \in \Omega_\theta$. Similarly, one can use (2.2.20) to obtain the pointwise asymptotic result for $G_M^N(\boldsymbol{\theta})$ in the case where the linear spline approximation method is employed.

2.3 Numerical Results

In this section, we use the motivating example in Section 2.1 to demonstrate our theoretic results through simulated data. Specifically, we consider the following nonparametric model

$$Y_j = |r(k_j; G_0)|^2 + \mathcal{E}_j, \quad j = 1, 2, 3, \dots, N, \quad (2.3.1)$$

with $r(k; G)$ given by (2.1.3). The simulated data is then generated by simulating

$$y_j = |r(k_j; G_0)|^2 + \epsilon_j, \quad j = 1, 2, 3, \dots, N. \quad (2.3.2)$$

In the above equation, G_0 is chosen as the cumulative distribution function of a truncated normal distribution with its corresponding probability density function p_0 given by

$$p_0(k_0) = \frac{\beta}{\sigma\sqrt{2\pi}} \exp\left(-\frac{(k_0 - \mu)^2}{2\sigma^2}\right), \quad k_0 \in [\underline{k}_0, \bar{k}_0],$$

where $\mu = 700$, $\sigma = 50$, $\underline{k}_0 = 400$, $\bar{k}_0 = 1090$, and β is the normalizing constant

$$\beta^{-1} = \int_{\underline{k}_0}^{\bar{k}_0} \frac{1}{\sigma\sqrt{2\pi}} \exp\left(-\frac{(k_0 - \mu)^2}{2\sigma^2}\right) dk_0.$$

The ϵ_j are realizations of \mathcal{E}_j , which are assumed to be normally distributed with zero mean and standard deviation $\sigma_0 = 0.002$. For all the simulations below, N is chosen as 70, the measurement wavenumber points are $k_j = 400 + 10(j - 1)$, $j = 1, 2, \dots, 70$, and the values for the rest of model parameters are chosen as

$$\tau = 0.03, \quad \varepsilon_s = 2.7, \quad \varepsilon_\infty = 2.5.$$

Since G_0 is chosen as an absolutely continuous function, we will use the linear spline approximation method in the simulations demonstrated below.

In the presentation below, we first use the Akaike Information Criterion to determine the optimal value of M , where the probability measure is obtained by the linear spline approximation method. We then compare the confidence band obtained using the asymptotic normality results with the one obtained with the Monte Carlo simulations.

2.3.1 Optimal Value of M

As we stated earlier in this section, we use the Akaike Information Criterion (AIC), one of the most widely used model selection criteria, to determine the optimal value for M . The AIC was developed by Akaike (in 1973), and it is based on Kullback-Leibler information (a well-known measure of “distance” between two probability density functions) and maximum likelihood estimation. There are several advantages in using the AIC. For example, it can be used to compare both nested models and non-nested models, and it can also be used to compare multiple models at a time. For the least squares case, it can be found (e.g., see [46, Section 2.2], [33, Section 4.3.1]) that if the measurement errors are i.i.d. normally distributed, then the AIC is given by

$$\text{AIC} = N \log\left(\frac{\text{RSS}}{N}\right) + 2(M + 1). \quad (2.3.3)$$

Here $M + 1$ is the total number of estimated parameters including the coefficients for the splines and the variance of measurement errors, and RSS denotes the residuals of sum squares given by

$$\text{RSS} = \sum_{j=1}^N (y_j - |r(k_j; \hat{G}_M^N)|^2)^2.$$

Given a prior set of candidate models, one calculates the AIC value for each model, and the best approximating model is the one with minimum AIC value. As might be expected, the AIC value depends on the data set used. Thus, when one tries to select a best model from a set of candidate models, one must use the same data set to calculate AIC values for each of the models. It should be noted that the AIC may perform poorly if the sample size N is small relative to the total number of estimated parameters (it is suggested in [46] that the AIC should be used only if the sample size is at least 40 times the total number of estimated parameters). Otherwise, one needs to use the small sample AIC, the so-called AIC_c , which is given by

$$\text{AIC}_c = \text{AIC} + \frac{2(M+1)(M+2)}{N-M-2}. \quad (2.3.4)$$

For more information on the AIC and its variations, we refer the interested reader to [46] and [33, Chapter 4].

The set of our candidate models is chosen as model (2.2.11) with $M = 5, 10, 15, 20, 25$ and 30 , and \mathcal{E}_j , $j = 1, 2, 3, \dots, N$, being i.i.d. normally distributed with zero mean and constant variance. Note that for all our models the sample size is less than 40 times total number of estimated parameters. Hence, we will use the AIC_c to select the best model. Figure 2.3 depicts the AIC_c values for each of these models. From this figure we see that the model with $M = 15$ is the one with the minimum AIC_c value and thus it is the best approximating model as measured by AIC_c .

2.3.2 Pointwise Confidence Band

In this section, we construct the pointwise confidence band for G_M^N by using both the asymptotic normality results presented in Section 2.2.4 and Monte Carlo simulations, where M is chosen as the optimal value of $M = 15$ obtained in the above analysis.

By (2.2.20) we know that for any sufficiently large N

$$G_M^N(k_0) \sim \mathcal{N}(\hat{G}_M^N(k_0), \frac{1}{N}(\mathbf{L}(k_0))^T \hat{\Sigma}_M^N \mathbf{L}(k_0)) \quad (2.3.5)$$

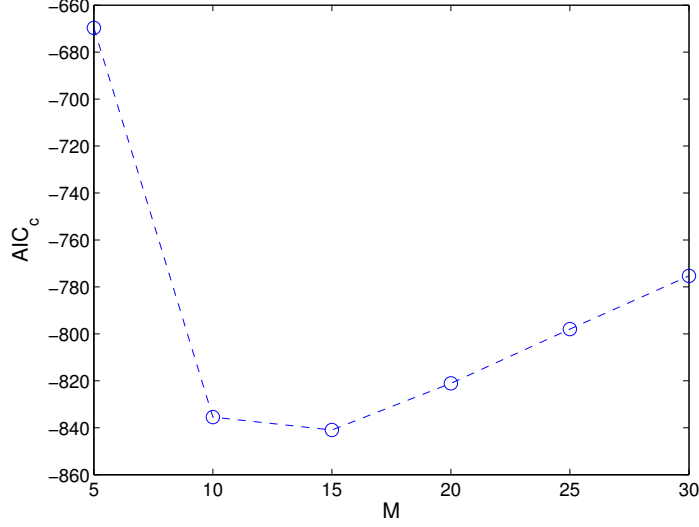


Figure 2.3: The AIC_c values for model (2.2.11) with $M = 5, 10, 15, 20, 25$ and 30 .

holds for any fixed $k_0 \in [\underline{k}_0, \bar{k}_0]$. In the above equation, $\hat{G}_M^N(k_0) = (\mathbf{L}(k_0))^T \hat{\mathbf{a}}_M^N$, where

$$\mathbf{L}(k_0) = \left(\int_{\underline{k}_0}^{k_0} l_1(\xi) d\xi, \int_{\underline{k}_0}^{k_0} l_2(\xi) d\xi, \dots, \int_{\underline{k}_0}^{k_0} l_M(\xi) d\xi \right)^T.$$

One can then use (2.3.5) to construct the pointwise $100(1 - \lambda)\%$ level confidence band, which is given by

$$\left[\hat{G}_M^N(k_0) - t_{1-\lambda/2} \text{SEP}_{\text{AN}}(k_0), \quad \hat{G}_M^N(k_0) + t_{1-\lambda/2} \text{SEP}_{\text{AN}}(k_0) \right], \quad k_0 \in [\underline{k}_0, \bar{k}_0].$$

Here $\text{SEP}_{\text{AN}}(k_0) = \sqrt{\frac{1}{N} (\mathbf{L}(k_0))^T \hat{\Sigma}_M^N \mathbf{L}(k_0)}$, and the critical value $t_{1-\lambda/2}$ is determined by $\text{Prob}\{T \geq t_{1-\alpha/2}\} = \lambda/2$, where T has a student's t distribution t^{N-M} with $N - M$ degrees of freedom. For the simulations illustrated below, l_j is the j^{th} piecewise linear spline element using equally spaced nodes, and central difference schemes are used to approximate the first and second order derivatives involved in the covariance matrix $\hat{\Sigma}_M^N$.

To construct a pointwise confidence band using the Monte Carlo simulations, we first generate K simulated data sets and then estimate the probability measure for each data set. We denote the estimated weights for the m th simulation as $\hat{\mathbf{a}}_M^{N,(m)}$ and the corresponding estimated probability measure as $\hat{G}_M^{N,(m)}$; that is, $\hat{G}_M^{N,(m)}(k_0) = (\mathbf{L}(k_0))^T \hat{\mathbf{a}}_M^{N,(m)}$. Then the mean vector and covariance

matrix for the estimator \mathbf{A}_M^N obtained using Monte Carlo simulations are computed as

$$\hat{\mathbf{a}}_{\text{MC}} = \frac{1}{K} \sum_{m=1}^K \hat{\mathbf{a}}_M^{N,(m)}, \quad \hat{\Sigma}_{\text{MC}} = \frac{1}{K-1} \sum_{m=1}^K (\hat{\mathbf{a}}_M^{N,(m)} - \hat{\mathbf{a}}_{\text{MC}})(\hat{\mathbf{a}}_M^{N,(m)} - \hat{\mathbf{a}}_{\text{MC}})^T,$$

and the mean and covariance for the corresponding probability measure estimator G_M^N are respectively given by

$$\hat{G}_{\text{MC}}(k_0) = \frac{1}{K} \sum_{m=1}^K \hat{G}_M^{N,(m)} = \frac{1}{K} \sum_{m=1}^K (\mathbf{L}(k_0))^T \hat{\mathbf{a}}_M^{N,(m)} = (\mathbf{L}(k_0))^T \hat{\mathbf{a}}_{\text{MC}}$$

and

$$\begin{aligned} (\text{SEP}_{\text{MC}}(k_0))^2 &= \frac{1}{K-1} \sum_{m=1}^K (\hat{G}_M^{N,(m)}(k_0) - \hat{G}_{\text{MC}}(k_0))^2 \\ &= \frac{1}{K-1} \sum_{m=1}^K \left[(\mathbf{L}(k_0))^T (\hat{\mathbf{a}}_M^{N,(m)} - \hat{\mathbf{a}}_{\text{MC}}) \right]^2 \\ &= (\mathbf{L}(k_0))^T \hat{\Sigma}_{\text{MC}} \mathbf{L}(k_0). \end{aligned}$$

The pointwise $100(1 - \lambda)\%$ level confidence band is then given by

$$[\hat{G}_{\text{MC}}(k_0) - t_{1-\lambda/2} \text{SEP}_{\text{MC}}(k_0), \hat{G}_{\text{MC}}(k_0) + t_{1-\lambda/2} \text{SEP}_{\text{MC}}(k_0)].$$

Figure 2.4 depicts the pointwise confidence bands for G_M^N obtained using both the pointwise asymptotic normality results and the Monte Carlo simulations, where α is chosen to be 0.1, and $K = 1,000$. We observe from this figure that the confidence bands obtained by these two approaches are similar except at the plateau regions where the confidence band obtained using the asymptotic results is wider than that obtained using the Monte Carlo simulations. To have some idea of this discrepancy, we calculate the confidence intervals of the coefficients for each spline obtained by using both the asymptotic normality results and the Monte Carlo simulations. By (2.2.20) we know that the $100(1 - \lambda)\%$ level confidence intervals for the coefficients obtained from the asymptotic normality results are given by

$$[\hat{a}_{M,j}^N - t_{1-\lambda/2} \text{SEA}_{\text{AN},j}, \hat{a}_{M,j}^N + t_{1-\lambda/2} \text{SEA}_{\text{AN},j}], \quad j = 1, 2, 3, \dots, M,$$

where $\hat{a}_{M,j}^N$ is the j^{th} element of $\hat{\mathbf{a}}_M^N$, and $\text{SEA}_{\text{AN},j} = \sqrt{\frac{1}{N} \hat{\Sigma}_{M,jj}^N}$ with $\hat{\Sigma}_{M,jj}^N$ being the $(j, j)^{\text{th}}$ element of $\hat{\Sigma}_M^N$. For the Monte Carlo method, the $100(1 - \lambda)\%$ level confidence intervals for the coefficients are calculated as

$$[\hat{a}_{\text{MC},j} - t_{1-\lambda/2} \text{SEA}_{\text{MC},j}, \hat{a}_{\text{MC},j} + t_{1-\lambda/2} \text{SEA}_{\text{MC},j}], \quad j = 1, 2, 3, \dots, M.$$

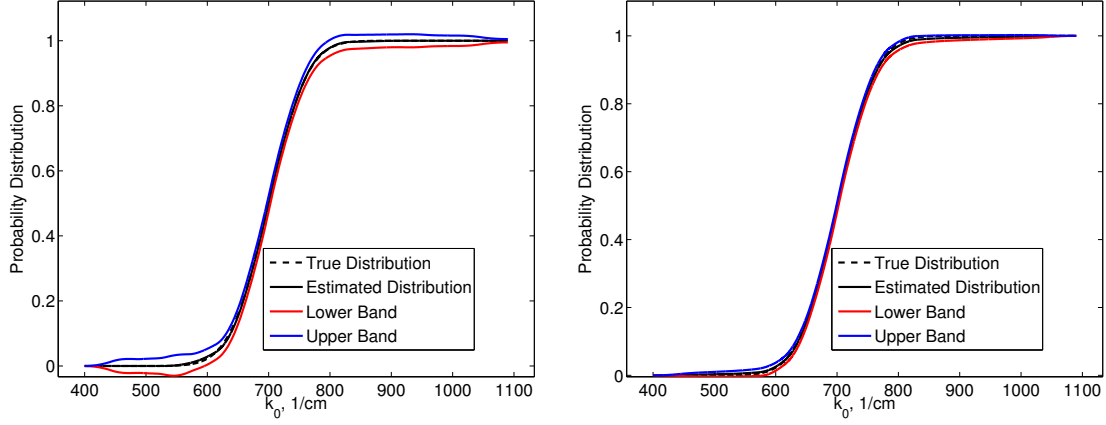


Figure 2.4: The pointwise confidence bands for the cumulative distribution function obtained using the pointwise asymptotic normality results (left) and the ones obtained using the Monte Carlo simulations (right).

Here $\hat{a}_{MC,j}$ is the j^{th} element of $\hat{\mathbf{a}}_{MC}$, and $SEA_{MC,j} = \sqrt{\hat{\Sigma}_{MC,jj}}$ with $\hat{\Sigma}_{MC,jj}$ being the $(j,j)^{th}$ element of $\hat{\Sigma}_{MC}$. In Table 2.1, we give the confidence intervals obtained by these two methods. From this table, we see that the confidence intervals obtained by the asymptotic normality results

Table 2.1: The confidence intervals (CI) computed using the pointwise asymptotic normality (AN) results and the ones obtained using the Monte Carlo (MC) simulations.

j	CI using AN method	CI using MC method
1	$[-0.0006, 0.0006]$	$[-0.0001, 0.0002]$
2	$[-0.0007, 0.0007]$	$[-0.0001, 0.0001]$
3	$[-0.0010, 0.0010]$	$[-0.0001, 0.0002]$
4	$[-0.0005, 0.0014]$	$[-0.0001, 0.0004]$
5	$[0.0006, 0.0018]$	$[0.0010, 0.0021]$
6	$[0.0055, 0.0066]$	$[0.0052, 0.0063]$
7	$[0.0080, 0.0091]$	$[0.0080, 0.0090]$
8	$[0.0051, 0.0056]$	$[0.0049, 0.0058]$
9	$[0.0012, 0.0018]$	$[0.0010, 0.0018]$
10	$[-0.0004, 0.0005]$	$[-0.0001, 0.0004]$
11	$[-0.0002, 0.0003]$	$[-0.0001, 0.0002]$
12	$[-0.0003, 0.0003]$	$[-0.0001, 0.0001]$
13	$[-0.0004, 0.0004]$	$[-0.0001, 0.0001]$
14	$[-0.0002, 0.0002]$	$[-0.0000, 0.0001]$
15	$[-0.0003, 0.0003]$	$[-0.0001, 0.0001]$

are wider than those obtained by the Monte Carlo simulations except for those with splines located in the middle region where we have a good match. This is in agreement with the plots in Figure 2.4. It is clear from (2.1.2) that the relative permittivity is less sensitive to the coefficients for those splines located in the far left and far right (i.e., the plateau regions of the cumulative distribution function) where the values of the corresponding probability density function are negligible. Hence, the model output, the reflectance $|r|^2$, is less sensitive to the coefficients for those splines located in these two regions. Thus, one would have wider confidence intervals (i.e., have less confidence in estimates) for these coefficients as we see from (2.2.21)–(2.2.23) that the covariance matrix for the coefficients obtained by the asymptotic normality results is dependent on the sensitivity of the model output with respect to the coefficients.

2.4 Concluding Remarks and Future Research Questions

A computational and theoretical framework was presented for nonparametric estimation of a probability measure G_0 in cases where the regression function is dependent on the sought-after probability measure. We also provided a consistency result for the probability measure estimator G^N . Moreover, we discussed the bias and the variance in the parameter estimation process where the infinite-dimensional parameter space $\mathcal{P}(\Omega_\theta)$ is approximated by a finite-dimensional parameter space $\mathcal{P}^M(\Omega_\theta)$, and we established the pointwise asymptotic normality for the approximated probability measure estimator G_M^N . Numerical results verify that we have a good match for the pointwise confidence band obtained by the pointwise asymptotic normality results and the Monte Carlo simulations in the region to which the model output is most sensitive.

Future efforts include investigation of convergence in distribution of the stochastic process $\sqrt{N}(G^N - G_0)$ to a certain Gaussian process. It is worth noting that the asymptotic normality of an infinite-dimensional parameter estimator in a statistic model with smooth regression function has been studied by a number of researchers (e.g., see [69] and the references therein). However, in those efforts the space for the infinite-dimensional parameter was required to be a compact set in a Hilbert space. Thus, the results established in those research efforts cannot be applied to our case as our parameter space $\mathcal{P}(\Omega_\theta)$ is a compact set in the space of all finite regular measures with weak norm $\left(\text{frm}(\Omega_\theta), \|\cdot\|_{\text{frm}(\Omega_\theta),w}\right)$, which is a separable normal linear space (e.g., see [93, Theorem IV.1.4]), but not a Hilbert space.

Use of Difference-Based Methods to Explore Statistical and Mathematical Model Discrepancy in Inverse Problems

Next we focus on methods for exploring the validity of the statistical model assumptions. In parameter estimation, one must always pair the mathematical model, which describes the underlying dynamics, with a statistical model that describes the observation process. The requirements about what must be specified in the statistical model depend upon the estimation method. For example in ordinary least squares, one must make assumptions about the first two moments of the measurement errors, and in a maximum likelihood or Bayesian estimation, the full distribution of the measurement errors must be specified. Misspecification in the statistical model can lead to improperly calibrated model parameters and meaningless uncertainty quantification, just as in the case of mathematical model discrepancy. The contents of this chapter are based upon the following publication [18]:

H.T. Banks, J. Catenacci, and S. Hu. Use of difference-based methods to explore statistical and mathematical model discrepancy in inverse problems. *Journal of Inverse and Ill-Posed Problems*. (in press).

3.1 Introduction

A number of difference-based methods have been proposed in the literature to estimate the variance of measurement errors in a nonparametric regression where the mean function of observations is unknown and estimated using some nonparametric methods (e.g., see [44, 54, 71, 73, 91] and the reference therein). These methods involve differencing the data and do not

require estimation of the mean function. Specifically, the estimated variance is defined as the weighted average of the squared normalized difference of $\nu + 1$ observations, where ν is an integer. These normalized differences of $\nu + 1$ observations are called *pseudo measurement errors* in this paper. The purpose of this paper is to illustrate how these pseudo measurement errors can be used as a possible way of detecting **statistical** model **misspecification** or discrepancy as well as **mathematical** model **misspecification** or discrepancy within the context of a least squares inverse problem. That is, given a set of observed data, a mathematical model describing the observed process is fitted to the data via a least squares formulation by estimating a set of unknown parameters. As has become conventional in inverse problems, we would also like to quantify the uncertainty present in the estimation of the mathematical model parameters using confidence intervals. To do this, one must have a correctly specified statistical model which describes the data collection process along with a mathematical model which is assumed to describe the process under observation. Typically, one uses residual plots as illustrated in [33, 40] to ensure that the assumptions made in specifying both the statistical and mathematical model are not violated. However, the residuals can only be computed **after** the inverse problem has been completed. Furthermore, if the residual plots do not illustrate the desired random patterns, it can be difficult, if not impossible to determine if this is caused by mathematical model discrepancy or statistical model discrepancy, or both. We will show how difference-based techniques can be used directly on the data to deduce if the assumptions of the statistical model have been violated prior to running the inverse problem. Then residual plots can be used afterwards to verify that the mathematical model is sufficiently accurate.

We consider inverse or parameter estimation problems in the context of a parameterized (with vector parameter $\mathbf{q} \in \Omega^{\kappa_q} \subset \mathbb{R}^{\kappa_q}$) n -dimensional vector dynamical system (for a physical or biological process) or **mathematical model** given by

$$\frac{d\mathbf{x}}{dt}(t) = \mathbf{h}(t, \mathbf{x}(t), \mathbf{q}), \quad (3.1.1)$$

$$\mathbf{x}(t_s) = \mathbf{x}_0, \quad (3.1.2)$$

with **observation process**

$$\mathbf{f}(t; \boldsymbol{\theta}) = \mathcal{C}\mathbf{x}(t; \boldsymbol{\theta}), \quad (3.1.3)$$

where $\boldsymbol{\theta} = (\mathbf{q}^T, \tilde{\mathbf{x}}_0^T)^T \in \Omega \subset \mathbb{R}^{\kappa_q + \tilde{n}} = \mathbb{R}^{\kappa_\theta}$, $\tilde{n} \leq n$, κ_q is the number of unknown dynamic parameters, \tilde{n} is the number of unknown initial conditions $\tilde{\mathbf{x}}_0$, and the observation operator \mathcal{C} maps \mathbb{R}^n to \mathbb{R}^m . The sets Ω^{κ_q} and Ω are assumed known restraint sets for the parameters.

We make some standard assumptions (see [33, 40]) underlying our inverse problem formulations.

- Assume that there exists a *true or nominal set* of parameters $\boldsymbol{\theta}_0 \in \Omega$.

- Ω is a compact subset of Euclidian space of $\mathbb{R}^{\kappa_\theta}$ and $\mathbf{f}(t; \boldsymbol{\theta})$ is continuous on $[0, T] \times \Omega$.

Denote $\hat{\boldsymbol{\theta}}$ as the estimated parameter for $\boldsymbol{\theta}_0 \in \Omega$. The inverse problem is based on statistical assumptions on the observation error in the data. We consider a special case of a general **statistical model** of the form

$$\mathbf{Y}_j = \mathbf{f}(t_j; \boldsymbol{\theta}_0) + \mathbf{g}(t_j; \boldsymbol{\theta}_0) \circ \boldsymbol{\mathcal{E}}_j, \quad j = 1, 2, \dots, N, \quad (3.1.4)$$

where $\mathbf{Y}_j = (Y_{1j}, Y_{2j}, \dots, Y_{mj})^T$, $\mathbf{f}(t_j; \boldsymbol{\theta}_0) = (f_1(t_j; \boldsymbol{\theta}_0), f_2(t_j; \boldsymbol{\theta}_0), \dots, f_m(t_j; \boldsymbol{\theta}_0))^T$ denotes observations of the mathematical model describing the underlying physical or biological process with the nominal parameters $\boldsymbol{\theta}_0$ at the measurement point t_j , and N is the total number of observations. The so called measurement or observation error at t_j is represented by $\mathbf{g}(t_j; \boldsymbol{\theta}_0) \circ \boldsymbol{\mathcal{E}}_j$, where \circ denotes component-wise multiplication of the vectors, and $\boldsymbol{\mathcal{E}}_j = (\mathcal{E}_{1j}, \mathcal{E}_{2j}, \dots, \mathcal{E}_{mj})^T$ is a $m \times 1$ random vector.

The simplest form of (3.1.4) is when $\mathbf{g}(t_j; \boldsymbol{\theta}_0)$ is $m \times 1$ vector with each element being 1, this is known as an **absolute error model**. Another popular choice for a statistical model is given by $\mathbf{g}(t_j; \boldsymbol{\theta}_0) = \mathbf{f}(t_j; \boldsymbol{\theta}_0)$ which results in a **relative error model**. In this work we will only concern ourselves with the special case of $\mathbf{g}(t_j; \boldsymbol{\theta}_0) = \mathbf{f}^\gamma(t_j; \boldsymbol{\theta}_0)$ so that

$$\mathbf{Y}_j = \mathbf{f}(t_j; \boldsymbol{\theta}_0) + \mathbf{f}^\gamma(t_j; \boldsymbol{\theta}_0) \circ \boldsymbol{\mathcal{E}}_j, \quad j = 1, 2, \dots, N, \quad (3.1.5)$$

where $\mathbf{f}^\gamma(t_j; \boldsymbol{\theta}_0) = (f_1^{\gamma_1}(t_j; \boldsymbol{\theta}_0), f_2^{\gamma_2}(t_j; \boldsymbol{\theta}_0), \dots, f_m^{\gamma_m}(t_j; \boldsymbol{\theta}_0))^T$ and $\gamma = (\gamma_1, \gamma_2, \dots, \gamma_m)$. Here $\mathbf{f}^\gamma \circ$ denotes the component-wise exponentiation by γ of the vector function \mathbf{f} followed by component-wise multiplication of the vectors $\mathbf{f}^\gamma(t_j; \boldsymbol{\theta}_0)$ and $\boldsymbol{\mathcal{E}}_j$. Furthermore, we assume that for any fixed j , \mathcal{E}_{ij} , $i = 1, 2, \dots, m$, are independent with mean zero and

$$\text{Var}(\mathcal{E}_{ij}) = \sigma_{0,i}^2.$$

There are numerous examples (especially in biological and biomedical problems involving assays and/or population counts) in which such statistical models have been found appropriate if a proper value of γ is chosen. These examples include modeling of HIV viral infections [8] for data consisting of CD4⁺ T cell counts with $\gamma_1 = 0$ and viral RNA counts with $\gamma_2 = 1.2$; prion aggregation kinetic models [25] with $\gamma_i = \gamma = 0.6$; insect populations undergoing pesticide treatments [6, 7] with $\gamma \approx .8$ or $.85$; and cell proliferation studies modeling flow cytometry data with $\gamma = 0.5$ [33, p. 87], [90] for a dividing population of lymphocytes labeled with the intracellular dye CFSE. In this latter example, as cells divide, the highly fluorescent intracellular CFSE is partitioned evenly between two daughter cells. A flow cytometer measures the CFSE fluorescence intensity (FI) of labeled cells as a surrogate for the mass of CFSE within a cell, thus providing an indication of the number of times a cell has divided. In these applications we

note that γ is a to-be-determined tuning parameter for the statistical model. These problems involve special cases of Generalized Least Squares (GLS) formulations [33, 48, 52, 53, 84] which have become central to many inverse problem efforts in recent years.

We remark that for the case where the measurement errors are heteroscedastic, the difference-based methods were specially designed for the general case (3.1.4), and where the problem of interest is to estimate the function \mathbf{g} in the case where \mathbf{f} is also unknown (\mathbf{f} is often referred to as a nuisance parameter). Specifically, the estimator of \mathbf{g} is a weighted average of squared pseudo measurement errors with weights being some kernel functions, where the bandwidth (a free parameter) of the kernel function has a strong influence on the resulting estimate. To our knowledge, a proper choice of bandwidth is still a current topic of research. Since in this thesis we only consider the special case (3.1.5) with γ unknown, we refer the interested reader to [44, 71] and the references therein for more information on this topic.

To represent a collected data set, we let $\mathbf{y}_j = (y_{1j}, y_{2j}, \dots, y_{mj})^T$ be a realization of \mathbf{Y}_j ,

$$\mathbf{y}_j = \mathbf{f}(t_j; \boldsymbol{\theta}_0) + \mathbf{f}^\gamma(t_j; \boldsymbol{\theta}_0) \circ \boldsymbol{\varepsilon}_j, \quad j = 1, 2, \dots, N,$$

where $\boldsymbol{\varepsilon}_j = (\varepsilon_{1j}, \varepsilon_{2j}, \dots, \varepsilon_{mj})^T$ is a realization of $\boldsymbol{\mathcal{E}}_j$, $j = 1, 2, \dots, N$. We remark that difference-based methods for calculation of pseudo measurement errors can also be used in the case where the components of \mathbf{Y}_j may be observed at different measurement points (that is, $Y_{ij} = f_i(t_{ij}; \boldsymbol{\theta}_0) + f_i^{\gamma_i}(t_{ij}; \boldsymbol{\theta}_0)\mathcal{E}_{ij}$, $j = 1, 2, \dots, N_i$, $i = 1, 2, \dots, m$). But for notational convenience, we only consider the case where all the components of \mathbf{Y}_j are observed at the same measurement time points.

Of course, our model $\mathbf{f}(t_j; \boldsymbol{\theta}_0)$ typically does not perfectly describe the underlying process in question. This results in what we will refer to as mathematical model misspecification or discrepancy. Additionally, even in our assumption that the measurement errors can be described by (3.1.5), the value of γ is not known a priori. We will refer to this as statistical model misspecification or discrepancy.

For the sake of clarity, we present a basic example to make our motives clear. Consider a population under observation which is believed to follow the well known logistic model given by

$$\dot{x}(t) = bx(t) \left(1 - \frac{x(t)}{\kappa}\right), \quad x(t_s) = x_0. \quad (3.1.6)$$

Here x denotes the number of individuals, r is the intrinsic growth rate, and κ represents the carrying capacity and we assume that we can observe the number of individuals at times t_j , $j = 1, 2, \dots, N$. In this case we would have the statistical model

$$Y_j = f(t_j; \boldsymbol{\theta}_0) + f(t_j; \boldsymbol{\theta})^\gamma \mathcal{E}_j, \quad j = 1, 2, \dots, N, \quad (3.1.7)$$

where $f(t_j; \boldsymbol{\theta}) = x(t_j; \boldsymbol{\theta})$ denotes the solution to (3.1.6), (i.e. $\mathcal{C} = I$), and $\boldsymbol{\theta} = (b, \kappa, x_0)^T$ are the unknown mathematical model parameters. Recall that if $\gamma = 0$ we have an absolute error model, which is interpreted as meaning that the observation errors are independent of the size of the population itself, and if $\gamma = 1$ we have a relative error model, which indicates that the observation errors are a multiple of the population size itself. In general, for any $\gamma > 0$ we are making the assumption that the observation errors are dependent on the size of the population itself. Notice that $\mathbb{E}(Y_j) = f(t_j; \boldsymbol{\theta}_0)$, and $\text{Var}(Y_j) = f(t_j; \boldsymbol{\theta}_0)^{2\gamma} \sigma_0^2$, thus the variance is non-constant provided $\gamma \neq 0$.

In practice, one often assumes a specific statistical model (i.e., assumes a specific value for γ_i) and then chooses an appropriate method to carry out parameter estimation (for example, if $\gamma_i = 0$, $i = 1, 2, \dots, m$, then an ordinary least squares method is appropriate). One can then use residual plots to determine whether or not the assumed statistical model is appropriate (e.g., see [33, Chapter 3]). If one assumes a statistical model with $\gamma_i = 0$, $i = 1, 2, \dots, m$, and the resulting residual plots exhibit a non random pattern, such as a fan shaped pattern, then the assumed statistical model is not reasonable. In the case where the assumed statistical model is inappropriate, one tries another set of values for γ_i 's and carries out another inverse problem. This may be done iteratively until one finds values $\hat{\gamma}_i$'s such that the plot of the modified residuals $r_{ij}/|y_{ij} - f_i(t_j; \hat{\boldsymbol{\theta}})|^{\hat{\gamma}_i}$ versus t_j forms a horizontal band around the horizontal axis (where $r_{ij} = y_{ij} - f_i(t_j; \hat{\boldsymbol{\theta}})$ is the residual and $\hat{\boldsymbol{\theta}}$ denotes the estimate for $\boldsymbol{\theta}_0$). We thus see that if the involved inverse problem is computationally expensive, then this procedure can become prohibitive to implement. In addition, as we see later in this paper (see Section 4), residual plots may provide incorrect information for the variance of measurement errors in cases where mathematical model misspecification is present. In this paper, we propose to use the information provided by the pseudo measurement errors to directly determine appropriate values for the γ_i 's. We note that difference-based methods used to calculate pseudo measurement errors *do not involve any inverse problem calculations* and are *independent* of the chosen mathematical model. Hence, if our proposed method is successful, it should provide a much more efficient and accurate way to determine appropriate values for the γ_i 's.

After determining appropriate values for the γ_i 's (i.e., an appropriate statistical model), one may then use pseudo measurement errors to determine whether there is a mathematical model error. Specifically, one first uses the appropriate statistical model (chosen based on the information provided by pseudo measurement errors) to carry out parameter estimation. Then one compares the residual plot and the plot of $\hat{\varepsilon}_{ij}$ versus t_j to determine whether there is a mathematical model misspecification. For example, if there is a discernible divergence between these two plots, then there is a mathematical model error and the degree of this error is determined by the degree of the divergence. The difference between residuals and $\hat{\varepsilon}_{ij}$'s provides some prior information on this error. However, we remark that no discernible divergence between

these two plots *does not imply* that there is no mathematical model error. This is because there are some cases where two different mathematical models could give the same solution in the given sampling time region. For example, one may have an alternative mathematical model that has exactly the same form as the true model in a certain time region and has different forms in other time regions. If the sampling time region happens to be the one where these two mathematical models are the same, then there is no difference between the residuals and $\hat{\varepsilon}_{ij}$'s.

In this chapter, we also propose to use the information provided by pseudo measurement errors to perform bootstrapping to quantify the uncertainty in parameter estimates. Bootstrapping is a popular tool for construction of confidence intervals for parameter estimators (e.g., see [33, Chapter 3] and [62]). It involves constructing a family of samples/data sets based on random sampling with replacement. One uses each of these data sets to solve the inverse problem to obtain a new estimate, and then constructs the confidence intervals based on this family of estimates for the parameter estimators. We remark that there are two common ways to construct a family of data sets. One involves resampling the original data set, and it is based on the assumption that the original data are independent and identically distributed (i.i.d.). However, this method does not work well for cases where models are used to describe dynamic systems as observations are often not identically distributed even in the case where measurement errors are independent and identically distributed. The other method involves resampling residuals from an initial estimation to the original data set, and this is based on the assumptions that the regression function correctly specifies the observed part of the system and the first two moments of measurement errors are correctly specified (that is, the given statistical model is correctly specified). We thus see that this method does not work for the case where there is a mathematical modeling misspecification, which is often the situation in describing a real system. To alleviate this difficulty, we propose to use difference-based methods to obtain the pseudo measurement errors and then create bootstrapping samples using random sampling with replacement from these pseudo measurement errors. As we shall see later in Section 3.4, our proposed method works quite well and is robust to mathematical model misspecification. This is expected as the pseudo measurement errors, unlike residuals, are independent of the chosen mathematical model.

The remainder of this chapter is organized as follows. In Section 3.2, we give an introduction to difference-based methods for variance calculations. We then apply these methods in Section 3.3 to simulated data sets to verify the accuracy of these methods and then use the obtained pseudo measurement errors to determine proper statistical models for several experimental data sets. In Section 3.4, we use the information provided by these pseudo measurement errors to determine whether there is possible mathematical model error and illustrate how to carry out bootstrapping to quantify the uncertainty of corresponding parameter estimators in the presence of model misspecification. Finally, in Section 3.5 we conclude the chapter with some summary

remarks and future research efforts.

3.2 Difference-Based Methods

All of the difference-based methods are based on the assumption that the true or nominal regression function is sufficiently smooth and the maximum of the length of sampling time intervals (i.e., $\max\{t_{j+1} - t_j, j = 1, 2, \dots, N - 1\}$) is sufficiently small. The estimated variance is defined as the weighted average of the squared normalized differences of $\nu + 1$ observations. Specifically, the normalized differences of $\nu + 1$ observations, *pseudo measurement errors*, are defined as being either symmetric around y_{ij} as in

$$\hat{\varepsilon}_{ij} = \sum_{k=0}^{\nu} w_k y_{i, j - \left[\frac{\nu+1}{2}\right] + k + 1}, \quad j = \left[\frac{\nu}{2}\right], \left[\frac{\nu}{2}\right] + 1, \dots, N - \left[\frac{\nu}{2}\right], \quad i = 1, 2, \dots, m, \quad (3.2.1)$$

or asymmetric about y_{ij} as in

$$\hat{\varepsilon}_{ij} = \sum_{k=0}^{\nu} w_k y_{i, j + k}, \quad j = 1, 2, \dots, N - \nu, \quad i = 1, 2, \dots, m. \quad (3.2.2)$$

Here $[a]$ denotes the smallest integer that is greater than or equal to a , and the w_k 's are some real numbers which satisfy the conditions

$$\sum_{k=0}^{\nu} w_k = 0, \quad \sum_{k=0}^{\nu} w_k^2 = 1. \quad (3.2.3)$$

We remark that the above conditions are necessary to obtain an asymptotically unbiased estimator for the variance (e.g., see [73]) and so that the choice of the form for the pseudo measurement errors (i.e., choosing either (3.2.1) or (3.2.2)) does not affect the asymptotic result (e.g., see [71]). It is also worth noting that for $\nu > 1$ there are many different choices for the weights that satisfy condition (3.2.3), and that the variance of the variance estimator in general depends on the choice of the weights (e.g., see [73] for details).

Based on the choice for the values of ν and w_k 's, we introduce here three of these difference-based methods. One of them involves first-order backward differencing data (i.e., $\nu = 1$) and the associated pseudo measurement errors are calculated as follows:

$$\hat{\varepsilon}_{ij}^{1st} = \frac{1}{\sqrt{2}}(y_{i, j-1} - y_{i, j}), \quad j = 2, 3, \dots, N, \quad i = 1, 2, \dots, m. \quad (3.2.4)$$

For the case $\gamma_i = 0$ (i.e., constant variance error), the estimate for $\sigma_{0,i}$ is then given by

$$\hat{\sigma}_{0,i}^{1\text{st}} = \sqrt{\frac{1}{N-1} \sum_{j=2}^N \left(\hat{\varepsilon}_{ij}^{1\text{st}} \right)^2}, \quad i = 1, 2, \dots, m. \quad (3.2.5)$$

Another method involves second-order differencing data; that is $\nu = 2$. The pseudo measurement errors are given by

$$\hat{\varepsilon}_{ij}^{2\text{nd}} = \frac{1}{\sqrt{6}}(y_{i,j-1} - 2y_{ij} + y_{i,j+1}), \quad j = 2, 3, \dots, N-1, \quad i = 1, 2, \dots, m. \quad (3.2.6)$$

For the case $\gamma_i = 0$, the associated estimate for $\sigma_{0,i}$ is then given by

$$\hat{\sigma}_{0,i}^{2\text{nd}} = \sqrt{\frac{1}{N-2} \sum_{j=2}^{N-1} \left(\hat{\varepsilon}_{ij}^{2\text{nd}} \right)^2}, \quad i = 1, 2, \dots, m. \quad (3.2.7)$$

The last method we consider involves applying a first-order differencing operator l times (referred to as an l th-order differencing method in this paper), where l is some integer. Let Δ^l denote the first order differencing operator applied l times with $\Delta y_{ij} = y_{i,j+1} - y_{ij}$, $j = 1, 2, \dots, N-1$, $i = 1, 2, \dots, m$. Then pseudo measurement errors are calculated as follows:

$$\hat{\varepsilon}_{ij}^{1\text{st}-l} = \sqrt{\binom{2l}{l}^{-1}} \Delta^l y_j, \quad j = 1, 2, 3, \dots, N-l, \quad i = 1, 2, \dots, m, \quad (3.2.8)$$

where $\binom{2l}{l} = \frac{(2l)!}{(l!)^2}$ with $l!$ be the factorial of l . For the case $\gamma_i = 0$, the estimate for $\sigma_{0,i}$ is then given by

$$\hat{\sigma}_{0,i}^{1\text{st}-l} = \sqrt{\frac{1}{N-l} \sum_{j=1}^{N-l} \left(\hat{\varepsilon}_{ij}^{1\text{st}-l} \right)^2}, \quad i = 1, 2, \dots, m. \quad (3.2.9)$$

It was suggested in [92] that the choice of $l = 3$ works well in practice. This is also the value that we use for l in all the numerical results shown in this paper.

We remark that for the case where one suspects that observation coordinates of \mathbf{Y}_j may have different constant variance (i.e., $\sigma_{0,i}$ may not be equal to $\sigma_{0,k}$), one usually uses an iterative process to carry out parameter estimation for mathematical model parameters and $\sigma_{0,i}$'s (e.g., see [33, Section 3.2.2] for details). However, by using the above methods one is able to obtain the estimates for $\sigma_{0,i}$'s and hence one does not need to use such an iterative inverse problem procedure. This can significantly speed up the desired inverse problem methodology.

3.3 Application on Determining an Appropriate Statistical Model

In this section, we first apply the three methods introduced in Section 3.2 to some simulated data sets to demonstrate the accuracy of these methods as well as the accuracy of the proposed method in using the information provided by pseudo measurement errors to determine an appropriate statistical model. We then apply these methods to some experimental data sets to determine the appropriate statistical models.

3.3.1 Numerical Results for Simulated Data Sets

We first consider applying the three methods introduced in Section 3.2 to two simulated data sets: one is generated using the logistic growth model and the other is generated using a classical SIR model. These examples are used to support the accuracy of the proposed method for using the information provided by pseudo measurement errors to determine appropriate values for the γ_i 's in (3.1.5).

Example 1: Logistic Growth Model

We consider the standard logistic growth model

$$\dot{x} = bx \left(1 - \frac{x}{\kappa}\right), \quad x(t_s) = x_0 \quad (3.3.1)$$

as described in Section 3.1.

We assume that we can observe the number of individuals; that is, $f = x$. To generate the simulated data, we simulate (3.3.1) with parameter values and initial values chosen as $b = 3, \kappa = 100, x_0 = 10$. We then impose a normal distribution on \mathcal{E}_j with zero mean and standard deviation $\sigma_0 = 0.05$, where the measurement time points are $t_j = t_s + (j - 1) \frac{t_f - t_s}{N - 1}$ with $t_s = 0, t_f = 2.5, j = 1, 2, \dots, N$ and $N = 201$. In other words, the simulated data set $\{y_j\}_{j=1}^N$ is generated as follows:

$$y_j = x(t_j) + x^\gamma(t_j)\varepsilon_j, \quad j = 1, 2, \dots, N, \quad (3.3.2)$$

where ε_j is a realization of \mathcal{E}_j . We first will confirm that the pseudo measurement errors provide a reasonable approximation of the true measurement errors ε_j . Then we show that the pseudo measurement errors can be used to determine the unknown value of γ .

Table 3.1 summarizes the estimates for σ_0 found using the three methods introduced in Section 3.2 for the case where $\gamma = 0$ in (3.3.2). From this table, we see that the last two methods give reasonable estimates for σ_0 while the first method considerably overestimates the value of σ_0 . But we do see from other numerical results (see the SIR example discussed in the next section) that this simple method does give a good estimate for some examples. But in summary,

this suggests that this first-order differencing method does not consistently perform well. This is consistent with the observation made in [54], wherein it is suggested that the first-order differencing method should not be used since it does not always behave well. We also observe from Table 3.1 that the estimate obtained by the third-order differencing method is slightly worse than the one obtained by the second-order differencing method. This is somehow contrary to the common finding in numerical analysis that the higher the order the better the result. However, as we mentioned in the beginning of Section 3.2, the variance of the estimator for σ_0 depends on the choice of the weights. This means that if the weights for a given method lead to a larger variance, then the variance estimator obtained by this method has larger uncertainty. This may be the reason why the estimate obtained by the third-order differencing method is slightly worse than that obtained by the second-order method.

Table 3.1: Results for the logistic example in the case where $\gamma = 0$: the true value of σ_0 as well as its estimates obtained using the three mentioned methods ($\hat{\sigma}_0^{1st}$ is obtained using the first-order differencing method, $\hat{\sigma}_0^{2nd}$ is obtained using the second-order differencing method, and $\hat{\sigma}_0^{1st-3}$ is obtained by the third-order differencing method).

σ_0	$\hat{\sigma}_0^{1st}$	$\hat{\sigma}_0^{2nd}$	$\hat{\sigma}_0^{1st-3}$
5.000e-02	3.930e-01	5.210e-02	5.216e-02

Figure 3.1 presents the plot of pseudo measurement errors $\hat{\varepsilon}_j^{1st}$ (obtained using the first-order differencing method and denoted as “estimates” in the legend of this figure) versus t_j and the plot of ε_j (simulated measurement errors and denoted as “true values” in the legend) versus t_j for the cases where $\gamma = 0$ (left column) and $\gamma = 1$ (right column) in (3.3.2). From this figure, we see that for the case where $\gamma = 0$ the plot of $\hat{\varepsilon}_j^{1st}$ versus t_j diverges from the plot of ε_j versus t_j except at the very end. This is consistent with considerable difference of the estimate $\hat{\sigma}_0^{1st}$ from its true value. However, for the case where $\gamma = 1$ the time plot for the pseudo measurement errors exhibits a pattern similar to that for the true values. This suggests that for this case this method works well. Figure 3.2 illustrates the results for the pseudo measurement errors $\hat{\varepsilon}_j^{2nd}$ obtained using second-order differencing method while Figure 3.3 depicts the results for the pseudo measurement errors $\hat{\varepsilon}_j^{1st-3}$ obtained by applying the first-order differencing operator 3 times. From these two figures, we see that the time plot for the pseudo measurement errors exhibits the same pattern as that for the true ones. This suggests that these two methods work well at approximating the true measurement errors for both the constant variance error case and the relative error case.

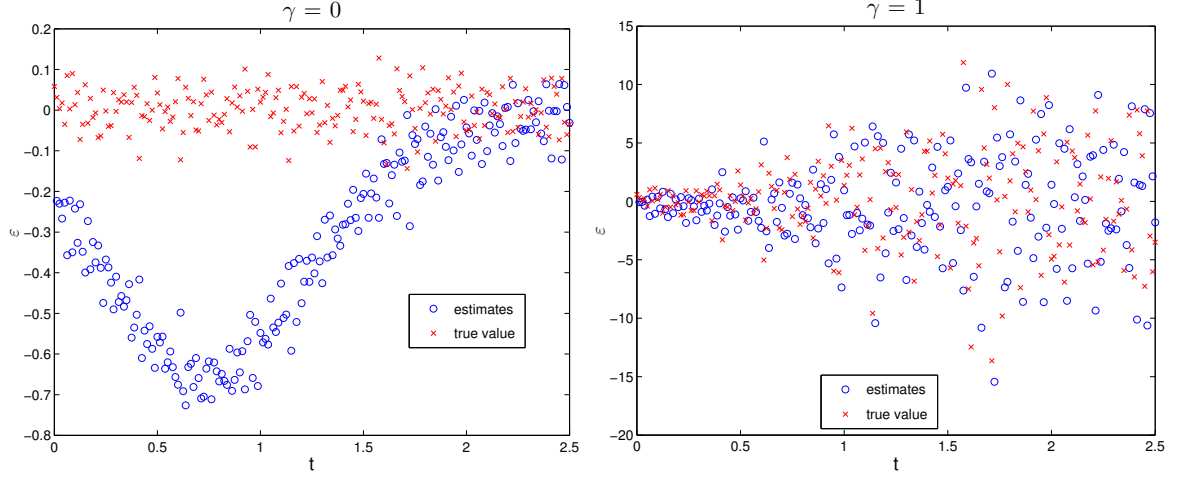


Figure 3.1: Comparison of the plot of $\hat{\varepsilon}_j^{1st}$ (denoted as “estimates” in the legend) versus t_j and the plot of ε_j (denoted as “true value”) versus t_j : (left panel) results obtained for $\gamma = 0$; (right panel) results obtained for $\gamma = 1$, where $\hat{\varepsilon}_j^{1st}$'s are obtained by the first-order differencing method.

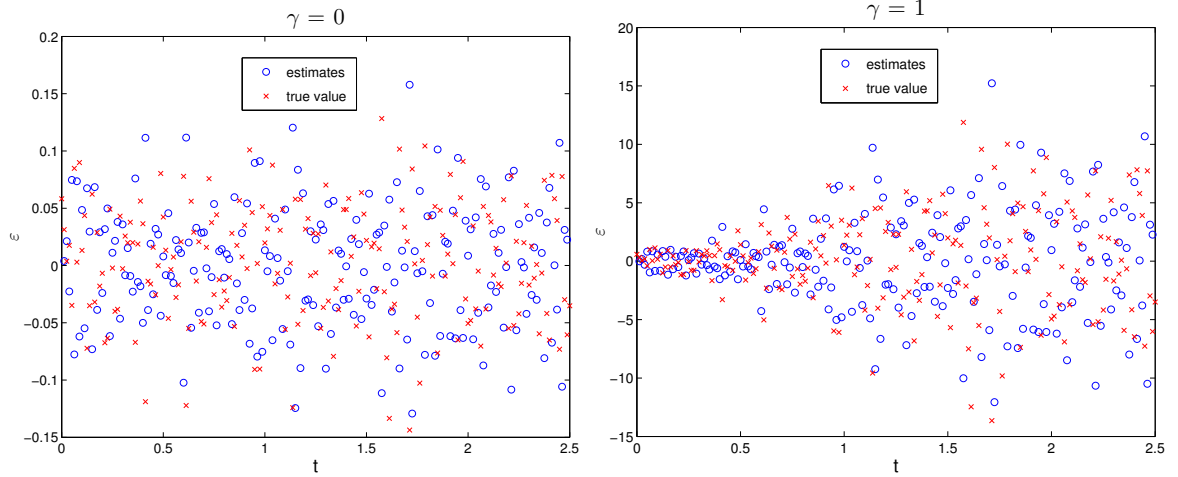


Figure 3.2: Comparison of the plot of the $\hat{\varepsilon}_j^{2nd}$ (denoted as “estimates” in the legend) versus t_j and the plot of ε_j (denoted as “true value”) versus t_j for the case $\gamma = 0$ (left panel) and the case $\gamma = 1$ (right panel), where the $\hat{\varepsilon}_j^{2nd}$ are obtained using the second-order differencing method.

Of course, in practice one does not have a value of the measurement errors themselves, rather only the data measurement $\{y_j\}_{j=1}^N$ is known. We claim that if the pseudo measurement errors provide a reasonable approximation of the true (but unknown) measurement errors, then we can use the pseudo measurement errors to determine an appropriate value for γ . For example, if the plot of pseudo measurement errors $\hat{\varepsilon}_j$ versus t_j seems to form a horizontal band around the

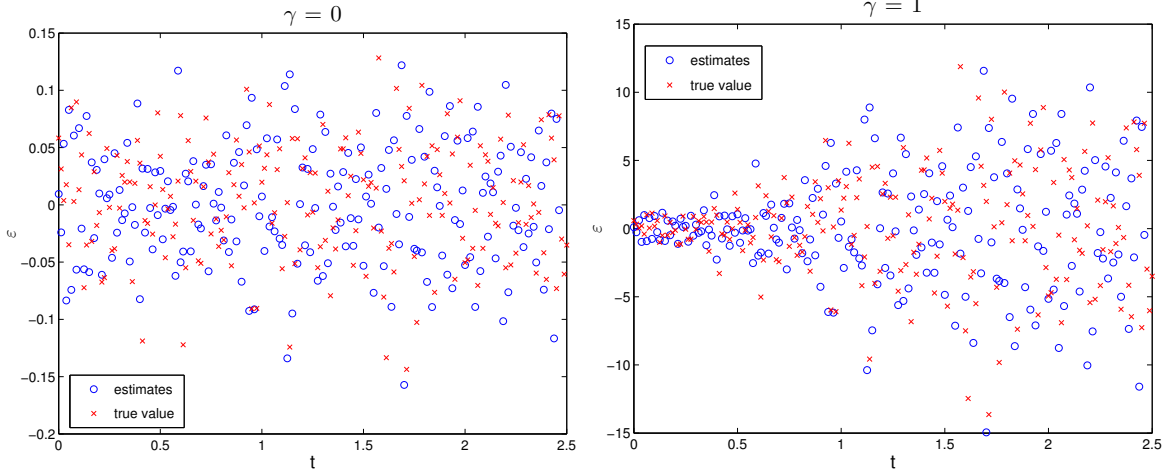


Figure 3.3: Comparison of the plot of the $\hat{\varepsilon}_j^{1st-3}$ (denoted as “estimates” in the legend) versus t_j and the plot of ε_j (denoted as “true value”) versus t_j for the case $\gamma = 0$ (left panel) and the case $\gamma = 1$ (right panel), where the $\hat{\varepsilon}_j^{1st-3}$ are obtained by applying the first-order differencing operator for 3 times.

horizontal axis, then $\gamma = 0$ may be appropriate. However, if one finds that the plot of $\hat{\varepsilon}_j$ versus t_j does not appear to be identically distributed, then $\gamma \neq 0$ and one needs to find a proper nonzero value for γ . To do this, we try different values for γ until one finds a value $\hat{\gamma}$ such that the plot of $\hat{\varepsilon}_j/|y_j - \hat{\varepsilon}_j|^{\hat{\gamma}}$ versus t_j forms a horizontal band around the horizontal axis. To verify whether or not this works, we take this logistic model with simulated data generated using $\gamma = 1$ as an example. We note that for this data set the plot of $\hat{\varepsilon}_j$ versus t_j (e.g., see the right panel of Figure 3.3) exhibits a fan shaped pattern. To begin with, we choose $\tilde{\gamma} = 2$. The resulting plot for $\eta_j^{\tilde{\gamma}} = \hat{\varepsilon}_j^{1st-3}/|y_j - \hat{\varepsilon}_j^{1st-3}|^{\tilde{\gamma}}$ versus t_j with $\tilde{\gamma} = 2$ is shown in the left panel of Figure 3.4, where the $\hat{\varepsilon}_j^{1st-3}$ are obtained by applying the first-order differencing operator three times. We observe from this plot that it has an inverted fan shaped pattern. This indicates that a proper value for γ is between 0 and 2. We then plotted $\eta_j^{\tilde{\gamma}}$ versus t_j with $\tilde{\gamma} = 1$ (shown in the right panel of Figure 3.4) and found that they appear to be identically distributed. Figure 3.5 depicts the results obtained using the second-order differencing method. We observe similar patterns. These results demonstrate that our proposed method works well. One may argue that this proposed method is somewhat subjective and that one can use difference-based methods to obtain directly the estimate for the variance of measurement errors using the kernel function approach mentioned in the Introduction. One could then use this estimate to obtain the estimate for γ . However, as we remarked in the introduction of this chapter, such an estimate for the variance highly depends on the value of the bandwidth and that a proper choice of bandwidth is still a subject of research. Hence, our proposed method provides an alternative and practical way to determine

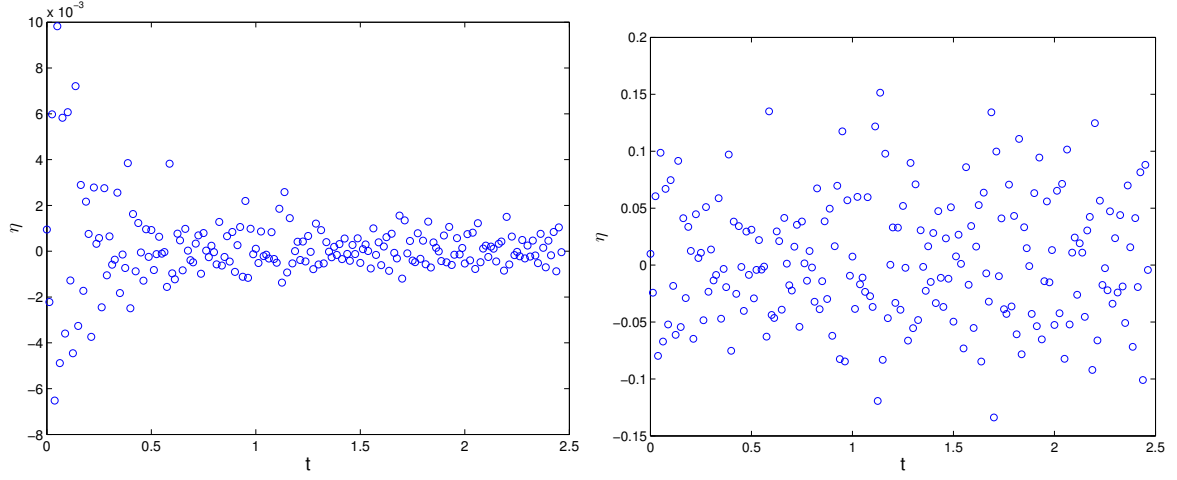


Figure 3.4: Plot of $\eta_j^{\tilde{\gamma}} = \hat{\varepsilon}_j^{1st-3} / |y_j - \hat{\varepsilon}_j^{1st-3}|^{\tilde{\gamma}}$ versus t_j for the case where the simulated data were generated with $\gamma = 1$: (left panel) $\tilde{\gamma} = 2$; (right panel) $\tilde{\gamma} = 1$.

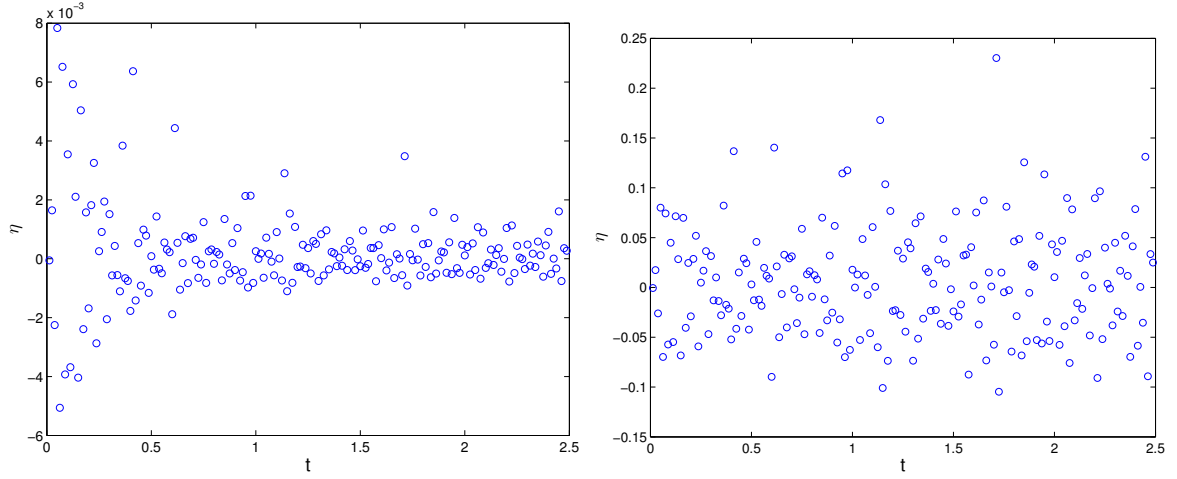


Figure 3.5: Plot of $\eta_j^{\tilde{\gamma}} = \hat{\varepsilon}_j^{2nd} / |y_j - \hat{\varepsilon}_j^{2nd}|^{\tilde{\gamma}}$ versus t_j for the case where the simulated data were generated with $\gamma = 1$: (left panel) $\tilde{\gamma} = 2$; (right panel) $\tilde{\gamma} = 1$.

a reasonable value for γ .

Example 2: SIR Model

We next consider a simple SIR model described by the following system of ordinary differential equations

$$\begin{aligned}\dot{S} &= -\beta SI, \\ \dot{I} &= \beta SI - \delta I, \\ \dot{R} &= \delta I, \\ (S(t_s), I(t_s), R(t_s)) &= (S_0, I_0, R_0).\end{aligned}\tag{3.3.3}$$

Here S , I and R respectively denote the ratios of the numbers of susceptible, infected, and recovered individuals to the total number of individuals (so they are dimensionless), β denotes the infection rate, and δ is the recover rate.

For demonstration purpose, we assume that we can observe all these three states; that is, $\mathbf{f} = (S, I, R)^T$. For all the results shown below, the parameter values and initial values are chosen as $\beta = 6, \delta = 3, S_0 = 0.7, I_0 = 0.2, R_0 = 0.1$. To generate the simulated data, we impose a normal distribution on \mathcal{E}_{1j} with zero mean and standard deviation $\sigma_{0,1} = 0.01$, a normal distribution on \mathcal{E}_{2j} with zero mean and $\sigma_{0,2} = 0.005$ and a normal distribution on \mathcal{E}_{3j} with zero mean and $\sigma_{0,3} = 0.02$, where the measurement time points are $t_j = t_s + (j-1)\frac{t_f-t_s}{N-1}$ with $t_s = 0$, $t_f = 2$ and $N = 201$, $j = 1, 2, \dots, N$.

Table 3.2 summarizes the estimates for $\sigma_{0,i}$ by using the three methods introduced in Section 3.2 for the case where $\gamma_i = 0$, $i = 1, 2, 3$. From this table, we see that all three methods give reasonable estimates for $\sigma_{0,i}$.

Table 3.2: Results for the SIR example in the case where $\gamma_i = 0$, $i = 1, 2, 3$: the value of $\sigma_{0,i}$ as well as its estimates obtained using the three methods introduced in Section 3.2.

$\sigma_{0,i}$	1.000e-02	5.000e-03	2.000e-02
$\hat{\sigma}_{0,i}^{1st}$	1.074e-02	5.295e-03	2.049e-02
$\hat{\sigma}_{0,i}^{2nd}$	1.039e-02	5.297e-03	2.009e-02
$\hat{\sigma}_{0,i}^{1st-3}$	1.043e-02	5.368e-03	1.996e-02

Figure 3.6 presents the plots of pseudo measurement errors $\hat{\varepsilon}_{ij}^{1st}$ (obtained using first-order differencing method and denoted as “estimates” in the legend of this figure) versus t_j and the plot of ε_{ij} (simulated measurement errors and denoted as “true value” in the legend of this figure) versus t_j for the cases where $\gamma_1 = \gamma_2 = \gamma_3 = 0$ (left column) and $\gamma_1 = \gamma_2 = \gamma_3 = 1$

(right column). From this figure, we see that for the case $\gamma_1 = \gamma_2 = \gamma_3 = 0$ the time plot for $\hat{\varepsilon}_i^{1st}$ exhibits exactly the same pattern as that for ε_i . However, for the case $\gamma_1 = \gamma_2 = \gamma_3 = 1$, there is a discernible divergence between the plot of $\hat{\varepsilon}_{2j}^{1st}$ versus t_j and the plot of ε_{2j} versus t_j . This again demonstrates that the first-order differencing method does not consistently perform well. Figure

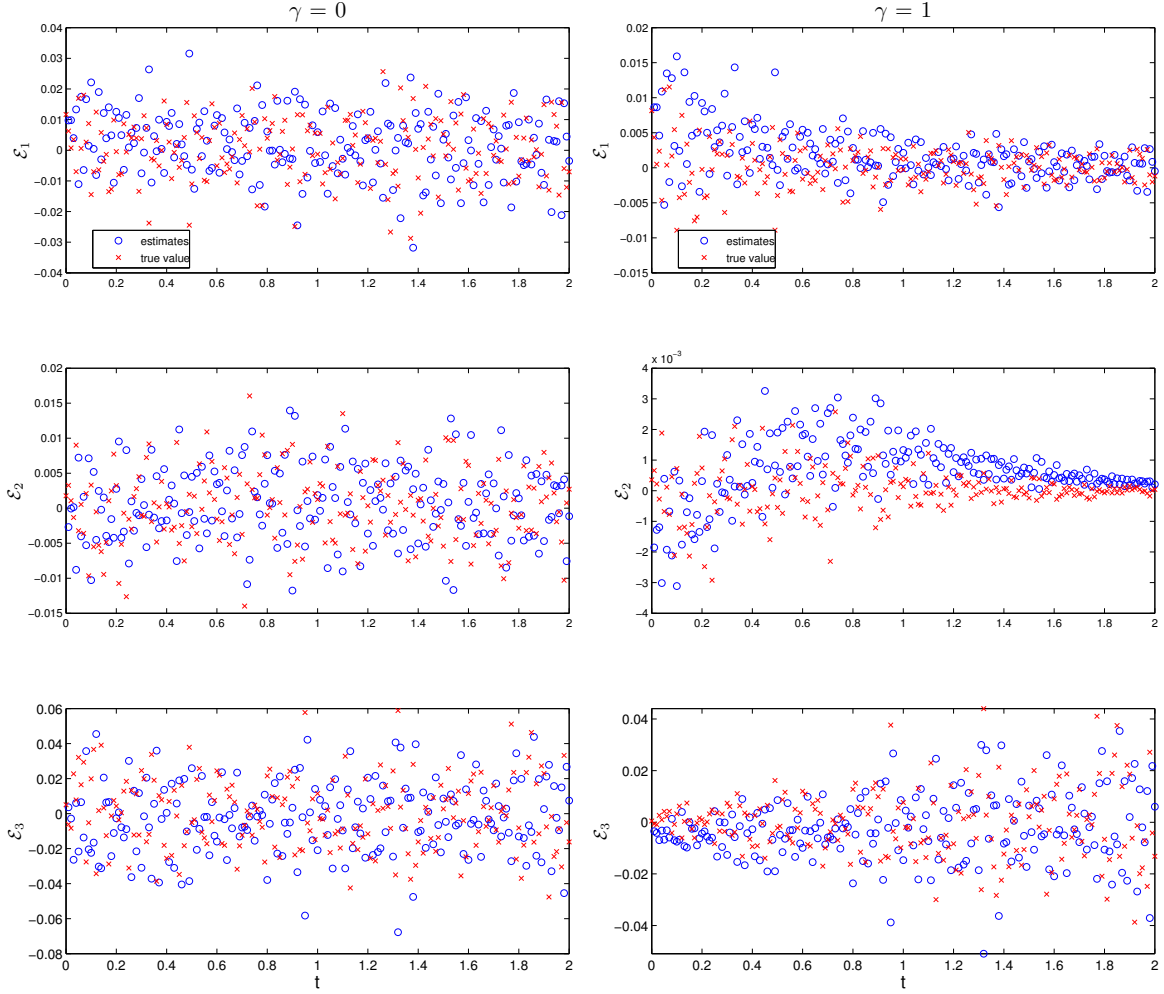


Figure 3.6: Comparison of the plot of $\hat{\varepsilon}_{ij}^{1st}$ (denoted as “estimates” in the legend) versus t_j and the plot of ε_{ij} (denoted as “true value”) versus t_j for the case $\gamma_1 = \gamma_2 = \gamma_3 = 0$ (left column) and the case $\gamma_1 = \gamma_2 = \gamma_3 = 1$ (right column).

3.7 illustrates the results for the pseudo measurement errors $\hat{\varepsilon}_{ij}^{2nd}$ obtained using the second-order differencing method while Figure 3.8 depicts the results for the pseudo measurement errors $\hat{\varepsilon}_{ij}^{1st-3}$ obtained by applying the first-order differencing operator 3 times. From these two figures, we

see that the time plots for the pseudo measurement errors exhibit the same pattern as that for the true ones. Hence, these two methods work well for both the constant variance error case and the relative error case.

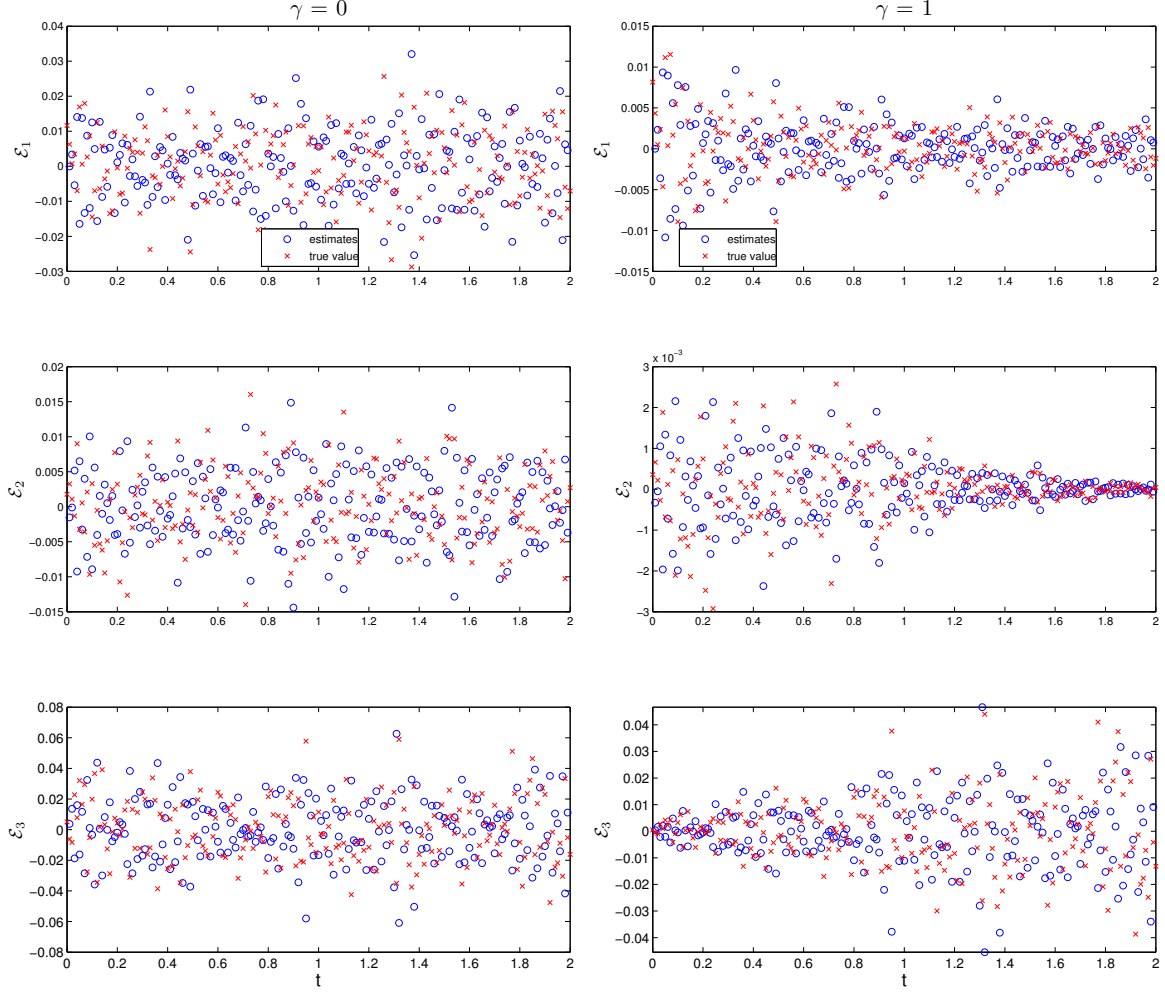


Figure 3.7: Comparison of the plot of $\hat{\varepsilon}_{ij}^{2\text{nd}}$ (denoted as “estimates” in the legend) versus t_j and the plot of ε_{ij} (denoted as “true value”) versus t_j for the case $\gamma_1 = \gamma_2 = \gamma_3 = 0$ (left column) and the case $\gamma_1 = \gamma_2 = \gamma_3 = 1$ (right column).

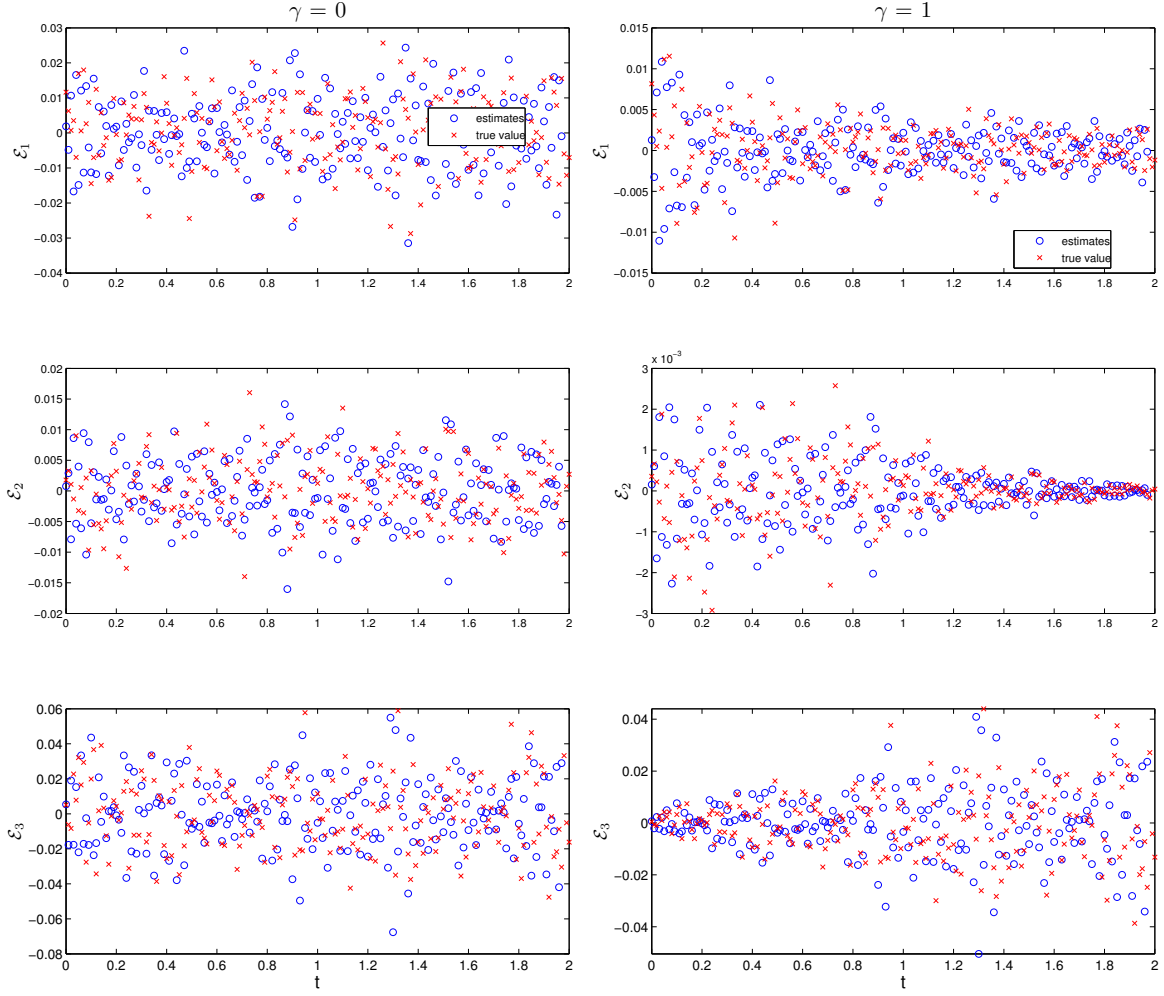


Figure 3.8: Comparison of the plot of $\hat{\varepsilon}_{ij}^{1st-3}$ (denoted as “estimates” in the legend) versus t_j and the plot of ε_{ij} (denoted as “true value”) versus t_j for the case $\gamma_1 = \gamma_2 = \gamma_3 = 0$ (left column) and the case $\gamma_1 = \gamma_2 = \gamma_3 = 1$ (right column).

The above numerical results again reveal that if difference-based methods work, then the obtained pseudo measurement errors can be used to play the role as measurement errors and hence can be used to determine appropriate values for γ_i 's. Here we take this SIR model with simulated data generated using $\gamma_1 = \gamma_2 = \gamma_3 = 1$ as another example to further verify the method used in Section 3.3.1 for determining appropriate values for γ_i 's in the case where the pseudo measurement errors do not appear to be identically distributed. Specifically, we try different values for γ_i until one finds a value $\hat{\gamma}_i$ such that the plot of $\hat{\varepsilon}_{ij}/|y_{ij} - \hat{\varepsilon}_{ij}|^{\hat{\gamma}_i}$ versus t_j forms a horizontal band around the horizontal axis. We note that for this data set both the plot of $\hat{\varepsilon}_{1j}$ versus t_j and the plot of $\hat{\varepsilon}_{2j}$ versus t_j (e.g., see the right column of Figure 3.8) exhibit a fan shaped pattern while the plot of $\hat{\varepsilon}_{3j}$ versus t_j exhibits an inverted fan shaped pattern. For a start, we choose $\tilde{\gamma}_i = 2$, $i = 1, 2, 3$. The resulting plots for $\eta_{ij}^{\tilde{\gamma}_i} = \hat{\varepsilon}_{ij}^{1st-3}/|y_{ij} - \hat{\varepsilon}_{ij}^{1st-3}|^{\tilde{\gamma}_i}$ versus t_j with $\tilde{\gamma}_i = 2$ and $i = 1, 2, 3$, are shown in the left column of Figure 3.9, where the $\hat{\varepsilon}_{ij}^{1st-3}$ are obtained by applying the first-order differencing operator for three times. We observe from these plots that the patterns for all these three plots are inverted (i.e., the plot previously having a fan shaped pattern now has an inverted fan shaped pattern, and the plot previously having an inverted fan shaped pattern now have a fan shaped pattern). This indicates that a proper value for γ_i is between 0 and 2, $i = 1, 2, 3$. We then plotted $\eta_{ij}^{\tilde{\gamma}_i}$ versus t_j with $\tilde{\gamma}_1 = \tilde{\gamma}_2 = \tilde{\gamma}_3 = 1$ (shown in the right column of Figure 3.9) and found that they all appear to be identically distributed. Figure 3.10 depicts the results using the second-order differencing method. We observe similar patterns. These results again demonstrate that our proposed method of using pseudo measurement errors to determine an appropriate value for γ works well.

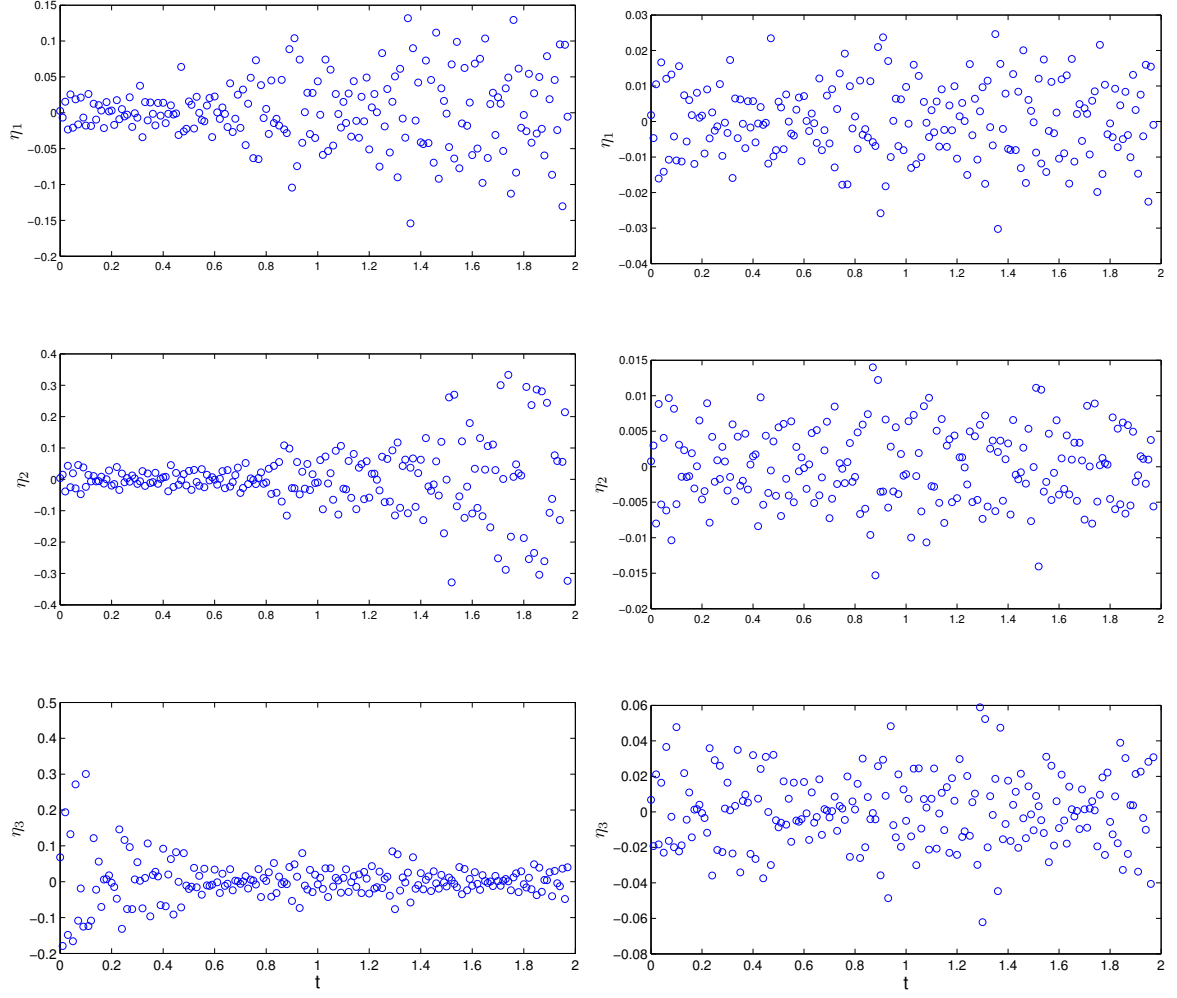


Figure 3.9: Plot of $\eta_{ij}^{\tilde{\gamma}_i} = \hat{\varepsilon}_{ij}^{1st-3} / |y_{ij} - \hat{\varepsilon}_{ij}^{1st-3}|^{\tilde{\gamma}_i}$ versus t_j for the case where the simulated data were generated with $\gamma_1 = \gamma_2 = \gamma_3 = 1$: (left panel) $\tilde{\gamma}_1 = \tilde{\gamma}_2 = \tilde{\gamma}_3 = 2$; (right panel) $\tilde{\gamma}_1 = \tilde{\gamma}_2 = \tilde{\gamma}_3 = 1$.

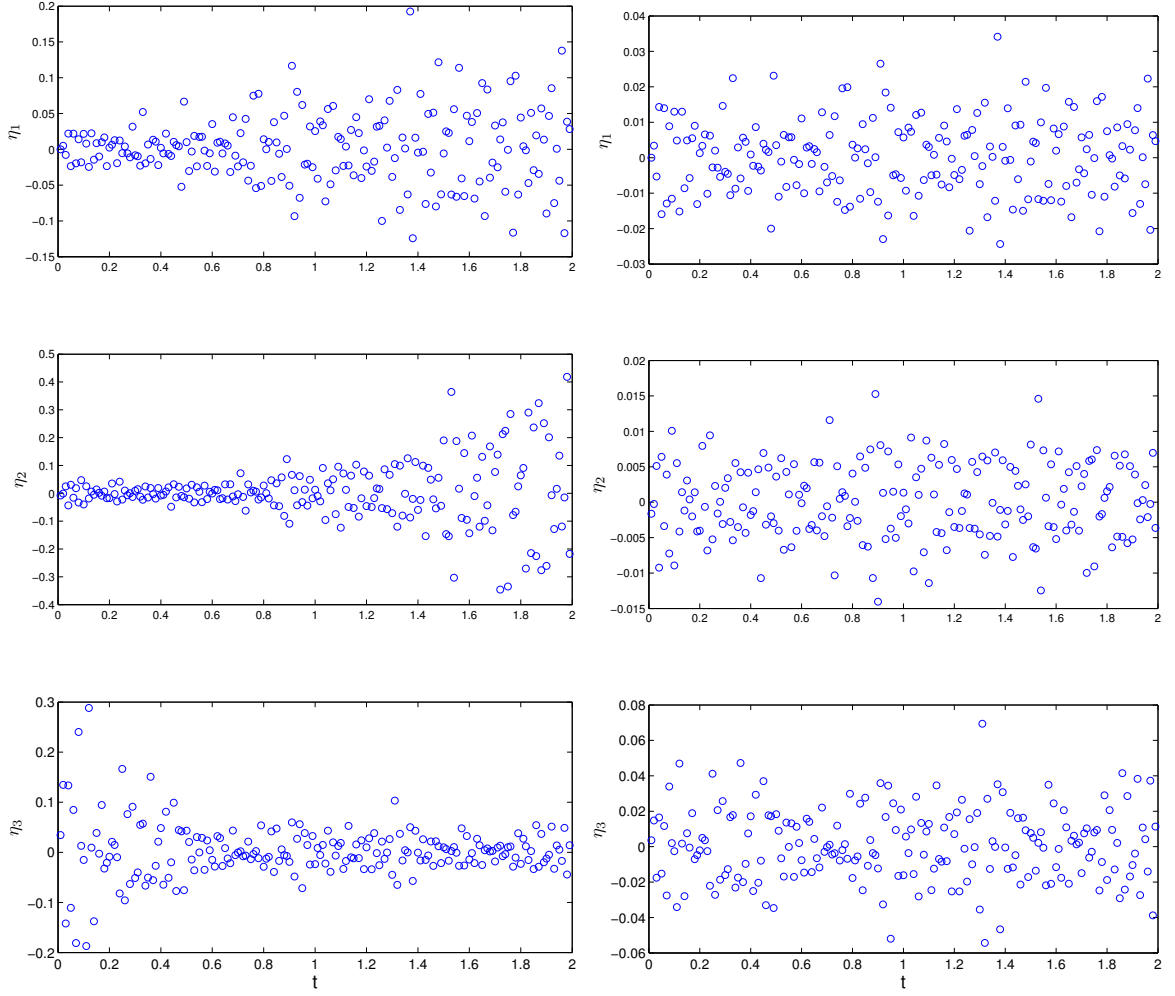


Figure 3.10: Plot of $\eta_{ij}^{\tilde{\gamma}_i} = \hat{\varepsilon}_{ij}^{2\text{nd}} / |y_{ij} - \hat{\varepsilon}_{ij}^{2\text{nd}}| \tilde{\gamma}_i$ versus t_j for the case where the simulated data were generated with $\gamma_1 = \gamma_2 = \gamma_3 = 1$: (left panel) $\tilde{\gamma}_1 = \tilde{\gamma}_2 = \tilde{\gamma}_3 = 2$; (right panel) $\tilde{\gamma}_1 = \tilde{\gamma}_2 = \tilde{\gamma}_3 = 1$.

3.3.2 Numerical Results for Experimental Data Sets

In this section, we apply the difference-based methods to some experimental data sets to determine an appropriate value for γ . Since the first-order differencing method does not consistently perform well, we only use the second-order differencing method and the method for applying the first-order differencing operator 3 times for these data sets.

Daphnia magna Data Set

Here we consider the survival data collected for *Daphnia magna* that were presented in [1]. Specifically, ninety daphnids (neonates) were longitudinally observed and survival was recorded daily, and an ordinary least squares method was used in this paper to estimate the mortality rate.

Figure 3.11 presents the time plot results for the pseudo measurement errors obtained using the second-order differencing method (left) and the method for applying the first-order differencing operator three times (right). We observe from the right plot of this figure that pseudo measurement errors form a horizontal band around the line $\varepsilon = 0$. The similar pattern can be observed from the left plot of Figure 3.11 except several outliers. This indicates that the absolute error model (i.e., $\gamma = 0$) may be correct for this case. This provides support for using ordinary least squares method for parameter estimation in [1].

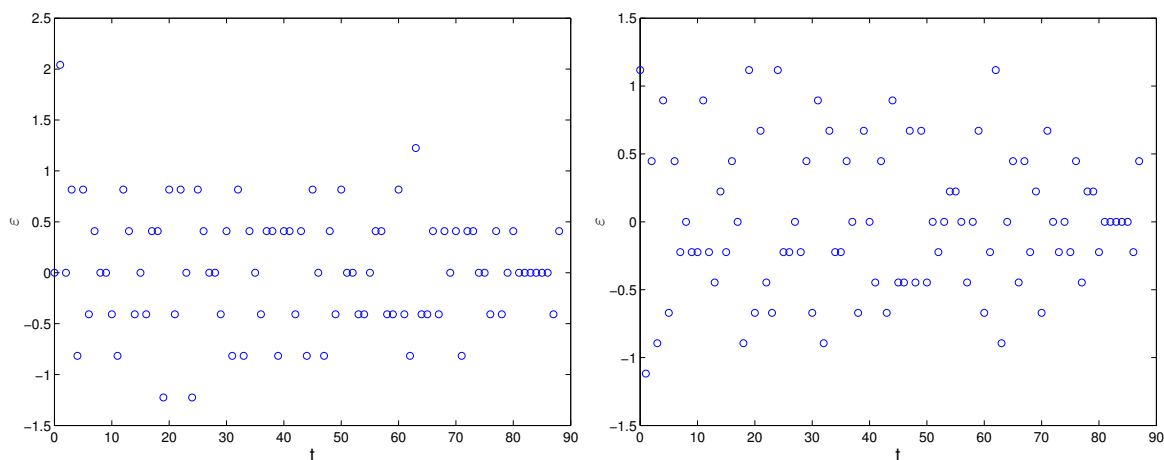


Figure 3.11: Time plots for pseudo measurement errors obtained for the *Daphnia* data set presented in [1]: (left panel) using the second-order differencing method; (right panel) using the method for applying the first-order differencing operator for three times (right).

CFSE Data Set

Here we consider the flow cytometry data presented in [33, Section 3.5.3] for a dividing population of lymphocytes labeled with the intracellular dye CFSE. The observable is the number of cells measured at time s_k with log-fluorescence intensity in the region $[z_i, z_{i+1})$, $k = 1, 2, \dots, 7$, $i = 1, 2, \dots, 513$. To be consistent with the notation introduced earlier, we re-index the data collection points $\{(s_k, z_i)\}$ by $\{t_j\}$; that is, the elements in the set $\{t_j\}_{j=513(k-1)+1}^{513k}$ correspond to the elements in the set $\{(s_k, z_i)\}_{i=1}^{513}$, $k = 1, 2, \dots, 7$.

Figure 3.12 depicts results obtained using the second-order differencing method. Specifically, the left panel shows the plot of pseudo measurement errors $\hat{\varepsilon}_j^{2\text{nd}}$ versus j , and the right panel illustrates the plot of $\eta_j^{\tilde{\gamma}} = \hat{\varepsilon}_j^{2\text{nd}}/|y_j - \hat{\varepsilon}_j^{2\text{nd}}|^{\tilde{\gamma}}$ versus j with $\tilde{\gamma} = 0.5$, where the vertical lines delineate the pseudo measurement errors obtained in time intervals $[s_k, s_{k+1})$, $k = 1, 2, \dots, 7$. We observe from the left panel of Figure 3.12 that pseudo measurement errors are far from

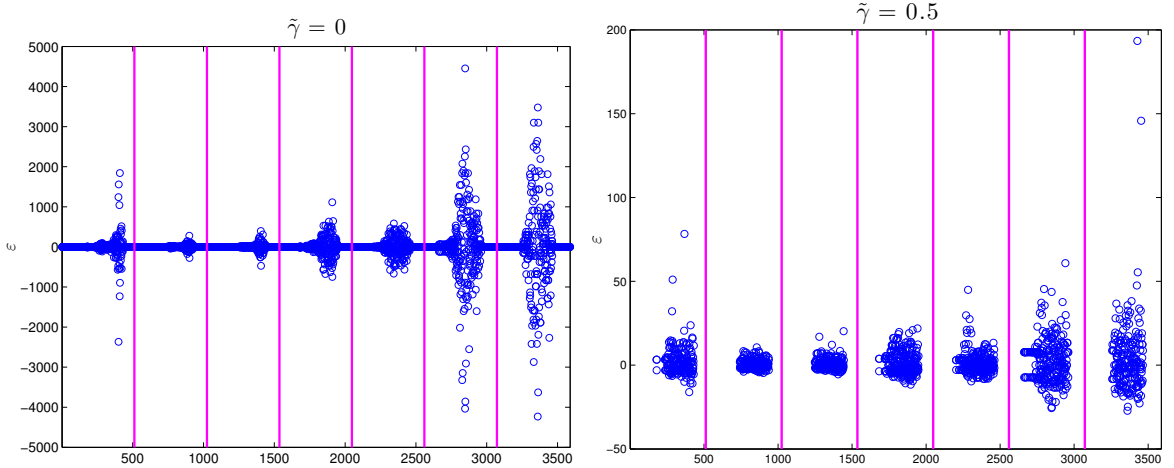


Figure 3.12: Plots for pseudo measurement errors obtained for the CFSE data set presented in [33, Section 3.5.3] by using the second-order differencing method: (left panel) plot of $\hat{\varepsilon}_j^{2\text{nd}}$ versus j ; (right panel) plot of $\eta_j^{\tilde{\gamma}} = \hat{\varepsilon}_j^{2\text{nd}}/|y_j - \hat{\varepsilon}_j^{2\text{nd}}|^{\tilde{\gamma}}$ versus j with $\tilde{\gamma} = 0.5$. The vertical lines delineate the pseudo measurement errors obtained in time intervals $[s_k, s_{k+1})$, $k = 1, 2, \dots, 7$.

identically distributed. This is also true even in each subinterval $[s_k, s_{k+1})$. Hence, $\gamma = 0$ is not a reasonable choice for this data set. This conclusion is consistent with the one made in [33, Section 3.5.3] where residual plots were used to determine an appropriate value for γ . Results in the right panel of Figure 3.12 imply that in each subinterval $[s_k, s_{k+1})$ the $\eta_j^{\tilde{\gamma}}$'s appear to be identically distributed except some outliers. This indicates that $\gamma = 0.5$ may be appropriate in each of these subintervals. We also observe from this plot that the bandwidth formed by the plot of $\eta_j^{\tilde{\gamma}}$'s

in the last two subintervals are larger than the ones for those subintervals located in the middle. This suggests that we may have different constant variance for $\eta_j^{\tilde{\gamma}}$ in these subintervals and the variance of $\eta_j^{\tilde{\gamma}}$ depends on when the measurement was taken. This observation is inconsistent with the conclusion made in [33, Section 3.5.3] where residual plots reveal that the modified residuals $r_j/|y_j - f(t_j; \hat{\theta})|^{\tilde{\gamma}}$ with $\tilde{\gamma} = 0.5$ appear to be identically distributed in the whole interval. Figure 3.13 demonstrates the results obtained by the third-order differencing method. We observe similar patterns as that obtained by the second-order differencing method. As we discussed earlier in the Introduction and also shown in the next section, this inconsistency suggests that there may be a mathematical model misspecification involved.

Motivated by the recent CFSE label division studies of Bocharov, Luzyanina and colleagues [43, 72] on asymmetric label division and time-lags to division in proliferating mouse cell data, we further investigated the data sets presented in [33, 34, 36, 67] and discussed then here. The Bocharov, et al., investigations raised the question of whether cell proliferation models which allowed for asymmetric label division might be better suited to describe our human cell proliferation data. In [35] we revisited these data sets for the possibility of mathematical model misspecification. In these investigations statistically based model comparison tests were employed and seemingly contradictory results were found. In one third of the data sets studied, support was found for the hypothesis that mathematical models permitting asymmetric label division *did not* improve the fits-to-data. However, for two thirds of the data sets, it was found that allowing asymmetric division does appear to lead to statistically significantly better agreement with the data. While there may be other confounding factors, the findings of [35] support the suggestion that there may be mathematical modeling error in the earlier CSFE labeled cell proliferation studies of [33, 34, 36, 67]. Thus, the findings in the present analysis are consistent with notion of a mathematical modeling misspecification in the earlier findings reported in [35].

3.4 Application on Detecting Mathematical Model Misspecification and Bootstrapping

In this section, we use an example to demonstrate that one could use pseudo measurement errors to determine whether there is a possible mathematical model error in the case where the statistical model is known to be correct. In addition, we use this example to demonstrate how to use the information provided by the pseudo measurement errors to carry out bootstrapping to quantify the uncertainty of parameter estimators, and show the robustness of this method in the presence of mathematical model misspecification.

For demonstration purpose, we use the simulated data set that was generated by the logistic growth model (3.3.1) using an absolute error model ($\gamma = 0$). Specifically, the data set $\{y_j\}$ is

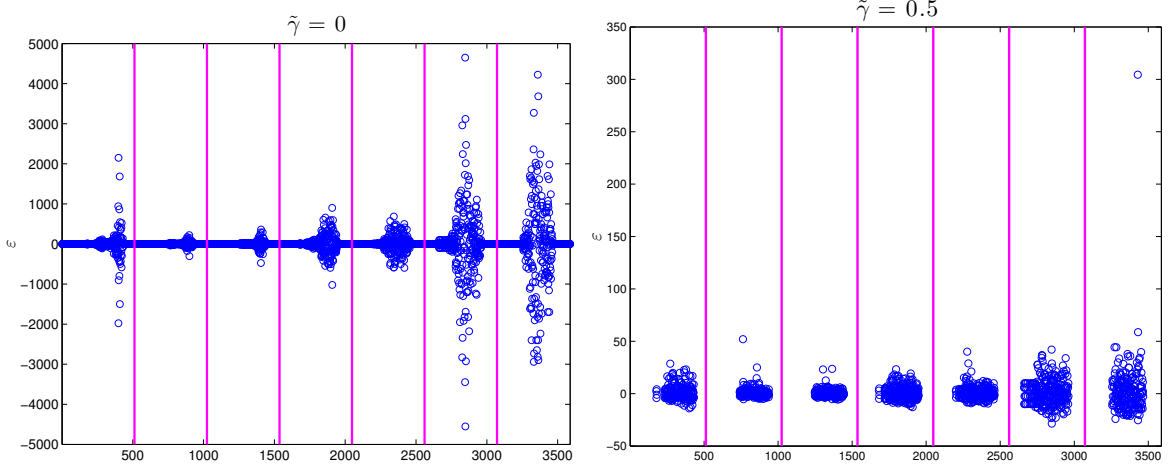


Figure 3.13: Plots for pseudo measurement errors obtained for the CFSE data set presented in [33, Section 3.5.3] by applying the first-order differencing operators for three times: (left panel) plot of $\hat{\varepsilon}_j$ versus j ; (right panel) plot of $\eta_j^{\tilde{\gamma}} = \hat{\varepsilon}_j^{1st-3} / |y_j - \hat{\varepsilon}_j^{1st-3}|^{\tilde{\gamma}}$ versus j with $\tilde{\gamma} = 0.5$. The vertical lines delineate the pseudo measurement errors obtained in time intervals $[s_k, s_{k+1})$, $k = 1, 2, \dots, 7$.

generated as follows: we first simulate (3.3.1) with model parameters and initial values given by $b = 0.8, \kappa = 200, x_0 = 10$; we then impose a normal distribution on \mathcal{E}_j with zero mean and standard deviation $\sigma_0 = 0.2$ to generate a realization ε_j of measure error \mathcal{E}_j (i.e., constant variance error), where again the measurement time points are $t_j = t_s + (j - 1) \frac{t_f - t_s}{N - 1}$ with $t_s = 0$, $t_f = 2$ and $j = 1, 2, \dots, N$, with $N = 201$. We finally add this noise to the simulated model solution (that is, $y_j = x(t_j) + \varepsilon_j$ with $x(t)$ the solution to the logistic model (3.3.1)). The resulting data are illustrated in Figure 3.14.

In practice, one has no idea how $\{y_j\}$ is generated. Based on the information provided by the plot of this data set, one may choose to use an exponential growth model to describe the data, i.e.,

$$\dot{\tilde{x}} = b\tilde{x}, \quad \tilde{x}(t_s) = x_0, \quad (3.4.1)$$

where the parameter b needs to be estimated from the data. Hence, the data is assumed to be generated by

$$Y_j = f(t_j; b_0) + \mathcal{E}_j, \quad j = 1, 2, \dots, N, \quad (3.4.2)$$

where $f(t; b) = \tilde{x}(t; b) = x_0 \exp(bt)$. In practice, one may have no knowledge of the measurement errors either. Since both second-order differencing method and the method for applying the first-order differencing operator 3 times work well, here we just use the second-order differencing method to determine a proper statistical model. The resulting plot for the pseudo measurement errors $\hat{\varepsilon}_j$ versus t_j is illustrated in the left panel of Figure 3.15. From this plot, we observe

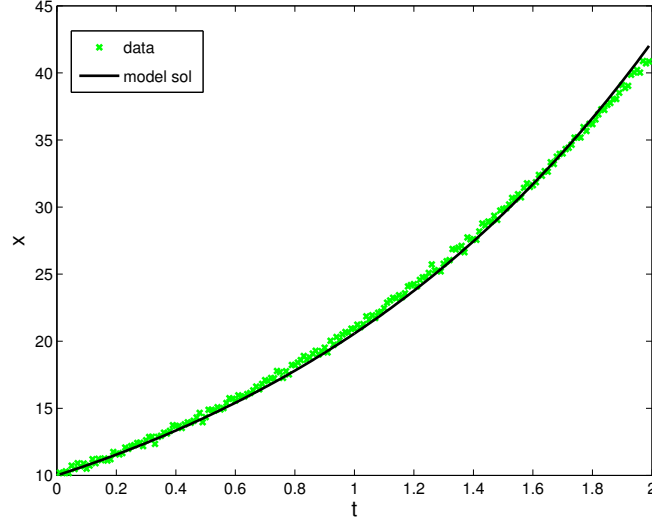


Figure 3.14: Results for fitting exponential growth model (3.4.1) to the simulated data generated by the logistic growth model (3.3.1).

that the obtained pseudo measurement errors form a horizontal band around the horizontal axis. This implies that $\gamma = 0$ is appropriate to use (it conforms with the actual data collection process). Based on this information, we use the following ordinary least squares method to do parameter estimation.

$$\hat{b} = \arg \min_{b \in [\underline{b}, \bar{b}]} \sum_{j=1}^N (y_j - f(t_j; b))^2, \quad (3.4.3)$$

where \underline{b} and \bar{b} are some constants. The resulting model fit is illustrated in Figure 3.14. From this figure, we see that we obtain a very good fit to the data. Hence, one might conclude there is no/negligible mathematical modeling error. However, when one plots the residuals $r_j = y_j - f(t_j; \hat{b})$ versus t_j (shown in the right panel of Figure 3.15), one clearly sees that residuals are far from identically distributed. This divergence between the residual plot and the plot of $\hat{\varepsilon}_j^{2\text{nd}}$ versus t_j implies that there is a mathematical model error. In addition, this example clearly demonstrates that residual plots may give incorrect information for the variance of measurement errors in the case where there is a mathematical model error. That is, if one looked solely at the residual plots, the conclusion might be drawn that the statistical model has been incorrectly specified. Hence, one needs to be cautious when one attempts to use only residual plots to determine whether or not the assumed statistical model is appropriate.

Here we consider how to use the information provided by the pseudo measurement errors to quantify uncertainty through bootstrapping, and demonstrate the robustness of this method in the presence of model misspecification. For simplicity, we take the scalar observation case (i.e.,

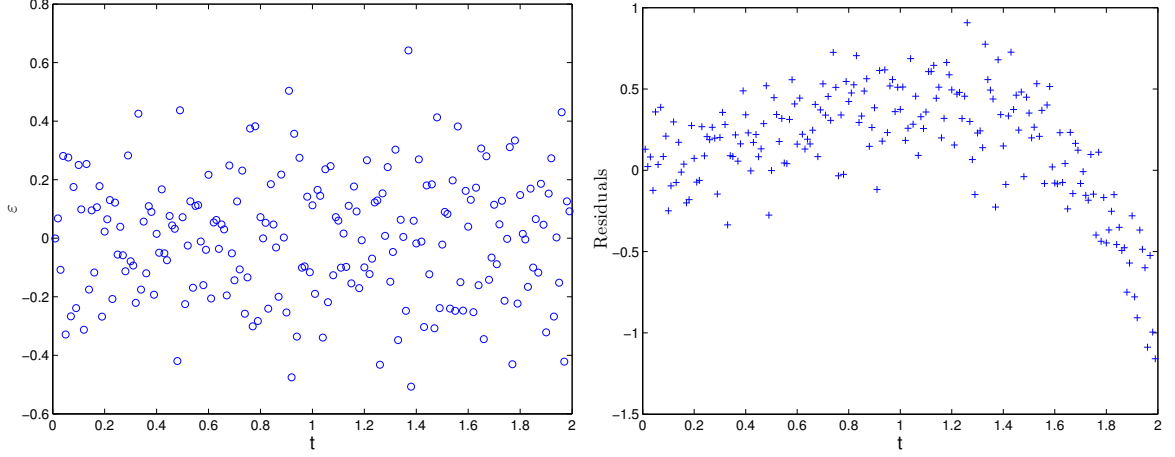


Figure 3.15: (left panel): plot of pseudo measurement errors $\hat{\varepsilon}_j^{2\text{nd}}$ versus t_j , where $\varepsilon_j^{2\text{nd}}$'s are obtained by applying the second-order differencing method to the simulated data generated by the logistic growth model (3.3.1); (right panel): residual plot (i.e., a plot of r_j versus t_j) obtained by fitting exponential growth model (3.4.1) to the simulated data generated by logistic growth model (3.3.1).

$m = 1$) as an example and assume an absolute error model. We use the second-order differencing method to obtain pseudo measurement errors. For a given data set $\{y_j\}_{j=1}^N$ that was generated by some unknown function $\psi(t; \boldsymbol{\vartheta}_0)$, we assume that we have a mathematical model $f(t; \boldsymbol{\theta}_0)$ which approximates $\psi(t; \boldsymbol{\vartheta}_0)$. That is, the data is generated by

$$y_j = \psi(t_j; \boldsymbol{\vartheta}_0) + \varepsilon_j, \quad j = 1, 2, \dots, N,$$

but since ψ is unknown, we assume the data was generated by

$$y_j = f(t_j; \boldsymbol{\theta}_0) + \varepsilon_j, \quad j = 1, 2, \dots, N, \quad (3.4.4)$$

where $f(t_j; \boldsymbol{\theta}_0)$ denotes the observed part of the solution of the chosen mathematical model with $\boldsymbol{\theta}_0 \in \mathbb{R}^{\kappa_\theta}$ (κ_θ is an integer) at the measurement point t_j . Algorithm 3.4.1 illustrates how to use the bootstrapping method to quantify uncertainty for parameter estimator in the presence of model misspecification when the pseudo measurement errors appear to be independent and identically distributed.

We then calculate the mean and covariance matrix for the bootstrapping estimator using the formulae

$$\begin{aligned} \hat{\boldsymbol{\theta}} &= \frac{1}{K} \sum_{k=1}^K \hat{\boldsymbol{\theta}}^{(k)}, \\ \hat{\Sigma} &= \frac{1}{K-1} \sum_{k=1}^K (\hat{\boldsymbol{\theta}}^{(k)} - \hat{\boldsymbol{\theta}})(\hat{\boldsymbol{\theta}}^{(k)} - \hat{\boldsymbol{\theta}})^T. \end{aligned} \quad (3.4.5)$$

Algorithm 3.4.1 Bootstrapping.

1. Apply the second-order differencing method to data set $\{y_j\}_{j=1}^N$ to obtain pseudo measurement errors $\hat{\varepsilon}_j^{2\text{nd}}$, $j = 2, 3, \dots, N-1$, and then use these pseudo measurement errors to obtain estimates for the true regression function at t_j 's by

$$\hat{\psi}_j = y_j - \hat{\varepsilon}_j^{2\text{nd}}, \quad j = 2, 3, \dots, N-1.$$

Set $k = 1$.

2. Create a bootstrapping sample using random sampling with replacement from $\{\hat{\varepsilon}_j^{2\text{nd}}\}_{j=2}^{N-1}$ to form a bootstrapping sample $\{\hat{\varepsilon}_2^{(k)}, \dots, \hat{\varepsilon}_{N-1}^{(k)}\}$.
3. Create bootstrapping sample points

$$y_j^{(k)} = \hat{\psi}_j + \hat{\varepsilon}_j^{(k)}, \quad j = 2, \dots, N-1.$$

4. Obtain an estimate $\hat{\boldsymbol{\theta}}^{(k)}$ from the bootstrapping sample $\{y_j^{(k)}\}$ using the ordinary least squares method given by

$$\hat{\boldsymbol{\theta}}^{(k)} = \underset{\boldsymbol{\theta} \in \Omega}{\operatorname{argmin}} \sum_{j=2}^{N-1} (y_j^{(k)} - f(t_j; \boldsymbol{\theta}))^2,$$

where Ω is some compact set in $\mathbb{R}^{\kappa_\vartheta}$.

5. Set $k = k + 1$ and repeat steps 2–5 until $k > K$ (e.g., typically $K = 1000$ as in our calculations below).
-

The standard error for the i th component of the bootstrapping estimator is then given by $\sqrt{\hat{\Sigma}_{ii}}$, where $\hat{\Sigma}_{ii}$ is the (i, i) th component of $\hat{\Sigma}$, $i = 1, 2, \dots, \kappa_\theta$. It is worth emphasizing that Algorithm 3.4.1 can be used not only for the case where model misspecification is due to modeling error but also for the case where model misspecification is due to some approximations such as approximating infinite-dimensional parameters by finite-dimensional parameters as was considered in [19].

To illustrate the robustness of this algorithm in the presence of model misspecification, we take the logistic example of this section, that is, ψ is the solution of the logistic model used to generate the data, and f is the solution to the exponential model which is used as the mathematical model. We compare the results obtained by Algorithm 3.4.1 and the results obtained by an algorithm similar to Algorithm 3.4.1 (referred to as Modified Algorithm 3.4.2) except that bootstrapping sample points are created by random sampling with replacement from

the simulated/true measurement errors $\{\varepsilon_j\}_{j=2}^{N-1}$ and then adding them to the true regression function. For the sake of clarity, we present the Modified Algorithm 3.4.2 below.

Algorithm 3.4.2 Bootstrapping: Modified.

1. Set $k = 1$, and create a bootstrapping sample using random sampling with replacement from the simulated/true measurement errors $\{\varepsilon_j\}_{j=2}^{N-1}$ to form a bootstrapping sample $\{\varepsilon_j^{(k)}\}_{j=2}^{N-1}$.
2. Create bootstrapping sample points

$$y_j^{(k)} = \psi(t_j; \boldsymbol{\vartheta}_0) + \hat{\varepsilon}_j^{(k)}, \quad j = 2, \dots, N-1.$$

3. Obtain an estimate $\hat{\boldsymbol{\theta}}^{(k)}$ from the bootstrapping sample $\{y_j^{(k)}\}$ using the ordinary least squares method given by

$$\hat{\boldsymbol{\theta}}^{(k)} = \underset{\boldsymbol{\theta} \in \Omega}{\operatorname{argmin}} \sum_{j=2}^{N-1} (y_j^{(k)} - f(t_j; \boldsymbol{\theta}))^2,$$

where Ω is some compact set in $\mathbb{R}^{\kappa_{\boldsymbol{\vartheta}}}$.

4. Set $k = k + 1$ and repeat steps 2–5 until $k > K$ (e.g., typically $K = 1000$ as in our calculations below).
-

Table 3.3 illustrates the mean and standard error of the bootstrapping estimator for the logistic example of this section obtained using Algorithm 3.4.1 and Modified Algorithm 3.4.2 for different values of σ_0 . From this table, we see that the mean and standard error for the bootstrapping estimators obtained by Algorithm 3.4.1 are quite similar to those obtained by Modified Algorithm 3.4.2 for both cases considered. This implies that Algorithm 3.4.1 works well, and is robust to model misspecification.

We also observe from Table 3.3 that the ratios of the standard errors to the corresponding means are very small for both cases considered. This suggests that we obtain very reliable estimates for b_0 . However, the estimated value for b_0 for each of these cases is smaller than its true value 0.8 (i.e., the value used to generate the data), and the true value lies outside the confidence interval. This clearly demonstrates that obtaining excellent fits to the data and very reliable estimates for parameters is not sufficient to obtain accurate estimates for the true values of the parameters with which to make reliable predictions. We remark that the effect of model misspecification on parameter estimates and model prediction has been addressed by a number

Table 3.3: The mean and standard error of the bootstrapping estimator for the logistic example of this section obtained using Algorithm 3.4.1 and Modified algorithm 3.4.2.

Value of σ_0	Algorithm	Mean	Standard error
$\sigma_0 = 0.2$	Algorithm 3.4.1	7.213e-01	4.095e-04
	Modified Algorithm 3.4.2	7.213e-01	3.978e-04
$\sigma_0 = 1$	Algorithm 3.4.1	7.218e-01	2.045e-03
	Modified Algorithm 3.4.2	7.220e-01	1.986e-03

of researchers (e.g., see [45] and the references therein). There have been numerous attempts to incorporate this error to obtain accurate estimates for parameters (e.g., see [2, 45, 92] and the recent review made in [55]). However, as remarked in [55], none of the approaches attempted so far is universally applicable due to the complexity and wide diversity of the underlying problems to be treated.

3.5 Concluding Remarks and Future Research Questions

We demonstrate with a number of examples how to employ pseudo measurement errors to determine an appropriate statistical model. Numerical results demonstrate that this method works well in practice and is more efficient and accurate than the traditional method of using residual plots to investigate statistical model errors. Once a proper statistical model is determined, we then use the information provided by pseudo measurement errors to determine whether there is a mathematical model error. This is done through comparing the plot for pseudo measurement errors and residual plots. We demonstrate this with an example where the assumed mathematical model has a different form than the model that is used to generate the data. We found that even though the model fit is superb, there is a discernible difference between residual plots and the plot for pseudo measurement errors. Thus, this method provides a much more reliable way to detect a mathematical modeling error.

We also investigated how to use the information provided by pseudo measurement errors to quantify uncertainty in parameter estimators through bootstrapping methods. Numerical results demonstrate the robustness of this method in the presence of model misspecification. In addition, these results reveal that even in the case where the modeling error is small, it is important to recognize it in order to avoid obtaining biased estimates and hence making false predictions. In the future, we hope to use the information provided by pseudo measurement errors and the ideas in [45] on using realistic priors for modelling error to properly calibrate parameters in the presence of model misspecification.

Estimation of Distributed Parameters in Permittivity Models of Composite Dielectric Materials Using Reflectance

4.1 Introduction

In this chapter we revisit the general permittivity model and impose a general distribution on the parameters. We consider here the cases where either the resonance wavenumber or the relaxation time is taken to be a distribution. We then investigate the specific form of data that is required to carry out the inverse problem, and point out the limitations of the existing computational algorithm for our problem. We then describe improvements to this algorithm, and demonstrate the capability of our proposed algorithm to accurately recover a probability measure which was used to generate the simulated data set. We also successfully apply this algorithm to estimate an unknown probability measure with experimental data. A version of this work has been published and can be found in [20]:

H.T. Banks, J. Catenacci, and S. Hu. Estimation of distributed parameters in permittivity models of composite dielectric materials using reflectance. *Journal of Inverse and Ill-Posed Problems*, 23(5):491–509, 2015.

4.2 The Model for the Complex Dielectric Constant and the Reflection Coefficient

In a homogeneous medium one might assume that the resonance wavenumbers k_0 or the relaxation times τ would be the same throughout the material particles, but for a composite

material these would vary across the population of material particles, thus requiring some type of distribution on these resonance wavenumbers or relaxation times in order to characterize the heterogeneous population of particles. To allow for a distribution G of either resonance wavenumbers, or relaxation times, over an admissible set $\mathcal{K} \subset \mathbb{R}$, we generalize the relative permittivity for the Lorentz model (1.2.14) to be

$$\widehat{\varepsilon}_r(k; G, q) = \varepsilon_\infty - \int_{\mathcal{K}} \frac{k_p^2}{k^2 - ik/\tau - k_0^2} dG, \quad (4.2.1)$$

where $G \in \mathcal{P}(\mathcal{K})$, the set of admissible probability measures on \mathcal{K} . In the case of assuming a distribution of resonance wavenumbers we take $q = (\varepsilon_s, \varepsilon_\infty, \tau)^T \in \mathcal{Q} \subset \mathbb{R}^3$ and in the case where there is a distribution on the relaxation times we take $q = (\varepsilon_s, \varepsilon_\infty, k_0)^T \in \mathcal{Q} \subset \mathbb{R}^3$ with \mathcal{Q} assumed to be compact for either case. Thus, for our composite materials the relative permittivity

$$\widehat{\varepsilon}_r(k) = \varepsilon_\infty - \frac{k_p^2}{k^2 - ik/\tau_k - k_0^2}$$

of (1.2.14) is replaced by

$$\widehat{\varepsilon}_r(k; G, q) = \varepsilon_\infty - \int_{\mathcal{K}} \frac{k_p^2}{k^2 - ik/\tau - k_0^2} dG$$

of (4.2.1).

We next turn our attention to obtaining a model for the reflectance. For simplicity, we assume that a monochromatic uniform wave of wavenumber k is normally incident on a plane interface between free space and a dielectric medium. In addition, we assume that the electric field is polarized perpendicular to the plane of incidence. With these assumptions the fully complex reflection coefficient is reduced to

$$r(k; G, q) = \frac{1 - \sqrt{\widehat{\varepsilon}_r(k; G, q)}}{1 + \sqrt{\widehat{\varepsilon}_r(k; G, q)}}. \quad (4.2.2)$$

An interferometer does not directly measure the reflection coefficient, rather the observable is the reflectance

$$R(k; G, q) = |r(k; G, q)|^2.$$

We remark that some interferometers have the capability to obtain the derivative of the reflectance. Specifically, the Bruker 80V two beam interferometer [76] is capable of calculating derivatives up to the fifth order using the Savitzky-Golay algorithm. This algorithm smoothes the data through fitting successive sub-sets of adjacent data points with a low-degree polynomial. Hence, we will also explore the use of derivative of the reflectance measurements, where

the derivative is taken with respect to the wavenumber k . To simulate how the Bruker 80V interferometer obtains derivative information, our derivative measurements will be obtained through the application of the Savitzky-Golay algorithm to the raw (simulated/experimental) reflectance data.

4.3 Computational Framework

In this section we examine an inverse problem methodology for estimating the probability measure G as well as the additional model parameters q .

4.3.1 Statistical Model

We consider a statistical model of the form

$$Y_j = h(k_j; G_0, q_0) + \mathcal{E}_j, \quad j = 0, 1, 2, \dots, N. \quad (4.3.1)$$

In the above equation, $h(k_j; G_0, q_0)$ corresponds to the observed part of the system with the “true” probability measure G_0 and “true” parameters q_0 at the measurement (input) wavenumber k_j , \mathcal{E}_j denotes the measurement error at the measurement wavenumber k_j , and $N + 1$ is the total number of observations. For simplicity in the current proof of concept discussion, we assume that \mathcal{E}_j , $j = 0, 1, 2, \dots, N$, are independent and identically distributed with zero mean and constant covariance matrix $\sigma_0^2 * I_c$, where I_c is an $\ell \times \ell$ identity matrix with ℓ being the dimension of h .

We note here that the usual statistical concept of longitudinal (in time) data is in our problem replaced by input wavenumber data as opposed to the more commonly encountered notion of time point observations found in mathematical and statistical formulations. Our observations depend on the population level probability measures where we have only “aggregate” population particle data for the heterogeneous material as opposed to individual data. More specifically, we do not have $h(k_j; q)$, $j = 0, 1, 2, \dots, N$, which would constitute individual population (particle) data, i.e., we don’t have data based on the particle permittivities $\hat{\epsilon}_r$ of (1.2.14) for individual material particles as a function of input wavenumbers k_j .

As discussed above, we consider two types of data. In the case that the observed part of the system is the reflectance, we have

$$h(k_j; G, q) = R(k_j; G, q). \quad (4.3.2)$$

In the case in which the data contains both the reflectance and the derivative of the reflectance,

h has two components and is given by

$$h(k_j; G, q) = \left(R(k_j; G, q), \frac{\frac{\partial}{\partial k} R(k_j; G, q)}{\max_j \frac{\partial}{\partial k} R(k_j; G, q)} \right)^T. \quad (4.3.3)$$

We remark that the reason for choosing the second component of h as above is because the magnitude of the derivative of the reflectance is extremely small compared to the value of the reflectance. A closed form analytical solution for the derivative of the reflectance has proved to be very difficult to obtain due to the form of $R(k; G, q)$. Hence, we approximate with a simple forward difference.

4.3.2 Inverse Problem

Under the assumptions for the measurement errors in the statistical model, the estimator of (G_0, q_0) can be obtained using the ordinary least squares formulation (e.g., see [33, 40] for details)

$$(G^N, q^N) = \underset{(G, q) \in (\mathcal{P}(\mathcal{K}) \times \mathcal{Q})}{\operatorname{argmin}} \sum_{j=0}^N (h(k_j; G, q) - Y_j)^T (h(k_j; G, q) - Y_j). \quad (4.3.4)$$

The corresponding realization of (G^N, q^N) can be calculated through

$$(\hat{G}^N, \hat{q}^N) = \underset{(G, \theta) \in (\mathcal{P}(\mathcal{K}) \times \mathcal{Q})}{\operatorname{argmin}} \sum_{j=0}^N (h(k_j; G, q) - y_j)^T (h(k_j; G, q) - y_j), \quad (4.3.5)$$

where y_j is a realization of Y_j , that is,

$$y_j = h(k_j; G_0, q_0) + \epsilon_j, \quad j = 0, 1, 2, \dots, N, \quad (4.3.6)$$

with ϵ_j being a realization of \mathcal{E}_j .

As discussed in Chapter 2, the existence of a minimizer to (4.3.4) or (4.3.5) can be established under the Prohorov metric framework as developed in [5, 9, 28, 30, 33, 37, 39] specifically to use with population level (aggregate) data as opposed to individual longitudinal data. The Prohorov metric was introduced in [79] as a means to define what is meant by the distance between arbitrary probability measures.

We recall that (4.3.5) is an infinite-dimensional optimization problem (as $\mathcal{P}(\mathcal{K})$ is an infinite-dimensional space). Hence, we need to approximate the infinite-dimensional space $\mathcal{P}(\mathcal{K})$ with finite-dimensional spaces $\mathcal{P}^M(\mathcal{K})$ so that we have a computationally tractable finite-dimensional

optimization problem given by

$$(\hat{G}_M^N, \hat{q}^N) = \underset{(G,q) \in (\mathcal{P}^M(\mathcal{K}) \times \mathcal{Q})}{\operatorname{argmin}} \sum_{j=0}^N (h(k_j; G, q) - y_j)^T (h(k_j; G, q) - y_j). \quad (4.3.7)$$

Of course, one needs to choose $\mathcal{P}^M(\mathcal{K})$ in a meaningful way so that \hat{G}_M^N approaches \hat{G}^N as M goes to infinity. In this Chapter we consider the approximation method that involves using Dirac measures to approximate the probability measure and can be used regardless of the smoothness of the underlying desired probability measures. This is especially useful in the situations where one has no knowledge of the sought-after probability measures. The theoretical foundation for such an approximation relies on the Prohorov metric framework and Theorem 2.2.3 (see [9], Chapter 2 for details). With this approximation, the least squares problem that we wish to solve is (4.3.7) with

$$\mathcal{P}^N(\mathcal{K}) = \left\{ G \in \mathcal{P}(\mathcal{K}) \mid G = \sum_{j=1}^N \alpha_j \Delta_{\xi_j}, \text{ where } \alpha_j \geq 0 \text{ and } \sum_{j=1}^N \alpha_j = 1 \right\}. \quad (4.3.8)$$

Under this computational framework the optimization problem (4.3.7) is reduced to a standard optimization problem over \mathbb{R}^{M+3} in which we seek to estimate the finite set of values $\{\alpha_m\}_{m=1}^M \cup \{\theta\}$.

We remark that the Dirac measure approximation method has been successfully used to estimate probability measures in a number of applications (e.g., see [27, 28, 30, 39]). However, it was noted in practice that a poor choice of nodes and improper number of nodes could both result in ill-conditioned inverse problems. As we shall see in the next section, this is also discerned in the problem we investigate here. To alleviate some of these difficulties, we propose to estimate both weights and nodes. The feasibility of this modified method is demonstrated in the next section with both simulated data and experimental data.

4.4 Numerical Results

In this section we present results for obtaining an estimation of a probability measure on the resonance wavenumber using both simulated data and experimental data sets for inorganic glass (taken from [58]) where h is given by (4.3.2). We begin by presenting results obtained using simulated data to explore the reliability and accuracy, as well as the limitations of the above approximation methods. We then improve these approximation methods by estimating both the weights and the nodes, and demonstrate the ability of our proposed methods to accurately recover a probability measure which was used to generate the simulated data set. Finally we use the proposed algorithm to estimate an unknown probability measure with experimental data

sets.

In addition, we also give results in which the probability measure is taken over the relaxation time rather than the resonance wavenumber. Using simulated data where h is given by (4.3.2), we show in this case that estimating both the weights and the nodes is not sufficient to give reliable results. We then show how the accuracy of the estimation of the probability measure can be improved by the use of derivative information. In order to obtain derivative data we use the Savitzky-Golay algorithm, which as was mentioned previously, is a common algorithm used by modern interferometers to obtain derivative measurements.

4.4.1 Results Obtained Using Simulated Data When Estimating a Probability Measure on the Resonance Wavenumber

In this section we will attempt to estimate a probability measure on the resonance wavenumber k_0 where h is given by (4.3.2). For the remainder of this section we will take the vector of fixed parameters to be $q = (\varepsilon_s, \varepsilon_\infty, \tau)^T$ and we will denote the nodes of the Dirac masses as $\xi_m = k_{0_m}$. First, we will use the simulated data to discuss the importance of the placement of nodes of the Dirac measures, i.e., the values of k_{0_j} , $j = 1, 2, \dots, N$. In all of the following results shown in this section, the data was generated by evaluating equation (4.3.6), where $k_j = 400 + 10j$, $j = 0, 1, 2, \dots, 69$, the true probability measure $G_0 = \sum_{m=1}^3 \alpha_m \Delta_{k_{0_m}}$ with

$$\alpha_1 = \alpha_2 = 0.05, \quad \alpha_3 = 0.9, \quad k_{0_1} = 570, \quad k_{0_2} = 580, \quad k_{0_3} = 850.$$

We used the true parameters $q_0 = (2.7, 1.9, 0.03)^T$, and ϵ_j was chosen as a realization of a normally distributed random variable with mean 0 and standard deviation $\sigma_0 = 0.005$.

To simplify the scenario, we first only estimate the weights of the Dirac measures, i.e., α_m , $m = 1, 2, \dots, M$, with q_0 assumed to be known. In Figure 4.1 we present the model fit and the estimated distribution where the nodes are chosen to be evenly spaced in the interval $[405, 1080]$, where $M = 25$. In this case the model and the estimated distribution are both an excellent fit to the data and the true distribution, respectively. However, by altering the node placement so that there are now 25 nodes evenly spaced in the interval $[405, 1100]$, the fit to the data is not as good as in the previous case, and the estimated distribution also fails to be as good a fit as before. These results are shown in Figure 4.2. Clearly, from this simple example, we see that our ability to achieve good fits to the data and accurate estimations of the distribution relies on the placement of the nodes.

In attempts to alleviate these difficulties, we seek to also optimize the node locations as well as the weights of the Dirac measures. We did so by including the node locations as additional

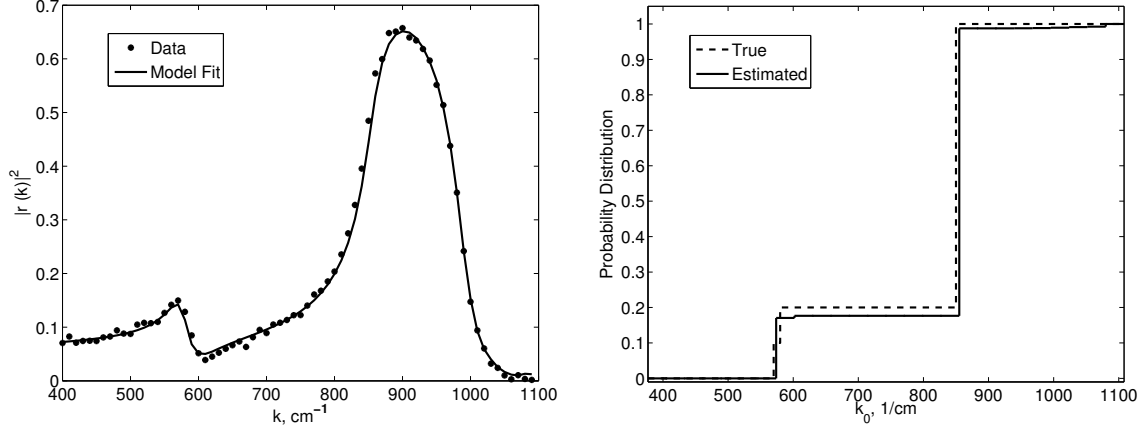


Figure 4.1: The model fit to the simulated data (left) and the estimated distribution of wavenumbers (right), where the nodes are evenly placed over $[405, 1080]$ with $M = 25$.

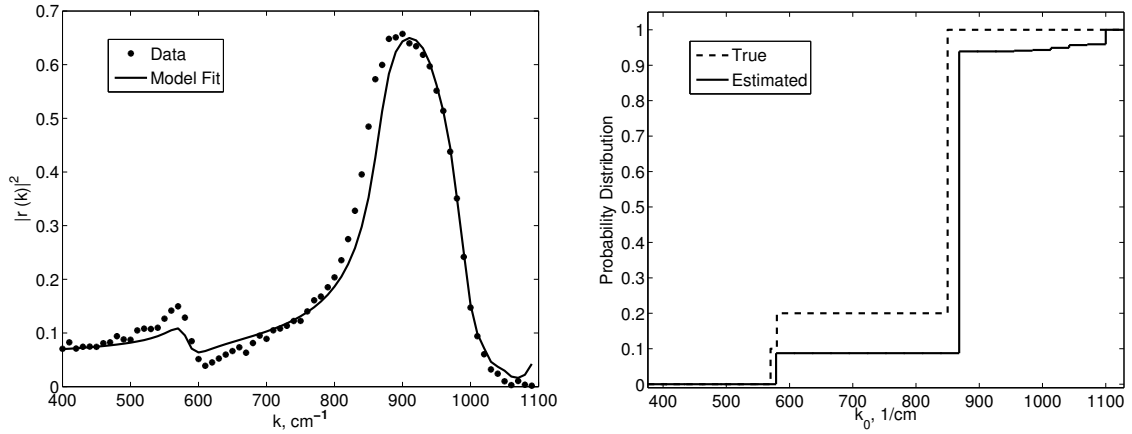


Figure 4.2: The model fit to the simulated data (left) and the estimated distribution of wavenumbers (right), where the nodes are evenly placed over $[405, 1100]$ with $M = 25$.

parameters in the minimization problem. Thus, we can reformulate the minimization problem as

$$(\hat{\alpha}^M, \hat{\mathbf{k}}_0^M) = \underset{\alpha \in \tilde{\mathbb{R}}_w^M, \mathbf{k}_0 \in \mathcal{K}^M}{\operatorname{argmin}} \sum_{j=0}^N (h(k_j; G, \theta_0) - y_j)^2, \quad (4.4.1)$$

where $G = \sum_{j=1}^M \alpha_j \Delta_{k_{0j}}$, and the weights and node locations are chosen respectively from

$$\begin{aligned} \tilde{\mathbb{R}}_w^M &= \left\{ \alpha = (\alpha_1, \alpha_2, \dots, \alpha_M)^T \mid \alpha_j \geq 0 \text{ and } \sum_{j=1}^M \alpha_j = 1 \right\}, \\ \mathcal{K}^M &= \{ \mathbf{k}_0 = (k_{01}, k_{02}, \dots, k_{0M})^T \mid k_{0j} \in \mathcal{K}, j = 1, 2, \dots, M \}. \end{aligned} \quad (4.4.2)$$

The estimated probability measure is then given by $\hat{G} = \sum_{j=1}^M \hat{\alpha}_j \Delta_{\hat{k}_{0j}}$, where $\hat{\alpha}_j$ and \hat{k}_{0j} are the j th element of $\hat{\alpha}^M$ and $\hat{\mathbf{k}}_0^M$, respectively. The results of this inverse problem are shown in Figure 4.3. In this case we see an excellent fit to the data, and the estimated distribution falls nearly precisely on the true distribution.

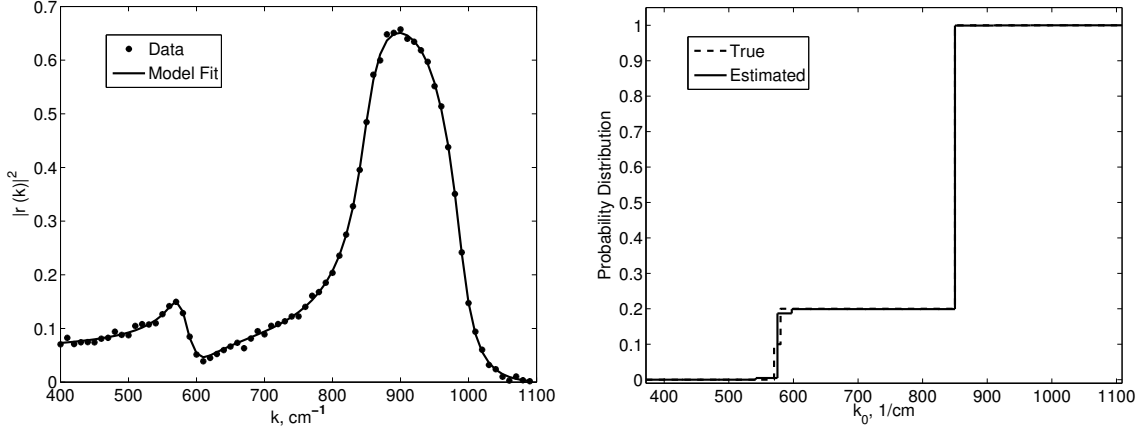


Figure 4.3: Model fit (left) and estimated distribution (right) where the parameters $\varepsilon_s, \varepsilon_\infty$ and τ are fixed and the weights and node locations were optimized with $M = 25$.

Next we consider the case where the parameters $\varepsilon_s, \varepsilon_\infty$ and τ are not known, and thus must also be estimated; that is, our minimization problem is given by

$$(\hat{\alpha}^M, \hat{\mathbf{k}}_0^M, \hat{q}) = \underset{\alpha \in \tilde{\mathbb{R}}_w^M, \mathbf{k}_0 \in \mathcal{K}^M, q \in \mathcal{Q}}{\operatorname{argmin}} \sum_{j=0}^N (h(k_j; G, q) - y_j)^2, \quad (4.4.3)$$

where $G = \sum_{j=1}^M \alpha_j \Delta_{k_{0j}}$, $\tilde{\mathbb{R}}_w^M$ and \mathcal{K}^M are defined by (4.4.2). In doing so, we impose the additional constraint that $\varepsilon_s > \varepsilon_\infty$. This was done to add stability to the inverse problem with respect to the initial guesses for the parameter values. The parameters and the distribution were estimated in this way for $M = 5, 10, 15, 20, 25$, and 30, and the results are given in Table 4.1 and Figures 4.4–4.9. For all of the various number of nodes chosen, the model is an excellent fit to the data. For the cases when a low number of nodes is used, e.g., $M = 5$ and 10, the estimated distribution coincides with the true distribution, and the estimated values for parameters $\varepsilon_s, \varepsilon_\infty$ and τ are very close to their corresponding true values. As M increases, we see that the estimated distributions begin to deviate from the true distribution and the estimation accuracy for parameters $\varepsilon_s, \varepsilon_\infty$ and τ decreases. This is especially true for the parameter τ , where the relative error for the cases of $M = 25$ and 30 is 0.14 and 0.30 respectively, and it is considerably

Table 4.1: Estimations obtained using the simulated data for various numbers of Dirac measures.

M	ε_s	ε_∞	τ (cm)
5	2.6749	1.8781	0.0298
10	2.6703	1.8703	0.0297
15	2.6618	1.8261	0.0303
20	2.6563	1.8163	0.0306
25	2.6713	1.8408	0.0341
30	2.6661	1.8441	0.0389
True Values	2.700	1.900	0.0300

higher than those obtained with a lower value of M (for $M = 5, 10, 15, 20$ the mean relative error is 0.06). We remark that the loss of estimation accuracy as M increases is in agreement with the common understanding that for a fixed number of observations the estimation accuracy in general decreases as the number of estimated parameters increases (e.g., see [19, 46]). Actually, this is how model selection criteria play a role as all model selection criteria such as the Akaike Information Criterion and the Bayesian Information Criterion are based to some extent on the *principle of parsimony* (a balance between the model accuracy and the estimation accuracy). We again refer the interested reader to [19, 46] for more information on this.

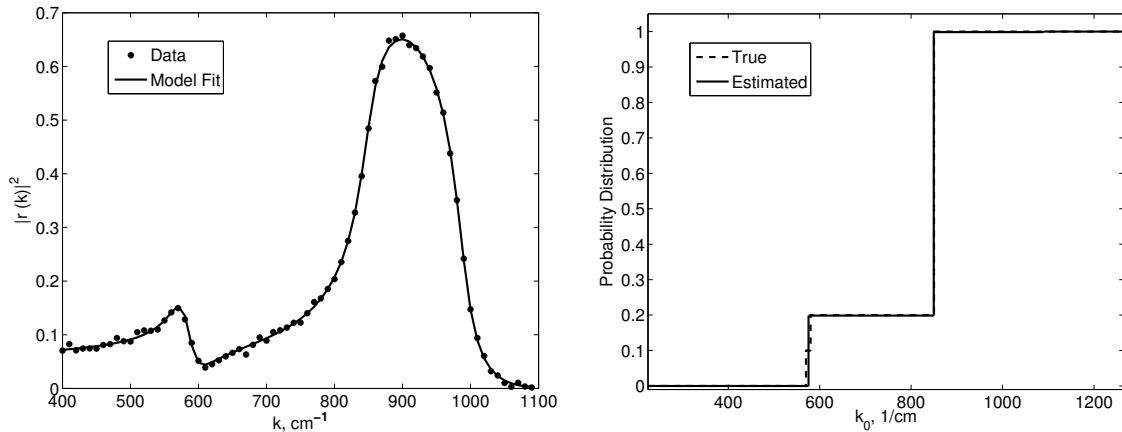


Figure 4.4: Model fit (left) and the estimated distribution (right) from the full inverse problem (4.4.3) where $M = 5$.

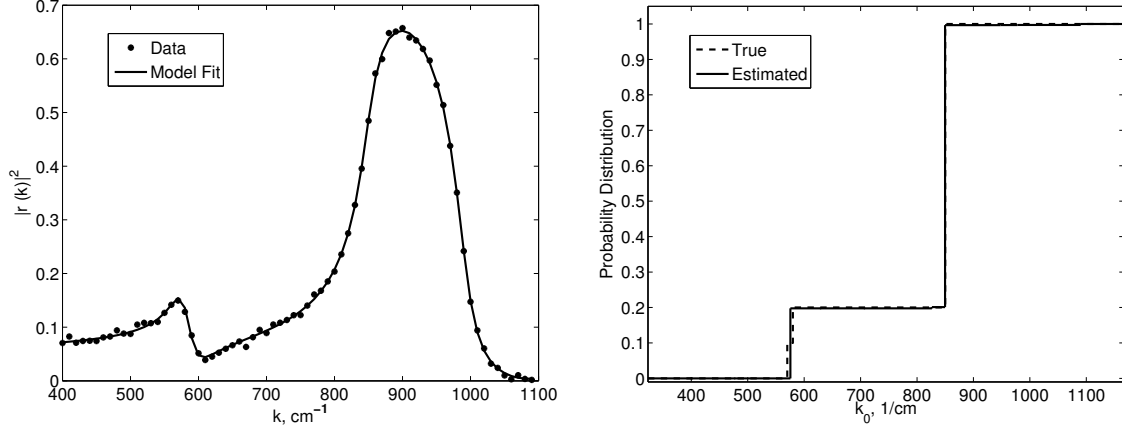


Figure 4.5: Model fit (left) and the estimated distribution (right) from the full inverse problem (4.4.3) where $M = 10$.

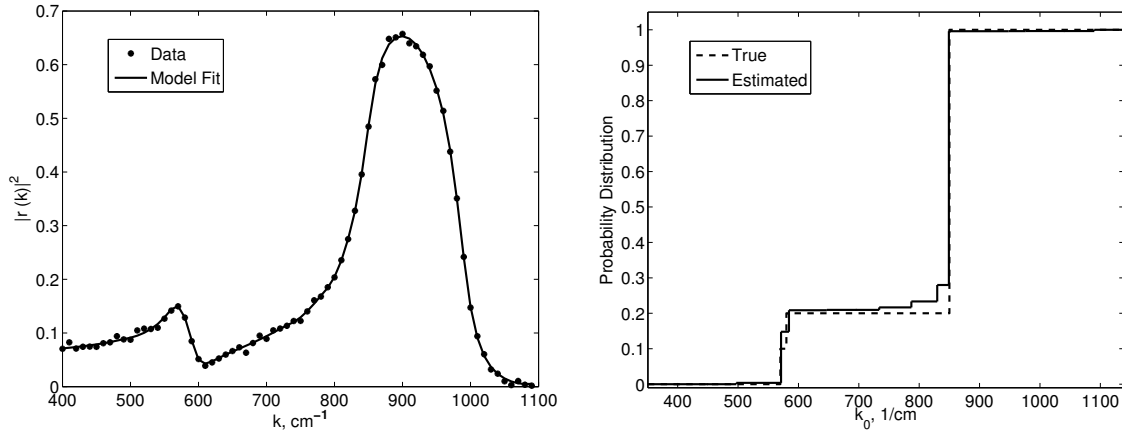


Figure 4.6: Model fit (left) and the estimated distribution (right) from the full inverse problem (4.4.3) where $M = 15$.

4.4.2 Results Obtained Using Inorganic Glass Data When Estimating a Probability Measure on the Resonance Wavenumber

To illustrate the feasibility of our approximation methods on experimental data sets, we present results obtained using inorganic glass data available in [58]. We first consider reflectance data collected from Vitreous Germania in the 400 to 1100 cm^{-1} range (see Table A7 in [58]). Using $M = 5, 10, 15, 20$ and 25 Dirac measures to estimate the distribution of resonance wavenumbers, the corresponding model fits and probability distribution estimations are given in Figures 4.10–4.14. Unlike when using the simulated data, we do see an improvement in the model fits as M is increased. Recall that the simulated data was generated using a true distribution of only 3

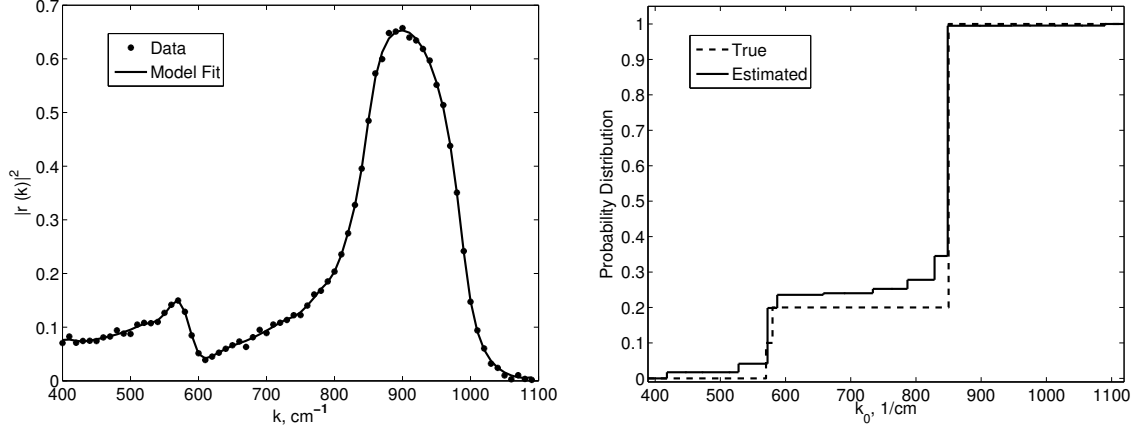


Figure 4.7: Model fit (left) and the estimated distribution (right) from the full inverse problem (4.4.3) where $M = 20$.

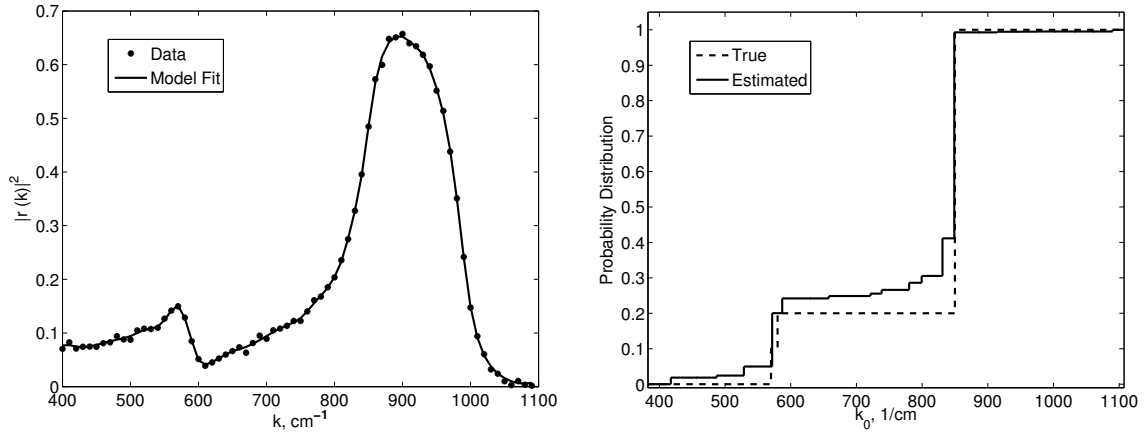


Figure 4.8: Model fit (left) and the estimated distribution (right) from the full inverse problem (4.4.3) where $M = 25$.

discrete measures, 2 of which were very close to each other. Therefore it is not surprising that we were able to obtain very good model fits using only a small number of Dirac measures in that case. Here, it appears as if the unknown distribution for the Vitreous Germania data is made up of either many more discrete measures which are closely clustered in the 500–600, and the 800–900 cm^{-1} range, or a continuous distribution whose probability density function only has nontrivial values over those before mentioned ranges. If this is indeed the case, then it follows that more Dirac measures are needed in order to obtain an accurate fit to the data. Observe that in Figure 4.15 where we superimpose the estimated probability distributions obtained using the various values of M , we see that the distributions exhibit a similar basic structure (with

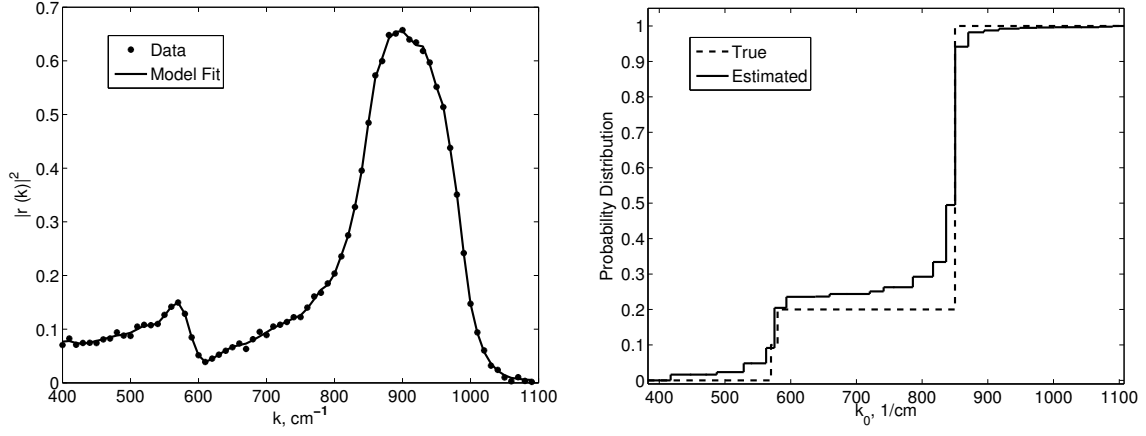


Figure 4.9: Model fit (left) and the estimated distribution (right) from the full inverse problem (4.4.3) where $M = 30$.

increases from 0 to ~ 0.2 – 0.3 over the 500–600 range, and a second increase to ~ 1 over the 800–900 range).

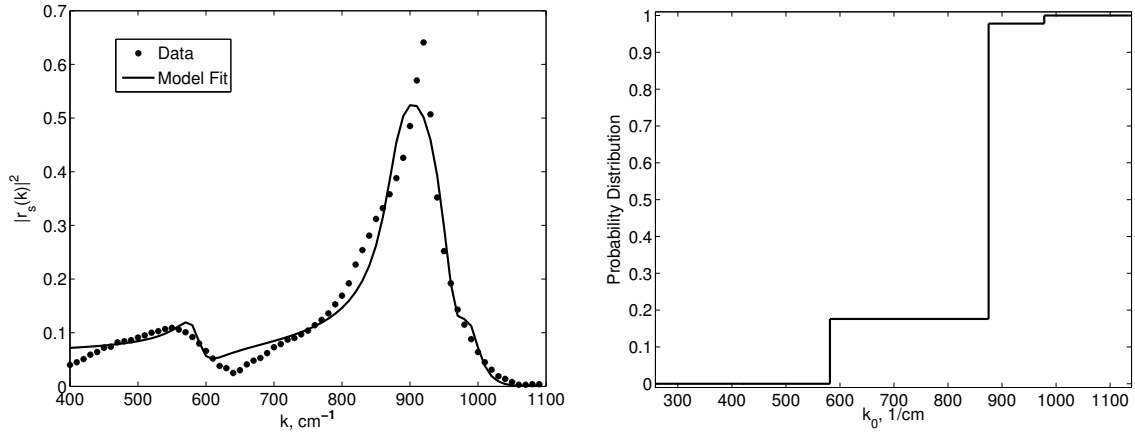


Figure 4.10: Model fit (left) and the estimated distribution (right) from the full inverse problem (4.4.3) where $M = 5$ for Vitreous Germania.

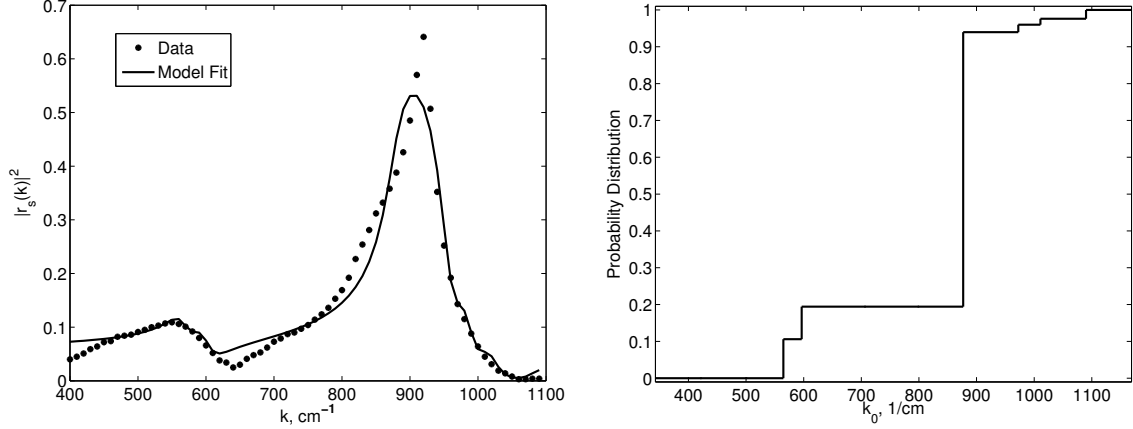


Figure 4.11: Model fit (left) and the estimated distribution (right) from the full inverse problem (4.4.3) where $M = 10$ for Vitreous Germania.

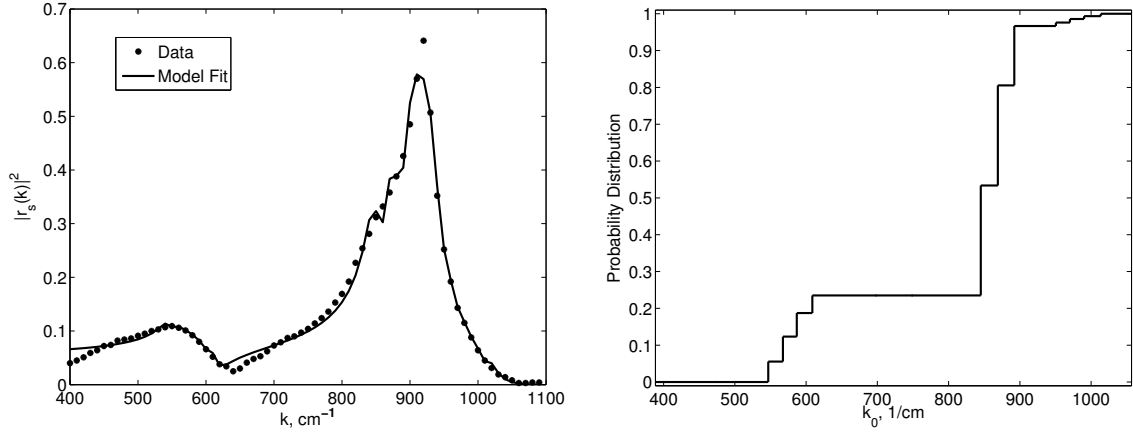


Figure 4.12: Model fit (left) and the estimated distribution (right) from the full inverse problem (4.4.3) where $M = 15$ for Vitreous Germania.

The parameter estimates for ε_s , ε_∞ and τ are given in Table 4.2. Since the material was not interrogated at wavenumbers lower than 400 cm^{-1} , we cannot expect to reliably estimate the “static” dielectric constant ε_s . With this in mind, we see that the estimated value of ε_∞ generally decreases as M increases. With the values of $M = 20$ and 25 , the estimates for ε_∞ are relatively close to each other. Similarly, the estimates for τ increase as M increases, and above the value of $M = 15$ at which the model better fits the data, the values for τ remain at approximately $0.05+$. This may suggest that once a sufficient number of nodes are used to provide a “good” model fit, the parameter estimates settle around stationary values even as M continues to increase. Again, we emphasize that the ideal number of nodes to use is a topic for

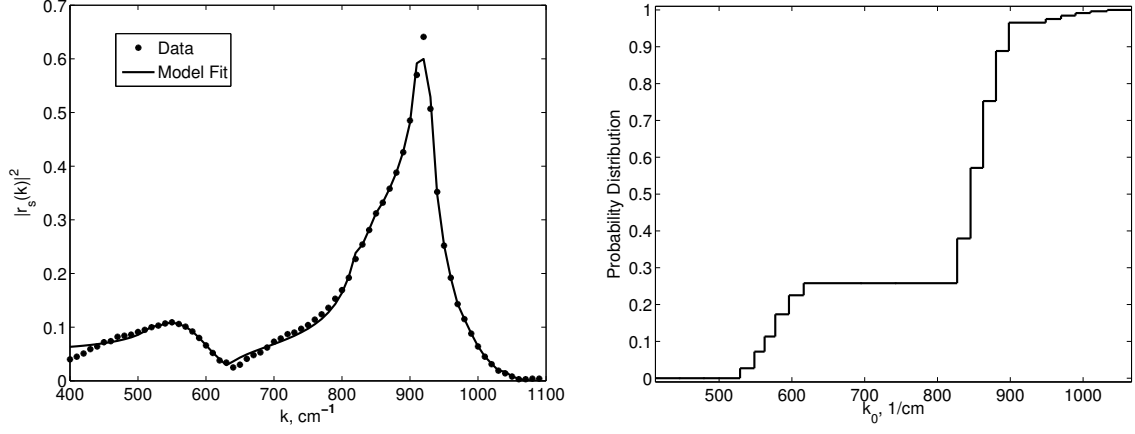


Figure 4.13: Model fit (left) and the estimated distribution (right) from the full inverse problem (4.4.3) where $M = 20$ for Vitreous Germania.

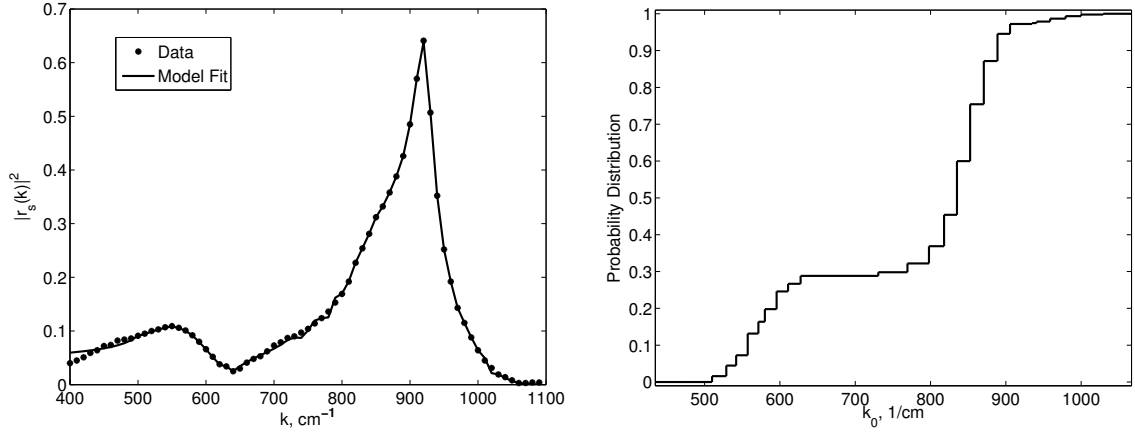


Figure 4.14: Model fit (left) and the estimated distribution (right) from the full inverse problem (4.4.3) where $M = 25$ for Vitreous Germania.

Table 4.2: Estimations obtained using the reflectance data for Vitreous Germania using various numbers of Dirac measures.

M	ε_s	ε_∞	τ (cm)
5	2.7677	2.1518	0.0275
10	2.5768	1.9634	0.0418
15	2.5999	1.9904	0.0525
20	2.4677	1.8341	0.0578
25	2.4361	1.7732	0.0581

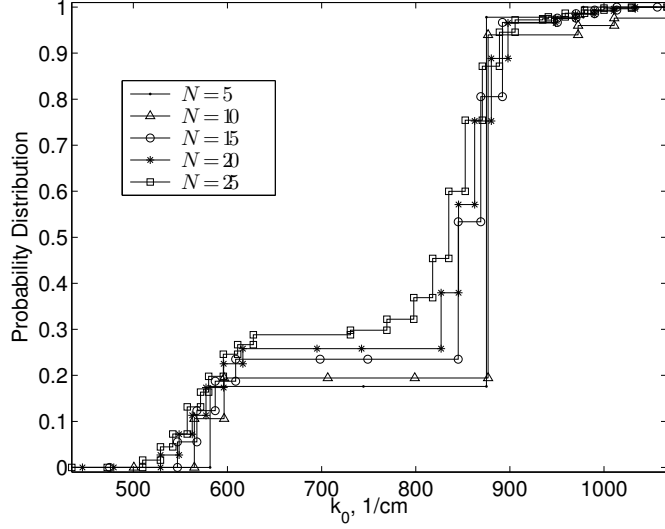


Figure 4.15: The estimated distributions for all values of M considered from the Vitreous Germania data.

further research and the corresponding solution will undoubtedly be dependent on the inherent underlying (and most likely unknown) properties of the material, specifically, the form of the underlying distribution of resonance wavenumbers.

As a second consideration, we solve the optimization problem using reflectance data obtained from Vitreous Silica (available in Table A3 in [58]) over the 200–900 cm^{-1} range. The resulting model fits and estimated distributions are given in Figures 4.16–4.20. Here, we again see that the model fits improve as M increases, and by $M = 25$ an excellent fit is obtained. As before, we plot the distributions obtained using different values of N on one graph in Figure 4.21. From this we see that all of the estimated distributions agree quite well with each other, with a major jump to 0.6 at around 450 cm^{-1} and a second jump of 0.4 at approximately 1080 cm^{-1} .

In Table 4.3 we present the estimated parameter values obtained. For the glass Vitreous Silica, baseline values for ε_s and ε_∞ which were obtained experimentally are available in [65]. This gives a general benchmark to determine if our estimates for these values are valid. In fact, our estimated values are in very good agreement with the experimental values, particularly for $M = 20$, and 25 which, not surprisingly, provide the best model fits to the data.

4.4.3 Results Obtained Using Simulated Data When Estimating a Probability Measure on the Relaxation Time

In this section we turn our focus to estimating a distribution of relaxation times rather than resonance wavenumbers. Therefore, in the remainder of this section we take $q = (\varepsilon_s, \varepsilon_\infty, k_0)^T$,

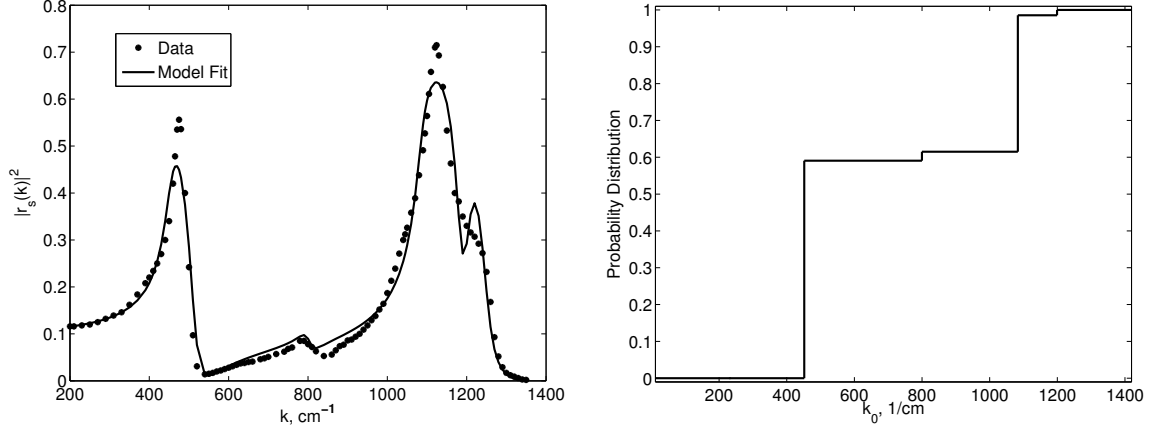


Figure 4.16: Model fit (left) and the estimated distribution (right) from the full inverse problem (4.4.3) where $M = 5$ for Vitreous Silica.

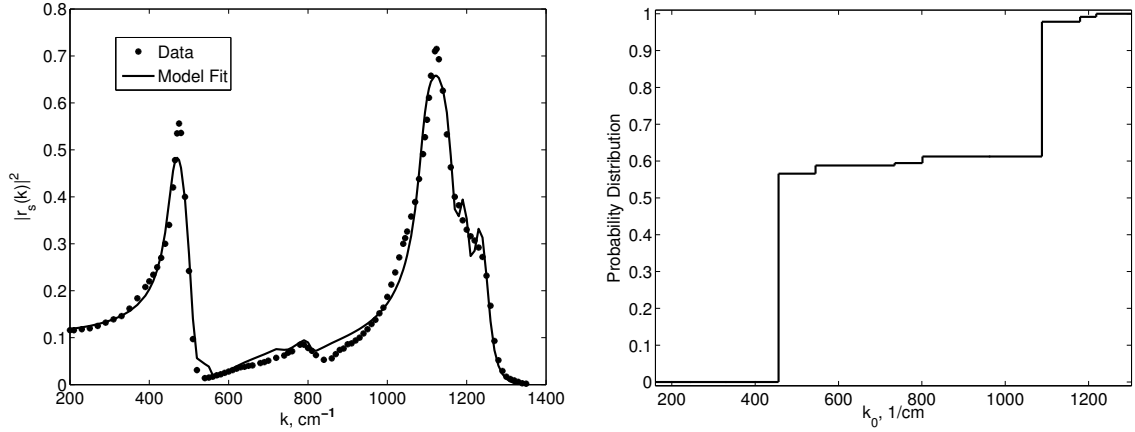


Figure 4.17: Model fit (left) and the estimated distribution (right) from the full inverse problem (4.4.3) where $M = 10$ for Vitreous Silica.

and denote the nodes of the Dirac masses as $\xi_m = \tau_m$. The data was generated by evaluating (4.3.6) with h given by (4.3.2), where $k_j = \omega_j$, with $\{\omega_j\}_{j=0}^{100} = \{10^{7+0.09j}\}_{j=0}^{100}$, and ϵ_j was chosen as a realization of a normally distributed random variable with mean 0 and standard deviation $\sigma_0 = 0.001$. The true probability measure G_0 was chosen as

$$G_0 = 0.6\Delta_{\tau_k^1} + 0.4\Delta_{\tau_k^2}, \quad (4.4.4)$$

where $\tau_k^1 = 2\pi c \cdot 7.14 \times 10^{-16}$ and $\tau_k^2 = 2\pi c \cdot 10^{-14}$, where c is the speed of light in cm/s. We used the true parameters $\theta_0 = (2.25, 1.25, k_0)^T$, where $k_0 = \omega_0/(2\pi c)$, $\omega_0 = 10^{14}$. We note that these choices for frequency ranges and parameter values are adapted from [42]. To keep the

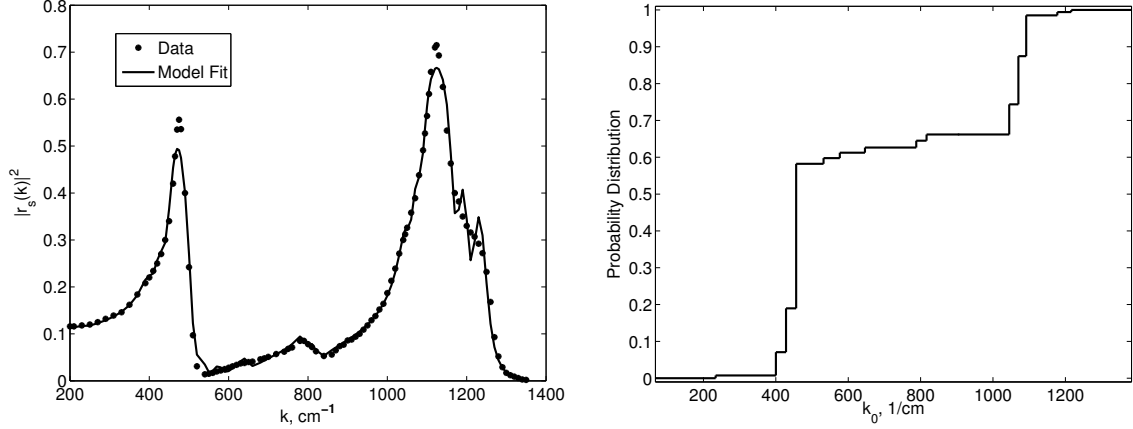


Figure 4.18: Model fit (left) and the estimated distribution (right) from the full inverse problem (4.4.3) where $M = 15$ for Vitreous Silica.

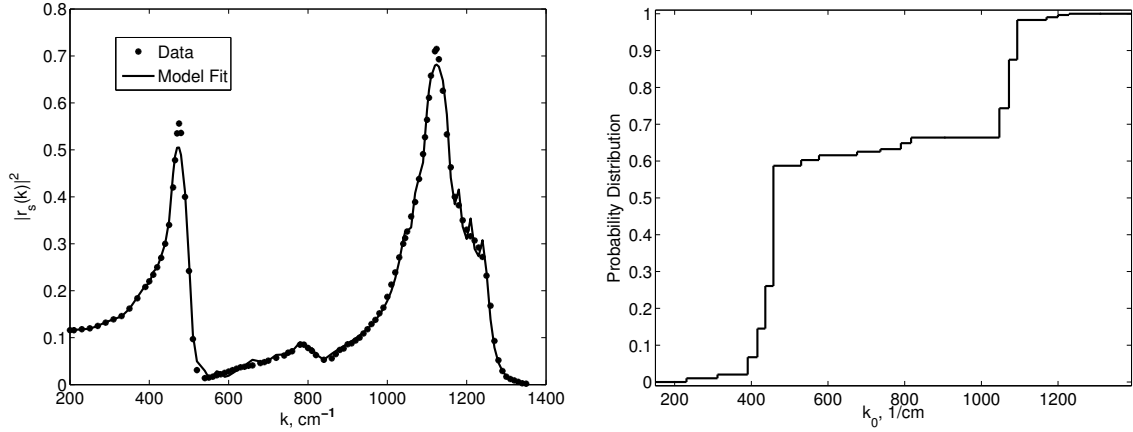


Figure 4.19: Model fit (left) and the estimated distribution (right) from the full inverse problem (4.4.3) where $M = 20$ for Vitreous Silica.

scenario simple, we take θ_0 to be known and only estimate the probability measure.

We first consider the case where the nodes are kept fixed and choose $\{\tau_m\}_{m=1}^M$ to be M evenly spaced nodes over the interval $2\pi c \cdot [10^{-17}, 2 \times 10^{-14}]$. In Figure 4.22 we give the model fit and the estimated probability measure for $M = 15$. Although the model fit is reasonable, the estimated distribution is nowhere near the true distribution. As we did in the case of estimating a distribution of wavenumbers, we will attempt to resolve this issue by optimizing the node locations as well. In Figure 4.23 we give the results where both the weights and the locations of the Dirac masses have been estimated. Compared to the case of fixed nodes, the model fit and the estimated distribution are both improved. However, the estimated distribution does

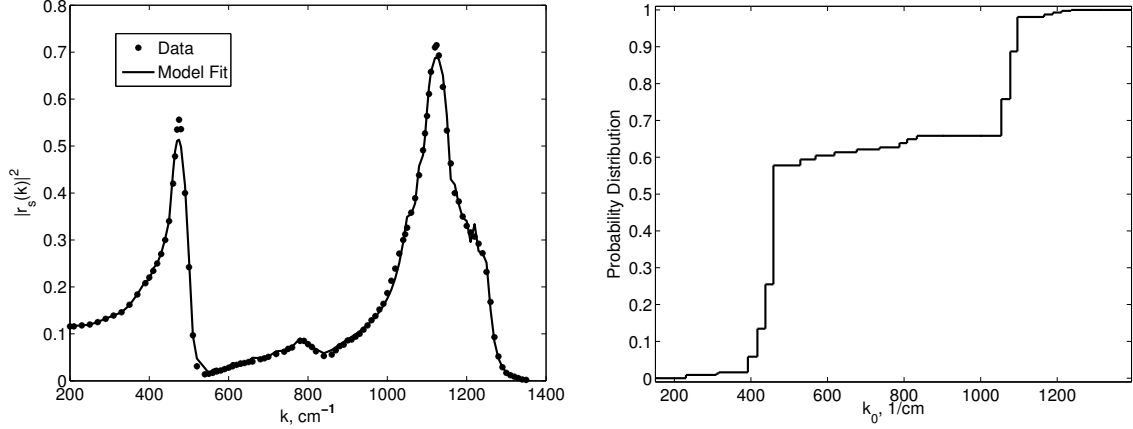


Figure 4.20: Model fit (left) and the estimated distribution (right) from the full inverse problem (4.4.3) where $M = 25$ for Vitreous Silica.

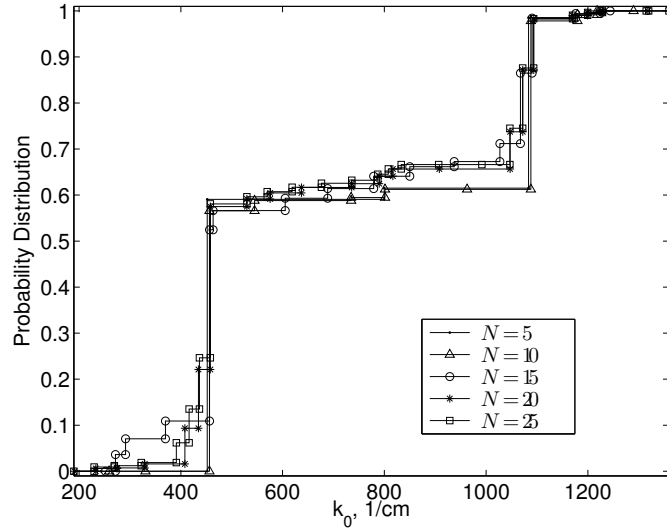


Figure 4.21: The estimated distributions for all values of M considered from the Vitreous Silica data.

not recover the single increase in the true distribution at approximately $\tau \approx 2 \text{ cm}$. Rather, the estimated distribution approximates the jump by slowly increasing from 0.6 at $\tau \approx 1.5 \text{ cm}$ to 1 at $\tau \approx 2.25 \text{ cm}$.

Finally, we consider the addition of derivative information into the minimization problem, hence, we take h as in (4.3.3). As before, both the node weights and the locations are being estimated. In Figure 4.24 we give the model and derivative fits, as well as the estimated distribution. The model fit is again quite good, and the derivative fit is reasonable. However, in

Table 4.3: Parameter estimates obtained using the reflectance data for Vitreous Silica employing various numbers of Dirac measures compared to experimental values (abbreviated as Expt. in the table) taken from [65].

M	ε_s	ε_∞	τ (cm)
5	3.8636	2.2615	0.0277
10	3.9546	2.3613	0.0323
15	3.9805	2.1704	0.0341
20	3.7402	2.0880	0.0397
25	3.7818	2.0879	0.0398
Expt.	3.8	2.1	

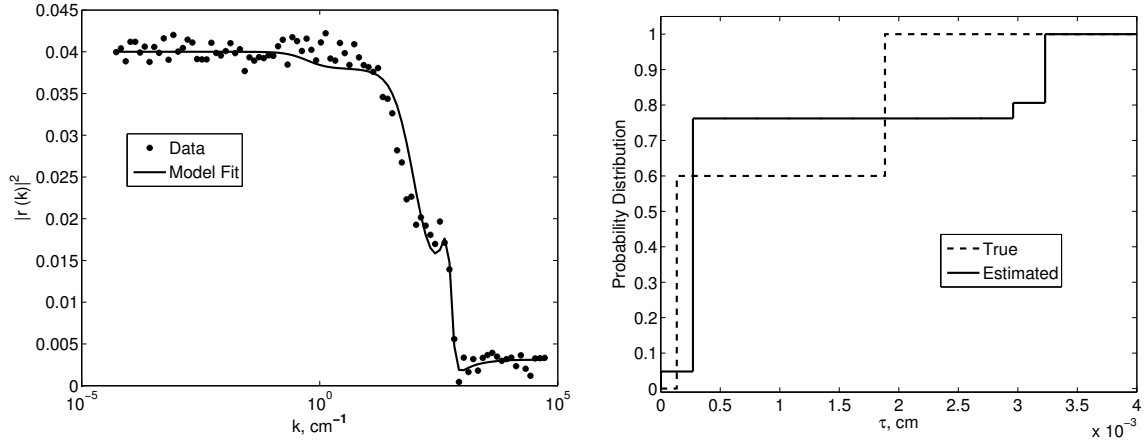


Figure 4.22: Model fit (left), and the estimated distribution (right) with $M = 15$ fixed nodes.

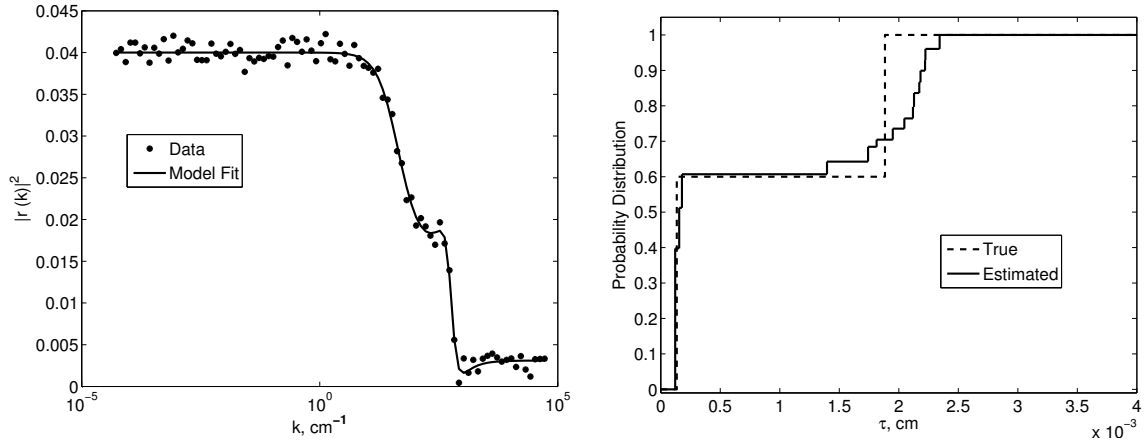


Figure 4.23: Model fit (left) and the estimated distribution (right) where both $M = 15$ node weights and locations were optimized.

this case, we are able to recover, almost precisely the true distribution.

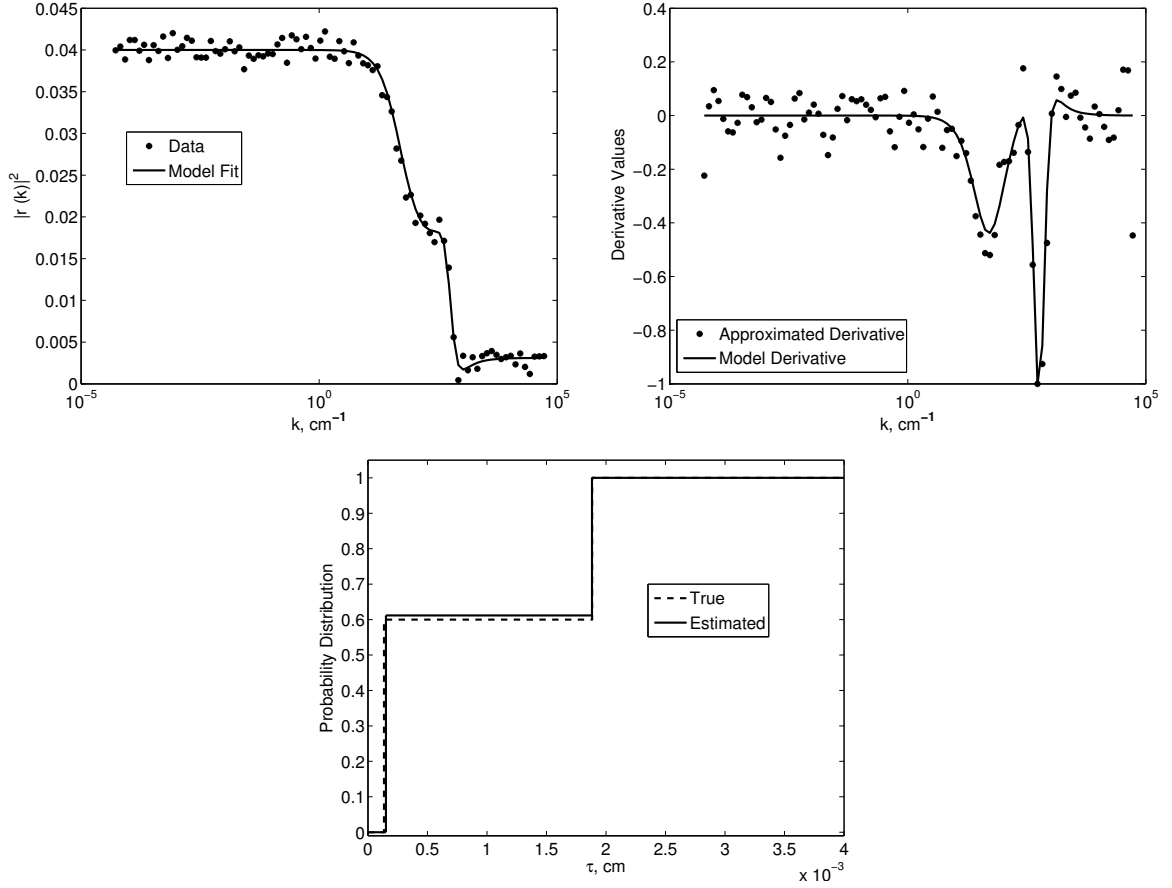


Figure 4.24: Model fit (left), the derivative of reflectance fit (right), and the estimated distribution (bottom) where both $M = 15$ node weights and locations were optimized.

4.5 Concluding Remarks and Future Research Efforts

In this chapter we imposed a probability measure on the resonance wavenumber as well as the relaxation time within the Lorentz polarization model. We then summarized an existing computational framework developed by our group to non-parametrically estimate the unknown probability measure. We carried out existing Dirac measure approximation methods on a set of simulated data to illustrate the basic feasibility and restrictions of these methods for this particular application. We then improved the existing approximation methods by optimizing both weights and nodes of the approximating Dirac measures, and demonstrated the capability of the

proposed methods to accurately recover a true distribution for the simulated data. Additionally, we applied our methods of estimating a distribution of resonance wavenumbers to available data sets of reflectance collected from inorganic glass. Using these data sets we were able to obtain very good fits to the data. The fits improved as the number of nodes M increased, and the estimated distributions and parameter values appeared to stabilize as the value of M was increased. When possible, we showed that our parameter estimates agreed well with available experimental values. Finally, using simulated data we showed that when estimating a distribution of relaxation times the use of derivative measurements increases the accuracy of the method.

Future efforts will include using a model selection criteria, namely the Akaike Information Criterion, in order to quantitatively determine an optimal number of approximating elements. Alternatively, one could devise a pseudo “mesh refinement” in which initially a low number of nodes is chosen, then during the optimization process more nodes are added until a desired accuracy is reached. Moreover, for particular applications, it may be necessary to simultaneously estimate a probability measure on the resonance wavenumbers and the relaxation times. Thus, our methods would require extension to such a case. It will also prove useful to investigate the robustness of the estimation procedure we have outlined on simulated data generated from a continuous, rather than discrete distribution. Moreover, one may wish to extend these results to the case where the unknown probability measure is known to be absolutely continuous so that the corresponding probability density function (PDF) exists and can be approximated by piecewise linear spline functions (see [39] for details). It was demonstrated in [23] that for such a case the spline-based approximation methods converge much faster than do the Dirac measure approximation methods and they also provide convergence for the associated PDFs while the Dirac measure approximation methods do not do this.

Another future effort involves quantifying uncertainties of the probability estimators obtained using this modified Dirac measure approximation method. The pointwise asymptotic normality result for the approximated probability measure estimators was established in our theoretic paper [19] (see Chapter 2) for the case where the original Dirac measure approximation method is used for approximation. It was based on the asymptotic normality results for the corresponding weights of the approximated probability measure estimator under the model “misspecification” due to approximation as well as the fact that the approximated probability measure estimator is linearly dependent on these weights. Numerical results demonstrated in [19] show that one has a good match for the confidence bands obtained by the pointwise asymptotic normality result and the Monte Carlo method in the region to which the model output is most sensitive. However, the pointwise asymptotic normality result established in [19] cannot be applied to the case where the modified Dirac measure approximation method is used as the obtained approximated probability measure estimator is not linearly dependent on its corresponding weights and node locations.

Method Comparison For Estimation Of Distributed Parameters In Permittivity Models Using Reflectance

5.1 Introduction

In this chapter we compare the two available approximation schemes under the PMF, Dirac masses and piecewise linear splines, to establish the accuracy and reliability for the estimation of the distribution of resonance wavenumbers. Additionally, we also carryout an alternative approach of imposing a normal distribution of the resonance wavenumbers and compare these results with those obtained using the PMF. In Section 5.2, we give the permittivity models which are embedded in the model for the reflection coefficient, and establish the foundation for the two approximation schemes under the PMF. In Section 5.3 we give the results obtained using both synthetic data sets and experimental data sets obtained from various inorganic glasses. Finally, in Section 5.4 we conclude the chapter with summary remarks and plans for future work. The results found in this Chapter have been published and can be found in [21]:

H.T. Banks, J. Catenacci, and S. Hu. Method comparison for estimation of distributed parameters in permittivity models using reflectance. *Eurasian Journal of Mathematical and Computer Applications*, 3(2):424, 2015.

5.2 The Model for the Complex Permittivity and the Reflection Coefficient

5.2.1 Efimov model for permittivity

In [58, 61], Efimov describes an observed band broadening in the spectra of glasses, which he contributes to the random distribution of particular realizations of microscopic structures. To handle this band broadening, Efimov chooses to approximate the broadening by using a Gaussian probability density function. This leads to a model for the relative permittivity given by

$$\widehat{\varepsilon}_r(k) = \varepsilon_\infty - \sum_{j=1}^J \frac{S_j}{\sqrt{2\pi}\sigma_j} \int_{-\infty}^{\infty} \frac{\exp\left(-(x - k_{0j})^2/2\sigma_j^2\right)}{k^2 - ik/\tau_j - x^2} dx, \quad (5.2.1)$$

where J is the number of oscillators. The above permittivity model can be considered a generalization of equation 1.2.15. We note that Efimov has made the tacit assumption to consider the intensities S_j as a “free” parameter. By this we mean, that had the relationship $S_j = \Delta\varepsilon_{0j}k_{0j}^2$ been enforced, then there would be a x^2 term multiplying the exponential function in the integration.

Efimov notes that the band broadening could be better approximated by a truncated Gaussian in order to ensure that the wavenumber ranges remain non-negative. We make this modification which results in what we will refer to as the *modified Efimov relative permittivity model*, given by

$$\widehat{\varepsilon}_r(k; q) = \varepsilon_\infty - \sum_{j=1}^J \frac{S_j}{c_j} \int_0^{\infty} \frac{\exp\left(-(x - k_{0j})^2/2\sigma_j^2\right)}{k^2 - ik/\tau_j - x^2} dx, \quad (5.2.2)$$

where

$$c_j = \int_0^{\infty} \exp\left(-(x - k_{0j})^2/2\sigma_j^2\right) dx. \quad (5.2.3)$$

In the above equation $q = (\varepsilon_\infty, \{S_j, \tau_j, k_{0j}, \sigma_j\}_{j=1}^J)^T \in \mathcal{Q} \subset \mathbb{R}^{4J+1}$ with Θ assumed to be compact.

5.2.2 Prohorov Metric Framework Model for Permittivity

As discussed previously, an alternate method which can be used to account for multiple dielectric mechanisms present in a material, is to impose a probability distribution on the dielectric parameters, or a subset of the dielectric parameters. Here, we take this approach and then will make use of the PMF to non-parametrically estimate the distribution(s). In this work we only consider the case where a distribution is placed on the resonance wavenumbers (distributions could also be put on the relaxation constants τ (see [20], Chapter 4).

To allow for a distribution G of resonance wavenumbers over an admissible set $\mathcal{K} \subset \mathbb{R}$, we recall that we generalize the relative permittivity for the Lorentz model (1.2.14) to be

$$\widehat{\varepsilon}_r(k; G, q) = \varepsilon_\infty - \int_{\mathcal{K}} \frac{k_p^2}{k^2 - ik/\tau - k_0^2} dG(k_0), \quad (5.2.4)$$

where $G \in \mathcal{P}(\mathcal{K})$, the set of admissible probability measures on \mathcal{K} . In the case of assuming a distribution of resonance wavenumbers we also have the constant parameter vector $q = (\varepsilon_s, \varepsilon_\infty, \tau)^T \in \mathcal{Q}$ with $\mathcal{Q} \subset \mathbb{R}^3$ assumed to be compact.

We remark the the Efimov model is not a subcase of the PMF models.

5.2.3 Reflection Coefficient

Next we focus on obtaining an appropriate model for the reflectivity for our situation of interest. As in the previous chapters, we assume that a monochromatic uniform wave of wavenumber k is incident on a plane interface between free space and a dielectric medium. We will deal with data which is obtained either at an incident angle of $\phi = 45^\circ$ or 0° . Both situations can be accurately described by assuming that the reflectance is composed of the parallel and perpendicular polarizations in equal weights. Thus we obtain the equation for the reflectivity

$$R(k; G, q) = \frac{1}{2} (|r_\perp(k; G, q)|^2 + |r_\parallel(k; G, q)|^2), \quad (5.2.5)$$

where

$$r_\perp(k; G, q) = \frac{\cos \phi - \sqrt{\widehat{\varepsilon}_r(k; G, q) - \sin^2 \phi}}{\cos \phi + \sqrt{\widehat{\varepsilon}_r(k; G, q) - \sin^2 \phi}}, \quad (5.2.6)$$

and

$$r_\parallel(k; G, q) = \frac{\sqrt{1 - \sin^2 \phi / \widehat{\varepsilon}_r(k; G, q)} - \sqrt{\widehat{\varepsilon}_r(k; G, q)} \cos \phi}{\sqrt{1 - \sin^2 \phi / \widehat{\varepsilon}_r(k; G, q)} + \sqrt{\widehat{\varepsilon}_r(k; G, q)} \cos \phi}. \quad (5.2.7)$$

Notice that if $\phi = 0^\circ$, then the equation for the reflectivity reduces to $R(k; G, q) = |r_\perp(k; G, q)|^2$. The equations (5.2.6) and (5.2.7) are the same as formulas (1.2.11) and (1.2.12) except that we have explicitly included the dependence on the probability measure G and the parameter vector q .

At this point we remark that when using the modified Efimov model for the complex permittivity, the distribution G is absent. In order to avoid cumbersome notation, when the modified Efimov model is used, we will ignore the input G mathematically, but not drop it notationally.

5.2.4 Statistical Model

Our goal is to estimate both the unknown probability measure G as well as the additional model parameters when using the PMF approach. Of course, when using the Efimov model we need only estimate the relevant model parameters. We consider a statistical model of the form

$$Y_j = R(k_j; G_0, q_0) + \mathcal{E}_j, \quad j = 0, 1, 2, \dots, N. \quad (5.2.8)$$

In the above equation Y_j is a random variable which is composed of the reflectance with G_0 the “true” probability measure and q_0 the “true” parameters at a sampling wavenumber k_j , and the measurement error \mathcal{E}_j . For simplicity, we consider that the errors \mathcal{E}_j are independent and identically distributed with mean 0 and constant variance.

5.2.5 Inverse Problem

With the assumptions we have made for the measurement errors in the statistical model, the estimates \hat{G} of G and \hat{q} of q can be obtained through an ordinary least squares formulation

$$(\hat{G}, \hat{q}) = \underset{(G, q) \in (\mathcal{P}(\mathcal{K}) \times \mathcal{Q})}{\operatorname{argmin}} J(G, q). \quad (5.2.9)$$

In the above equation, the cost functional J is defined as

$$J(G, q) = \sum_{j=0}^N (R(k_j; G, q) - y_j)^2 \quad (5.2.10)$$

and y_j is a realization of Y_j , $j = 0, 1, \dots, N$ in (6.4.1). That is,

$$y_j = R(k; G_0, q_0) + \epsilon_j, \quad j = 0, 1, 2, \dots, N. \quad (5.2.11)$$

We note that (5.2.9) is an infinite-dimensional optimization problem in the case of using the PMF. Thus, we need to approximate the infinite dimensional space $\mathcal{P}(\mathcal{K})$ with a finite dimensional space $\mathcal{P}^M(\mathcal{K})$ in order to have a computationally tractable finite-dimensional optimization problem

$$(\hat{G}, \hat{q}) = \underset{(G, q) \in (\mathcal{P}^M(\mathcal{K}) \times \mathcal{Q})}{\operatorname{argmin}} J(G, q). \quad (5.2.12)$$

We will consider two finite-dimensional spaces, $\mathcal{P}_D^M(\mathcal{K})$ and $\mathcal{P}_S^M(\mathcal{K})$, to approximate $\mathcal{P}(\mathcal{K})$. The space \mathcal{P}_D^M involves the use of Dirac measures, and the space \mathcal{P}_S^M involves the use of piecewise

linear splines. We define these two spaces as

$$\mathcal{P}_D^M(\mathcal{K}) = \left\{ G \in \mathcal{P}(\mathcal{K}) \mid G = \sum_{m=1}^M \alpha_m \Delta_{x_m}, \text{ where } \alpha_m \geq 0 \text{ and } \sum_{m=1}^M \alpha_m = 1 \right\} \quad (5.2.13)$$

and

$$\mathcal{P}_S^M(\mathcal{K}) = \left\{ G \in \mathcal{P}(\mathcal{K}) \mid G' = \sum_{m=1}^M \alpha_m l_m(k_0), \text{ where } \alpha_m \geq 0 \text{ and } \sum_{m=1}^M \alpha_m \int_{\mathcal{K}_m} l_m(\xi) d\xi = 1 \right\} \quad (5.2.14)$$

where Δ_{x_m} is a Dirac measure with atom at x_m , and l_m is the m th linear spline element with support \mathcal{K}_m . With either of these spaces we have reduced the infinite-dimensional problem to a finite-dimensional problem in which we only need to estimate q and the weights $\boldsymbol{\alpha} = \{\alpha_m\}_{m=1}^M$. Following the work in [20] we will estimate the Dirac atom locations $\mathbf{x} = \{x_m\}_{m=1}^M$ as well. Hence, when using the Delta approximation method we have the minimization problem

$$(\hat{\boldsymbol{\alpha}}, \hat{\mathbf{x}}, \hat{q}) = \arg \min_{(\boldsymbol{\alpha}, \mathbf{x}, q) \in (\mathbb{R}_D^M \times \mathcal{K}^M \times \mathcal{Q})} J \left(\sum_{m=1}^M \alpha_m \Delta_{x_m}, q \right), \quad (5.2.15)$$

where

$$\begin{aligned} \mathbb{R}_D^M &= \left\{ \boldsymbol{\alpha} = (\alpha_1, \alpha_2, \dots, \alpha_M)^T \mid \alpha_m \geq 0, \text{ and } \sum_{m=1}^M \alpha_m = 1 \right\}, \\ \mathcal{K}^M &= \{ \mathbf{x} = (x_1, x_2, \dots, x_M)^T \mid x_m \in \mathcal{K}, m = 1, 2, \dots, M \}. \end{aligned}$$

Using the spline method we have the minimization problem

$$(\hat{\boldsymbol{\alpha}}, \hat{q}) = \underset{(\boldsymbol{\alpha}, q) \in (\mathbb{R}_S^M \times \mathcal{Q})}{\operatorname{argmin}} J(G, q), \quad G' = \sum_{m=1}^M \alpha_m l_m(k_0) \quad (5.2.16)$$

where

$$\mathbb{R}_S^M = \left\{ \boldsymbol{\alpha} = (\alpha_1, \alpha_2, \dots, \alpha_M)^T \mid \alpha_m \geq 0, \text{ and } \sum_{m=1}^M \alpha_m \int_{\mathcal{K}_m} l_m(\xi) d\xi = 1 \right\}.$$

When using the modified Efimov model, we simply have the standard minimization problem

$$\hat{q} = \underset{q \in \mathcal{Q}}{\operatorname{argmin}} J(q), \quad (5.2.17)$$

where $\mathcal{Q} \subset \mathbb{R}^{4J+1}$ is compact.

5.3 Results

The results section is laid out as follows. First we investigate the differences between the Dirac and spline approximation methods and the modified Efimov approach using simulated data sets. We consider two simulated data sets, the first using a “true” distribution G_0 which is discrete, and the second distribution being continuous. Next we compare the methods using reflectance data obtained from three different inorganic glasses.

For the modified Efimov model we must choose the number of oscillators J which describe the interrogated material. This is done by starting with a low value of oscillators and then increasing J until the model fit gives a reasonable approximation to the data.

5.3.1 Simulated Data

The simulated data was generated by evaluating (5.2.11) at $k = 600 + j\Delta k$, where $\Delta k = 0.8$ and $j = 0, 1, 2, \dots, N = 1000$. The errors, ϵ_j , were chosen as a realization of a normally distributed random variable with mean 0 and standard deviation $\sigma_0 = 0.001$. The number of interrogating wavenumbers which we use here is similar to sampling capabilities of a modern FTIR spectrometer.

As noted above, for the true distribution G_0 , we consider two cases. In the first case we take G_0 to be a discrete distribution, which is depicted as the true distribution (along with a number of graphs for the results from optimized PMF based fits-to-data) in Figure 5.2 below. In the second case we take G_0 to be a continuous distribution. For this we chose to take G_0 as a truncated bivariate normal distribution which can be seen in Figure 5.4 (again along with a number optimized fits-to-data). For both cases we used the scalar parameters $q_0 = (\epsilon_{s_0}, \epsilon_{s_0}, \tau_0) = (1.6, 1.32, 0.017)$ and the incident angle was set to $\phi = 45^\circ$.

Discrete Distribution

The “true” discrete distribution G_0 used to simulate the data has 30 Dirac measures. There are two regions, between 650 and 1100 cm^{-1} , and between 1100 and 1400 cm^{-1} , in which the jump discontinuities present in the distribution produce relatively small increases. At $k_0 = 1100 \text{ cm}^{-1}$ there is a relatively large jump of 0.34. It is reasonable assumption to expect a distribution of similar characteristics to describe a CMC which is in a crystalline state.

In Figure 5.1 we give the model fit for both PMF approximation schemes using $M = 45$ as well as for the modified Efimov approach with $J = 6$. We see that both PMF methods obtain an excellent model fit, and similar fits were obtained for other values of M . The model using the modified Efimov approach fits the data well except for wavenumbers $k > 1350 \text{ cm}^{-1}$. We present the estimated distributions using the spline and Dirac methods in Figure 5.2 and the

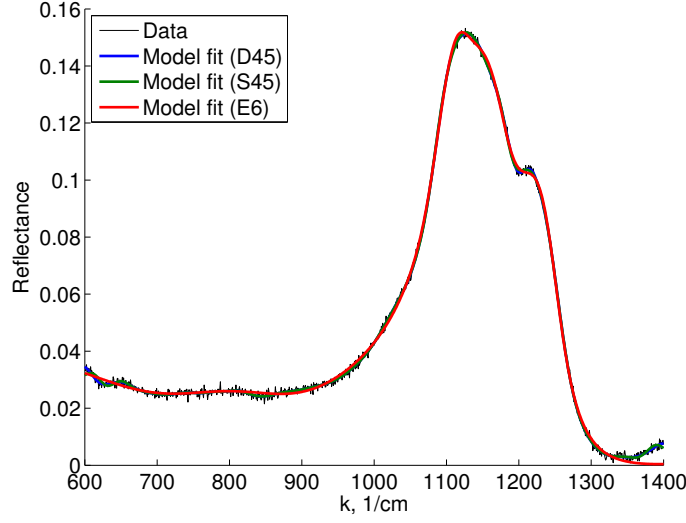


Figure 5.1: The model fits to the simulated data generated with a discrete distribution. The model fit using the Dirac approximation scheme is labeled as D45 and the spline approximation schemes as S45, where 45 is the number of nodes M , and the model fit using the modified Efimov method is labeled as E6 where $J = 6$ oscillators were used.

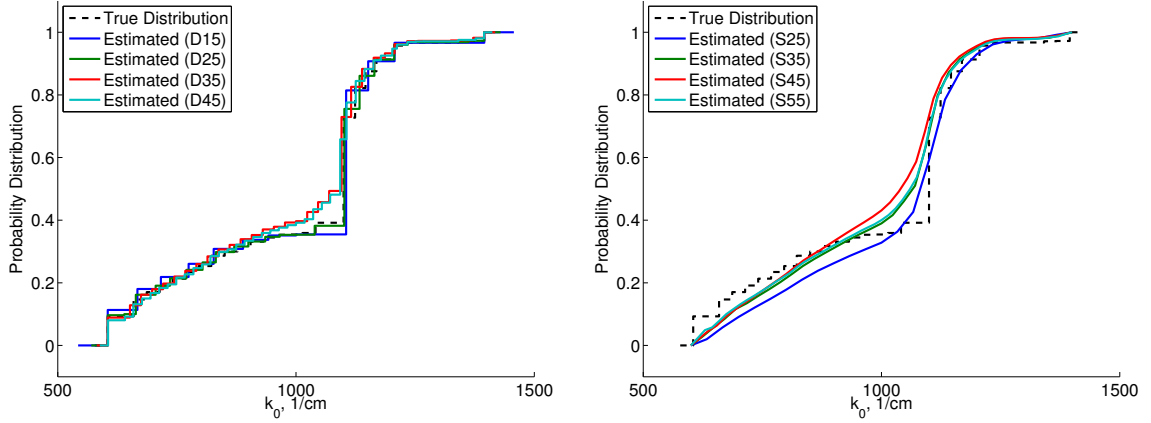


Figure 5.2: The estimated distributions to the simulated data using a discrete distribution using the Dirac approximation method with $M = 15, 25, 35$ and 45 nodes (left) and using the spline approximation method with $M = 25, 35, 45$ and 55 nodes (right).

estimated scalar parameters can be found in Table 5.1.

We see an interesting feature as M is increased using the Dirac approximation. With a low number of nodes, specifically for $M = 15$ and 25 , the estimation results match the true parameters and distribution very well. However, for M greater than 25 , the estimation results

begin to deviate from the true values. This is most likely due to an over parameterization of the problem. This increased freedom allows for the approximate model to begin to fit the noise present in the data.

Table 5.1: The estimated parameters using the Dirac and spline approximation methods for the discrete distribution.

Delta Approximation				Spline Approximation				Efimov Method		
M	ε_s	ε_∞	τ	M	ε_s	ε_∞	τ	J	ε_s	ε_∞
15	1.6187	1.3299	0.0142	25	1.7243	1.4931	0.0513	8	1.9850	1.6000
25	1.6055	1.3252	0.0164							
35	1.5707	1.2869	0.0192							
45	1.5668	1.2860	0.0194							
			45							
			55	1.7068	1.4502	0.0332				
q_0	1.6	1.32	0.017	q_0	1.6	1.32	0.017	q_0	1.6	1.32

Table 5.2: The estimated values of the intensities S_j , the relaxation times τ_j , the resonance wavenumbers k_{0j} and the standard deviations σ_j for each oscillator using the modified Efimov approach, using the simulated data with a discrete distribution.

Oscillator (j)	S_j	τ_j	k_{0j}	σ_j
1	6.2021e+04	0.0060	600.22	88.37
2	1.9846e+04	0.0135	839.29	56.89
3	1.6175e+02	0.0064	839.87	119.82
4	2.7413e+04	0.0968	1103.13	14.17
5	1.7871e+05	0.0124	1123.55	19.92
6	1.3596e+04	0.0317	1207.65	17.02

The estimated distribution using the spline method is not able to replicate the large jump at $k_0 = 1100 \text{ cm}^{-1}$, even when using as many as $M = 55$ nodes. However, in general, the estimated distributions are reasonable approximations to the true distribution. This result is somewhat unexpected since we only can guarantee convergence of the spline method if the probability density function is absolutely continuous [39]. The estimated scalar values are all over estimated, and in particular the estimated values of τ are not close to the true value. This is consistent with the results in [20], in which it was shown that it is extremely difficult to accurately estimate the relaxation time τ .

In Table 5.2 we give the estimated values for the individual oscillators using the modified

Efimov model. We expect to see an oscillator centered near 1100 cm^{-1} with a narrow broadening (i.e. a small standard deviation) to describe the jump discontinuity in the distribution. Indeed, we see that the *4th* oscillator is centered at $k_{0_4} = 1103.13 \text{ cm}^{-1}$ and has a standard deviation of $\sigma_j = 14.17$. Unexpectedly we also see that the *5th* and *6th* oscillators also have a narrow broadening. Furthermore, using the Efimov approach, it is difficult to associate the oscillator directly to the size of the jump discontinuity in the distribution, one must look at the magnitude of the intensity S_j relative to the other intensities to understand the relative “importance” of each oscillator. That is, from Table 5.2 we would deduce that the *5th* oscillator with an intensity on the order to 10^5 has more importance compared to the *3rd* oscillator which has an intensity of 10^2 three orders of magnitude lower.

Continuous Distribution

In this example we consider the case where the true distribution G_0 is taken as a truncated bivariate normal distribution with corresponding probability density function g_0 given by

$$G_0(k_0) = \frac{\beta}{\sigma_1 \sqrt{2\pi}} \exp\left(-\frac{(k_0 - \mu_1)^2}{2\sigma_1^2}\right) + \frac{\beta}{\sigma_2 \sqrt{2\pi}} \exp\left(-\frac{(k_0 - \mu_2)^2}{2\sigma_2^2}\right), \quad k_0 \in [\underline{k}_0, \bar{k}_0]. \quad (5.3.1)$$

In the above equation, we take $\mu_1 = 850 \text{ cm}^{-1}$, $\mu_2 = 1050 \text{ cm}^{-1}$, $\sigma_1 = 70$, $\sigma_2 = 60$, $\underline{k}_0 = 600 \text{ cm}^{-1}$, $\bar{k}_0 = 1400 \text{ cm}^{-1}$ and β is the normalizing constant

$$\beta^{-1} = \int_{\underline{k}_0}^{\bar{k}_0} \frac{1}{\sigma_1 \sqrt{2\pi}} \exp\left(-\frac{(k_0 - \mu_1)^2}{2\sigma_1^2}\right) + \frac{1}{\sigma_2 \sqrt{2\pi}} \exp\left(-\frac{(k_0 - \mu_2)^2}{2\sigma_2^2}\right) dk_0. \quad (5.3.2)$$

We expect that a CMC in an amorphous state would best be represented by a continuous distribution.

Table 5.3: The estimated parameters using the Dirac and spline approximation methods for the simulated data with a continuous distribution.

Delta Approximation				Spline Approximation				Efimov Method		
M	ε_s	ε_∞	τ	M	ε_s	ε_∞	τ	J	ε_s	ε_∞
10	1.4519	1.1613	0.0101	10	1.9299	1.7017	0.0264	2	1.5747	1.3013
15	1.4107	1.1239	0.0112	15	1.5768	1.3040	0.0156			
20	1.4011	1.1174	0.0116	20	1.5751	1.3074	0.0195			
25	1.3909	1.1090	0.0124	25	1.5717	1.3077	0.0261			
q_0	1.6	1.32	0.017	q_0	1.6	1.32	0.017	q_0	1.6	1.32

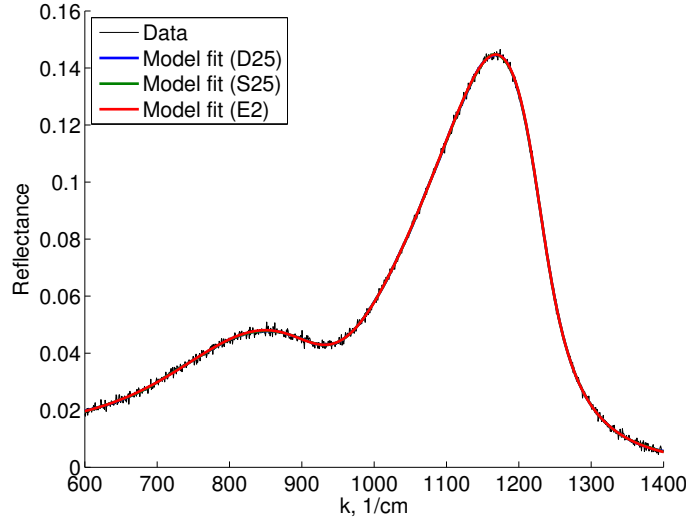


Figure 5.3: The model fits to the simulated data generated with a continuous distribution. For the Dirac and spline approximation schemes the number of nodes was taken as $M = 25$ (labeled as D25 and S25 respectively) and for the Efimov approach we have $J = 2$ (labeled as E2).

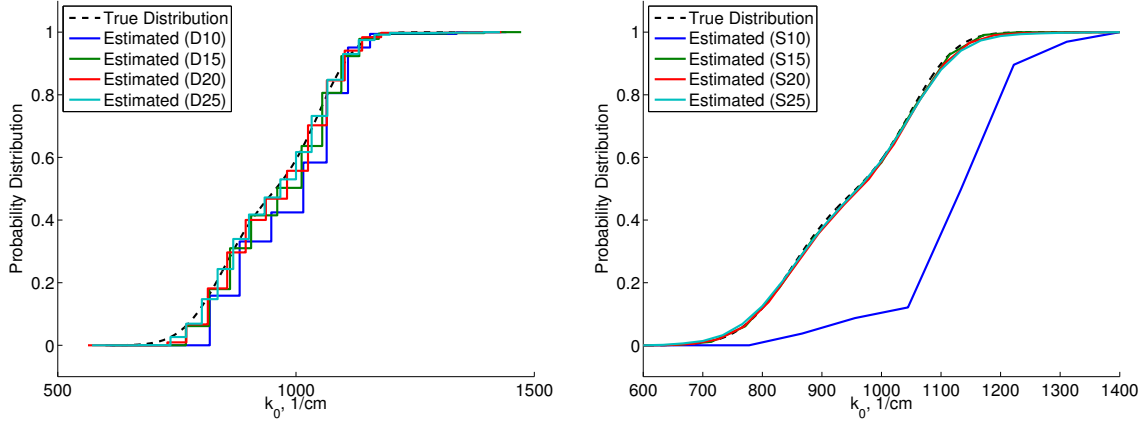


Figure 5.4: The estimated distributions to the simulated data using a continuous distribution using the Dirac approximation method (left) and using the spline approximation method (right). For both methods we chose the number of nodes to be $M = 10, 15, 20$ and 25 .

In Figure 5.3, we see that both PMF methods achieve a very good fit to the data where we set $M = 25$. Using the Dirac method, we see in Figure 5.4 that the estimated distribution using $M = 10$ nodes is shifted to the right of the true distribution. As M is increased, the estimated distribution becomes a reasonable approximation of the continuous distribution. The estimated distribution using the spline method gives an excellent approximation of the true distribution

Table 5.4: The estimated values of the intensities S_j , the relaxation times τ_j , the resonance wavenumbers k_{0j} and the standard deviations σ_j for each oscillator using the modified Efimov approach using the simulated data with a continuous distribution.

Oscillator (j)	$S_j(1 \times 10^5)$	τ_j	k_{0j}	σ_j
1	1.0170	0.0139	861.23	66.61
2	1.4794	0.0175	1057.06	60.07

except when $M = 10$. In this case, there simply are not enough elements in the approximation scheme to accurately fit the data. The Efimov approach is able to accurately fit the data with only $J = 2$ oscillators, which is not surprising since the true distribution is composed of two normal distributions.

From Table 5.3, we see that the constant parameters are more accurately estimated using the spline approximation scheme and the Efimov approach. However, again the value for τ is difficult to estimate correctly.

In Table 5.4 we see that we obtain a good estimate for the relaxation time for the second oscillator, but not for the first. The resonance wavenumbers and the standard deviations for both oscillators are a good estimation of the mean and standard deviations of the bivariate normal distribution.

5.3.2 Inorganic Glass Data

To compare our approximation methods on experimental data sets, we present results obtained using inorganic glass data available in [58]. These inorganic glasses have properties similar to the materials which comprise the matrix in many CMCs. For these data sets the incident angle is approximately $\phi \approx 0^\circ$.

Vitreous Silica

We first consider reflectivity data collected from Vitreous Silica in the 200 to 1350 cm^{-1} range (see Table A2 in [58]). In Figure 5.5 we present the model fits to the data using the Dirac and spline approximations with $M = 50$ for both methods and using the modified Efimov method with $J = 8$. We see that all of the methods are able to obtain a good fit to the data.

In Figure 5.6 we present the estimated distributions using both PMF methods. It is clear the the Dirac method gives consistent results for $M = 30, 50$ and 80, indicating that the method has converged for a relatively low value of M . The spline method gives consistent results for $M = 50$ and 80; the distribution obtained using $M = 30$ has the same general characteristic shape as the other two distributions, but it is clearly an outlier. Thus, we may assume that the spline method has not converged at $M = 30$, but has by $M = 50$. In fact, once both methods have

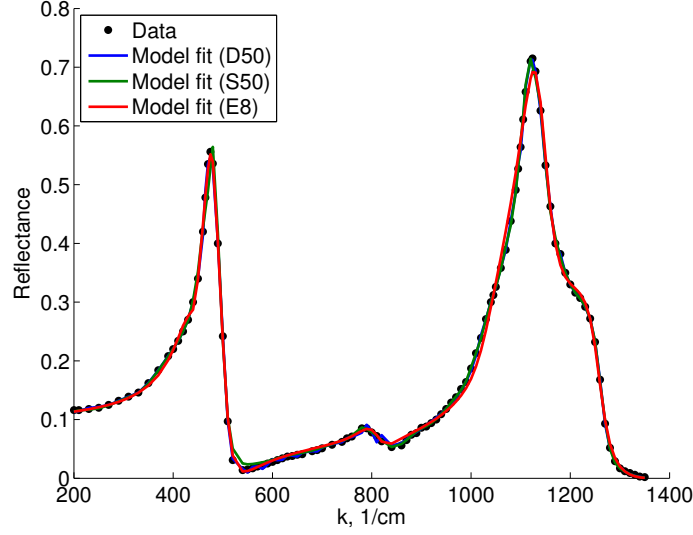


Figure 5.5: The model fits to the Vitreous Silica data.. For the Dirac and spline approximation schemes the number of nodes was taken as $M = 50$ (labeled as D50 and S50 respectively) and for the Efimov approach we have $J = 8$ (labeled as E8).

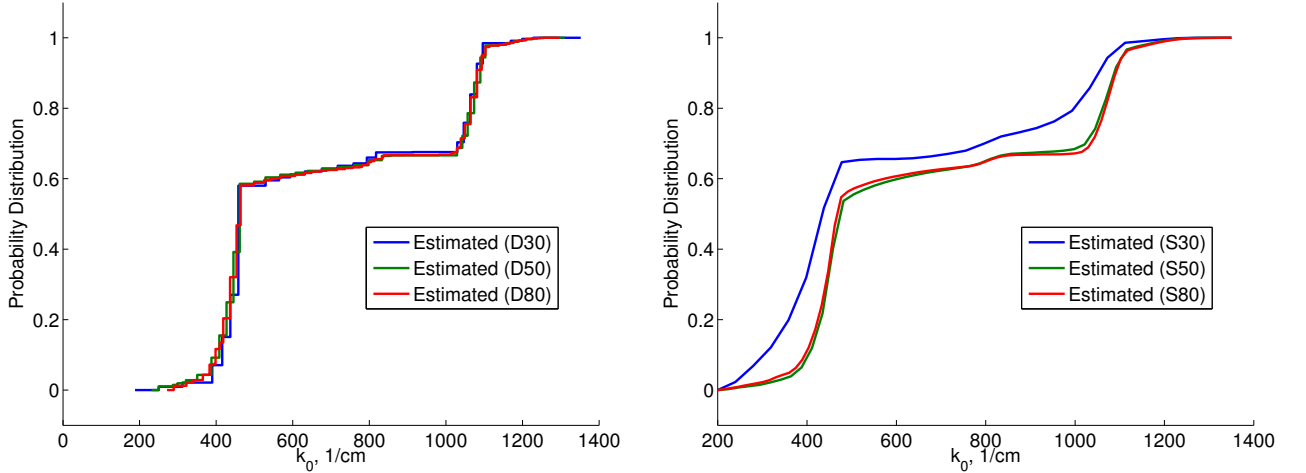


Figure 5.6: The estimated distributions to the Vitreous Silica data using the Dirac approximation method (left) and using the spline approximation method (right). For both methods we chose the number of nodes to be $M = 30, 50$ and 80 .

converged, they have converged to the same distribution. Although the estimated distribution has large jumps near $k_0 = 400 \text{ cm}^{-1}$ and 1050 cm^{-1} , we again see the surprising result that the spline approximation method is able to handle these regions of rapid change in the distribution.

In Table 5.5, we present the estimated parameter values using both PMF methods. Notice

Table 5.5: The estimated parameter values using the Dirac and spline approximation methods to fit the Vitreous Silica data. The “true” parameter values θ_0 are the experimental values taken from [65].

Delta Approximation				Spline Approximation				Efimov Method		
M	ε_s	ε_∞	τ	M	ε_s	ε_∞	τ	J	ε_s	ε_∞
30	3.7535	2.0845	0.0398	30	3.3489	1.5553	0.1032	8	3.7530	2.1384
50	3.7183	2.0487	0.0522	50	3.7079	2.0581	0.2020			
80	3.6780	2.0153	0.0564	80	3.7019	2.0675	0.1851			
q_0	3.8	2.1		q_0	3.8	2.1		q_0	3.8	2.1

Table 5.6: The estimated values of the intensities S_j , the relaxation times τ_j , the resonance wavenumbers k_{0j} and the standard deviations σ_j for each oscillator using the modified Efimov approach on the Vitreous Silica data.

Oscillator (j)	$S_j(1 \times 10^5)$	τ_j	k_{0j}	σ_j
1	3.6176e+03	0.0183	311.63	66.62
2	1.4231e+05	0.0190	435.59	4.89
3	4.4941e+04	0.8445	459.17	8.71
4	1.8884e+04	0.0165	677.56	87.54
5	2.7526e+04	0.0282	806.88	9.48
6	1.4019e+03	0.0178	1014.97	34.98
7	5.2605e+05	1.6468	1077.90	21.29
8	1.1559e+05	0.0373	1166.09	46.83

that the estimated values of ε_s and ε_∞ are very similar for $M = 30$, 50 and 80 using the Dirac approximation method. However, the values for ε_s and ε_∞ using the spline method do not match the values obtained using the Dirac approximation at $M = 30$, but do for $M = 50$ and 80. Thus, again indicating that the Dirac method converges for a lower value of M than the spline method. We also see that the high and low frequency limits are well approximated by the modified Efimov method.

The estimated values of the individual oscillators using the modified Efimov method are given in Table 5.6. The 2nd, 3rd and 5th oscillators, centered at approximately 435, 459 and 806 cm^{-1} , respectively, each have a very narrow broadening. The 2nd and 3rd oscillators correspond to the first large jump in the estimated distribution using the PMF methods. The 5th oscillator is present in a region where the estimated distribution does not contain a sharp jump.

Vitreous Germania

We next consider reflectivity data collected from Vitreous Germania in the 200 to 1350 cm^{-1} range (see Table A7 in [58]). In Figure 5.7 we present the model fit and the estimated distributions

using both the Dirac and spline methods with $M = 50$ and using the modified Efimov method with $J = 8$. Once again, we obtain very good fits to the data in all cases.

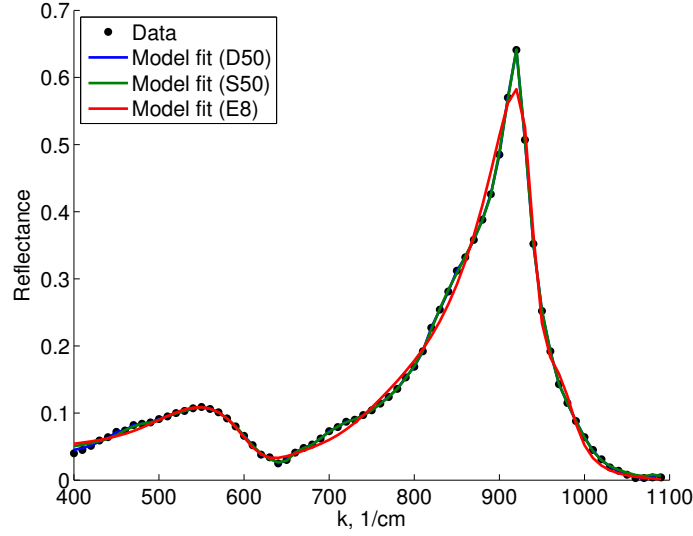


Figure 5.7: The model fits to the Vitreous Germania data. For the Dirac and spline approximation schemes the number of nodes was taken as $M = 50$ (labeled as D50 and S50 respectively) and for the Efimov approach we have $J = 8$ (labeled as E8).

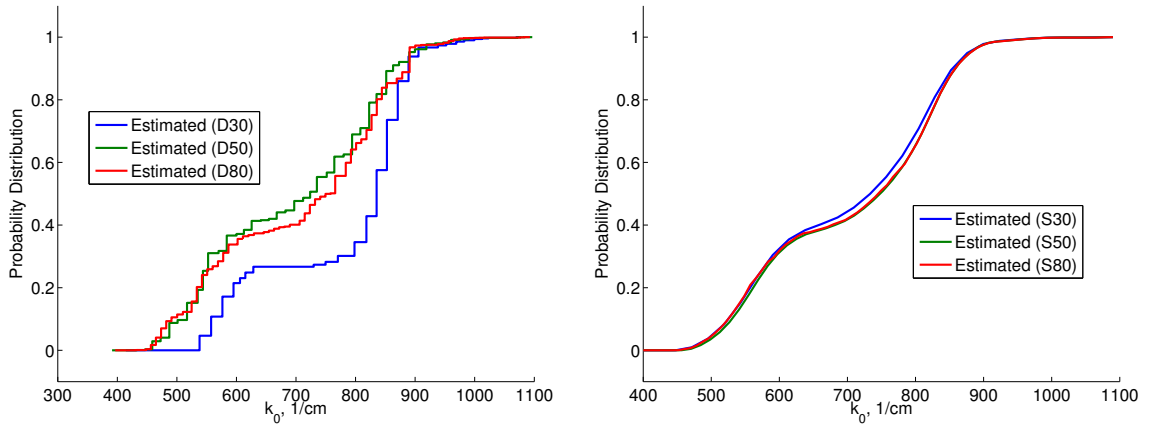


Figure 5.8: The estimated distributions to the Vitreous Germania data using the Dirac approximation method (left) and using the spline approximation method (right). For both methods we chose the number of nodes to be $M = 30, 50$ and 80 .

From Figure 5.8 we see that each estimation using the spline method gives consistent results, and the estimation with $M = 30$ using the Dirac method does not match the results using $M = 50$ and 80. In this case, the results suggest that the spline method converges for a lower number of nodes than the Dirac method, but both methods do converge to the same distribution. This should be expected since it appears as if the estimated distribution is sufficiently smooth, and it is known [39] that the spline method will outperform the Dirac method in this case.

In Table 5.7 we present the estimated parameter values for both methods. This time we see that the spline method gives consistent values for ε_s and ε_∞ , whereas for $M = 30$, the values estimated using the Dirac method are the outliers. The estimated values for ε_s and ε_∞ using the modified Efimov approach are slightly higher than the estimates using the PMF methods.

Table 5.7: The estimated parameter values using the Dirac and spline approximation methods to fit the Vitreous Germania data.

Delta Approximation				Spline Approximation				Efimov Method		
M	ε_s	ε_∞	τ	M	ε_s	ε_∞	τ	J	ε_s	ε_∞
30	2.3992	1.7707	0.0779	30	2.0034	1.3320	0.4989	8	2.1844	1.5200
50	1.8961	1.3013	0.7741	50	2.0567	1.3854	0.2581			
80	1.9068	1.3435	0.6250	80	2.0254	1.3659	0.4964			

Table 5.8: The estimated values of the intensities S_j , the relaxation times τ_j , the resonance wavenumbers k_{0j} and the standard deviations σ_j for each oscillator using the modified Efimov approach on the data obtain from Vitreous Germania.

Oscillator (j)	$S_j(1 \times 10^5)$	τ_j	k_{0j}	σ_j
1	1.5434e+03	0.0159	511.79	68.73
2	2.6232e+03	0.0178	540.71	51.28
3	5.9389e+04	0.1661	565.51	35.91
4	4.4435e+04	0.0160	696.72	68.21
5	1.4581e+05	0.6777	812.01	40.25
6	9.9376e+04	1.1347	852.97	30.93
7	6.1715e+02	0.0157	940.72	69.75
8	7.1409e+03	0.4162	958.32	19.93

In Table 5.8 we present the individual oscillator estimates obtain from the modified Efimov approach. In this case we see that the only oscillator which has a somewhat narrow broadening is present at 958 cm^{-1} . This oscillator has an intensity of 10^3 , two orders of magnitude lower than

the largest estimated intensity. This indicates that the modified Efimov approach agrees with the results seen using the PMF, that there are no sharp jumps in the resonance wavenumber which characterize the Vitreous Germania data.

Sodium Silicate

As a final consideration, we use reflectivity data collected from Sodium Silicate in the 40 to 1260 cm^{-1} range (see Table A3 in [58]). In Figure 5.9 we give the model fit to the data and the estimated distributions using the Dirac and spline approximation schemes using $M = 25$ and using the modified Efimov approach with $J = 9$.

We see that the estimated distributions using both methods agree very well for the relatively low number of nodes, and the agreement is increased for $M = 30$ as is seen from Figure 5.10. Additionally, in Table 5.9 we see that the estimated values of ε_s and ε_∞ agree well for $M = 30$. Thus, it appears in this case that both the spline and Dirac approximation methods have converged at a relatively low number of nodes. It should be noted, that for this particular data set, there were 62 data points, which is why we did not use a larger number of nodes than $M = 30$. Using the modified Efimov approach, the estimated value of ε_∞ is consistent with the results using the PMF, but the value of ε_s does not match.

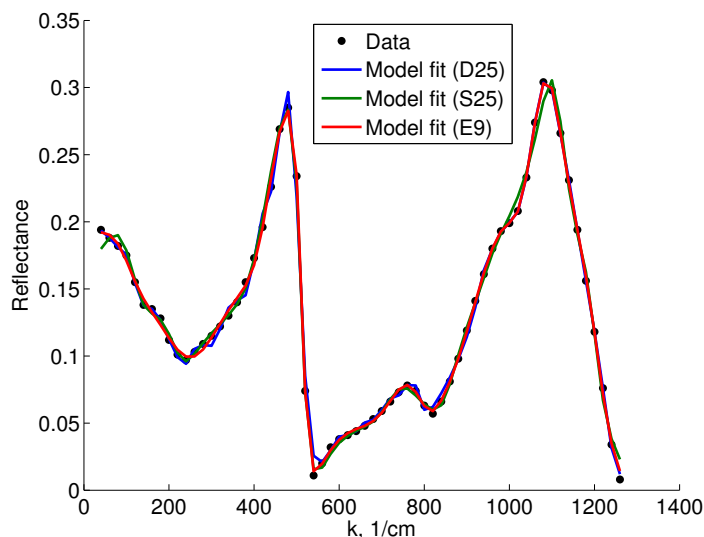


Figure 5.9: The model fits to the Sodium Silicate data. For the Dirac and spline approximation schemes the number of nodes was taken as $M = 25$ (labeled as D25 and S25 respectively) and for the Efimov approach we have $J = 9$ (labeled as E9).

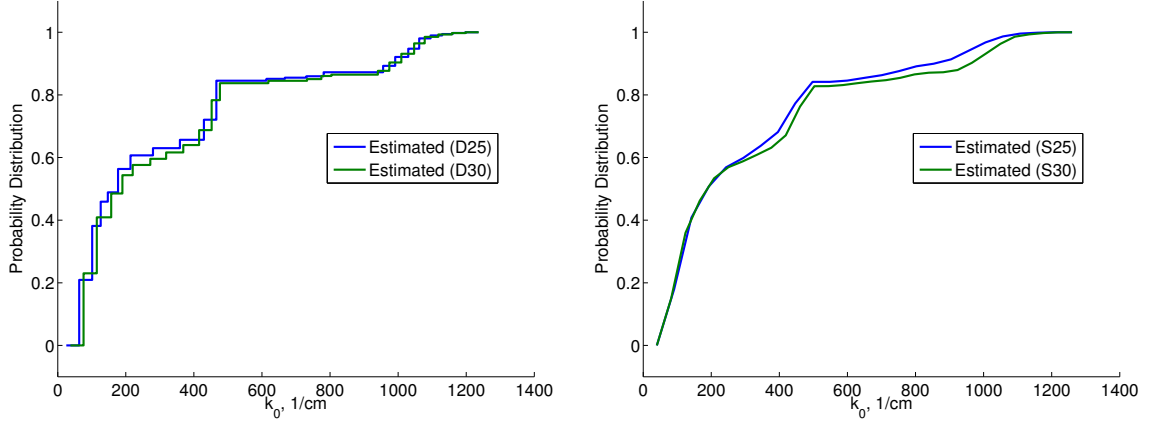


Figure 5.10: The estimated distributions to the Sodium Silicate data using the Dirac approximation method (left) and using the spline approximation method (right). For both methods we chose the number of nodes to be $M = 25$ and 30 .

Table 5.9: The estimated parameter values using the Dirac and spline approximation methods as compared to the Efimov method to fit the Sodium Silicate Silica data.

Delta Approximation				Spline Approximation				Efimov Method		
M	ε_s	ε_∞	τ	M	ε_s	ε_∞	τ	J	ε_s	ε_∞
25	6.3266	2.1110	0.0200	25	5.7623	1.5496	0.0269	9	7.4048	2.1179
30	5.9747	2.0939	0.0240	30	5.9068	1.9573	0.0305			

Table 5.10: The estimated values of the intensities S_j , the relaxation times τ_j , the resonance wavenumbers k_{0_j} and the standard deviations σ_j for each oscillator using the modified Efimov approach on the Sodium Silicate data.

Oscillator (j)	$S_j(1 \times 10^5)$	τ_j	k_{0_j}	σ_j
1	8.7256e+03	0.0191	95.82	24.06
2	3.7072e+04	0.0208	187.11	62.71
3	7.1957e+04	0.0292	412.24	53.15
4	9.0464e+04	0.0764	459.40	23.43
5	2.6822e+04	0.0279	638.16	53.20
6	3.9439e+04	0.0491	778.93	29.66
7	1.8828e+05	0.5529	986.26	40.27
8	2.7424e+05	0.0154	1057.79	13.43
9	9.9229e+04	0.0775	1122.55	65.13

In Table 5.10 we present the estimation results for the oscillators using the modified Efimov approach. In this case, the oscillator with the most narrow broadening is the $8th$ oscillator which is centered at 1057 cm^{-1} . This oscillator corresponds to a region of relatively gradual increase

in the estimated distribution.

5.4 Concluding Remarks and Future Work

Two contrasting methods of modeling the complex permittivity of a material in which the number of dielectric mechanisms is unknown were compared in this chapter. Using the PMF, we imposed a distribution on the resonance wavenumber and considered two approximation schemes for estimating the unknown distribution. We also considered a method which uses a convolution of Lorentz and Gaussian functions, the modified Efimov approach. We considered both simulated and experimental data sets. Within the context of the PMF, it is clear that considering the model fits alone are not sufficient to determine which approximation scheme to use, since both consistently give good model fits even if the estimated distributions vary. It is not surprising that the Dirac methods are better suited to estimate a discontinuous distribution and that the spline method are better suited to handle estimating a continuous distribution. In practice of course, there in general is no prior knowledge as to the form of the unknown distribution (continuous or discontinuous). Fortunately, we have illustrated in the examples presented in this work that the spline approximation method gives reasonable estimates even for the cases where the true distribution possesses discontinuities. Thus, it is our recommendation that initially both methods should be used to do the inverse problem. Once it is established that the estimated distributions using both methods sufficiently agree, then the results obtained using the lowest number of nodes possible to achieve this agreement should be used. This should minimize any effects of over parameterization. Only after the distributions agree should the decision be made as to whether the distribution appears to obtain discontinuities. If discontinuities (or regions of relative rapid change) are present in the distribution, then the results using the Dirac method would be preferred, and the results from the spline approximation would be preferred for distributions which appear continuous in nature.

Using the modified Efimov method, we were also able to obtain very good model fits to the data for both the simulated data and the inorganic glass data. It was seen that using this approach, regions of rapid increase in the distribution will correspond to oscillators with a narrow broadening. However, one pitfall to this approach is the difficulty in ascertaining the relative “importance” of each oscillator, for which the only indication is the estimated intensity. One advantage that the PMF approach has over the modified Efimov approach is that the estimated distribution can easily be interpreted. Furthermore, there is a strong theoretical foundation for the PMF approximation schemes to converge as $M \rightarrow \infty$ (with the assumption that the density function is absolutely continuous in the case of using splines), however, there is no known sense of convergence as $J \rightarrow \infty$ in the Efimov approach.

In the following chapter, we consider experimental data sets obtained from CMCs which

have undergone various levels of heat treatment and attempt to use the methods described here to ascertain levels of degradation. Additionally, we concern ourselves with the mathematical and statistical model discrepancy present in this problem, and use this in an effort to appropriately quantify the uncertainty in the probability distribution estimators.

Quantifying the Degradation in Thermally Treated Ceramic Matrix Composites

In this chapter we focus on a silicon nitride carbon based CMC in which our collaborators at Wright-Patterson Air Force Base have a specific interest. This SiC/SiCN CMC has a silicon carbon fiber and a silicon nitride carbon matrix. Exposure to high temperature environments induces oxidation in the CMC, producing SiO_2 and SiN . The contents of this chapter are based on a manuscript which has been accepted for publication [17]:

H.T. Banks, J. Catenacci, and A. Criner. Quantifying the degradation in thermally treated ceramic matrix composites. *The 17th International Symposium on Applied Electromagnetics and Mechanics (ISEM2015)*. (in press).

6.1 Introduction

Data sets have been provided by researchers at the Air Force Research Lab at Wright-Patterson Air Force Base, which were collected using a Bruker Vertex 80V FTIR spectrometer. CMC samples were placed in a 1200°C oven for either 10 or 100 hours, then the reflectance was measured. Three samples, sample 4, 16, and 32, underwent the heat treatment for 10 hours, and two samples, sample 1 and 13, underwent the heat treatment for 100 hours. The dimensions of the samples were $15.7 \times 1.3 \times 0.2$ cm. Each sample was divided along its length into 11 blocks of equal area, and three measurements were taken within each block for a total of 33 measurements per sample (typically the measurements contain greater than 200 data points). Since the beam width of the interrogating electromagnetic wave is significantly smaller than

the size of each block, we assume that each of the three measurements within each block are spatial independent. An example data set from sample 4 and sample 1 is given in Figure 6.1. It is known that SiN will give peaks at approximately 640 and 1200 cm^{-1} , and SiO₂ will give peaks at approximately 800 and 1080 cm^{-1} , and for both data sets we see peaks in these regions. Yet, it is not possible to ascertain from the data alone how much SiN or SiO₂ is present, or how much oxidation has occurred. To aid in this analysis we will develop a mathematical model for the reflectance, and through an inverse problem we will fit the mathematical model to the experimental data to obtain parameter estimates for each data set. We will then show that we can detect differences in the estimated model inputs resulting from the inverse problem using data collected from the samples which underwent different lengths of heat exposure.

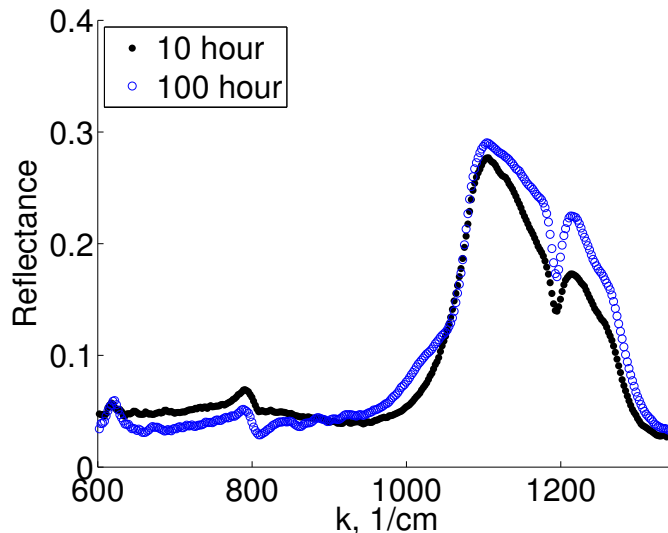


Figure 6.1: Example reflectance data sets from sample 4 which was heat treated for 10 hours (the black dots) and from sample 1 which was heat treated for 100 hours (the blue circles).

6.2 The Model for the Complex Permittivity and the Reflectance

Due to the heterogeneous structure of the CMCs, which we would like to characterize, we precede as in the previous chapters by imposing a distribution on the resonance wavenumber in the permittivity model. Treating the resonance wavenumber in this way allows us to account for the contributions from different molecular components of the material. Therefore, to allow for a distribution G of resonance wavenumbers over an admissible set $\mathcal{K} \subset \mathbb{R}$, we generalize the

relative permittivity for the Lorentz model to be

$$\widehat{\varepsilon}_r(k; G, q) = \varepsilon_\infty - \int_{\mathcal{K}} \frac{k_p^2}{k^2 - ik/\tau - k_0^2} dG(k_0), \quad (6.2.1)$$

where $G \in \mathcal{P}(\mathcal{K})$, the set of admissible probability measures on \mathcal{K} and $q = (\varepsilon_s, \varepsilon_\infty, \tau)^T \in \mathcal{Q}_\alpha \subset \mathbb{R}^3$, where \mathcal{Q}_α is compact.

The data we consider in this document is obtained at an incident angle of $\phi = 45^\circ$, therefore we further assume that the reflectance is composed of the parallel and perpendicular polarizations in equal weights. Thus, we make use of the equation for the reflectivity given by (5.2.5)–(5.2.7).

6.3 Interferogram to Spectrum

An FTIR spectrometer does not measure the reflectance spectrum (given in percent reflectance) directly; rather an interferogram (measure of intensity) is collected. This is then converted to a reflectance spectrum. An interferogram can be single sided or double-sided. A single sided interferogram is the result of measuring only on one side of zero path difference (ZPD), whereas a double sided interferogram is collected by measuring both sides of the ZPD. Additionally, the data can be acquired during forward movement of the mirror only or during forward and backward movement of the mirror, which results in a single-direction or bi-directional interferogram, respectively. Here, we will consider the case of a double sided, bi-directional interferogram. We give an example of such an interferogram in Figure 6.2, the two large spikes in signal are the ZPD, the first being measured during the forward mirror movement, the second during the backward mirror movement.

Reflectance data sets were provided by the Air Force Research Lab at Wright-Patterson Air Force Base which we collected using a Bruker Vertex 80V FTIR spectrometer. Here we will detail the process used by the software on the instrument to convert the interferograms to a spectrum.

An interferogram contains out-of-phase elements, which are a results of optical path differences in the spectrometer. In order for the spectrum to be photometrically accurate, the data must be phase corrected. When using a bi-directional interferogram, each half of the interferogram needs to be phase corrected separately. The most common phase correction method is the Mertz method, which we describe here. The first step is to apodize the interferogram, this was done using a three-term Blackman-Harris window function. Then the data is zero padded using a zerofilling factor of 8 (the number of data points was multiplied by 8, then zero filled until the next power of 2 is reached). The data is then shifted about its maximum value and a FFT is

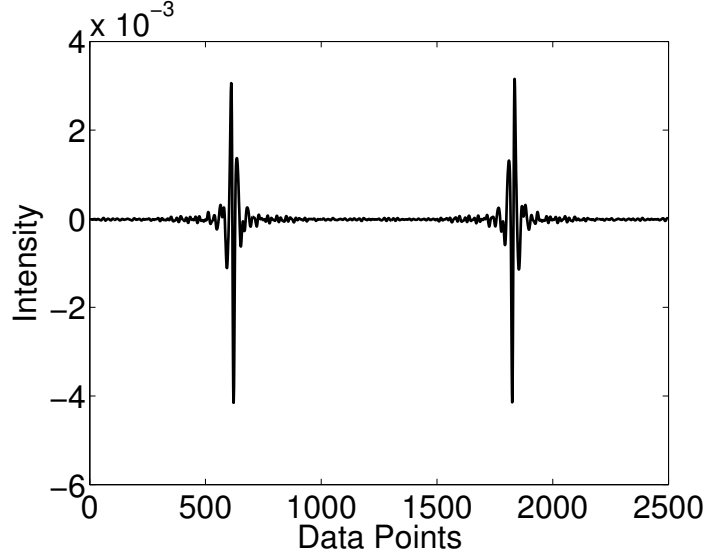


Figure 6.2: Double sided, bi-directional interferogram.

taken resulting a complex signal Y . The phase curve is computed by

$$\phi = \arctan \frac{Im(Y)}{Re(Y)}, \quad (6.3.1)$$

where $Re(Y)$ and $Im(Y)$ are the real and imaginary parts of Y , respectively. Finally, the spectrum, B , is computed by

$$B = Re(Y) \cos \phi + Im(Y) \sin \phi. \quad (6.3.2)$$

Once both halves of the interferogram are converted into a spectrum separately, the spectrums are averaged together.

In order to obtain reflectance data of a sample, two interferograms are collected, one from the sample (the sample interferogram), and one with the sample removed (the reference interferogram). Then the reflectance data is obtained by taking the ratio of the spectrum computed from the sample and reference interferograms. For further details on converting an interferogram to a spectrum and using this to obtain the reflectance, see [66, Section 4.3].

6.3.1 Measurement Errors

Since we are interested in quantifying the uncertainty in the estimates resulting from the inverse problem, we must understand the measurement error process in order to correctly specify a statistical model. Because an FTIR spectrometer does not directly measure the reflectance,

we must take extra care to avoid as much as possible altering the measurement errors in the conversion of the interferograms to the spectrum. To illustrate some of the possible pitfalls, we give the estimated measurement errors in the reflectance data obtained using three different methods of converting the interferograms to reflectance. The measurement errors are estimated using a second order difference

$$\hat{\nu}_j = \frac{1}{\sqrt{6}}(y_{j-1} - 2y_j + y_{j+1}), \quad (6.3.3)$$

where the $\{y_j\}$ are the observed data (see [73, 92] for further details) where as usual endpoints are formed with one-sided differences.

There are several methods one might use to preprocess the data. This first method is the method used by the software associated with the Bruker Vertex 80V (the method described in detail above), in which a zerofilling factor of 8 was used, and the spectrums from the first and second ZPD are averaged. In Figure 6.3 we see that the estimated measurement errors using this method exhibit an oscillatory behavior. The second method, which we consider, also uses a zerofilling factor of 8, but this time only the spectrum from the first ZPD is used. The estimated measurement errors, shown in Figure 6.4, again have oscillations present, however the magnitude of the errors is more consistent in the middle of the interrogating range. The final method we consider uses no zero padding, and only uses the spectrum from the first ZPD. In Figure 6.5, we now see that the estimated measurement errors do not have any oscillations present, and the magnitude of the error is fairly consistent throughout the entire wavenumber sample, with slightly larger errors occurring at the ends of the interrogating range. For this reason, for the remainder of the results we present here, we use the third method in which there is no zero padding and only the spectrum from the first ZPD is used.

6.4 Inverse Problem

6.4.1 Statistical Model

In the previous section we observed that if we do not zero pad the interferogram and only use the spectrum from the first ZPD, we can avoid the oscillations in the plots of the estimated measurement errors. However, in Figure 6.5, we see that the estimated measurement errors are larger at the two ends of the data set, near 600 and 1600 cm^{-1} . Additionally, if we inspect more closely, we see that the measurement errors increase in magnitude near 850, 1050, and 1200 cm^{-1} . In Figure 6.6 we show the estimated measurement errors for a typical data set obtained from the 100 hour heat treated sample 1. In this case, it is even more clear that we cannot assume our data sets contain measurement errors which are independent and identically

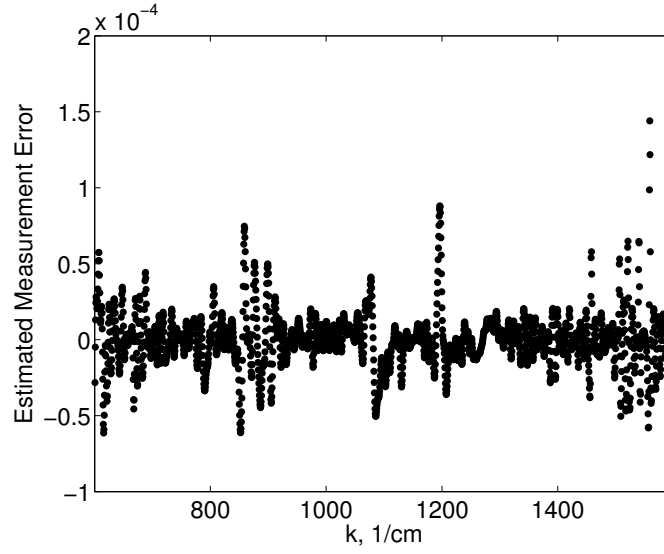


Figure 6.3: Estimated measurement error, in percent reflectance, obtained when using a zerofilling factor of 8 and averaging the spectrum from first and second ZPD.

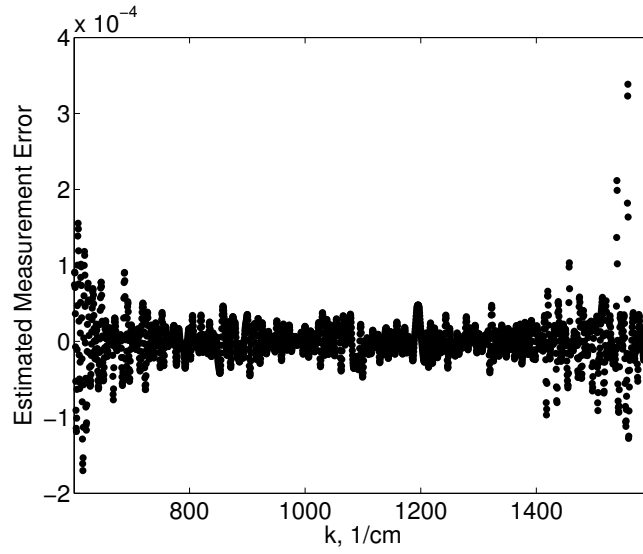


Figure 6.4: Estimated measurement error obtained, in percent reflectance, when using a zerofilling factor of 8 and using only the spectrum from first ZPD.

distributed (i.i.d.). Thus, we need to take care in choosing an appropriate statistical model so that we can carryout a meaningful uncertainty quantification.

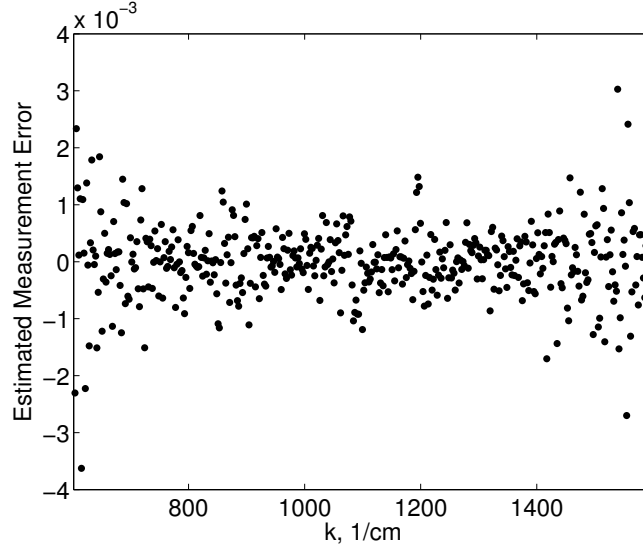


Figure 6.5: Estimated measurement error obtained, in percent reflectance, when using no zero padding and using only the spectrum from first ZPD.

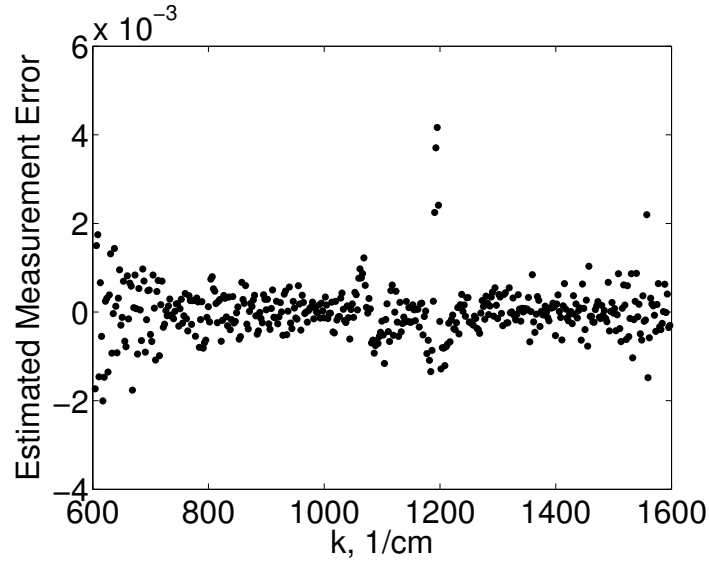


Figure 6.6: Estimated measurement error from a data set from Sample 1 obtained when using no zero padding and using only the spectrum from first ZPD.

We consider a weighted error statistical model of the form

$$Y_j = R(k_j; G_0, q_0) + w_j \mathcal{E}_j, \quad j = 1, 2, \dots, N. \quad (6.4.1)$$

In the above equation Y_j is a random variable which is composed of the reflectance with G_0 the

nominal or “true” probability measure and q_0 the nominal or “true” parameters at a sampling wavenumber k_j , and the measurement error \mathcal{E}_j with weight w_j . For simplicity, we consider that the errors \mathcal{E}_j are independent and identically distributed random variables with mean 0 and constant variance σ_0^2 and realizations ϵ_j . We must choose the weights w_j in a way which represents our knowledge of the measurement errors present in the data collection process. The increase in the magnitude of the estimated measurement errors, which occurs at the beginning and end of the data set, could be a result of the measurements occurring at the fringes of the detector’s capabilities in the spectrometer. The larger measurement errors which occur near 1050 and 1200 cm^{-1} , and near 850 cm^{-1} in some of the data sets, correspond to regions of rapid change in the magnitude of the reflectance signal. With this in mind we choose the weights as

$$w_j = c_1(k_j - \bar{k})^2 + c_2|y''(k_j)| + 1, \quad j = 1, 2, \dots, n. \quad (6.4.2)$$

where \bar{k} is the center of the interrogating wavenumber interval, $y''(k_j)$ is the second derivative of the reflectance data, and c_1 and c_2 are scaling parameters. The second derivative is calculated using central differences for the interior points, and single sided differences for the end points. Figure 6.7 presents the weights w_j and the estimated measurement errors which are now computed by $\hat{\eta}_j = w_j^{-1}\hat{\nu}_j$, where $\hat{\nu}_j$ is given in (6.3.3), $c_1 = 1.5/(600 - \bar{k})$, and $c_2 = 7 \times 10^3$. From here we see that the values $\hat{\eta}$ form an approximate horizontal band centered about 0 as desired.

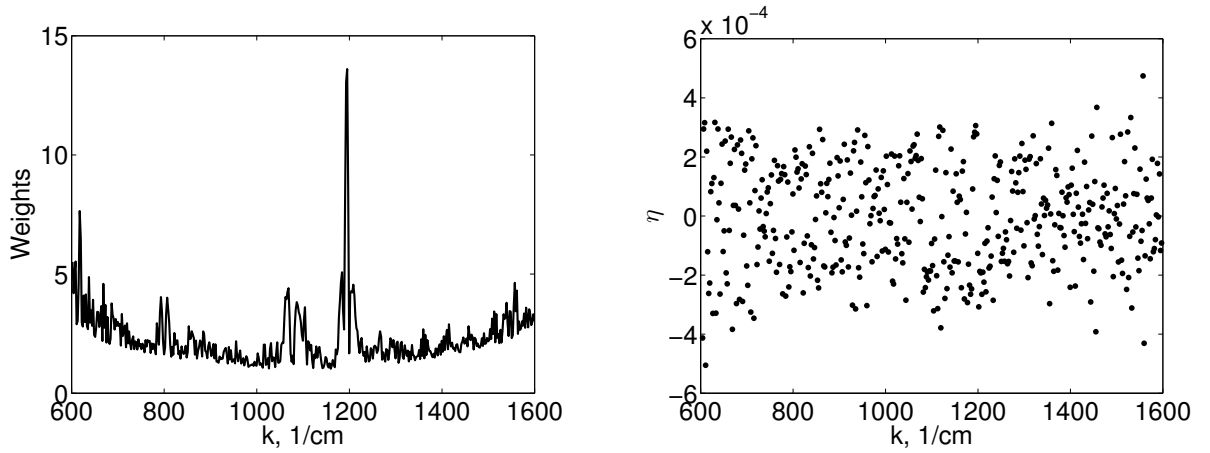


Figure 6.7: Plot of the weights w_j (left) and $\hat{\eta}_j = w_j^{-1}\hat{\nu}_j$ (right) for the 100 hour heat treated sample 1.

6.4.2 Weighted Least Squares

With the assumptions we have made for the measurement errors in the statistical model, the estimators $\theta = (G, q^T)^T = (G, \epsilon_s, \epsilon_\infty, \tau)^T$ can be obtained through a weighted least squares formulation

$$\theta_{WLS} = \arg \min_{(G, q) \in (\mathcal{P}(\mathcal{K}) \times \mathcal{Q}_\alpha)} J(Y; \theta), \quad (6.4.3)$$

with realizations

$$\hat{\theta}_{WLS} = \arg \min_{(G, q) \in (\mathcal{P}(\mathcal{K}) \times \mathcal{Q}_\alpha)} J(y; \theta). \quad (6.4.4)$$

In the above equation, the cost functional J is defined as

$$J(y; \theta) = \sum_{j=1}^N w_j^{-2} (R(k_j; \theta) - y_j)^2 \quad (6.4.5)$$

where y_j is a realization of Y_j , $j = 1, \dots, N$ in (6.4.1).

That is,

$$y_j = R(k; G_0, q_0) + w_j \epsilon_j, \quad j = 1, 2, \dots, N, \quad (6.4.6)$$

with ϵ_j a realization of \mathcal{E}_j .

We note that (6.4.3) is an infinite-dimensional optimization problem. Thus, we need to approximate the infinite dimensional space $\mathcal{P}(\mathcal{K})$ with a finite dimensional space $\mathcal{P}^M(\mathcal{K})$ in order to have a computationally tractable finite-dimensional optimization problem

$$(G_M, q)_{WLS} = \operatorname{argmin}_{(G_M, q) \in (\mathcal{P}^M(\mathcal{K}) \times \mathcal{Q}_\alpha)} J(Y; G_M, q). \quad (6.4.7)$$

We will consider the finite-dimensional $\mathcal{P}_S^M(\mathcal{K})$, a space defined using piecewise linear splines, to approximate $\mathcal{P}(\mathcal{K})$. We define this space as

$$\mathcal{P}_S^M(\mathcal{K}) = \left\{ G_M \in \mathcal{P}(\mathcal{K}) \left| G'_M = \sum_{m=1}^M \alpha_m l_m(k_0), \text{ where } \alpha_m \geq 0 \text{ and } \sum_{m=1}^M \alpha_m \int_{\mathcal{K}_m} l_m(\xi) d\xi = 1 \right. \right\} \quad (6.4.8)$$

where l_m is the m th linear spline element with support \mathcal{K}_m . With this we have reduced the infinite-dimensional problem to a finite-dimensional problem in which we only need to estimate q and the weights $\alpha = \{\alpha_m\}_{m=1}^M$. This leads to the minimization problem

$$(\hat{\alpha}, \hat{q}) = \arg \min_{(\alpha, q) \in (\mathbb{R}_S^M \times \mathcal{Q}_\alpha)} J(y; G_M, q), \quad G'_M = \sum_{m=1}^M \alpha_m l_m(k_0) \quad (6.4.9)$$

where

$$\mathbb{R}_S^M = \left\{ \boldsymbol{\alpha} = (\alpha_1, \alpha_2, \dots, \alpha_M)^T \mid \alpha_m \geq 0, \text{ and } \sum_{m=1}^M \alpha_m \int_{\mathcal{K}_m} l_m(\xi) d\xi = 1 \right\}.$$

Unfortunately, sample calculations (see below) reveal that this inverse problem is ill-posed, due to a lack of identifiability in the parameters. To resolve this issue we re-parameterize the permittivity model as follows. Using the spline approximation scheme, we have the model for the complex permittivity

$$\widehat{\varepsilon}_r(k; \{\alpha_m\}_{m=1}^M, q) = \varepsilon_\infty - \sum_{m=1}^M \alpha_m \int_{\mathcal{K}_m} \frac{(\varepsilon_s - \varepsilon_\infty) k_0^2}{k^2 - ik/\tau - k_0^2} l_m(k_0) dk_0. \quad (6.4.10)$$

Let $\beta_m = (\varepsilon_s - \varepsilon_\infty) \alpha_m$. Then the permittivity model is transformed into

$$\widehat{\varepsilon}_r(k; \{\beta_m\}_{m=1}^M, q_\beta) = \varepsilon_\infty - \sum_{m=1}^M \beta_m \int_{\mathcal{K}_m} \frac{k_0^2}{k^2 - ik/\tau - k_0^2} l_m(k_0) dk_0, \quad (6.4.11)$$

where $q_\beta = (\varepsilon_\infty, \tau)^T \in \mathcal{Q}_\beta \subset \mathbb{R}^2$. Observe that the constraint

$$\sum_{m=1}^M \alpha_m \int_{\mathcal{K}_m} l_m(\xi) d\xi = 1$$

becomes

$$\varepsilon_\infty + \sum_{m=1}^M \beta_m \int_{\mathcal{K}_m} l_m(\xi) d\xi = \varepsilon_s, \quad (6.4.12)$$

which can be enforced after the optimization has been performed. Therefore we have transformed the constrained optimization problem (6.4.9) into an unconstrained optimization problem given by

$$(\widehat{\boldsymbol{\beta}}, \widehat{q}_\beta) = \underset{(\boldsymbol{\beta}, q_\beta) \in (\mathbb{R}_S^N \times \mathcal{Q}_\beta)}{\operatorname{argmin}} J(y; G_M, q_\beta), \quad G'_M = \sum_{m=1}^M \beta_m l_m(k_0). \quad (6.4.13)$$

6.4.3 Uncertainty Quantification

The standard weighted least squares estimator θ_M , where we define $\theta_M = (\boldsymbol{\beta}^T, q_\beta^T)$ to be the vector of all the model parameters, has the asymptotic properties [33, 52, 53]:

$$\theta_M \sim \mathcal{N}(\theta_{M_0}, \Sigma_0), \quad (6.4.14)$$

where θ_{M_0} is the nominal parameter vector, and the $(M+2) \times (M+2)$ covariance matrix is given approximately by

$$\Sigma_0 \approx \sigma_0^2 (F^T(\theta_{M_0}) W F(\theta_{M_0}))^{-1}.$$

Here the $N \times (M+2)$ sensitivity matrix is given by

$$F(\theta) = \left(\frac{\partial R(k_i; \theta)}{\partial \theta_j} \right),$$

and the matrix W is defined as $W^{-1} = \text{diag}(w_1^2, \dots, w_N^2)$. Since θ_{M_0} is unknown, we will use the estimates

$$\Sigma_0 \approx \hat{\Sigma} = \hat{\sigma}_0^2 (F^T(\hat{\theta}_M) W F(\hat{\theta}_M))^{-1},$$

where we use the approximation

$$\hat{\sigma}_0^2 = \frac{1}{N - M - 2} \sum_{j=1}^N w_j^{-2} (R(k_j; \hat{\theta}_M) - y_j)^2. \quad (6.4.15)$$

We can then construct the $100(1 - \lambda)\%$ level confidence intervals by

$$\left[(\hat{\theta}_M)_j - t_{1-\lambda/2} SE_j, (\hat{\theta}_M)_j + t_{1-\lambda/2} SE_j \right], \quad (6.4.16)$$

where $SE_j = \sqrt{\hat{\Sigma}_{jj}}$, and the critical value $t_{1-\lambda/2}$ is determined by $\text{Prob}\{T > t_{1-\lambda/2}\} = \lambda/2$, where T has a student's t distribution with $N - M - 2$ degrees of freedom.

Additionally, we would like to construct a pointwise confidence band for the distribution $G_M(k_0)$ and the density $G'_M(k_0)$. To do this we follow the ideas presented in [19], however we ignore the contributions of model discrepancy. We assume that the effects of model discrepancy are negligible. For this to be a reasonable assumption, we must check that the residual plots do not show any major signs of model discrepancy (see Section 6.5.4 below).

Define the vectors

$$\mathbf{T}_M(k_0) = \left(\int_{\underline{k_0}}^{k_0} l_1(\xi) d\xi, \dots, \int_{\underline{k_0}}^{k_0} l_M(\xi) d\xi, 0, 0 \right)^T,$$

and

$$\mathbf{L}_M(k_0) = (l_1(k_0), \dots, l_M(k_0), 0, 0)^T.$$

Then, using the spline approximation for the probability measure, we have, for any $G_M \in \mathcal{P}_S^M(\mathcal{K})$

$$G_M(k_0) = \mathbf{T}_M(k_0)^T \theta_M, \quad G'_M(k_0) = \mathbf{L}_M(k_0)^T \theta_M.$$

Then by (6.4.14) we know that for any sufficiently large n

$$G_M(k_0) \sim \mathcal{N}(\mathbf{T}_M(k_0)^T \hat{\theta}_M, \mathbf{T}_M(k_0)^T \hat{\Sigma} \mathbf{T}_M(k_0)), \quad (6.4.17)$$

and

$$G'_M(k_0) \sim \mathcal{N}(\mathbf{L}_M(k_0)^T \hat{\theta}_M, \mathbf{L}_M(k_0)^T \hat{\Sigma} \mathbf{L}_M(k_0)). \quad (6.4.18)$$

Now we can compute the $100(1 - \lambda)\%$ level confidence intervals for the pointwise estimates by

$$\left[\hat{G}_M(k_0) - t_{1-\lambda/2} SE_{G_M}(k_0), \hat{G}_M(k_0) + t_{1-\lambda/2} SE_{G_M}(k_0) \right], \quad (6.4.19)$$

and

$$\left[\hat{G}'_M(k_0) - t_{1-\lambda/2} SE_{dG_M}(k_0), \hat{G}'_M(k_0) + t_{1-\lambda/2} SE_{dG_M}(k_0) \right], \quad (6.4.20)$$

where $SE_{G_M}(k_0) = \sqrt{\mathbf{T}_M(k_0)^T \hat{\Sigma} \mathbf{T}_M(k_0)}$ and $SE_{dG_M}(k_0) = \sqrt{\mathbf{L}_M(k_0)^T \hat{\Sigma} \mathbf{L}_M(k_0)}$.

6.5 Results

In this section we present various results of the inverse problem using data obtained from the thermally treated SiC/SiCN CMC samples.

6.5.1 Consistency as M Increases

Before making any claims about the model's ability to fit the data and the resulting estimations, we must first ensure that we have convergence of the spline approximation scheme as M increases. As was mentioned previously, the inverse problem (6.4.9) has been observed to be ill-posed. In Figure 6.8 we show the model fits and the estimated density using one data set obtained from the 10 hour heat treated sample 32 where the number of spline nodes was taken to be $M = 74$ and 75. We see that the model fits both agree very well with the data, however, the estimated densities are quite different, as well as the estimated parameters which are given in Table 6.1. We see a similar phenomenon in Figure 6.9 and Table 6.2 in which we fit a data set obtained from the 100 hour heat treated sample 13. Again, both model fits, using $M = 72$ and 74, agree well with the data, but the estimated densities and parameters are quite different. If we choose to use this inverse problem, it is not clear which approximation is more "correct".

To alleviate this issue, we consider the re-parameterization of the model which results in the inverse problem (6.4.13). In Figure 6.10 we show the model fit and estimated density using a data set obtained from the 10 hour heat treated sample 4. As before, the model fits agree very well with the data, but now the estimated densities using $M = 70, 71$ and 80 also are in good agreement. We do note that the estimated parameter values of ε_∞ and τ for $M = 80$ are

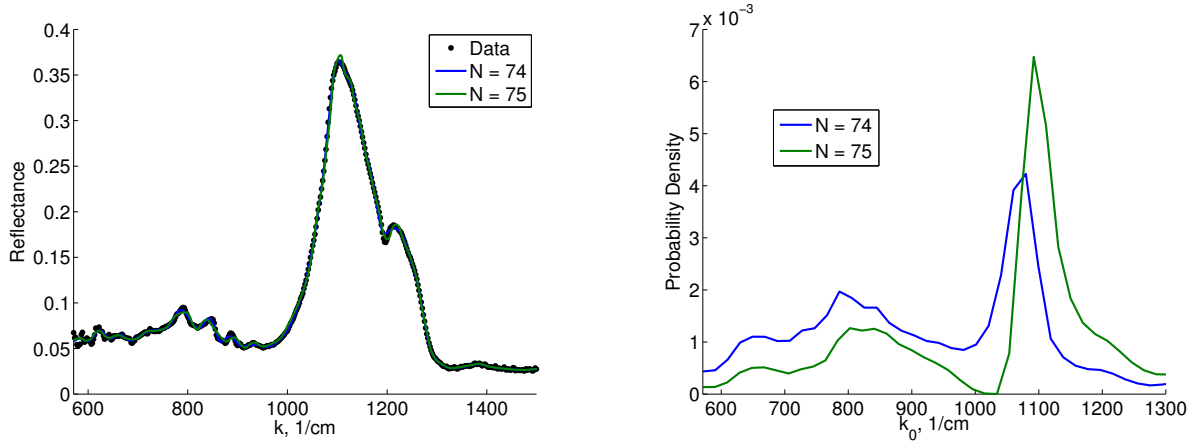


Figure 6.8: Using a data set from the 10 hour heat treated sample 32, the model fit to the data (left) and the estimated density (right) using $M = 74$ and 75 nodes.

Table 6.1: The estimated parameters using a data set from the 10 hour heat treated sample 32 for $M = 74$ and 75.

M	ε_s	ε_∞	τ	J
74	1.9249	1.3232	0.0676	2.323e-03
75	2.2091	1.6051	0.4491	4.423e-03

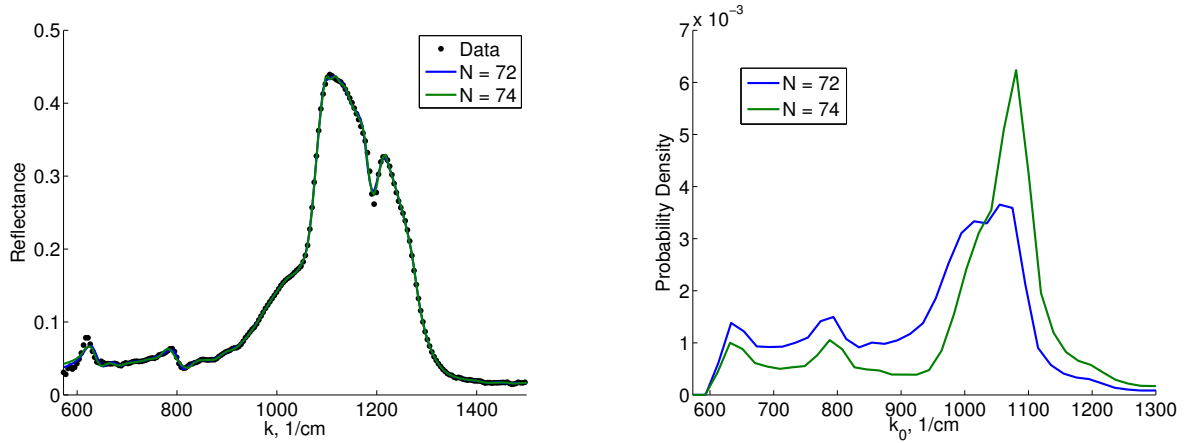


Figure 6.9: Using a data set from the 100 hour heat treated sample 13, the model fit to the data (left) and the estimated density (right) using $M = 72$ and 74 nodes.

dissimilar to the values found using $M = 70$ and 71. It is also important to remark that the parameters in the model for reflectance will at some level be unidentifiable due to the absolute values in the reflectance model (5.2.5).

Table 6.2: The estimated parameters using a data set from the 100 hour heat treated sample 13 for $M = 72$ and 74.

M	ε_s	ε_∞	τ	J
72	1.7311	1.2435	0.1063	2.752e-03
74	1.8984	1.3734	0.1724	2.558e-03

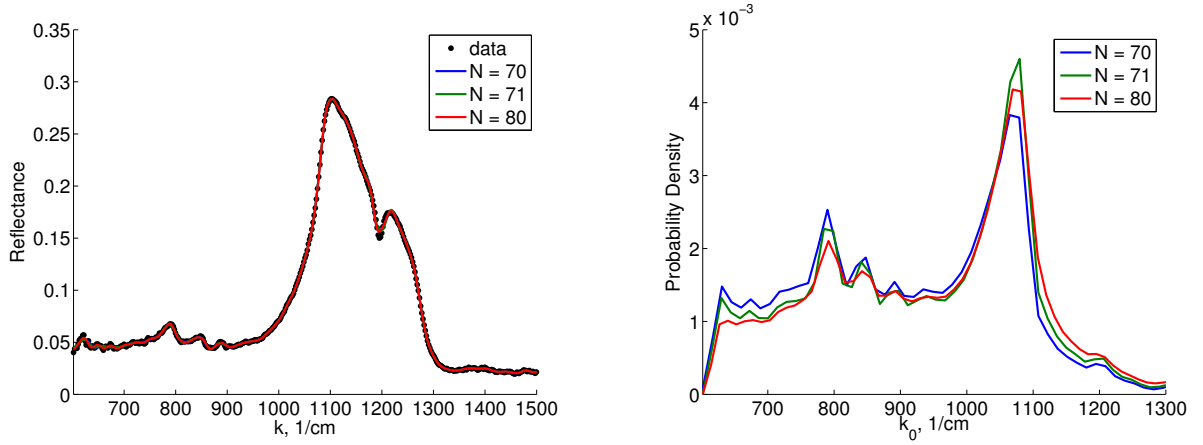


Figure 6.10: Using a data set from the 10 hour heat treated sample 4, the model fit to the data (left) and the estimated density (right) using $M = 70, 71$ and 80 nodes.

Table 6.3: The estimated parameters using a data set from the 10 hour heat treated sample 4 for $M = 70, 71$ and 80.

M	ε_s	ε_∞	τ	J
70	3.4922	3.0752	0.0433	8.603e-04
71	3.5226	3.0965	0.0441	8.831e-04
80	3.6259	3.2090	0.1031	6.486e-04

6.5.2 Optimal Value of M

One needs a way of determining the value of M in the inverse problem. To determine the optimal value of M we use the model selection criteria the Aikakie Information Criterion (AIC). The AIC (as summarized in [33, Chap. 4]) is given by

$$\text{AIC} = -2 \ln \mathcal{L}(\theta_{MLE}|y) + 2\kappa, \quad (6.5.1)$$

where

$$\mathcal{L}(\theta_{MLE}|y) = \prod_{j=1}^N \left[\frac{1}{\sqrt{2\pi}\sigma w_j} \exp \left(-\frac{(R(k_j; \theta_{MLE}) - y_j)^2}{2\sigma^2 w_j^2} \right) \right]$$

is the likelihood function, θ_{MLE} is the maximum likelihood estimate of the parameters θ , $y = [y_1, \dots, y_N]^T$ is the vector of observations, and κ is the total number of parameters estimated (the number of unknown parameters in the mathematical model and the statistical model).

Under the assumption of the errors \mathcal{E}_j , $j = 1, \dots, N$, being i.i.d. $\mathcal{N}(0, \sigma^2)$ with weighting terms w_j for the statistical model (6.4.1), we have that $\{Y_j\}_{j=1}^N$ are independent with mean $\mathbb{E}(Y_j) = R(k_j; G_0, q_0)$, and variance $\text{Var}(Y_j) = \sigma^2 w_j^2$.

Taking the natural log of the likelihood function gives

$$\ln(\mathcal{L}(\theta_{MLE}|y)) = -\frac{N}{2} \ln(2\pi) - \sum_{j=1}^N \ln(w_j) - N \ln(\sigma) - \frac{1}{2\sigma^2} \sum_{j=1}^N \frac{(R(k_j; \theta_{MLE}) - y_j)^2}{2\sigma^2 w_j^2}. \quad (6.5.2)$$

We remark that maximizing the log-likelihood function to obtain the maximum likelihood estimate $(\beta_{MLE}, q_{\beta_{MLE}})$ of (β, q_β) is the same as minimizing the cost function (6.4.13). Hence, the weighted least squares and maximum likelihood estimates are identical, that is $(\hat{\beta}, \hat{q}_\beta) = (\beta_{MLE}, q_{\beta_{MLE}})$, where $(\hat{\beta}, \hat{q}_\beta)$ solves (6.4.13)—see [33, Chap. 4].

Once the estimate $\hat{\theta}_M$ is obtained, we can solve the equation

$$\frac{\partial \ln(\mathcal{L}(\hat{\theta}_M|y))}{\partial \sigma} = 0$$

to obtain the maximum likelihood estimate σ_{MLE} of σ . It can be easily verified that

$$\frac{\partial \ln(\mathcal{L}(\hat{\theta}_M|y))}{\partial \sigma} = -\frac{N}{\sigma} + \frac{1}{\sigma^3} \sum_{j=1}^N \frac{(R(k_j; \hat{\theta}_M) - y_j)^2}{w_j^2}.$$

Thus, we find that the maximum likelihood estimate σ_{MLE} of σ is given by

$$\sigma_{MLE}^2 = \frac{1}{N} \sum_{j=1}^N \frac{(R(k_j; \hat{\theta}_M) - y_j)^2}{w_j^2},$$

which is different than the estimate for σ given by the approximated finite dimensional weighted least squares procedure (6.4.15).

Substituting these estimates $\hat{\theta}_M$ and σ_{MLE} into (6.5.2) we obtain

$$\ln(\mathcal{L}(\hat{\theta}_M|y)) = -\frac{N}{2} \ln(2\pi) - \sum_{j=1}^N \ln(w_j) - \frac{N}{2} \ln \left(\frac{1}{N} \sum_{j=1}^N \frac{(R(k_j; \hat{\theta}_M) - y_j)^2}{w_j^2} \right) - \frac{N}{2}.$$

Then, by (6.5.1) we have

$$\text{AIC} = N(\ln(2\pi) + 1) + 2 \sum_{j=1}^N \ln(w_j) + N \ln \left(\frac{1}{N} \sum_{j=1}^N \frac{(R(k_j; \hat{\theta}_M) - y_j)^2}{w_j^2} \right) + 2\kappa. \quad (6.5.3)$$

Note that the first term of the above equation is constant for a fixed number of observations N , so we may omit these terms.

It is known that the AIC may perform poorly if the sample size N is small relative to the total number of estimated parameters. It is recommended [46] that the AIC should only be used if $N/\kappa \geq 40$. We have $N = 448$ for a typical reflectance data set used in this work, and thus we will use a small sample AIC, denoted by AIC_c , which is given by

$$\text{AIC}_c = \text{AIC} + \frac{2\kappa(\kappa + 1)}{N - \kappa - 1}. \quad (6.5.4)$$

We remark that for our reflectance model, $\kappa = M + 3$ since we are using M spline elements, for each of which there is an associate weight β_m to be estimated, and we also estimate the additional mathematical model parameters ε_∞ and τ as well as the statistical model parameter σ .

For each data set, the AIC_c values were computed to determine the optimal value of M . In Figure 6.11 a snapshot of the AIC_c values are presented where a data set from 10 hour heat treated sample 4 was used, and $M = 50, 51, \dots, 120$ was considered. Typically, for each data set considered the optimal value of M was found to be between $M = 80$ and 90 .

6.5.3 Comparison of Heat Treated Samples

In this section we compare the results of the inverse problem (6.4.13) obtained using the 10 and 100 hour heat treated samples. For all of the following results the number of spline functions was determined using the AIC_c . In Figures 6.12–6.14 we give the model fits and the estimated densities using the data obtained from the first three locations of the 10 hour heat treated samples 4, 16, and 32, respectively. In Figures 6.15–6.16 we present the model fits and the estimated densities using the data obtained from the first three locations (approximately 1.4 cm apart) of the 100 hour heat treated samples 1 and 13, respectively. In Table 6.4, we give the estimated parameters and the value of the cost function for each of the first three locations from each sample.

We see in each case that there is variation in the magnitude of the reflectance data, yet the model is able to fit all of the data sets very well. Additionally, for each sample, the estimated densities are similar.

To better illustrate the differences in the estimated densities between the 10 and 100 hour

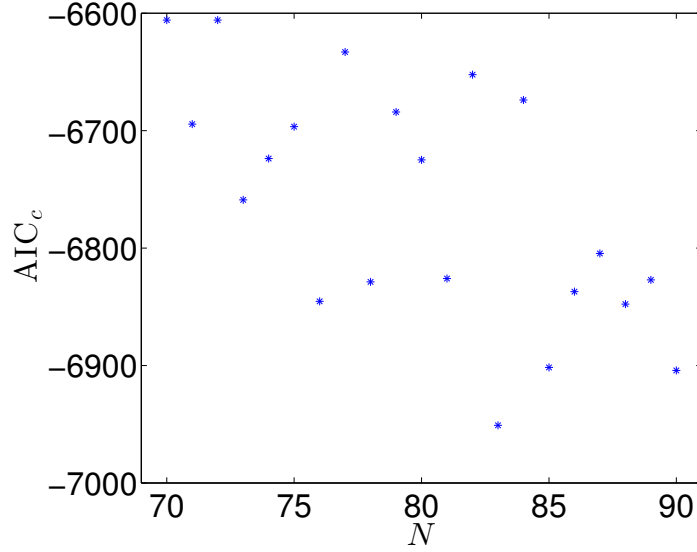


Figure 6.11: A snapshot of the AIC_c values using a data set obtained from the 10 hour heat treated sample 4 with $M = 70, 71, \dots, 90$.

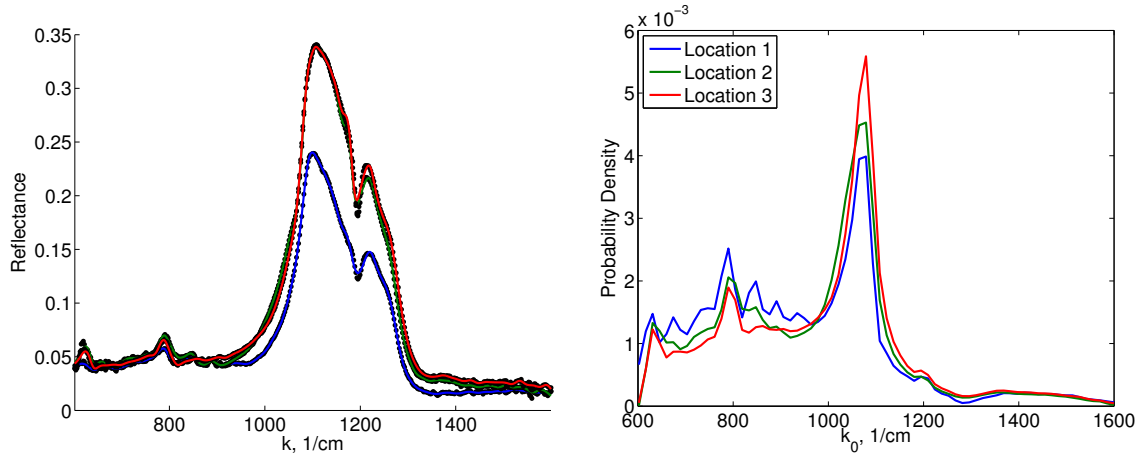


Figure 6.12: The model fits (left) and estimated densities (right) using the first three locations of the data obtained from the 10 hour heat treated sample 4.

heat treated samples, we show the densities from each location for the 10 hour heat treated samples in Figure 6.17 and for the 100 hour heat treated samples in Figure 6.18. We also computed the mean density for each sample, which can be seen in Figure 6.19. Recall that for SiO_2 we should see oscillators at approximately 800 and 1080 cm^{-1} . We see that the estimated densities from the 100 hour samples have larger peaks near 1080 cm^{-1} compared to the estimated densities from the 10 hour samples. Near 800 cm^{-1} , the estimated densities have peaks which

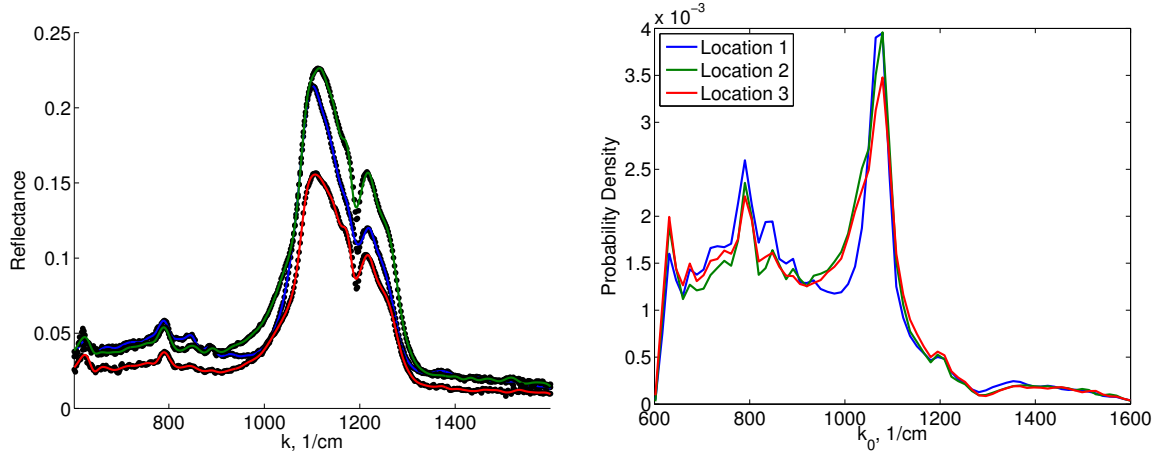


Figure 6.13: The model fits (left) and estimated densities (right) using the first three locations of the data obtained from the 10 hour heat treated sample 16.

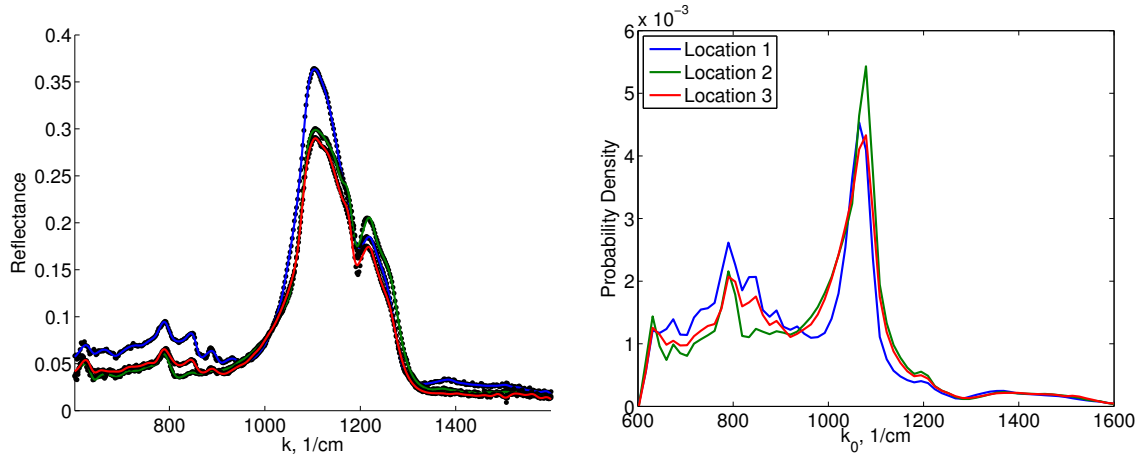


Figure 6.14: The model fits (left) and estimated densities (right) using the first three locations of the data obtained from the 10 hour heat treated sample 32.

are wider for the 10 hour samples than for the 100 hour samples which has sharper peaks. For the SiN peaks, at approximately 640 and 1200 cm^{-1} , we do not see a distinguishable difference between the estimated densities using the 10 and 100 hour data samples.

The larger peaks near 1080 cm^{-1} in the estimated densities using the 100 hour samples may indicate more SiO_2 content compared to the 10 hour samples, which we would expect. However, the estimated densities for both the 10 hour and 100 hour samples indicate that there is little difference in the SiN content. Additionally, the broader peaks in the estimated densities for the 10 hour samples near 800 cm^{-1} may indicate that the SiO_2 present in the 10 hour samples is

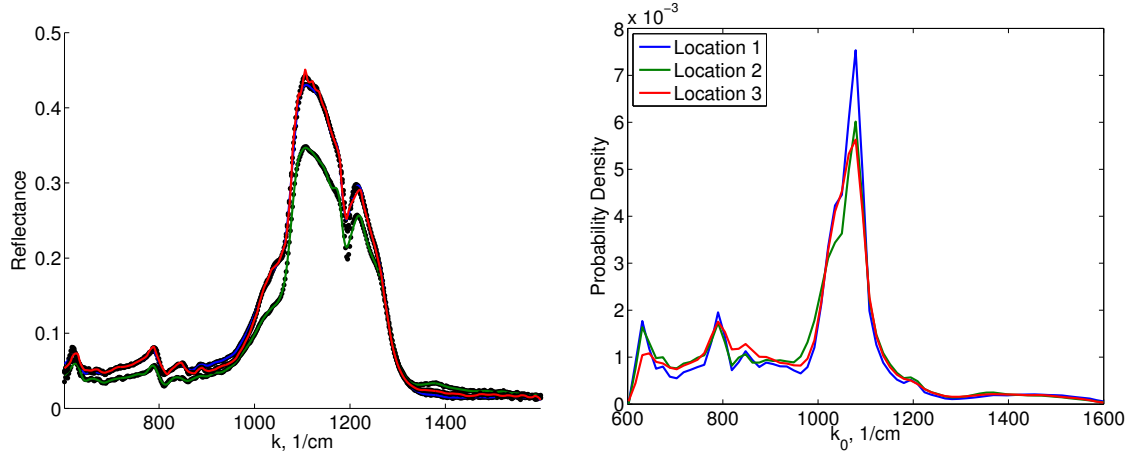


Figure 6.15: The model fits (left) and estimated densities (right) using the first three locations of the data obtained from the 100 hour heat treated sample 1.

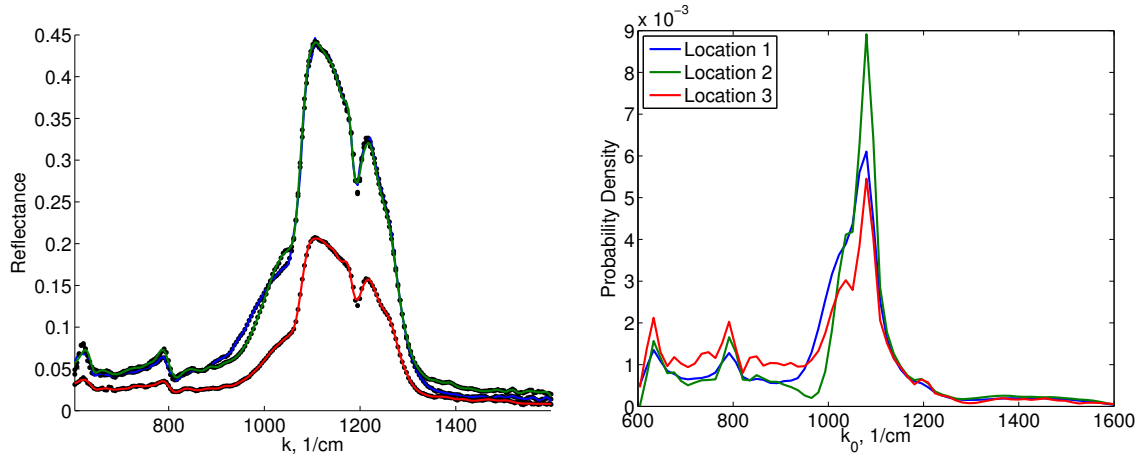


Figure 6.16: The model fits (left) and estimated densities (right) using the first three locations of the data obtained from the 100 hour heat treated sample 13.

in more of an amorphous state and the SiO_2 present in the 100 hour samples is in more of a crystalline state.

6.5.4 Pointwise Confidence Bands

In order to understand the uncertainty present in the estimated quantities in our mathematical model, we will compute the 95% confidence intervals for the model parameters ε_∞ and τ according to (6.4.16), and construct the pointwise asymptotic confidence band for the probability density using (6.4.20). Modified residual plots will be used as a way as to assist in the determination

Table 6.4: Estimated parameters using the first 3 locations from each sample.

	Location	ε_s	ε_∞	τ	J
10 hr. sample 4	1	3.7115	3.3314	0.0370	6.263e-04
	2	3.5406	3.1149	0.0924	1.612e-03
	3	3.5483	3.1208	0.0837	1.691e-03
10 hr. sample 16	1	3.8316	3.4704	0.0415	4.173e-04
	2	3.7615	3.3902	0.0409	7.992e-04
	3	4.6257	4.3448	0.0486	5.744e-04
10 hr. sample 32	1	3.1822	2.6740	0.0622	1.026e-03
	2	3.7688	3.3790	0.0622	1.801e-03
	3	3.7276	3.3277	0.0804	1.208e-03
100 hr. sample 1	1	3.4428	2.9400	0.0589	2.600e-03
	2	3.6429	3.2286	0.0812	2.552e-03
	3	3.4873	3.0082	7.5718	4.252e-03
100 hr. sample 13	1	3.5733	3.1072	5.1994	1.595e-03
	2	3.4479	2.9473	0.0790	1.252e-03
	3	4.4069	4.0966	0.0386	2.673e-04

of whether or not the form of the measurement errors was correctly specified. The modified residuals are computed by

$$r_j = w_j^{-1}(R(k_j; \hat{G}_M, \hat{q}_\beta) - y_j), \quad j = 1, \dots, N.$$

Since we have a large number of data sets (33 per sample for a total of 165 data sets), we will only present a subset of the data sets, which show typical results. We consider a data set obtained from the 10 hour heat treated sample 32 and a data set obtained from the 100 hour heat treated sample 1. The modified residuals are plotted against the wavenumber k , and against the model solution value in Figure 6.20 for sample 32 and in Figure 6.21 for sample 1. We see that the modified residuals from both data sets show a random pattern centered about zero when plotted against the interrogating wavenumber k and the model solution value. This suggests that the error model is correctly specified.

The pointwise 95% confidence band was computed according to (6.4.20) for the estimated density from each inverse problem and is presented in Figure 6.22 and Figure 6.23 for the data sets from Sample 32 and 1, respectively. In both cases, we observe very narrow confidence bands around the estimated density. Additionally, the 95% confidence intervals were computed using (6.4.16) for the additional model parameters are given in Table 6.5. The confidence interval for the estimated value of ε_∞ is extremely narrow for both data sets, however there is more uncertainty in our estimate for τ . This is consistent with previous work in which it was determined that the reflectance model has a low sensitivity to the relaxation time τ .

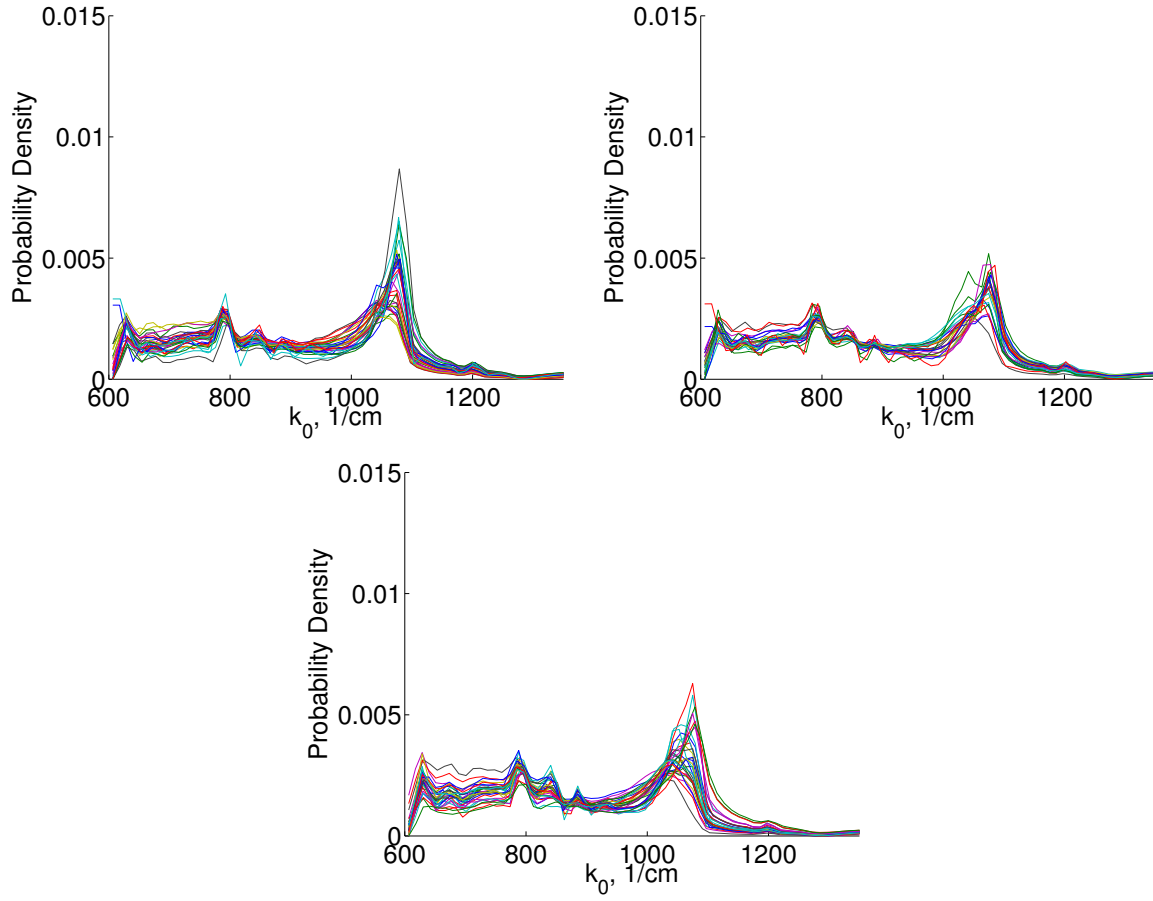


Figure 6.17: The estimated densities for each location from the 10 hour heat treated data obtained from sample 4 (top left), sample 16 (top right), and sample 32 (bottom center).

Table 6.5: The 95% confidence intervals for the estimated model parameters from a representative data set from the 10 and 100 hour heat treated samples.

	parameter	estimate	95% CI
10 hr. sample 32	ε_{∞}	3.0149	[3.0005, 3.0292]
	τ	0.2179	[0.1544, 0.2814]
100 hr. sample 1	ε_{∞}	3.3599	[3.3459, 3.3739]
	τ	0.1498	[0.1189, 0.1808]

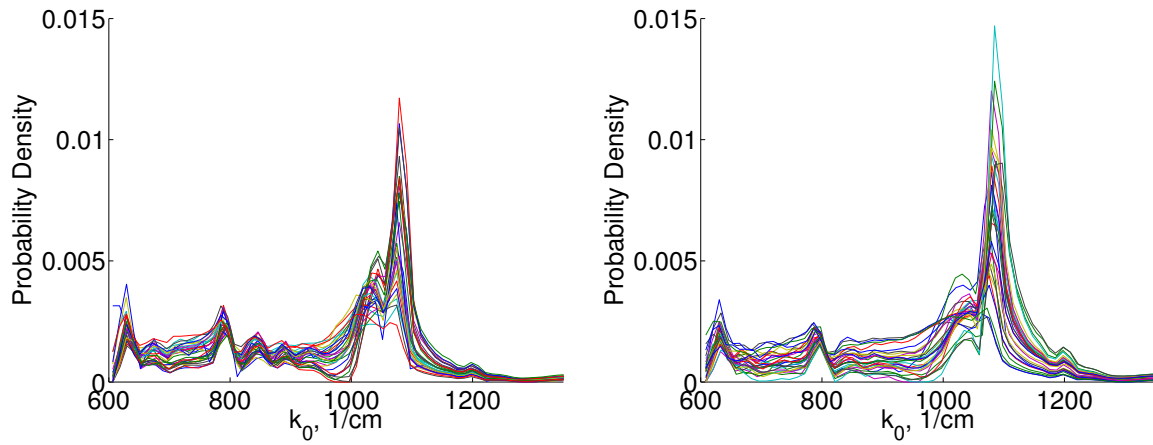


Figure 6.18: The estimated densities for each location from the 100 hour heat treated data obtained from sample 1 (left) and sample 13 (right).

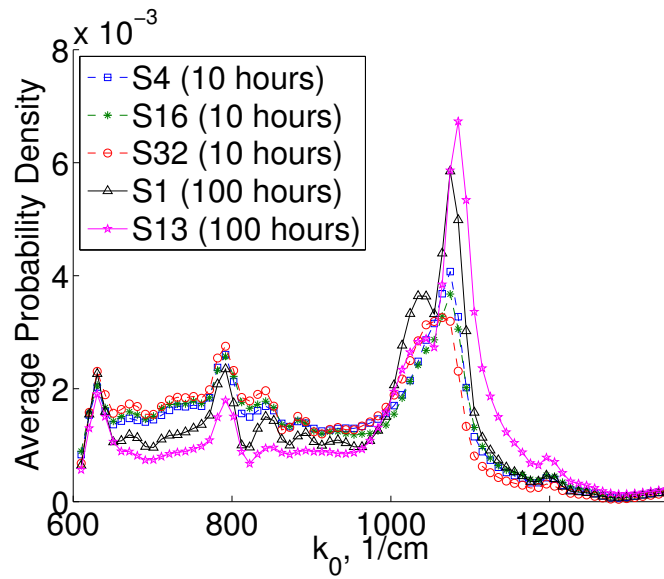


Figure 6.19: The mean density for each sample.

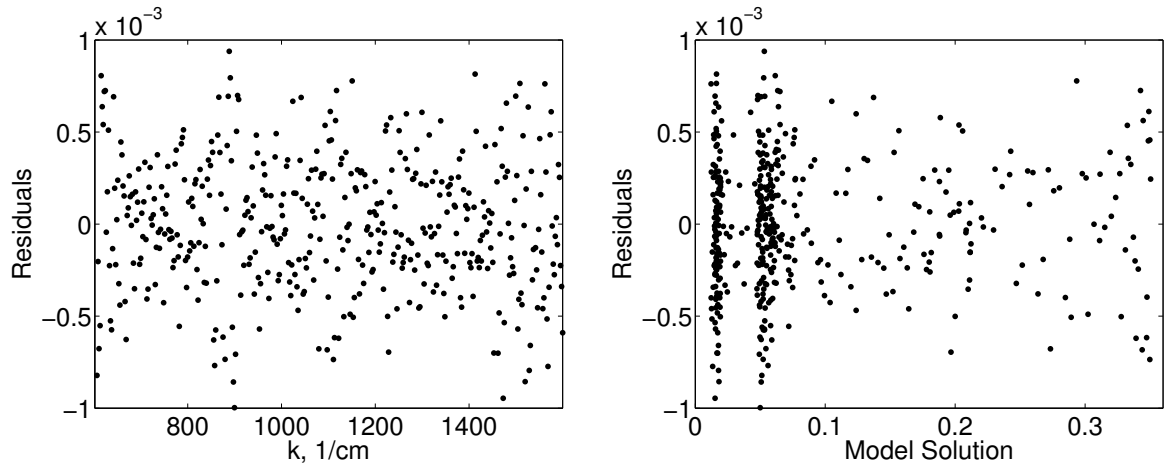


Figure 6.20: The modified residuals versus wavenumber k (left) and versus the model solution (right) for the 10 hour heat treated sample 32.

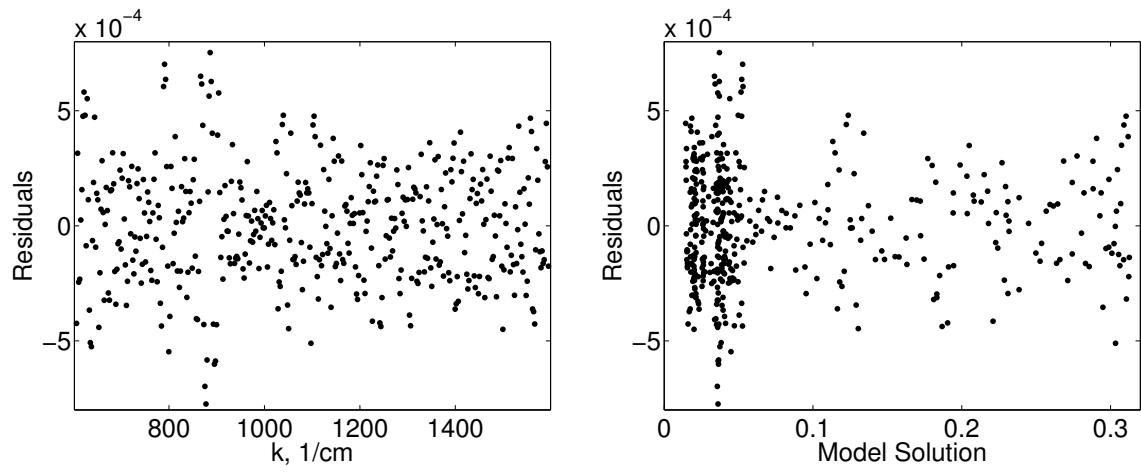


Figure 6.21: The modified residuals versus wavenumber k (left) and versus the model solution (right) for the 100 hour heat treated sample 1.

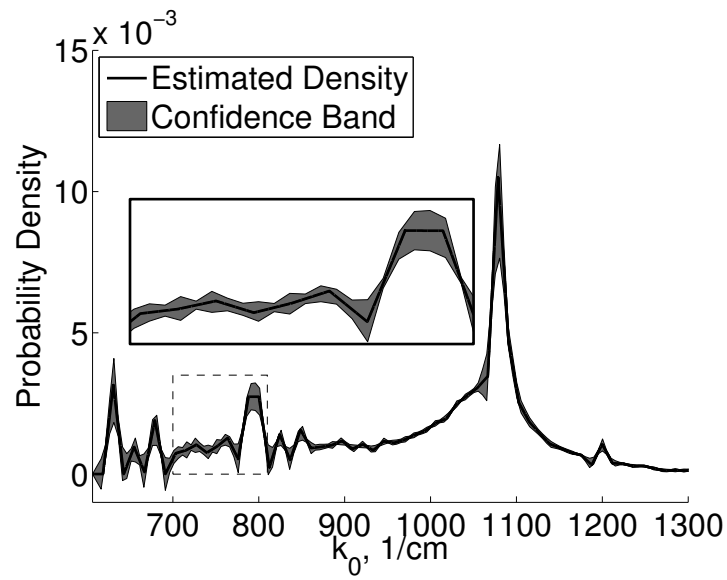


Figure 6.22: The estimated density and the corresponding pointwise confidence band for a data set obtained from the 10 hour heat treated sample 32.

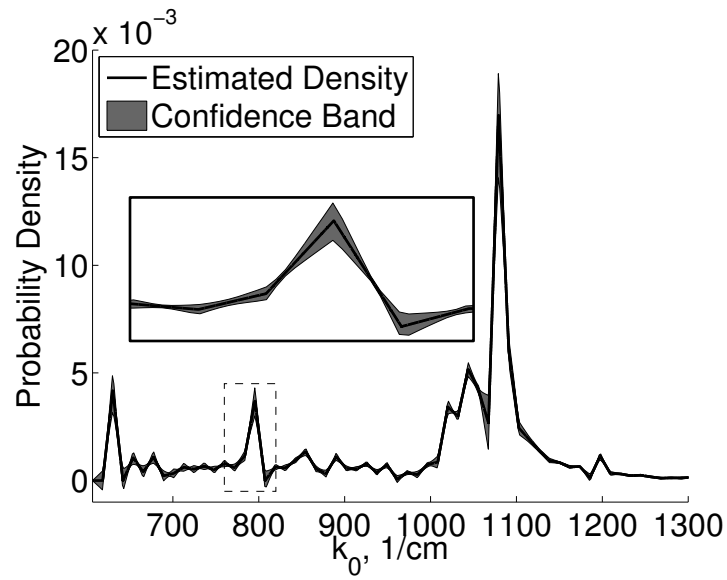


Figure 6.23: The estimated density and the corresponding pointwise confidence band for a data set obtained from the 100 hour heat treated sample 1.

6.5.5 Comparison to Bootstrapping and Bayesian Estimation

Previously in Chapter 2 we compared the confidence band for the estimated probability measure using the pointwise asymptotic approach with Monte Carlo simulations. Since we are dealing with experimental data rather than synthetic data, we will compare the pointwise asymptotic confidence bands shown here with confidence bands constructed using both bootstrapping and Bayesian parameter estimation.

Bootstrapping is a frequentist based methodology, in which the robustness of the parameter estimates is tested by resampling the residuals to construct “simulated” data sets. The inverse problem is then solved using these additional data sets and the estimation results are used to construct the statistics of the estimators. The bootstrapping procedure requires that many inverse problems be solved, however, the trade off is a relaxation of assumptions compared to the standard asymptotic approach. Here we make use of a standard bootstrapping algorithm (rather than the algorithm given in Chapter 3 which takes into consideration model discrepancy).

Algorithm 6.5.1 Standard Bootstrapping

1. Find $\hat{\theta}_{M,WLS} = (\hat{\beta}, \hat{q}_\beta)$ according to (6.4.13).
2. Define the standardized residuals as

$$\tilde{r}_j = \sqrt{\frac{N}{N - \kappa}} w_j^{-1} (y_j - R(k_j; \hat{\theta}_{M,WLS})), \quad j = 1, \dots, N.$$

3. For $m = 0, \dots, \mathcal{M}$
 - (a) Create a sample of size N by random sampling with replacement from the set of standardized residuals \tilde{r}_j to form the bootstrap sample $\{r_j^m\}_{j=1}^N$.
 - (b) Create the simulated data set

$$R_j^m = R(k_j; \hat{\theta}_{M,WLS}) + w_j r_j^m, \quad j = 1, \dots, N.$$

- (c) Solve the inverse problem with the simulated data $\{R_j^m\}_{j=1}^N$ to obtain a new estimate $\hat{\theta}_M^m$.
-

Once we have complete \mathcal{M} runs, we can compute the mean and covariance for the bootstrap

estimator by

$$\begin{aligned}\hat{\theta}_{M,Boot} &= \frac{1}{\mathcal{M}} \sum_{m=1}^{\mathcal{M}} \hat{\theta}_M^m, \\ \hat{\Sigma}_{Boot} &= \frac{1}{\mathcal{M}-1} \sum_{m=1}^{\mathcal{M}} (\hat{\theta}_M^m - \hat{\theta}_{M,Boot})(\hat{\theta}_M^m - \hat{\theta}_{M,Boot})^T.\end{aligned}$$

The confidence intervals for the estimated parameters $\hat{\theta}_{M,Boot}$ are computing according to (6.4.16). For our computations, we performed $\mathcal{M} = 1,000$ runs.

In a Bayesian framework, one assumes that the unknown parameters are random variables with associated probability densities. We denote the prior density by $\pi_0(\theta_M)$, which is taken as an uniform prior, and we further assume that the measurement errors are independent and identically distributed with normally distribution with mean 0 and variance σ_0^2 and individual weight w_j . With these assumptions, the likelihood function is given by

$$\pi(y|\theta_M) = \frac{1}{(2\pi\sigma_0^2)^{N/2}} \exp \left\{ -\frac{1}{2\sigma_0^2} \sum_{j=1}^N w_j^{-2} (y_j - R(k_j; \theta_M))^2 \right\}. \quad (6.5.5)$$

Then the posterior density can be obtained through

$$\pi(\theta_M|y) = \frac{\pi(y|\theta_M)\pi_0(\theta_M)}{\pi(y)} = \frac{\pi(y|\theta_M)\pi_0(\theta_M)}{\int_{\mathbb{R}^p} \pi(y|\theta_M)\pi_0(\theta_M)d\theta_M}. \quad (6.5.6)$$

The posterior density was approximated using the delayed rejection adaptive Metropolis (DRAM) algorithm (available at [70]) with a burn-in phase and chain length of 10^4 and 10^5 , respectively. There are many sources available which provide an extensive discussion on the DRAM algorithm (e.g. [88]), here we will not go into further details, but only give the outline of the algorithm in 6.5.2 and 6.5.3.

All three methods for performing the parameter estimation result in similar estimates. We remark that we will abbreviate both the Bayesian credible intervals and the frequentist confidence intervals by CI, although it should be understood that there is a fundamentally different interpretation for each. For the parameters ε_∞ and τ , we obtain tighter bounds through the Bayesian credible intervals compared to the confidence intervals given by bootstrapping and asymptotic theory, see Tables 6.6–6.7. In fact, it was consistently observed that the CI's obtain through asymptotic theory for ε_∞ and τ were larger compared to the other methods. As noted earlier, it has been established that the model is not very sensitive to τ . The CI's using asymptotic theory are based upon the sensitivity equations, and hence we fully expect the insensitivity to τ to be manifested in large CI's. What is unexpected, is that the CI's using the

other methods (particularly for the Bayesian estimation) are relatively tight.

Table 6.6: The 95% confidence intervals (credible intervals for the Bayesian estimation) for the estimated model parameters from a representative data set from the 10 hour heat treated sample 32 using asymptotic theory (WLS), bootstrapping, and Bayesian estimation.

	WLS		Bootstrapping		Bayesian	
	estimate	95% CI	estimate	95% CI	estimate	95% CI
ε_∞	3.3126	[3.2142, 3.4111]	3.2724	[3.2200, 3.3248]	3.3156	[3.2932, 3.3396]
τ	0.0494	[0.0285, 0.0703]	0.0493	[0.0491, 0.0495]	0.0502	[0.0480, 0.0521]

Table 6.7: The 95% confidence intervals (credible intervals for the Bayesian estimation) for the estimated model parameters from a representative data set from the 100 hour heat treated sample 1 using asymptotic theory (WLS), bootstrapping, and Bayesian estimation.

	WLS		Bootstrapping		Bayesian	
	estimate	95% CI	estimate	95% CI	estimate	95% CI
ε_∞	3.3715	[3.3154, 3.4275]	3.3430	[3.3232, 3.3628]	3.3621	[3.3406, 3.3811]
τ	0.0474	[0.0360, 0.0589]	0.0435	[0.0388, 0.0483]	0.0484	[0.0461, 0.0499]

In Figures 6.24 and 6.26 we present the estimated densities using an example data set from a 10 and 100 hour heat treated sample, respectively. We see that the estimated densities agree remarkable well. In Figures 6.25 and 6.27 we plot the endpoints of the 95% CI's using each method for the corresponding densities. For the CI's on the estimated weights, generally less of a discrepancy between the three methods was observed, yet Bayesian estimation again provided the tightest uncertainty bounds.

At this point, one might argue that Bayesian estimation is the preferred method for completing the parameter estimation since similar estimates are found using each method, and the Bayesian estimation consistently results in the highest degree of confidence in the parameter values. However, in choosing a estimation method one must balance the decrease in parameter uncertainty obtained using Bayesian analysis with the increase in computational load. To complete a typical WLS procedure, the gradient based optimization routine completed roughly 300 iterations. Standard gradient based optimization routines will employ a finite difference scheme on the cost functional in order to approximate the gradient (see our discussions in the next chapter for how this can be improved). Thus, for each optimization approximately $300(M+1)$ function evaluations of the reflectance model are required. For bootstrapping, this becomes $300(M+1)(\mathcal{M}+1)$

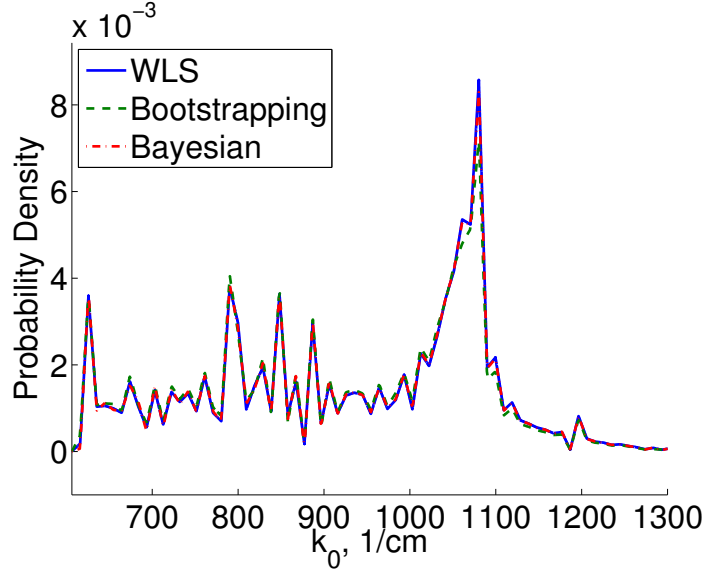


Figure 6.24: Comparison of the estimated density using weighted least squares (WLS), bootstrapping, and Bayesian estimation for a 10 hour heat treated data set from sample 1.

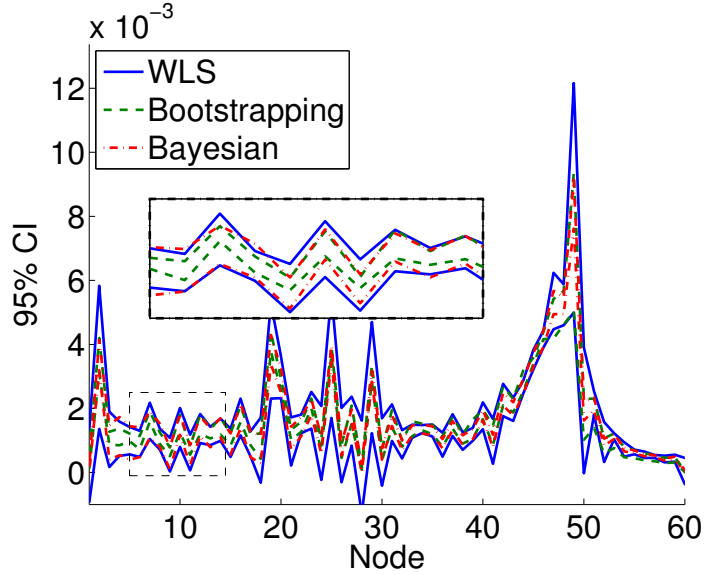


Figure 6.25: Comparison of the 95% confidence/credible intervals (CI) for the estimated weights using asymptotic theory (WLS), bootstrapping, and Bayesian estimation for a 10 hour heat treated data set from sample 1.

function evaluations, roughly 10^7 for a typical data set. We ran the DRAM algorithm for 10^5 iterations and typical runs resulted in a rejection rate of approximately 40%, which yields

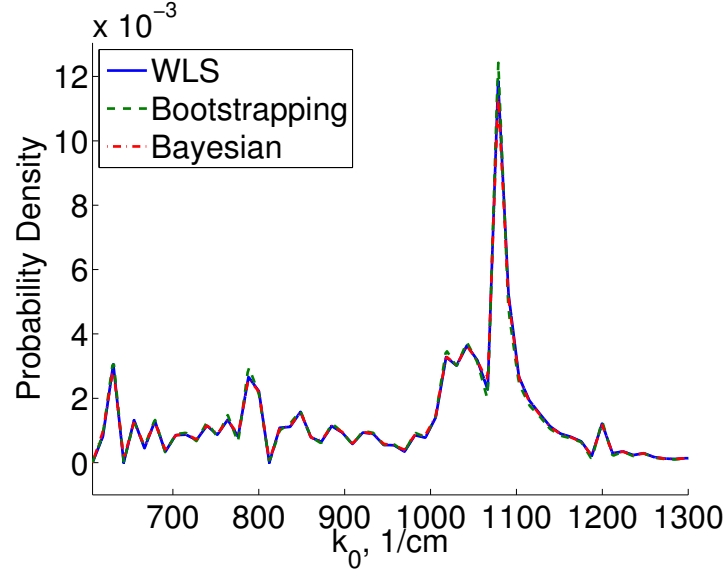


Figure 6.26: Comparison of the estimated density using weighted least squares (WLS), bootstrapping, and Bayesian estimation for a 100 hour heat treated data set from sample 1.

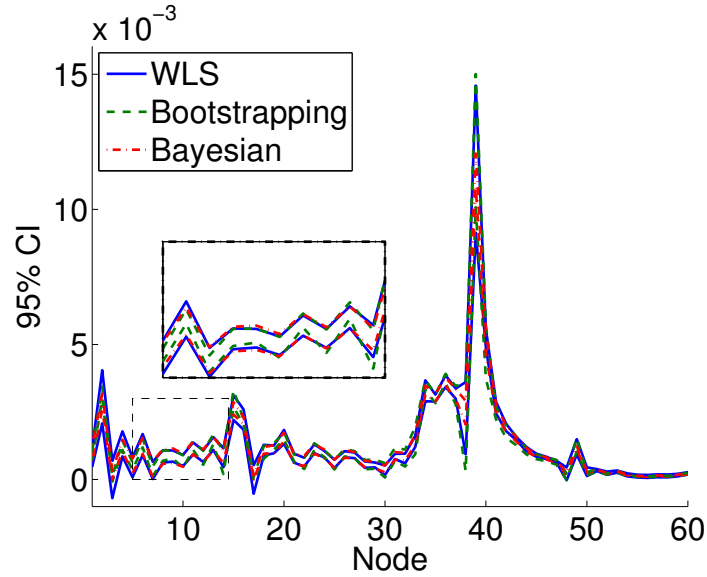


Figure 6.27: Comparison of the 95% confidence/credible intervals (CI) for the estimated weights using asymptotic theory (WLS), bootstrapping, and Bayesian estimation for a 100 hour heat treated data set from sample 1.

approximately 10^5 function evaluations. Therefore, the number of function evaluations for a typical data set are 10^4 , 10^5 , and 10^7 for the WLS, Bayesian, and bootstrapping methods,

respectively. By making use of the gradient evaluation procedure outlined in the following chapter the typical cpu time¹ needed to complete the WLS procedure was 4 minutes, while for the Bayesian estimation procedure the time to completion was on the order of 2 hours, and bootstrapping required more than a staggering 2.5 days!

6.6 Concluding Remarks

We are able to obtain accurate fits of our mathematical model for the reflectance, which includes a probability distribution of resonance wavenumbers, to experimental data sets. By re-parameterizing the inverse problem, we were able to establish the convergence of the estimated probability measure. The average estimated probability density was calculated for each sample, and with this we were able to see that the samples which were heat treated for 10 hours have lower peaks near 1080 cm^{-1} and broader peaks near 800 cm^{-1} when compared to the 100 hour average densities. This indicates that there is more SiO_2 present in the 100 hour samples and it is in more of a crystalline state than the 10 hour samples. We were not able to detect a difference in the amount of SiN present between the 10 and 100 hour samples.

The uncertainty associated with the estimated parameters and the estimated density was computed. It was found that we have a high degree of confidence for the relative permittivity at infinite frequency ε_∞ and the estimated density and have a relatively low degree of confidence in the estimate for the relaxation time τ . The uncertainty computing using standard asymptotic theory was compared with results obtained using bootstrapping, and also Bayesian estimation, and all three methods were found to be in agreement.

¹The nonlinear optimization was performed in MATLAB using the built-in routine `fmincon` on a 12 core machine. The reflectance model and the gradient calculations were run in parallel, all of which was written in C++ and converted to a MEX file that was called by MATLAB. The DRAM algorithm is by nature serial, so no parallelization was employed on the algorithm itself. The DRAM algorithm computed the reflectance model using an identical C++ program (converted to a MEX file) to the one used in the WLS problem, with the only modification being that the gradient computations were omitted (parallelization was still used to compute the reflectance model).

Algorithm 6.5.2 DRAM

1. Set design parameters n_s , σ_s^2 , the length of the non adaptive interval m_0 and the number of chain iterates \mathcal{C} .
2. Find $\hat{\theta}_{M,WLS} = (\hat{\beta}, \hat{q}_\beta)$ according to (6.4.13).
3. Set

$$\theta^0 = \hat{\theta}_{M,WLS}, \quad SS_{\theta^0} = \sum_{j=1}^N w_j^{-2} (y_j - R(k_j; \theta^0))^2$$

4. Compute initial variance estimate: $s_0^2 = \frac{1}{N-\kappa} SS_{\theta^0}$
5. Construct covariance estimate $V = s_0^2 (F^T(\theta^0) F(\theta^0))^{-1}$ and $R = \text{chol}(V)$.
6. For $m = 1, \dots, \mathcal{C}$

- (a) Sample $z_m \sim \mathcal{N}(0, 1)$
- (b) Construct candidate $\theta^* = \theta^{m-1} + R z_m$
- (c) Sample $u_{\mathcal{A}} \sim \mathcal{U}(0, 1)$
- (d) Compute

$$SS_{\theta^*} = \sum_{j=1}^N w_j^{-2} (y_j - R(k_j; \theta^*))^2.$$

- (e) Compute
$$\mathcal{A}(\theta^* | \theta^{m-1}) = \min \left(1, e^{-(SS_{\theta^*} - SS_{\theta^{m-1}}) / 2s_{m-1}^2} \right)$$
 - (f) If $u_{\mathcal{A}} < \mathcal{A}$,
Set $\theta^m = \theta^*$, $SS_{\theta^m} = SS_{\theta^*}$
else
Enter DR Algorithm
end if
 - (g) Update $s_m \sim \text{Inv-gamma}(a_{val}, b_{val})$, where
 $a_{val} = 0.5(n_s + n)$, $b_{val} = 0.5(n_s \sigma_s^2 + SS_{\theta^m})$.
 - (h) if $\text{mod}(m, m_0) = 1$
Update $V_m = s_m \text{cov}(\theta^0, \theta^1, \dots, \theta^m)$.
else
 $V_m = V_{m-1}$
end if
 - (i) Update $R_m = \text{chol}(V_m)$
-

Algorithm 6.5.3 Delayed Rejection (DR)

1. Set the design parameter $\gamma_2 = \frac{1}{5}$
2. Sample $z_m \sim \mathcal{N}(0, 1)$
3. Construct second stage candidate $\theta^{*2} = \theta^{m-1} + \gamma_2 R_m z_m$
4. Sample $u_{\mathcal{A}} \sim \mathcal{U}(0, 1)$
5. Compute

$$SS_{q^{*2}} = \sum_{j=1}^N w_j^{-2} (y_j - R(k_j; \theta^{*2}))^2.$$

6. Compute

$$\mathcal{A}(\theta^{*2} | \theta^{m-1}, \theta^*) = \min \left(1, \frac{\pi(\theta^{*2} | y) J_d(\theta^* | \theta^{*2}) [1 - \mathcal{A}(\theta^* | \theta^{*2})]}{\pi(\theta^{m-1} | y) J_d(\theta^* | \theta^{m-1}) [1 - \mathcal{A}(\theta^* | \theta^{m-1})]} \right),$$

where $J_d(\cdot | \cdot)$ is the jumping distribution.

7. If $u_{\mathcal{A}} < \mathcal{A}$
 Set $\theta^m = \theta^{*2}$, $SS_{\theta^m} = SS_{\theta^{*2}}$
 else
 Set $\theta^m = \theta^{m-1}$, $SS_{\theta^m} = SS_{\theta^{m-1}}$
 end if
-

Aggregate Data and the Prohorov Metric Framework: Efficient Gradient Computation

In this final chapter before concluding, our goal is to show how the gradient of a least squares objective function can be found in an efficient manner for inverse problems involving the estimation of a probability measure using the PMF. The following work has been accepted for publication [16]:

H.T. Banks and J. Catenacci. Aggregate data and the prohorov metric framework: efficient gradient computation. *Applied Math Letters*, 56:1–9, 2016.

7.1 Introduction

For years even simple population models based on individual models (see, e.g., the Hare-Lynx models [83, p. 30] and the bacterial growth and diffusion models [83, p. 33], [85], [86, p. 139]) have been based on aggregate population level data for parameter estimation and validation. However, with increased interest in uncertainty quantification and recognition that statistical models for the data collection procedures drive uncertainty statements about the parameters in the underlying mathematical models, the interest in determining correct statistical models as part of parameter estimation or inverse problems has grown. Moreover, it is now recognized that aggregate data is widely (and frequently incorrectly) employed to quantify uncertainty in individual models. This occurs in a ubiquitous range of applied problems including food chemistry efforts [56, 82, 87], tracking of labeled substances in proliferating cell populations (e.g., Propagons or prion seeds in amyloid growth in yeast [47, 51, 75, 77, 89]), as well as structured population

models in marine population studies such as those for mosquitofish [14] and shrimp [24]. In such individual models, one has a mathematical model which describes the behavior of one “individual” which is characterized by a single parameter set which must be estimated using population level or aggregate data.

In a second class of problems (the aggregate model case), the dynamic mathematical models explicitly depend upon a distribution that must be estimated using aggregate data. This is the case in electromagnetic interrogation problems with a distribution of polarization permittivity and relaxation time parameters for molecules [17, 29, 30, 33], in HIV cellular models [12, 13], and in wave propagation in viscoelastic materials [32, 33, 39]. Again in these examples, only aggregate data is available to estimate the imbedded probability distributions.

One method for such non-parametric estimation problems of a probability measure is through the Prohorov Metric Framework [5, 33] developed specifically to treat aggregate data problems (for a summary see [33, Chapter 5]). The PMF provides a theoretical and computational framework in which to estimate an unknown probability measure for which the space $\mathcal{P}(\Omega)$ of probability measures over a compact set Ω is approximated by a finite dimensional space $\mathcal{P}^M(\Omega)$ of dimension M . There are many choices for the approximating space $\mathcal{P}^M(\Omega)$; two popular choices involve using a basis of Dirac measures (zero order splines) or piecewise linear splines to approximate the distributions.

7.2 Problem framework

We assume to have a general mathematical model for a dynamical system which is dependent upon a probability measure G as well as Euclidean parameters $\mathbf{q} \in \mathcal{Q}$. We assume that the solution to this system can be obtained either analytically or numerically and denote the solution as $u(x, t; G, \mathbf{q})$. Furthermore we assume that we have a set of observations

$$y_j = u(x_j, t_j; G_0, \mathbf{q}_0) + \epsilon_j, \quad j = 1, \dots, n,$$

where G_0 and \mathbf{q}_0 are the true or nominal probability measure and parameters, respectively, and ϵ_j is a realization of the measurement error in the observation process.

Given a set of observations y_j at the points (x_j, t_j) , $j = 1, \dots, N$, we would like to estimate the unknown parameters $\mathbf{q} \in \mathcal{Q} \subset \mathbb{R}^\kappa$ and the unknown distribution $G(\theta) \in \mathcal{P}(\Omega)$, where $\mathcal{P}(\Omega)$ is the set of admissible probability measures on $\Omega \subset \mathbb{R}$. Thus, we would like to solve

$$(G, \mathbf{q}) = \underset{(G, \mathbf{q}) \in (\mathcal{P}(\Omega) \times \mathcal{Q})}{\operatorname{argmin}} J(G, \mathbf{q}), \quad (7.2.1)$$

where

$$J(G, \mathbf{q}) = \sum_{j=1}^N (y_j - u(t_j, x_j; G, \mathbf{q}))^2. \quad (7.2.2)$$

We note that (7.2.1) is an infinite-dimensional optimization problem. Thus, we need to approximate the infinite dimensional space $\mathcal{P}(\Omega)$ with a finite dimensional space $\mathcal{P}^M(\Omega)$ in order to have a computationally tractable finite-dimensional optimization problem

$$(\hat{G}, \hat{\mathbf{q}}) = \underset{(G, \mathbf{q}) \in (\mathcal{P}^M(\Omega) \times \mathcal{Q})}{\operatorname{argmin}} J(G, \mathbf{q}). \quad (7.2.3)$$

We will consider two finite-dimensional spaces, $\mathcal{P}_D^M(\Omega)$ and $\mathcal{P}_S^M(\Omega)$, to approximate $\mathcal{P}(\Omega)$. The space \mathcal{P}_D^M involves the use of Dirac measures, and the space \mathcal{P}_S^M involves the use of piecewise linear splines. We define these two spaces as

$$\mathcal{P}_D^M(\Omega) = \left\{ G \in \mathcal{P}(\Omega) \mid G = \sum_{m=1}^M \alpha_m \Delta_{z_m}, \text{ where } \alpha_m \geq 0 \text{ and } \sum_{m=1}^M \alpha_m = 1 \right\}, \quad (7.2.4)$$

and

$$\mathcal{P}_S^M(\Omega) = \left\{ G \in \mathcal{P}(\Omega) \mid G' = \sum_{m=1}^M \alpha_m l_m(\theta), \text{ where } \alpha_m \geq 0 \text{ and } \sum_{m=1}^M \alpha_m \int_{\Omega_m} l_m(\xi) d\xi = 1 \right\}, \quad (7.2.5)$$

where Δ_{z_m} is a Dirac measure with atom at z_m , and l_m is the m th linear spline element with support Ω_m . With both of these spaces we have reduced the infinite-dimensional problem to a finite-dimensional problem in which we only need to estimate the parameters \mathbf{q} and the weights $\boldsymbol{\alpha} = \{\alpha_m\}_{m=1}^M$. Hence, when using the Delta approximation method we have the minimization problem

$$(\hat{\boldsymbol{\alpha}}, \hat{\mathbf{q}}) = \underset{(\boldsymbol{\alpha}, \mathbf{q}) \in (\mathbb{R}_D^M \times \mathcal{Q})}{\operatorname{argmin}} J(\boldsymbol{\alpha}, \mathbf{q}), \quad (7.2.6)$$

where

$$\mathbb{R}_D^M = \left\{ \boldsymbol{\alpha} = (\alpha_1, \alpha_2, \dots, \alpha_M)^T \mid \alpha_m \geq 0, \text{ and } \sum_{m=1}^M \alpha_m = 1 \right\}.$$

Using the spline method we have the minimization problem

$$(\hat{\boldsymbol{\alpha}}, \hat{\mathbf{q}}) = \underset{(\boldsymbol{\alpha}, \mathbf{q}) \in (\mathbb{R}_S^M \times \mathcal{Q})}{\operatorname{argmin}} J(\boldsymbol{\alpha}, \mathbf{q}), \quad (7.2.7)$$

where

$$\mathbb{R}_S^M = \left\{ \boldsymbol{\alpha} = (\alpha_1, \alpha_2, \dots, \alpha_M)^T \mid \alpha_m \geq 0, \text{ and } \sum_{m=1}^M \alpha_m \int_{\Omega_m} l_m(\xi) d\xi = 1 \right\}.$$

In solving (7.2.6) or (7.2.7) one may wish to use a gradient based nonlinear optimization method, particularly if there are a large number of parameters to be estimated, which is the case in problems where M needs to be taken large in order to obtain a reasonable approximation. This requires the the computation of

$$\nabla J(\boldsymbol{\alpha}, \mathbf{q}) = \left[\frac{\partial J}{\partial \alpha_1}, \dots, \frac{\partial J}{\partial \alpha_M}, \frac{\partial J}{\partial q_1}, \dots, \frac{\partial J}{\partial q_\kappa} \right]^T. \quad (7.2.8)$$

The most common method for the approximating the above partial derivatives is to use a finite difference. If a forward difference is used, then this results in the approximations

$$\begin{aligned} \frac{\partial J}{\partial q_k} &\approx \frac{J(\boldsymbol{\alpha}, \mathbf{q} + h_k \mathbf{e}_k^\kappa) - J(\boldsymbol{\alpha}, \mathbf{q})}{h_k} \\ \frac{\partial J}{\partial \alpha_k} &\approx \frac{J(\boldsymbol{\alpha} + h_k \mathbf{e}_k^N, \mathbf{q}) - J(\boldsymbol{\alpha}, \mathbf{q})}{h_k}, \end{aligned} \quad (7.2.9)$$

where \mathbf{e}_k^m is the k -th standard unit basis vector of length $m = \kappa$ or $m = M$. Since the evaluation of $J(\boldsymbol{\alpha}, \mathbf{q})$ is already required, we must evaluate only the first term in each of the above numerators. This requires a total of $1 + \kappa + M$ evaluations of the cost functional J .

7.2.1 Individual models

In the situation of an individual model, we have a model that depends wholly on a single parameter set. We denote this individual model by $v(x, t; \theta, \mathbf{q})$, where θ is a parameter upon which the individual model is dependent, but where the values are expected to vary across the population. In contrast, the parameters \mathbf{q} are assumed to be population level parameters, i.e., \mathbf{q} is not expected to vary significantly across individuals. In this situation, we can formulate a population level model as

$$u(x, t; G, \mathbf{q}) = \int_{\Omega} v(x, t; \xi, \mathbf{q}) dG(\xi). \quad (7.2.10)$$

If the Dirac mass approximation scheme is used, we obtain the model

$$u(x, t; \boldsymbol{\alpha}, \mathbf{q}) = \sum_{m=1}^M \alpha_m v(x, t; z_m, \mathbf{q}), \quad (7.2.11)$$

and if the spline approximation scheme is used, we obtain

$$u(x, t; \boldsymbol{\alpha}, \mathbf{q}) = \sum_{m=1}^M \alpha_m \int_{\Omega_m} v(x, t; \xi, \mathbf{q}) l_m(\xi) d\xi. \quad (7.2.12)$$

Using either approximation scheme, if one computes the gradient of the objective function according to (7.2.8)–(7.2.9) then $v(t, x; \cdot, \mathbf{q})$ must be evaluated at least $M^2 + (\kappa + 1)M$ times. If a p point quadrature is used to numerical evaluate (7.2.12), then $v(t, x; \cdot, \mathbf{q})$ will be evaluated $p(M^2 + (\kappa + 1)M)$ times.

Observe that

$$\begin{aligned} \frac{\partial J}{\partial q_k} &= -2 \sum_{j=1}^N (y_j - u(x_j, t_j; \boldsymbol{\alpha}, \mathbf{q})) \frac{\partial u(x_j, t_j; \boldsymbol{\alpha}, \mathbf{q})}{\partial q_k} \\ \frac{\partial J}{\partial \alpha_k} &= -2 \sum_{j=1}^N (y_j - u(x_j, t_j; \boldsymbol{\alpha}, \mathbf{q})) \frac{\partial u(x_j, t_j; \boldsymbol{\alpha}, \mathbf{q})}{\partial \alpha_k}. \end{aligned} \quad (7.2.13)$$

The derivatives of $u(x, t; \boldsymbol{\alpha}, \mathbf{q})$ can be obtained from the sensitivity equations [33, 68]. However, for complex models the sensitivity equations can be difficult to derive and in most cases the term $\frac{\partial}{\partial q_k} u(x, t; \boldsymbol{\alpha}, \mathbf{q})$ will still need to be approximated by a finite difference. If a forward difference is used, then we have

$$\frac{\partial u(x, t; \boldsymbol{\alpha}, \mathbf{q})}{\partial q_k} \approx \frac{u(t, x; \boldsymbol{\alpha}, \mathbf{q} + h_k \mathbf{e}_k^\kappa) - u(t, x; \boldsymbol{\alpha}, \mathbf{q})}{h_k}. \quad (7.2.14)$$

Note that we are already required to compute the term $u(x, t; \boldsymbol{\alpha}, \mathbf{q})$ for the cost function $J(\boldsymbol{\alpha}, \mathbf{q})$, so an efficiently implemented optimization scheme will take advantage of this information rather than computing the term multiple times.

Since the coefficients α_k appear linearly in the population level model we can compute the derivatives of $u(x, t; \boldsymbol{\alpha}, \mathbf{q})$ exactly in (7.2.13). Thus,

$$\frac{\partial u(x, t; \boldsymbol{\alpha}, \mathbf{q})}{\partial \alpha_k} = v(t, x; z_k, \mathbf{q}) \quad (7.2.15)$$

if using the Dirac approximation method, and

$$\frac{\partial u(x, t; \boldsymbol{\alpha}, \mathbf{q})}{\partial \alpha_k} = \int_{\Omega_m} v(t, x; \xi, \mathbf{q}) l_m(\xi) d\xi \quad (7.2.16)$$

if using the spline approximation method. In either case, these values are already required to be computed to obtain the cost function $J(\boldsymbol{\alpha}, \mathbf{q})$. Taking advantage of these precomputed values greatly reduces the computational expense in approximating the gradient of $J(\boldsymbol{\alpha}, \mathbf{q})$.

If we compute the gradient according to (7.2.13)–(7.2.16), then only $(\kappa + 1)M$ evaluations of $v(x, t; \cdot, \mathbf{q})$ are required ($p(\kappa + 1)M$ if using a p point quadrature rule to approximate (7.2.16)). Additionally, since we are computing the derivative exactly in this case, there is zero truncation error in the derivative computation of (7.2.15) or (7.2.16) and the only source of truncation error is from (7.2.14).

7.2.2 Aggregate models

In the case of an aggregate model, the model is explicitly dependent upon a probability measure G . Thus, our model $u(x, t; G, \mathbf{q})$ does not have the form of (7.2.10). However, $u(x, t; G, \mathbf{q})$ will include at least one term of the form

$$\int_{\Omega} f(x, t; \xi; \mathbf{q}) dG(\xi), \quad (7.2.17)$$

and again we will be able to exploit the linearity of the approximation terms to reduce computational times. Using the PMF approximation, the model reduces to $u(x, t; \boldsymbol{\alpha}, \mathbf{q})$, which now depends on a term of the form

$$\sum_{m=1}^M \alpha_m f(x, t; z_m, \mathbf{q}), \quad (7.2.18)$$

if using the Dirac approximation scheme, and if the spline approximation scheme is used we obtain

$$\sum_{m=1}^M \alpha_m \int_{\Omega_m} f(x, t; \xi, \mathbf{q}) l_m(\xi) d\xi. \quad (7.2.19)$$

Hence, just as in the case of using an individual model, computing the gradient of $J(\boldsymbol{\alpha}, \mathbf{q})$ according to (7.2.13) requires $(\kappa + 1)M$ evaluations of $f(x, t; \cdot, \mathbf{q})$, whereas computing the gradient according to (7.2.9) requires $M^2 + (\kappa + 1)M$ evaluations of $f(x, t; \cdot, \mathbf{q})$. Again, as before if using a p point quadrature rule to approximate (7.2.19) then the number of evaluations is multiplied by p .

7.3 Example: Sinko-Streifer Model

Consider the case where an individual Sinko-Streifer model can be used to model the size-structured population. The model provided here is adapted from [14] where the goal was to estimate individual growth rates for a mosquito fish population, but only aggregate data was available. A similar problem arose in the population modeling examples for shrimp [24].

We assume that the growth rate varies according to each individual, but the death (or removal rate) is constant across the population. For simplicity we assume that there is no

recruitment into the system. The model is given by

$$\begin{aligned}
\frac{\partial v}{\partial t} + \frac{\partial}{\partial x}(gv) &= -\mu v, \quad x_0 < x < x_1, \quad t > 0 \\
v(x, 0) &= \Phi(x) \\
g(x_0, t)v(x_0, t) &= 0 \\
g(x_1, t) &= 0,
\end{aligned} \tag{7.3.1}$$

where $v(t, x)$ represents the population density, and t and x denote time and size, respectively, $g(x)$ is the size dependent growth rate term, and μ is the removal rate. From [14], the admissible growth rates of an individual fish we will consider are of the form

$$g(x; \theta, \gamma) = \begin{cases} \theta(\gamma - x), & x_0 \leq x \leq \gamma, \\ 0, & \text{otherwise,} \end{cases}$$

where θ and γ denote the intrinsic growth rate and maximum size, respectively. For simplicity we assume that $\gamma = 1$. The collection of admissible growth rates is given by

$$\mathcal{G} = \{g(x; \theta) \mid \theta \in \Omega\},$$

where Ω is a compact set.

The solution to (7.3.1) can be found using the method of characteristics. Data was simulated according to

$$y_{ij} = \int_{\Omega} v(x_i, t_j; \theta, \mu) dG_0(\theta) + \epsilon_{ij}, \quad i = 1, \dots, N_x, \quad j = 1, \dots, N_t \tag{7.3.2}$$

where $v(x, t; \theta, \mu)$ is the solution to (7.3.1), and ϵ_{ij} are realizations of a normally distributed random variable with 0 mean and variance 0.01. The distribution G_0 was taken to be a normal distribution with mean 4.5 and variance 0.25, and the death rate was chosen to be $\mu_0 = 1.0$. The initial condition was taken as

$$\Phi(x) = \begin{cases} \sin^2 10\pi x & 0 \leq x \leq 0.1 \\ 0 & x > 0.1 \end{cases} \tag{7.3.3}$$

and is assumed to be known. Hence, in this example we need to estimate the probability measure G and the removal rate μ . G is estimated using the Delta approximation scheme, where the nodes were placed in a uniform grid over the interval [3, 6].

The Matlab routine `fmincon` was used to preform the resulting optimization problems for 100 independent simulated data sets. We considered 2 methods for computing the gradients.

For method 1, we computed the gradient using a forward difference of the objective function $J(\boldsymbol{\alpha}, \mu)$. This method is equivalent to the default method for computing the gradient if the user does not supply the gradient to `fmincon`. For method 2 we computed the gradient according to (7.2.13)–(7.2.15). In Figure 7.1 we depict the average cpu time required to complete the optimization using both methods for 100 independent data sets as M , the number of elements in the approximation scheme, increases.

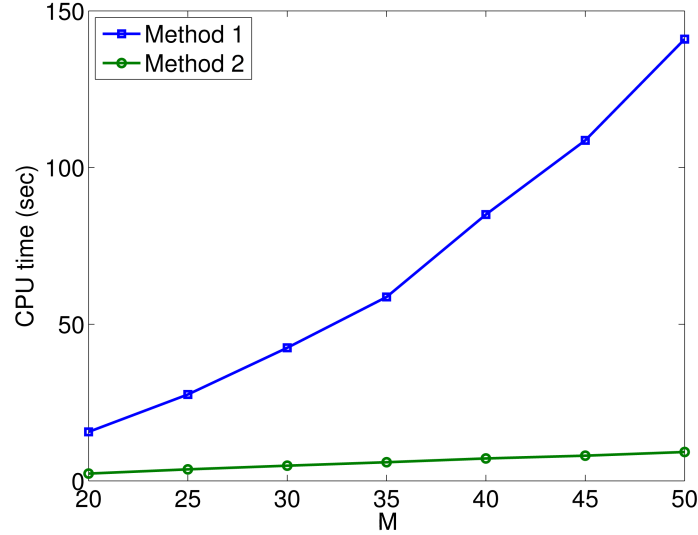


Figure 7.1: The average cpu time (for 100 independent data sets) required to complete the optimization as M increases using both methods.

Using method 1 requires $M^2 + M(\kappa + 1)$ evaluations of $v(x, t; \theta, \mu)$, whereas method 2 only requires $(\kappa + 1)M$ evaluations. This agrees with Figure 7.1 where method 1 exhibits an approximately quadratic increase in time to perform the optimization as M increases, and method 2 has an approximately linear increase in time.

7.4 Example: Reflectance Spectroscopy Model

Here we describe an example from [17] where the model is an aggregate model. In this project, the goal is to develop a noninvasive technique to characterize the degradation of a complex nonmagnetic dielectric material by assessing the small physical and chemical changes in the material using reflectance spectroscopy. This involves determining the components of the permittivity of the dielectric medium using the measured spectral responses. The distributed

relative permittivity of the dielectric medium is described by

$$\widehat{\varepsilon}_r(k; G, \mathbf{q}) = \varepsilon_\infty - \int_{\Omega} \frac{k_p^2}{k^2 - ik/\tau - k_0^2} dG(k_0). \quad (7.4.1)$$

In the above equation, ε_∞ denotes the relative permittivity of the dielectric medium at infinite frequency, k is the wavenumber ($k = \omega/(2\pi c)$, where ω is the angular frequency and c is the speed of light), k_0 represents the resonance wavenumbers, and τ denotes the relaxation time. The composite parameter k_p is given by $k_p = k_0\sqrt{\varepsilon_s - \varepsilon_\infty}$ with ε_s being the relative permittivity of the medium at zero frequency, $i = \sqrt{-1}$ is the imaginary unit, and $\theta = k_0 \in \Omega \subset \mathbb{R}$. If we assume that a monochromatic uniform wave is incident at an angle of $\phi = 45^\circ$ on a plane interface between free space and a nonmagnetic dielectric medium with the electric field composed of the parallel and perpendicular polarizations in equal weights, then the reflection coefficient is given by

$$R(k; G, \mathbf{q}) = \frac{1}{2} (|r_\perp(k; G, \mathbf{q})|^2 + |r_\parallel(k; G, \mathbf{q})|^2), \quad (7.4.2)$$

where

$$r_\perp(k; G, \mathbf{q}) = \frac{\cos \phi - \sqrt{\widehat{\varepsilon}_r(k; G, \mathbf{q}) - \sin^2 \phi}}{\cos \phi + \sqrt{\widehat{\varepsilon}_r(k; G, \mathbf{q}) - \sin^2 \phi}}, \quad (7.4.3)$$

and

$$r_\parallel(k; G, \mathbf{q}) = \frac{\sqrt{1 - \sin^2 \phi / \widehat{\varepsilon}_r(k; G, \mathbf{q})} - \sqrt{\widehat{\varepsilon}_r(k; G, \mathbf{q})} \cos \phi}{\sqrt{1 - \sin^2 \phi / \widehat{\varepsilon}_r(k; G, \mathbf{q})} + \sqrt{\widehat{\varepsilon}_r(k; G, \mathbf{q})} \cos \phi}. \quad (7.4.4)$$

In this application, the reflectance $R(k; G, \mathbf{q})$ is measured at various wave numbers k in order to determine the distribution $G(\theta) = G(k_0)$ of resonance wave numbers as well as the parameters $\mathbf{q} = [\varepsilon_s, \varepsilon_\infty, \tau]^T$. Data sets which were collected using a Bruker Vertex 80V FTIR spectrometer have been provided by researchers at the Air Force Research Lab at Wright-Patterson Air Force Base. For a full description of the model, data collection, and subsequent inverse problems, see [17].

In this case the spline approximation scheme was used to estimate the probability measure $G(\theta)$, thus the permittivity model can be written as

$$\widehat{\varepsilon}_r(k; G, \mathbf{q}) = \varepsilon_\infty - \sum_{m=1}^M \alpha_m \int_{\Omega_m} \frac{\theta^2(\varepsilon_s - \varepsilon_\infty)}{k^2 - ik/\tau - \theta^2} l_m(\theta) d\theta. \quad (7.4.5)$$

Again we use two methods to compute the gradient of $J(\alpha, \mathbf{q})$, where method 1 computes the gradient according to (7.2.9) and method 2 employs (7.2.13) where the integral terms in (7.4.5) were computed only once. In Figure 7.2 we show the average over 100 trials of the cpu time required to perform the first 10 iterations of the optimization problems as M is increased. As expected, we see that method 1 increases quadratically and method 2 linearly.

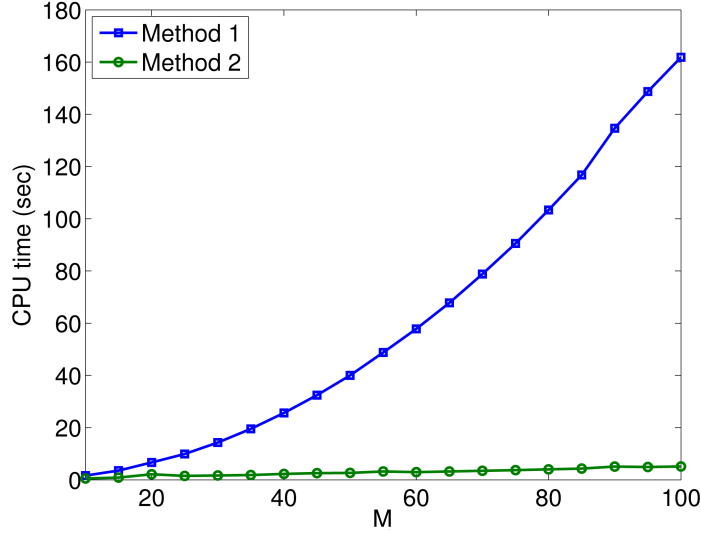


Figure 7.2: The average cpu time (for 100 independent data sets) required to compute the first 10 iterations of the optimization problems as M increases using both methods.

7.5 Conclusions

In this chapter we consider the case of non-parametric estimation of a probability measure under the Prohorov Metric Framework in a least squares problem. It is demonstrated that the gradient computation can be reduced by exploiting the linearity of the coefficients to be estimated which appear in the approximation schemes under the PMF.

For individual models the number of forward solves of the underlying model v is reduced from $\mathcal{O}(M^2)$ to $\mathcal{O}(M)$, where M is the number of elements in the approximation. Due to the use of the exact partial derivatives in computing the gradient, there is no truncation error present from a finite differencing of the objective function. An example using a Sinko-Streifer model with aggregate data is discussed and the expected linear increase in cpu time as M increases was observed.

For aggregate models the reduction of computational expense in computing the gradient of the objective function is not as straight forward. This is due directly to the fact that the model depends *explicitly* on the probability measure for aggregate models. However, we still can reduce the number of evaluations of the kernel function f in (7.2.17) from $\mathcal{O}(M^2)$ to $\mathcal{O}(M)$. The practical degree to which any speed up can be obtained in the inverse problem depends directly on the complexity of the kernel function f . If f is relatively cheap to evaluate, then the speed up may be negligible, even though we have reduced the number of evaluations. However, if f is costly to evaluate, then the speed up may be significant. We demonstrated this in an example arising in an application using reflectance spectroscopy, and the cpu time was observed

to have the expected linear behavior.

Concluding Remarks

In this work we first introduced a standard model for the reflection coefficient due to perpendicular and parallel polarizations. We considered a Lorentz oscillator model, which can be used to describe the complex permittivity of a complex dielectric material. The standard permittivity model was extended to account for the unknown heterogenous structure of a material such as a ceramic matrix composite. This extension was completed by imposing an unknown probability measure on a subset of the dielectric parameters.

The estimation of the probability measure was carried out through the Prohorov metric framework, which is a means for a nonparametric estimation. Once we carefully established both the theoretical and computational tools necessary for the estimation problem, we compared two competing approximation schemes, one which uses Dirac measures, and the second uses linear splines. Both of these methods were compared to a competing permittivity model developed by Efimov. All three methods provided adequate model fits, however, the spline approximation lends itself to the most discernible results since it estimates the unknown *density* directly.

Care was taken to provide the uncertainty quantification of the fixed parameters present in the permittivity model, as well as constructing a confidence band about the estimated density/distribution. The uncertainty was computed using asymptotic analysis, bootstrapping and Bayesian estimation, and it was observed that all three methods provided similar results.

The current Dirac measure approximation scheme was initially observed to be ill-posed for the particular application of focus in this work. This was resolved by allowing the node locations for the Dirac masses to vary as well. Additionally, the efficiency of the gradient computations needed for the gradient based optimization routine was improved upon by removing redundancies present

in the standard finite difference approach. This lead to a reduction in computational time from $\mathcal{O}(M^2)$ to $\mathcal{O}(M)$, with M being the number of approximating elements. These results may have implications in improving the computational efficiency of Bayesian estimation. Recently, there has been an interest in the Hamiltonian Monte Carlo method which uses gradient approximations to drive the random walk of the Monte Carlo procedure. When applicable, this leads to a faster convergence of the Monte Carlo chain. Implementing the efficient gradient calculation provided for this problem may lead to a significant speed up for the Bayesian estimation method, resulting in computational times which are more competitive to the WLS approach.

A major contribution of this work was the development of the statistical model used in the estimation problem with the data provided by Wright-Patterson Air Force Base. Through the use of the difference based methods, a methodology was developed to aid in determining if a statistical model discrepancy is present. This approach does not require the computation of any inverse problems, and thus is extremely efficient. Using these methods we established a weight least squares error model to encapsulate our belief of the measurement error process. Implementing the WLS model lead to residual plots which displayed the desired i.i.d. behavior, thus validating our uncertainty quantification arguments.

All of this was culminated in our ability to detect significantly higher relative levels of the oxidation products SiO_2 and SiN for CMC samples which underwent longer heat treatment. We remark that our results should be validated by collecting the reflectance from samples heated for various amounts of time. At this point we have only considered samples which were heated for either 10 or 100 hours. Analyzing samples heated in the interim times would lead to a better understanding of the resolution to which we can detect the oxidation products. Furthermore, it may prove useful to develop a time dependent model for the oxidation of the material, where the measurable is the level of SiO_2 and SiN present, as estimated by our reflectance model. If an accurate model can be constructed, even an empirical model may be suitable, then it may be used to better understand and predict the oxidation behavior of the CMCs under inspection.

REFERENCES

- [1] K. Adoteye, H.T. Banks, K.B. Flores, and G.A. LeBlanc. Estimation of time-varying mortality rates using continuous models for daphnia magna. *Applied Mathematics Letters*, 44:12–16, 2015.
- [2] P.D. Arendt, D.W. Apley, and W. Chen. Quantification of model uncertainty: Calibration, model discrepancy, and identifiability. *Journal of Mechanical Design*, 134(10):100908, 2012.
- [3] C.A. Balanis. *Advanced engineering electromagnetics*. 1989.
- [4] P. Baldus, M. Jansen, and D. Sporn. Ceramic fibers for matrix composites in high-temperature engine applications. *Science*, 285:699–703, 1999.
- [5] H.T. Banks. *Functional analysis framework for modeling, estimation and control in science and engineering*. Chapman and Hall/CRC Press, Boca Raton, FL, 2012.
- [6] H.T. Banks, J.E. Banks, N. Murad, J.A. Rosenheim, and K. Tillman. Modelling pesticide treatment effects on *lygus hesperus* in cotton fields. *Center for Research in Scientific Computation Technical Report CRSC-TR15-09, NC State University, Raleigh, NC*, 2015.
- [7] H.T. Banks, J.E. Banks, J. Rosenheim, and K. Tillman. Modeling populations of *lygus hesperus* on cotton fields in the san joaquin valley of california: The importance of statistical and mathematical model choice. *Journal of Biological Dynamics*. (in press).
- [8] H.T. Banks, R. Baraldi, K. Cross, K. Flores, C. McChesney, L. Poag, and E. Thorpe. Uncertainty quantification in modeling hiv viral mechanics. *Mathematical Biosciences and Engineering*, 12:937–964, 2015.
- [9] H.T. Banks and K.L. Bihari. Modeling and estimating uncertainty in parameter estimation. *Inverse Problems*, 17:95–111, 2001.
- [10] H.T. Banks, V.A. Bokil, and N.L. Gibson. Analysis of stability and dispersion in a finite

- element method for debye and lorentz dispersive media. *Center for Research in Scientific Computation Technical Report CRSC-TR06-21, NC State University, Raleigh, NC*, 2006.
- [11] H.T. Banks, V.A. Bokil, and N.L. Gibson. Parameter estimation versus homogenization techniques in time-domain characterization of composite dielectrics. *Journal of Inverse and Ill-posed Problems*, 15(2):117–135, 2007.
 - [12] H.T. Banks and D.M. Bortz. Inverse problems for a class of measure dependent dynamical systems. *Journal of Inverse and Ill-posed Problems*, 13:103–121, 2005.
 - [13] H.T. Banks, D.M. Bortz, and S.E. Holte. Incorporation of variability into the modeling of viral delays in hiv infection dynamics. *Mathematical Biosciences*, 183(1):63–91, 2003.
 - [14] H.T. Banks, L.W. Botsford, F. Kappel, and C. Wang. Modeling and estimation in size structured population models. In *Proceedings 2nd Course on Mathematical Ecology*, pages 521–541. Wold Press, 1988.
 - [15] H.T. Banks, M.W. Buksas, and T. Lin. *Electromagnetic material interrogation using conductive interfaces and acoustic wavefronts*, volume 21. SIAM, Philadelphia, PA, 2000.
 - [16] H.T. Banks and J. Catenacci. Aggregate data and the prohorov metric framework: efficient gradient computation. *Applied Mathematics Letters*, 56:1–9, 2016.
 - [17] H.T. Banks, J. Catenacci, and A. Criner. Quantifying the degradation in thermally treated ceramic matrix composites. *The 17th International Symposium on Applied Electromagnetics and Mechanics (ISEM2015)*. (in press).
 - [18] H.T. Banks, J. Catenacci, and S. Hu. Use of difference-based methods to explore statistical and mathematical model discrepancy in inverse problems. *Journal of Inverse and Ill-Posed Problems*. (in press).
 - [19] H.T. Banks, J. Catenacci, and S. Hu. Asymptotic properties of probability measure estimators in a nonparametric model. *SIAM/ASA Journal on Uncertainty Quantification*, 3:417–433, 2015.

- [20] H.T. Banks, J. Catenacci, and S. Hu. Estimation of distributed parameters in permittivity models of composite dielectric materials using reflectance. *Journal of Inverse and Ill-Posed Problems*, 23(5):491–509, 2015.
- [21] H.T. Banks, J. Catenacci, and S. Hu. Method comparison for estimation of distributed parameters in permittivity models using reflectance. *Eurasian Journal of Mathematical and Computer Applications*, 3(2):4–24, 2015.
- [22] H.T. Banks, J. Catenacci, S. Hu, and Z.R. Kenz. Decomposition of permittivity contributions from reflectance using mechanism models. In *American Control Conference (ACC)*, 2014, pages 367–372. IEEE, 2014.
- [23] H.T. Banks and J.L. Davis. A comparison of approximation methods for the estimation of probability distributions on parameters. *Applied Numerical Mathematics*, 57:753–777, 2007.
- [24] H.T. Banks, J.L. Davis, S.L. Ernstberger, S. Hu, E. Artimovich, and A.K. Dhar. Experimental design and estimation of growth rate distributions in size-structured shrimp populations. *Inverse Problems*, 25(9):095003, 2009.
- [25] H.T. Banks, M. Doumic, C. Kruse, S. Prigent, and H. Rezaei. Information content in data sets for a nucleated-polymerization model. *Journal of Biological Dynamics*, 2015.
- [26] H.T. Banks and B.G. Fitzpatrick. Statistical methods for model comparison in parameter estimation problems for distributed systems. *Journal of Mathematical Biology*, 28(5):501–527, 1990.
- [27] H.T. Banks and B.G. Fitzpatrick. Estimation of growth rate distributions in size-structured population models. *Quarterly of Applied Mathematics*, 49:215–235, 1998.
- [28] H.T. Banks, B.G. Fitzpatrick, L.K. Potter, and Y. Zhang. *Estimation of probability distributions for individual parameters using aggregate population data*. Springer, 1999.
- [29] H.T. Banks and N.L. Gibson. Well-posedness in maxwell systems with distributions of polarization relaxation parameters. *Applied Mathematics Letters*, 18(4):423–430, 2005.

- [30] H.T. Banks and N.L. Gibson. Electromagnetic inverse problems involving distributions of dielectric mechanisms and parameters. *Quarterly of Applied Mathematics*, 64:749–795, 2006.
- [31] H.T. Banks, S.L. Grove, S. Hu, and Y. Ma. A hierarchical bayesian approach for parameter estimation in hiv models. *Inverse Problems*, 21(6):1803–1822, 2005.
- [32] H.T. Banks, S. Hu, Z.R. Kenz, C. Kruse, S. Shaw, J.R. Whiteman, M.P. Brewin, S.E. Greenwald, and M.J. Birch. Material parameter estimation and hypothesis testing on a 1d viscoelastic stenosis model: Methodology. *Journal of Inverse and Ill-Posed Problems*, 21(1):25–57, 2013.
- [33] H.T. Banks, S. Hu, and W.C. Thompson. *Modeling and Inverse Problems in the Presence of Uncertainty*. Taylor/Francis-Chapman/Hall-CRC Press, Boca Raton, FL, 2014.
- [34] H.T. Banks, D.F. Kapraun, K.G. Link, W.C. Thompson, C. Peligero, J. Argilaguet, and A. Meyerhans. Analysis of variability in estimates of cell proliferation parameters for cyton-based models using cfse-based flow cytometry data. *Journal of Inverse and Ill-posed Problems*, 23(2):135–171, 2015.
- [35] H.T. Banks, D.F. Kapraun, C. Peligero, J. Argilaguet, and A. Meyerhans. Evaluating the importance of mitotic asymmetry in cyton-based models for cfse-based flow cytometry data. *International Journal of Pure and Applied Mathematics*, 100(1):131–156, 2015.
- [36] H.T. Banks, D.F. Kapraun, W.C. Thompson, C. Peligero, J. Argilaguet, and A. Meyerhans. A novel statistical analysis and interpretation of flow cytometry data. *Journal of Biological Dynamics*, 7(1):96–132, 2013.
- [37] H.T. Banks, Z.R. Kenz, and W.C. Thompson. A review of selected techniques in inverse problem nonparametric probability distribution estimation. *Journal of Inverse and Ill-Posed Problems*, 20:429–460, 2012.

- [38] H.T. Banks and K. Kunisch. *Estimation techniques for distributed parameter systems*. Birkhäuser, Boston, 1989.
- [39] H.T. Banks and G.A. Pinter. A probabilistic multiscale approach to hysteresis in shear wave propagation in biotissue. *Multiscale Modeling & Simulation*, 3:395–412, 2005.
- [40] H.T. Banks and H.T. Tran. *Mathematical and experimental modeling of physical and biological processes*. CRC Press, Boca Raton, FL, 2009.
- [41] P. Billingsley. *Convergence of Probability Measures*. Wiley & Sons, New York, 1968.
- [42] J.G. Blaschak and J. Fanzen. Precursor propagation in dispersive media from short-rise-time pulses at oblique incidence. *Journal of the Optical Society of America A*, 12:1501–1512, 1995.
- [43] G. Bocharov, T. Luzyanina, J. Cupovic, and B. Ludewig. Asymmetry of cell division in cfse-based lymphocyte proliferation analysis. *Frontiers in Immunology*, 4, 2013.
- [44] L.D. Brown and M. Levine. Variance estimation in nonparametric regression via the difference sequence method. *The Annals of Statistics*, 35(5):2219–2232, 2007.
- [45] J. Brynjarsdóttir and A. O’Hagan. Learning about physical parameters: The importance of model discrepancy. *Inverse Problems*, 30(11):114007, 2014.
- [46] K.P. Burnham and D.R. Anderson. *Model selection and inference: a practical information-theoretical approach*. Springer-Verlag, New York, 2 edition, 2002.
- [47] L.J. Byrne, D.J. Cole, B.S. Cox, M.S. Ridout, B.J. Morgan, and M.F. Tuite. The number and transmission of [psi+] prion seeds (propagons) in the yeast *saccharomyces cerevisiae*. *PLoS One*, 4(3):e4670, 2009.
- [48] R.J. Carroll and D. Ruppert. *Transformation and weighting in regression*, volume 30. CRC Press, 1988.

- [49] N. Choudhuri, S. Ghosal, and A. Roy. Bayesian methods for function estimation. *Handbook of Statistics*, 25:373–414, 2005.
- [50] A.T. Cooney, R.Y. Flattum-Riemers, and B.J. Scott. Characterization of material degradation in ceramic matrix composites using infrared reflectance spectroscopy. In *Review of progress in quantitative nondestructive evaluation: Volume 30A; Volume 30B*, volume 1335, pages 950–955. AIP Publishing, 2011.
- [51] B.S. Cox, F. Ness, and M.F. Tuite. Analysis of the generation and segregation of propagons: entities that propagate the $[\psi+]$ prion in yeast. *Genetics*, 165(1):23–33, 2003.
- [52] M. Davidian. Nonlinear models for univariate and multivariate response. <http://www4.stat.ncsu.edu/davidian/courses.html>, 2007.
- [53] M. Davidian and D. Giltinan. Nonlinear models for repeated measurement data: An overview and update. *Journal of Agricultural, Biological, and Environmental Statistics*, 8:387–419, 2003.
- [54] H. Dette, A. Munk, and T. Wagner. Estimating the variance in nonparametric regression – what is a reasonable choice? *Journal of the Royal Statistical Society: Series B (Statistical Methodology)*, 60(4):751–764, 1998.
- [55] J. Doherty and D. Welter. A short exploration of structural noise. *Water Resources Research*, 46(5), 2010.
- [56] C.J. Doona, F.E. Feeherry, and E.W. Ross. A quasi-chemical model for the growth and death of microorganisms in foods by non-thermal and high-pressure processing. *International Journal of Food Microbiology*, 100(1):21–32, 2005.
- [57] R.M. Dudley. *Real Analysis and Probability*. Cambridge University Press, Cambridge, UK, 2002.
- [58] A.M. Efimov. *Optical Constants of Inorganic Glasses*. CRC Press, Boca Raton, FL, 1995.

- [59] A.M. Efimov. Quantitative ir spectroscopy: Applications to studying glass structure and properties. *Journal of Non-Crystalline Solids*, 203:1–11, 1996.
- [60] A.M. Efimov. Vibrational spectra, related properties, and structure of inorganic glasses. *Journal of Non-Crystalline Solids*, 253:95–118, 1999.
- [61] A.M. Efimov and E.G. Makarova. Dispersion equation for the complex dielectric constant of vitreous solids and dispersion analysis of their reflection spectra. *Fizika i Khimiya Stekla (Journal of Applied Spectroscopy)*, 11(4):385–401, 1985.
- [62] B. Efron and R.J. Tibshirani. *An introduction to the bootstrap*. CRC press, 1994.
- [63] J.I. Eldridge, C.M. Spuckler, and R.E. Martin. Monitoring delamination progression in thermal barrier coatings by mid-infrared reflectance imaging. *International Journal of Applied Ceramic Technology*, 3(2):94–104, 2006.
- [64] R.Y. Flattum and A.T. Cooney. Non-destructive evaluation of degradation in eb-pvd thermal barrier coatings by infrared reflectance spectroscopy. In *Review of progress in quantitative nondestructive evaluation: volume 32*, volume 1511 (1), pages 1125–1132. AIP Publishing, 2013.
- [65] L. Giacomazzi and A. Pasquarello. Vibrational spectra of vitreous SiO_2 and vitreous GeO_2 from first principles. *Journal of Physics: Condensed Matter*, 19:112–121, 2007.
- [66] D.J. Griffiths. *Introduction to electrodynamics*. Prentice Hall, Upper Saddle River, New Jersey, 3 edition, 1999.
- [67] D.F. Kapraun. *Cell proliferation models, CFSE-based flow cytometry data, and quantification of uncertainty*. PhD thesis, North Carolina State University, Raleigh, NC, 2014.
- [68] C.T. Kelley. *Iterative methods for optimization*, volume 18. SIAM, 1999.
- [69] A.G. Kukush. Asymptotic normality of the estimator of an infinite-dimensional parameter in the model with a smooth regression function. *Mathematical Methods of Statistics*, pages

343–356, 1996.

- [70] M. Laine. MCMC toolbox for matlab, 2015. URL: <http://helios.fmi.fi/~lainema/mcmc/>.
- [71] M. Levine. Bandwidth selection for a class of difference-based variance estimators in the nonparametric regression: a possible approach. *Computational Statistics & Data Analysis*, 50(12):3405–3431, 2006.
- [72] T. Luzyanina, J. Cupovic, B. Ludewig, and G. Bocharov. Mathematical models for cfse labelled lymphocyte dynamics: asymmetry and time-lag in division. *Journal of Mathematical Biology*, 69(6-7):1547–1583, 2014.
- [73] H.G. Müller and U. Stadtmüller. Estimation of heteroscedasticity in regression analysis. *The Annals of Statistics*, pages 610–625, 1987.
- [74] H. Ohnabe, S. Masaki, M. Onozuka, K. Miyahara, and T. Sasai. Potential application of ceramic matrix composites to aero-engine components. *Composites Part A: Applied Science and Manufacturing*, 30(4):489–496, 1999.
- [75] P. Olofsson and S.S. Sindi. A crump-mode-jagers branching process model of prion loss in yeast. *Journal of Applied Probability*, 51(2):453–465, 2014.
- [76] OPUS, Ettlingen, Germany. *Bruker OPUS spectroscopic software reference manual*, 4.2 edition, 2003.
- [77] K.J. Palmer, M.S. Ridout, and B.J. Morgan. Kinetic models of guanidine hydrochloride-induced curing of the yeast [psi+] prion. *Journal of Theoretical Biology*, 274(1):1–11, 2011.
- [78] S.R. Pina, L.C. Pardini, and I.V. Yoshida. Carbon fiber/ceramic matrix composites: processing, oxidation and mechanical properties. *Journal of Material Science*, 42:4245–4253, 2007.

- [79] Y.V. Prohorov. Convergence of random processes and limit theorems in probability theory. *Theory of Probability & Its Applications*, 1:157–214, 1956.
- [80] G. Qi, C. Zhang, H. Hu, F. Cao, S. Wang, Y. Jiang, and B. Li. Crystallization behavior of three-dimensional silica fiber reinforced silicon nitride composite. *Journal of Crystal Growth*, 284:293–296, 2005.
- [81] V. Raman, G. Bhatia, P.R. Sengupta, A.K. Srivastava, and K.N. Sood. Synthesis of silicon carbide nanorods from mixture of polymer and sol-gel silica. *Journal of Material Science*, 42:5891–5895, 2007.
- [82] E.W. Ross, I.A. Taub, C.J. Doona, F.E. Feeherry, and K. Kustin. The mathematical properties of the quasi-chemical model for microorganism growth–death kinetics in foods. *International Journal of Food Microbiology*, 99(2):157–171, 2005.
- [83] S.I. Rubinow. *Introduction to mathematical biology*. John Wiley & Sons, New York, NY, 1975.
- [84] G.A. Seber and C.J. Wild. *Nonlinear regression*. Wiley, Hoboken, NJ, 2003.
- [85] L.A. Segel. *Mathematical models in molecular and cellular biology*, 1980.
- [86] L.A. Segel. *Modeling dynamic phenomena in molecular and cellular biology*. Cambridge University Press, 1984.
- [87] V. Serment-Moreno, G. Barbosa-Cánovas, J.A. Torres, and J. Welti-Chanes. High-pressure processing: kinetic models for microbial and enzyme inactivation. *Food Engineering Reviews*, 6(3):56–88, 2014.
- [88] R.C. Smith. *Uncertainty quantification: theory, implementation, and applications*, volume 12. SIAM, 2013.
- [89] M. Tanaka, S.R. Collins, B.H. Toyama, and J.S. Weissman. The physical basis of how prion conformations determine strain phenotypes. *Nature*, 442(7102):585–589, 2006.

- [90] W.C. Thompson. *Partial differential equation modeling of flow cytometry data from CFSE-based proliferation assays*. PhD thesis, North Carolina State University, Raleigh, NC, 2011.
- [91] T. Tong, A. Liu, and Y. Wang. Relative errors of difference-based variance estimators in nonparametric regression. *Communications in Statistics-Theory and Methods*, 37(18):2890–2902, 2008.
- [92] J.A. Vrugt, C.G.H. Diks, H.V. Gupta, W. Bouten, and J.M. Verstraten. Improved treatment of uncertainty in hydrologic modeling: Combining the strengths of global optimization and data assimilation. *Water Resources Research*, 41(1), 2005.
- [93] J. Warga. *Optimal control of differential and functional equations*. Academic Press, New York, 1972.
- [94] H. White. Consequence and detection of misspecified nonlinear regression models. *Journal of the American Statistical Association*, 76:419–433, 1981.
- [95] W. Whitt. *Stochastic-process limits*. Springer-Verlag, New York, 2002.